FERMILAB-TM-1696

Proceedings of the Fermilab III Instabilities Workshop

Held at Fermilab, June 25-29, 1990

Edited by
S. Peggs and M. Harvey

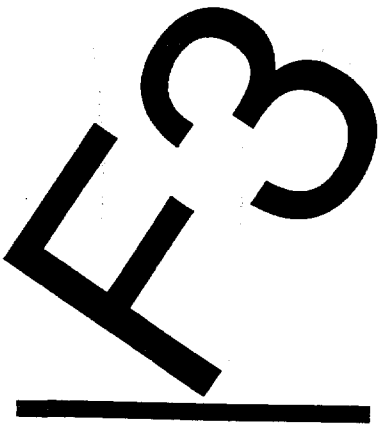

Fermi National Accelerator Laboratory
Batavia, Illinois

Operated by Universities Research Association, Inc.
Under contract with the United States Department of Energy

TABLE OF CONTENTS

TRANSITION CROSSING INSTABILITIES

TRANSVERSE INSTABILITIES AND IMPEDANCES

PREFACE

The purpose of the Fermilab III upgrade program is to extend the discovery potential of the Fermilab accelerator complex during the period leading up to the use of the SSC, and to leave Fermilab in a flexible position at the start of the SSC era. In particular, the collider physics goal is to achieve a luminosity greater than 5×10^{31} cm^{-2} sec^{-1}, in order to

1) guarantee observation of the top quark within the framework of the standard model,
2) double the mass reach for as yet unobserved particles, and
3) reach the factory domain in the production of W's, b's, and t's.

At present (1988-89) the maximum luminosity is about 1.6×10^{30} cm^{-2} sec^{-1}.

The upgrade program affects all of the Fermilab accelerators. During collider run III, new low beta optics will operate in the Tevatron, the proton and antiproton orbits will be separated to allow for a larger number of bunches, and there will be significant improvements in the Antiproton Source. A rebuilt Linac will inject protons into the Booster at twice the present energy, during collider run IV. A new synchrotron, the 150 GeV Main Injector, will replace the Main Ring in delivering high energy protons and antiprotons to the Tevatron, during collider run V.

In order to achieve the goal of a factor of 30 increase in maximum luminosity, all of the Fermilab accelerators will be stressed further by higher performance demands. The Fermilab III Instabilities Workshop was created as a forum in which experts and friends from accelerator laboratories around the world could convene to discuss and evaluate the threat posed by the various instabilities which might be expected.

Four major areas of potential instabilities were identified, and were separately attacked by working groups. The groups were Ion Trapping, Longitudinal Instabilities and Impedances, Transition Crossing, and Transverse Instabilities and Impedances. The proceedings which follow are also organized under the same four headings. They record the work that was performed during and immediately after the workshop, and constitute a reference source which will be valuable for a long time to come.

Steve Peggs

ACKNOWLEDGEMENTS

We would like to thank the many people who contributed to the successful smooth running of the workshop. In particular, we would like to recognize the patience and dedication of the leaders and scientific secretaries of the working groups, Daniel Boussard, Swapan Chattophadhyay, SY Lee, Alain Poncet, Gerry Jackson, Jim MacLachlan, Bill Ng, and Jamie Rosenzweig. Eileen Singer played a crucial role in helping to provide office support. The workshop banquet at Chez Leon was deliciously well prepared, thanks to the visible and invisible staff. The staff at the Pheasant Run conference center were always cooperative and helpful, beyond a strict definition of their responsibilities.

Finally, the editors would like to thank the workshop participants, and the contributors to the proceedings, for the high quality of their workmanship. We hope that they are as pleased with the final product as we are.

Marge Harvey,
Steve Peggs

LIST OF PARTICIPANTS

NAME	WORKING GROUP	HOME INSTITUTION
Bogacz, Alex	Transition	Fermilab
Boussard, Daniel	Longitudinal (leader)	CERN
Cappi, Roberto	Transverse	CERN
Chattophadhyay, Swapan	Transverse (leader)	LBL
Chou, Weiren		SSC
Colestock, Pat	Transverse	Fermilab
Crisp, Jim		Fermilab
Dugan, Gerry		Fermilab
Gai, Wei		ANL
Griffin, Jim	Longitudinal	Fermilab
Harfoush, Fady	Transition	Fermilab
Harkay, Kathy		Fermilab
Harrison, Mike		Fermilab
Holmes, Steve		Fermilab
Jackson, Gerry	Transverse (secretary)	Fermilab
Kourbanis, Ioanis	Transition	Fermilab
Lee, SY	Transition (leader)	U. of Indiana
Linnecar, Trevor	Longitudinal	CERN-SL
Lu, Xianping		Fermilab
MacLachlan, Jim	Longitudinal (secretary)	Fermilab
Marriner, John		Fermilab
Marsh, Bill	Ion	Fermilab
Martin, Phil		Fermilab
Meisner, Keith	Transition	Fermilab
Neuffer, Dave		LANL
Ng, Bill	Transition (secretary)	Fermilab
Ostiguy, Jean-Francois		Fermilab
Peggs, Steve	Transition	Fermilab
Pires, Rui-Alves	Ion	CERN
Poncet, Alain	Ion (leader)	CERN
Rosenzweig, Jamie	Ion (secretary)	Fermilab
Saritepe, Selcuk	Transverse	Fermilab
Schill, Robert	Longitudinal	UIC
Trbojevic, Dejan	Transition	Fermilab
Wei, Jie	Transition	BNL
Wildman, Dave		Fermilab
Xhang, Xi		UIC
Zhou, Ping	Ion	Fermilab

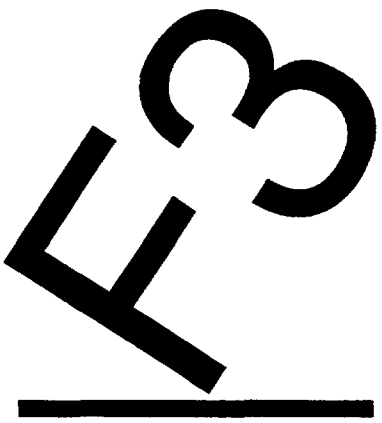

ION TRAPPING INSTABILITIES

Fermilab III Instability Workshop
Ion Trapping

R. Alves Pires(RAP), J. Marriner(JM), W. Marsh(WM),
A. Poncet(AP), J. Rosenzweig(JR), P. Zhou(PZ)

August 15, 1990

Summary

Foreword

In considering Ion Trapping, one has to address the basic questions:

(1) is ion trapping likely to happen ?

(2) what neutralisation will be reached ?

(3) what will be the effects on the beam ?

(4) what are the cures ?

Without prior experimental evidence and experience, the only question which can usually be rather easily answered is the first one.

The physical aspects of neutralisation (ion dynamics, drifts, ion species ...) are far from being understood, therefore starting from scratch would be very difficult to give satisfactory answers to questions 2 & 3. Concerning cures, qualitative arguments also dominate – no one has yet found absolute preventive cures.

In our study, question (1) only applies to the Tevatron with separation and more bunches, since ion trapping has already been observed in the accumulator. For this latter, question (2) to (4) are relevant in the frame of the

upgrade (up to 2×10^{12} pbars). Answers depend on the analysis of present experience in both FNAL and CERN machines (see Table 1 below for parameters), with proper scaling up. Therefore much time was spent during the workshop in trying to understand what happens in these machines and it was found that our knowledge is limited and that much ought to be done to improve it. This will appear clearly in our recommendation summary.

Tevatron

A detailed analysis of the stability of ions has been conducted using both linear theory and simulation for the various upgrade parameters (cases 1 to 3 see [1]). It is found that ion trapping should not be a problem, the worst case being 18 + 18 bunches, $N_{\bar{p}} = 3.4 \times 10^{10}, N_p = 10^{11}$. In this case ions of charge to mass ratios larger than 20 could be trapped in regions of large β's and separation (i.e. mainly in the vicinity of B0) and D0 interaction points (IP). Although it is doubtful that such high mass gas species might exist in the cold bore at $4°K$, the possibility of trapped dust particles generated for instance by break downs in electrostatic separators should be kept in mind.

Accumulator

Present

Although not precisely known, the neutralisation coefficient (ratio of ions to pbar numbers) of the machine is probably of a few percent.

Trapped ions manifest themselves in the present machine above 5×10^{11} pbar both through the excitation of a coherent transverse beam mode at $\omega_n = (n - Q)\omega_r = 850kHz$, and an incoherent emittance blow up (at least partially cured by shaking near the fractional tune, at 240 kHz). Both effects limit the minimum emittance achievable through cooling (together with intrabeam scattering). The incoherent effect (excitation of non linear resonances – probably 18th order – by ion space charge in pockets) cause the loss of high betatron amplitude pbars, thus reducing the stacking rate. Up to now, shaking the beam at a fixed frequency (240 kHz) via the damper active system has been successful in sufficiently diluting the ions in transverse phase space so as to limit the incoherent heating effect.

Table 1: Parameters of CERN & FNAL AA

	FNAL		CERN
	present	future	
Circumference (m)	460		156
Kinetic Energy (GeV)	7.9		3.5
γ	9.5		3.6
ω_r (kHz)	629		1,855
Q_H, Q_V	6.61, 8.61		2.26
$\beta_{H,V}$ (m)	12, 12		12, 15
max α_p (m)	10		10
% circumference with $\alpha_p < 2$m	66		25
$\eta = \left[\frac{df}{f}\right]\left[\frac{dp}{p}\right]^{-1}$	0.023		-0.085
$\xi = \left[\frac{dQ}{Q}\right]\left[\frac{dp}{p}\right]^{-1}$	-0.065		~ 0
Final $\frac{Dp}{p}$ RMS (5×10^{11} Pbars)	5.2×10^{-4}	2×10^{-4}	6.3×10^{-4}
Final emittance $\epsilon_{H,V}$	$< 2\pi$		$2\pi(6 \times 10^{11})$
Max stack	8×10^{11}	2×10^{12}	1.2×10^{12} (3π)
Average pressure (Torr)	5×10^{-10}		2×10^{-11}
Number of clearing electrodes	~ 100		~ 50
Electrode voltage (V)	(≤ 100)		400/800
Neutralisation coefficient	a few percent(?)		$\leq 1\%$

Future

With the upgrade, meaning more pbars with reduced longitudinal emittance, the neutralisation coefficient is likely to increase with intensity if the voltage on clearing electrodes is not raised (this is presently limited by the BPM at -100 Volts). But even at constant neutralisation the absolute force exerted by ion pockets on pbars would be expected to increase with intensity. For incoherent effects this means higher heating rates for identified non linear resonances, and perhaps excitation of additional resonances due to higher spreads in betatron frequencies. The by now well known cure of shaking the beam to reduce losses and heating might have to be improved to be able to cope with higher ion bounce frequencies, eventually away from natural beam modes. This may mean using a special high power shaker at different simultaneous frequencies (see [3]), going up with stack intensity.

However, of utmost importance is the concern about the transverse coherent effects. Actors on the post-ACOL CERN AA scene, have not forgotten the unexpected stack killer behind an ion driven quadrupolar coherent instability!

With upgrade, one expects a larger overlap of the ion bounce frequencies spectrum (due to increased pbars phase space density) with the beam's transverse mode spectrum, thus the likelihood of more instabilities at different frequencies. In addition, loss of Landau damping is to be expected for lower neutralisation thresholds than present due to increased ion bounce frequencies, and reduced frequency spreads if the planned longitudinal density increase is achieved. This concerns up to 4 dipole modes in each plane between 240 and 2200 kHz (see [2]). The present damper system actually barely copes with a dipolar instability at 850 kHz (rise time $\sim$ 1 ms).

A linear extrapolation (coherent neutralisation) leads to consider doubling at least the gain of the amplifiers in the frequency range considered. Quadrupolar instabilities are likely to happen at higher neutralisation thresholds than dipolar ones with the present tune settings ($Q_H \approx Q_V$). However their occurrence cannot be excluded, with dipole modes actually damped, (current theory shows an increase in Landau damping thresholds, going up as the ion bounce frequency to the third power).

Suggested experiments and preventive cures

The subject of ion trapping and cures is a complex one. On the one hand it is not understood why a neutralisation of a few percent subsists in a machine with 100 clearing electrodes (much of the experimental evidence on various machines suggests ion trapping in dipoles), while on the other hand a detailed prediction of likely ion effect supposes the precise knowledge of the neutralisation map!

Therefore we would suggest to tackle the problem on the two usual fronts:

- experiments and hardware to understand the physics of neutralisation.
- preventive cures based on previous experience.

Many experiments are possible to asses on neutralisation, the most basic one being the measurement of the average machine neutralisation from incoherent tune shifts. This case is treated in more detail in [4]. It could shed some light on the average transverse distribution of ions, thus allowing a better understanding of the excitation of non linear resonances (odd resonances are excited, mainly horizontally). Other experiments require the possibility of measuring currents on individual clearing electrodes, together with the individual control of the voltage, like on the CERN AA.

This permits identification of neutralisation pockets around the machine, monitoring of neutralisation to better understand instabilities, etc. For instance, it was suggested during the workshop to install multi-strip electrodes at bending magnets extremities, allowing the determination of the transverse distribution of drifting ions. A strong asymmetry in transverse distributions in bending magnets, if verified, would be a useful ingredient to explain the observed high order nonlinear resonances (which still need to be identified).

The chapter of preventive cures already partly discussed can be summarized as follows:

- lower the pressure ($P_{FNAL} \geq 20 P_{CERN}$) with more pumps and better bakeout.
- install more clearing electrodes (in particular in bending magnets, since their vacuum chambers need to be rebuilt).
- *increase the clearing voltage (100 volts will most likely not be enough with upgrade).

*• increase the transverse damper gain (by more than a factor of 2).

*• install a high power shaker, eventually with frequency modulation, so as to get beam amplitudes of up to 10μm away from natural modes. (The actual source of 4 different simultaneous shaking frequencies could be used in conjunction with it, eventually with frequency modulation).

• install a quadrupolar pickup and kicker (the kicker could be a variant of the high power shaker; same device with different connections). This could be useful to

(1) damp quadrupolar modes,

(2) measure stability diagrams to assess on mode stability,

(3) be used as a quadrupolar shaker ...

Much of this is discussed in more detail in the following contributions.

In conclusion we would like to stress the points ear-marked (*) as being essential ingredients to reach the design goal of the upgraded accumulator.

References

[1] P. Zhou and J.B. Rosenzweig, "Ion Trapping in Tevatron with Separated Orbits", This proceeding.

[2] J.B. Rosenzweig and P. Zhou , "Coherent Beam-Ion Instabilities in the Fermilab Antiproton Accumulator", This proceeding.

[3] R. Alves Pires, "Beam Shaking for the Fermilab Antiproton Accumulator", This proceeding.

[4] W. Marsh, In preparation.

Coherent Beam-Ion Instabilities in the Fermilab Antiproton Accumulator

J.B. Rosenzweig and P. Zhou
Fermi National Accelerator Laboratory
P. O. Box 500, Batavia, Illinois 60510

August 23, 1990

Introduction

The antiproton accumulator at Fermilab will be improved in performance in the next few years to provide the higher fluxes of cooled antiprotons necessary for the higher luminosity collider physics program to be undertaken in the Fermilab III upgrade.[1] The improvements in accumulator performance will mean that higher density (more particles in the stack; emittances nearly constant) beams will circulate in the machine. This situation will certainly aggravate the problems associated with coherent instabilities that can accompany ion trapping, as higher densities of trappable ions will be created, clearing efficiency will be degraded due to the larger beam self-fields, and the higher ion bounce frequencies will allow more beam modes to have unstable interactions with the trapped ion cloud.

In this note we investigate some quantities of interest in the physics on coherent beam-ion instabilities. These quantities include (i) level of neutralization in the machine, which is dependent on vacuum quality, beam density, vacuum chamber geometry, clearing electrode efficiency and externally driven beam shaking, (ii) the beam modes which may be candidates for excitation by coherent ion motion; these are dependent on the the beam density and ion charge-to-mass ratio, and (iii) the thresholds and growth rates for these unstable modes, which depend on spreading parameters of the beam and ion

populations, the beam density and level of neutralization. The theory of coupled beam-ion motion that we use in determination of the potentially unstable modes and their stability characteristics is quite well developed. Only results will be quoted here; interested readers should consult the reference list.[2–4]

Levels of Neutralization

The expected level of neutralization is a very complicated subject, and cannot be well addressed quantitatively. Many qualitative statements can be made, however. If all clearing and shaking are turned off then the only clearing mechanism is by slow Coulomb heating and one expects nearly full neutralization, $\eta \lesssim 1$. With clearing electrodes and shaking effectively deployed, most parts of the ring azimuth should be nearly free of trapped ions, with a few regions ("pockets") that ions cannot be well cleared from. Pockets can form in potential depressions of less than a volt. This is the experience of the CERN AA, where instability has been shown to be driven by a short pocket near a portion of ceramic beam pipe.[5] A precise calculation of the potential at beam center as a function of azimuth is presently being undertaken.[6] It is also difficult to clear ions from the dipoles, as the $\mathbf{E} \times \mathbf{B}$ longitudinal drift can be negated by the neutralization itself. This clogging mechanism is mitigated by beam shaking, which removes the stationary point of zero $\mathbf{E}$ field (no longitudinal drift) about which the neutralization can seed.

The level of neutralization has been determined experimentally[7] in the FNAL accumulator to be roughly a few percent with moderate size stacks ($N = 5 \times 10^{11}$). With stacks four times larger than this planned for the accumulator the neutralization level is sure to rise unless greater efforts are made at clearing. The peak clearing field presently used in the accumulator is of the order 1 kV/m, whereas the peak trapping field on the ions is over 4 kV/m for typical beam parameters in the upgrade scenario. Thus the clearing voltage must be raised, and attention must be paid to enhancing the clearing through beam shaking. Improvements in the vacuum pressure, which could be achieved through lowering the temperature of the accumulator environment, would also be desirable from this point of view.

The stance we adopt for the remainder of this note, then, is to specify the acceptable levels of neutralization in order for the instabilities to be mitigated

Collider Run #	III	IV	V
Rms Emittance ϵ_n (mm-mrad)	2π	2π	2π
Antiproton Stack N ($\times 10^{10}$)	82	137	198
Rms Momentum Spread ($\times 10^{-4}$)	1.3	2.1	2.75

Table 1: Beam parameter list for accumulator during upgrade.

with the design beam parameters need for the upgrade. These parameters are listed in Table 1 for convenience.

Coherent Dipole Modes

Coherent dipolar motion of the beam can be excited at the betatron sideband frequencies

$$f = f_0(n \pm Q_{H(V)})$$

where $f_0 = 628.71$ kHz is the circulation frequency in the ring, n is an integer and Q is the fractional tune in a given plane. Assuming the neutralization $\eta \ll 1$, a dipole instability can occur when the angular frequency of small amplitude (bounce) motion for the ions in $x(y)$, normalized to the angular circulation frequency $\omega_0 = 2\pi f_0$,

$$q_b \equiv \frac{\omega_b}{\omega_0} = \left[\frac{N r_p R Z_i}{\pi A_i \sigma_{x(y)}(\sigma_x + \sigma_y)}\right]^{1/2}$$

lies within a stopband of half-width

$$|q_b - (n - Q)| \leq \delta Q \simeq \frac{q_b Q_b}{\sqrt{q_b Q_0}}$$

of the slow-wave mode in question (Q_0 is the tune of the beam in either plane: $Q_{0H} = 6.611$, $Q_{0V} = 8.611$). Here N is the number of stack antiprotons, r_p is the classical radius of the proton, R is the radius of the machine Z_i is the charge state of the ion, and A_i is the atomic mass number of the ion. Assuming the ion and beam transverse distributions are similar, the

frequency of beam oscillations in the space-charge field of the ions is

$$Q_b = q_b\sqrt{\frac{\eta A_i}{\gamma}}$$

and

$$\delta Q = \sqrt{\frac{q_b^3 \eta A_i}{\gamma Q_0}}$$

For typical beam sizes encountered in the upgrade $q_b \simeq 3$, and this width is approximately $\delta Q = 0.6\sqrt{\eta}$ (where we have taken the mode to be vertical), which for one percent neutralization is $\delta Q = 0.06$, or a frequency spread of 40 kHz. The bounce frequencies are shown as a function of a representative portion of the azimuth in Figure 1, for the largest stack (Run V) and $Z_i/A_i = 1$ (doubly ionized molecular hydrogen). The relevant dipolar lines are also shown; note that the most likely offending modes are now the $3 - Q$ and $4 - Q$, or 1.502 MHz and 2.131 MHz, respectively.

The fastest growth rate occurs in the center of the unstable mode band, and is approximately $1/\tau = (\Omega_0/2)\delta Q \simeq 20$ kHz. This growth rate gives an upper limit on the necessary performance of an active damping system, as its derivation does not include the ameliorating effects of Landau damping.

Landau Damping of Dipole Modes

These potentially unstable beam-ion dipole modes can be stabilized by Landau damping if the frequency spreads associated with the ion and $\bar{\text{p}}$ motion, Δ_i and $\Delta_{\bar{p}}$, obey the following relations, inclusively:

$$\Delta_{\bar{p}} > |Q_{sc}^2/Q_0| \quad ; \quad \Delta_i > |q_{sc}^2/q_b| \quad \text{and} \quad \Delta_{\bar{p}}\Delta_i > |Q_b^2 q_b/Q_0|.$$

Here Q_{sc} is the defocusing strength parameter due to the space charge of the $\bar{\text{p}}$ beam acting on itself, and q_{sc} is the equivalent ion parameter due to collective effect of the ion space charge. The quantities inside of the first two absolute value expressions above are the relative tune shifts associated with these effects, and both have been assumed to be much smaller than unity. Thus the first two inequalities are the standard single species stability requirements,

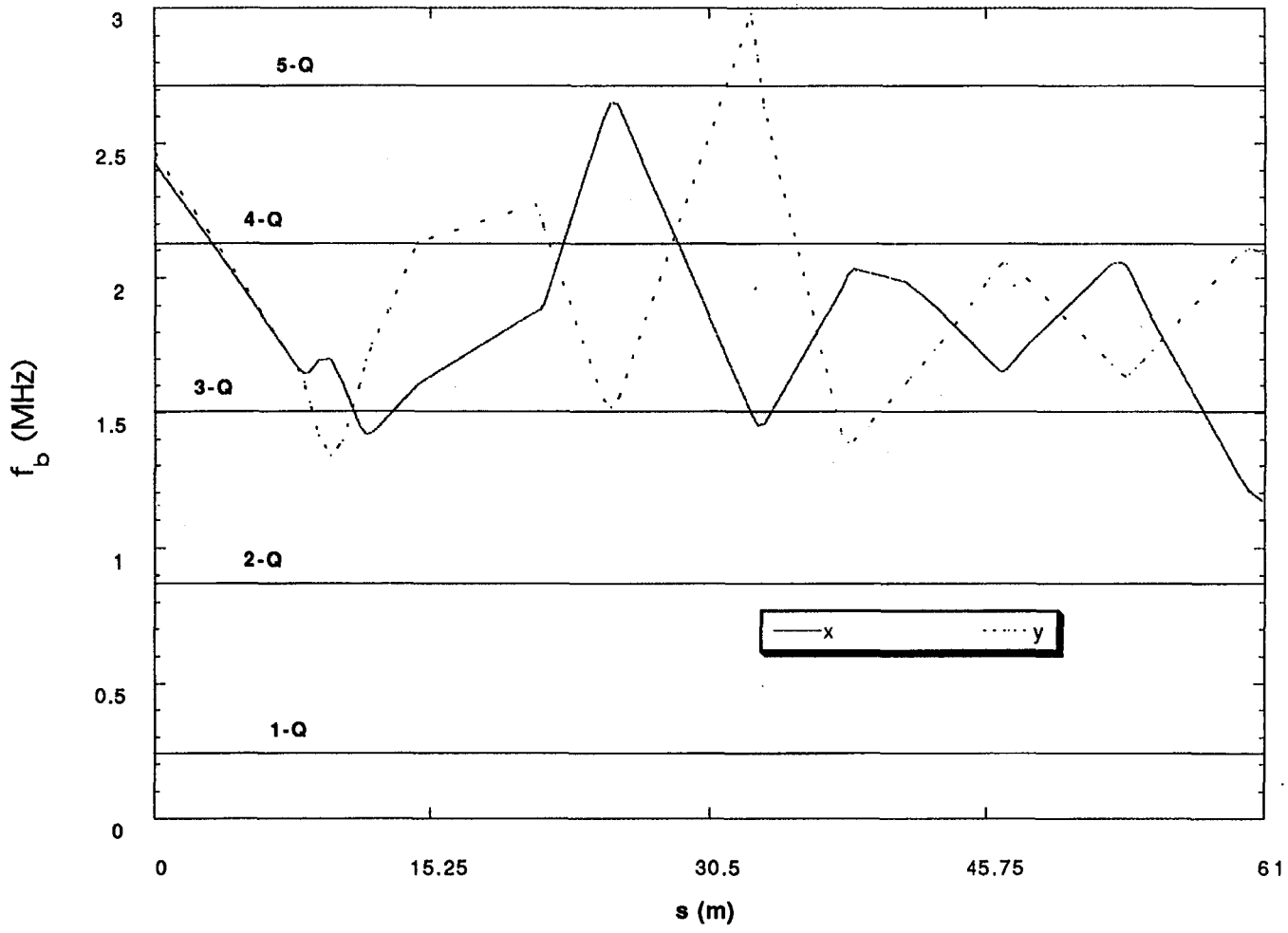

Figure 1. Ion bounce frequencies (Z/A=1) as a function of position in the azimuth. Horizontal lines indicate (n-Q) dipole modes.

while the third expresses a two-species stability condition. Explicitly, these quantities are

$$Q_{sc} = \left[\frac{Nr_pR}{\pi\sigma_{x(y)}(\sigma_x+\sigma_y)\beta^2\gamma^3}\right]^{1/2}$$

and, again assuming the ions have the same transverse dimensions as the beam,

$$q_{sc} = Q_{sc}\sqrt{\frac{Z_i^2\gamma^3\eta}{A_i}}.$$

For the upgrade parameters, the beam space tune shift is

$$|Q_{sc}^2/Q_0| = 1.1\times 10^{-3}$$

and the ion space charge tune shift is ($\eta = 0.01$)

$$|q_{sc}^2/q_b| = 9.4\times 10^{-3}.$$

The beam frequency spread parameter is

$$\Delta_{\bar{p}} = |(n-Q)\eta_p - Q_0\xi|\frac{\delta p}{p}$$

where $\eta_p = \gamma_t^{-2} - \gamma^{-2} = 0.023$ and $\xi = -0.065$ is the chromaticity. The ion frequency spread Δ_i can be estimated from inspection of Figure 1, and is evidently of order unity, unless the instability is driven by a very localized pocket, in which case Δ_i may be much smaller.

As an example, we take the mode near $3-Q$, which yields a beam frequency spread of

$$\Delta_{\bar{p}} = 1.6\times 10^{-4}.$$

Thus the first of the above inequalities is not satisfied for upgrade parameters, although it is satisfied for present running conditions. Unfortunately, there is not much one can do to improve the future scenario, as this shift parameter is a function of wanting so much beam with such a small emittance; the neutralization level does not affect this parameter. This analysis is crude, however, and may overestimate the tune shift and underestimate the beam spreading parameter due to lack of precise knowledge of the chromaticity. It is nonetheless a warning that Landau damping my not be reliable for suppressing the growth of these instabilities.

The second (ion) inequality usually is satisfied for low neutralization, however, as the ion frequency spread is so large. The third two-species inequality is satisfied, with

$$|Q_b^2 q_b / Q_0| \simeq |q_b^3 \eta / \gamma Q_0| = 0.3\eta,$$

as long as $\Delta_i/\eta > 2000$. Taking the Δ_i at minimum to be 0.5, this requires the neutralization to be less than $\eta = 2.5 \times 10^{-4}$. This analysis may underestimate the necessary degree of ion neutralization if the unstable mode is driven by a short pocket, as then Δ_i may be quite small, and this should be kept in mind in the future. In any case, it appears that extrapolating accumulator performance without improvement in the ion clearing is dangerous, as neutralization above the percent level can possibly take the beam-ion instability above the threshold where it is Landau damped. In addition, it would seem prudent to improve damping systems, so as to avoid relying on Landau damping to control the dipole instabiliies.

Quadrupole Instability

Unstable beam quadrupole modes can be excited at frequencies corresponding to

$$f = f_0(m - 2Q_{H(V)}).$$

The parameters of interest which are needed to predict quadrupole instability have already been introduced in the discussion of dipole modes, as the derivation of the physics and results are quite similar. In summary, for the symmetric quadrupole modes the unstable bands are narrower by a factor of two over the dipole case, while the peak growth rate is approximately the same. The required spreads for the single species conditions are smaller by a factor of two, and the two-species product of spreads is smaller by a factor of four compared to the dipole modes. Thus if the two-species frequency spread condition is the most stringent, the threshold neutralization is a factor of four higher for quadrupole modes.

This situation is encouraging, but with one dark cloud on the horizon. The unstable dipole modes can usually be suppressed by dipole shaking above their mode frequency, as the offending parts of the machine, and thus the relevant bounce frequencies identify themselves. Thus dipole shaking, which is efficient precisely near these betatron sidebands, effectively clears exactly

the right portions of the machine. One unfortunately does not have this state of affairs with quadrupole modes because they do not lie on betatron sidebands. High power dipole or resonant quadrupole shaking must be employed if there is a problem with quadrupole modes.

Conclusions

While the present level of clearing fields and beam-shaking appears to be adequate to control coherent beam-ion instabilities in the accumulator, improvements in stack size and transverse cooling may bring instabilities above threshold. These instabilities can be controlled by efficient clearing to achieve neutralization below the percent level. It may be necessary to have higher clearing fields, more powerful shaking, quadrupole shaking, or cyclotron resonance shaking[8] to achieve efficent clearing in the accumulator. Lower residual gas pressure would also help in this regard, as it would lengthen the neutralization time. If the clearing proceeds at a certain rate (as opposed to a pocket which fills up to full neutralization and saturates) then longer neutralization time implies a lower equilibrium neutralization. Lower neutralization levels eases the requirements for control of unstabe modes through Landau or active damping.

References

1. John Marriner, "Longitudinal and Transverse Density of the Accumulator Anti-proton Stack", *Physics at Fermilab in the 1990's - Collected Reports of the Accelerator and Beam Line Working Groups,* E. Malamud and G. Dugan, Eds. Fermilab, 1990.

2. R. Alves-Pires, D. Möhl, Y. Orlov, F. Pedersen, A. Poncet, S. van der Meer, "On the Theory of Coherent Instabilities Due to the Coupling Between a Dense Cool Beam and Charged Particles From the Residual Gas," *Proceedings of the 1989 Particle Accelerator Conference,* F. Bennett and J. Kopta, Eds., 800 (IEEE 1989), and R. Alves-Pires and D. Möhl, "Landau Damping of Quadrupole Modes" PS/AR/Note 90-09, CERN Internal Note, 1990.

3. D.G. Koshkarev and P.R. Zenkevich, "Resonance of Coupled Transverse Oscillations in Two Circular Beams," *Particle Accelerators* **3,** 1 (1972).

4. L.J. Laslett, A.M. Sessler, D. Möhl, "Transverse Two-Stream Instability in the Presence of Strong Species-Species and Image Forces," *Nucl. Instr. Meth.* **121,** 517 (1974).

5. G. Carron, D. Möhl, Y. Orlov, F. Pedersen, A. Poncet, S. van der Meer, and D.J. Williams, "Observation of Transverse Quadrupole Mode Instabilities in Intense Cooled Antiproton Beams in the AA," *Proceedings of the 1989 Particle Accelerator Conference,* F. Bennett and J. Kopta, Eds., 803 (IEEE 1989).

6. R. Alves-Pires and P. Zhou, private communication.

7. J. Marriner and A. Poncet, "Neutralisation Experiments with Proton and Antiproton Stacks - Ion Shaking", $\bar{p}$-Note 481, Fermilab Internal Note, 1989.

8. J.B. Rosenzweig and P. Zhou, these proceedings.

Beam Shaking for the Fermilab Antiproton Accumulator

R. Alves Pires
PS Division, CERN, CH-1211 GENEVA 23, Switzerland

3 August 1990

1 Introduction

Beam shaking at a fixed frequency in the Fermilab antiproton accumulator has helped in the past to cure the excitation of coherent transverse modes and incoherent emittance blow up [1]. In the future, however, the present level of shaking will not be sufficient, as the higher density beams required by the Fermilab upgrade plan [2] will have as a consequence higher densities of positively charged ions, trapped and oscillating in the beam potential well, and interacting with the antiproton beam. Incoherent effects induced by nonlinear interaction of the beam with ion pockets are susceptible to increase the heating rates and the losses by diffusion, reducing the stacking rate and limiting the minimum achievable emittances. In addition, and of more concern, more and new (namely quadrupole) coherent transverse modes are expected to be excited inducing rapid beam blows up and losses [3].

Some known results of the theory and practice of shaking [1, 4, 5, 6, 7] are reviewed and used below, to sketch the new experiments and procedures that

should be done in the Fermilab antioproton accululator in order to reduce these machine performance limitations.

2 Some of what is known

Beam shaking is essentially the application of a voltage to the beam, varying sinusoidally with a frequency ω. Under its action, the beam oscillates with the same frequency and an amplitude A, affecting its own potential well. As a consequence of the nonlinearity of the perturbed potential well, a pattern of nonlinear ion motion resonances displaying hysteresis appears, leading to the dilution of the ions density near the beam.

Figure 1 shows the variation of the equilibrium amplitudes of the ions oscillations for two different values of A as a function of the ratio ω_0/ω, where ω_0 is the ions bounce frequency [6, 7]. For a beam with a transverse bi-gaussian charge distribution, it is

$$\omega_{0H,V} = \left[\frac{q\lambda}{2\pi\varepsilon_0 m\sigma_{H,V}(\sigma_H+\sigma_V)}\right]^{1/2} = \left[\frac{2r_p c^2 N_{\bar{p}} Z_i}{A_i C\sigma_{H,V}(\sigma_H+\sigma_V)}\right]^{1/2},$$

where q, m, Z_i and A_i are respectively the ion electric charge, mass, charge state number and atomic mass number, λ and $N_{\bar{p}}$ are the beam linear charge density (electric charge per metre) and total number of particles, σ_H and σ_V and its horizontal and vertical r.m.s. sizes, C is the machine circumference, ε_0, c and r_p are the vacuum electric permeability, the speed of light and the classical proton radius, respectively.

The limited influence of the beam oscillation amplitude A is evident from inspection of Figure 1, meaning that even with very small amplitudes the shaking will be efficient, which was experimentally verified [1, 5]. Thus, the relevant parameter here is ω_0/ω.

A qualitative explanation of the efficiency of beam shaking can be obtained from Figure 1, by looking to what happens to the most harmful ions (those

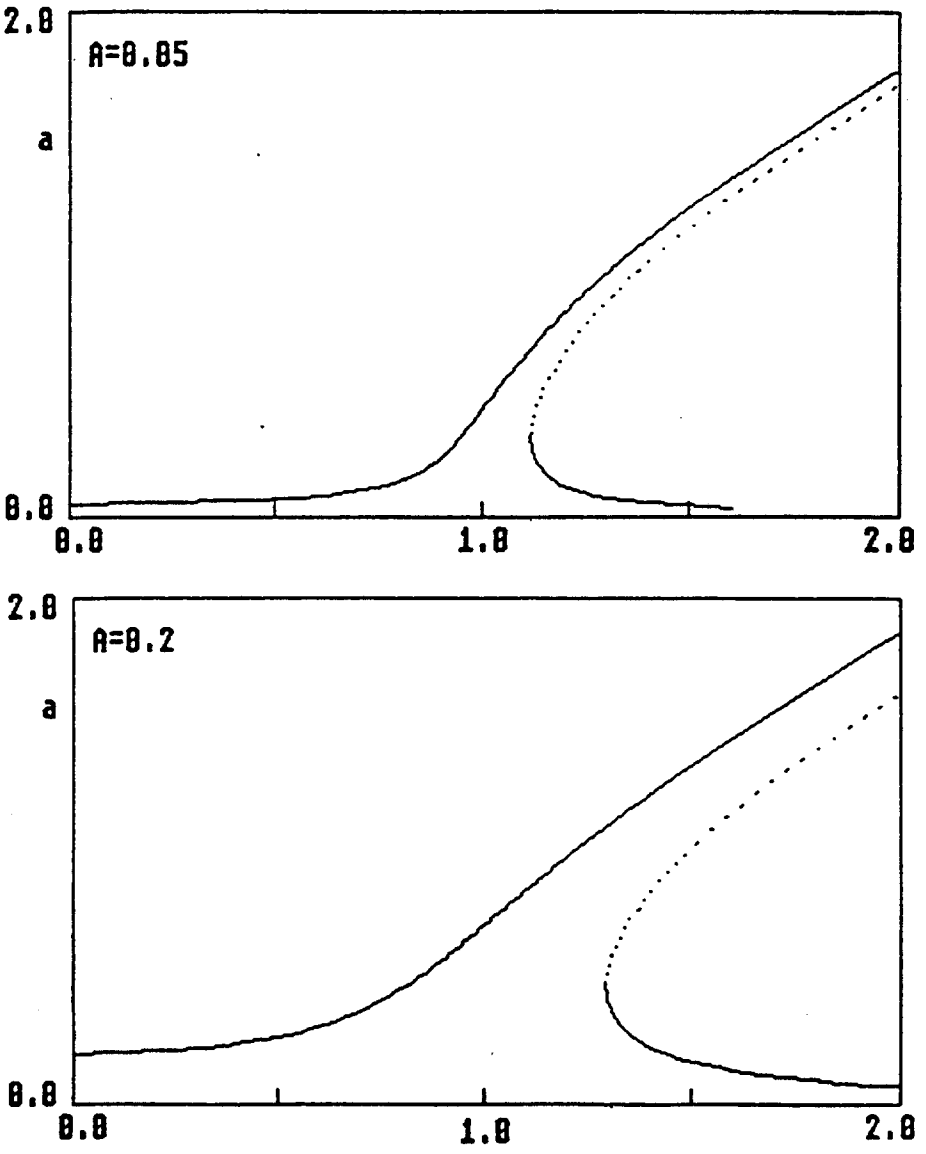

Figure 1: Equilibrium amplitudes for an ion as a function of the ratio ω_0/ω, for two different values of the beam amplitude A (normalized to 2σ), [7].

initially oscillating with small amplitude) when the ratio ω_0/ω is changed adiabatically.

Two distinct regions can be seen there: a first region for ω_0/ω below a transition value, where there is only a (stable) equilibrium amplitude, and a second region above that transition value, where there are three equilibrium amplitudes, two stable (denoted by heavy lines) and one unstable (denoted by a dotted line). If ω_0/ω is initially higher than the transition value, those ions are oscillating with an amplitude near the lowest solid line. If ω_0/ω is decreased, the amplitude will follow that line until near the transition, and then will accompany the uppermost solid line, passing through the linear resonance $\omega_0 = \omega$ without a much sensitive change of amplitude. However, if now ω_0/ω is increased, the ions amplitudes will remain near this large amplitudes solid line, and increase without limit.

This hysteresis phenomena (the amplitudes do not return to their initial values) permits to dilute the concentration of small amplitude ions, if ω_0/ω is varied adiabatically around the transition value. The choice of the shaking frequency is thus very important: ω must be such that ω_0/ω is near the transition value. As this is approximately 1, it must be $\omega \simeq \omega_0$, that is, the shaking frequency must be in the range of the ions bounce frequencies.

3 Fixed frequency shaking

If the beam is shaken at a fixed frequency, the variation of the ratio ω_0/ω is due only to the variation of the accelerator beta functions along the azimuth, which vary σ_H and σ_V and consequently ω_0. For example, for a hydrogen H^+ ion in the Fermilab AA, and for Run V, the vertical ion bounce frequencies vary from 1.5 to 3 MHz, all around the machine [3].

A longitudinal motion of the ions to make their bounce frequencies vary, is thus essential. But the variation of ω_0/ω is adiabatical only if the longitudinal velocities of the ions lie in a limited range [6]. This is the main disadvantage

of this method, as it will not be efficient for too slow or too fast ions.

Two different shaking modes must be distinguished here: resonant mode shaking and rigid mode shaking.

3.1 Resonant mode shaking

In this mode, the shaking frequency is fixed near one of the so-called betatron side-bands, $\omega \simeq (n \pm Q)\omega_{rev}$, where n is an integer, Q is the machine tune and ω_{rev} is the beam revolution frequency in the machine. As the beam is resonantly excited, even a very small shaking voltage can produce significant beam oscillation amplitudes, typically of the order of 10μm [5].

As dipole coherent instabilities are induced by ions oscillating with frequencies near those side-bands, this is very efficient in to cure those instabilities. Incoherent effects however are not likely to be cured, because ion pockets can exist in locations where the bounce frequencies are not close to an existing side-band.

For the upgraded Fermilab accumulator, shaking experiments should be done in all the side-bands that overlap the new ions frequency spectrum [3] to choose the frequencies for the actual source of various simultaneous shaking frequencies.

3.2 Rigid mode shaking

In order to cope with the effects not cured by the resonant shaking, shaking away of the side-bands must be considered. To achieve the same beam oscillation amplitudes as in the resonant case, it is necessary a high-power shaker producing high shaking voltages. This was tested once with success in the CERN Antiproton Accumulator [8], but was never repeated.

The necessary peak electric field E_0 can be easily computed from the

formula [9, pgs. 7, 22]

$$A \simeq \left(\frac{eE_0 l}{cp}\right)\frac{\beta^*}{2}\sin(\pi Q).$$

As for the Fermilab AA the average beta function is $\beta^* \sim 12$ m, the tune is $Q = 8.61$ and the momentum is $pc/e = 9.5$ GeV, the peak electric field times the shaker plates length must be of the order of $E_0 l \sim 14$ kV to produce a beam amplitude of 10 μm. A similar calculation for the CERN AA leads to 6 kV, and the typical values used[10] were electric fields of 20/30 kV/m for plates with a length $l = 0.35$ m.

4 Frequency modulation shaking

In order to shake also ions with speeds outside the range referred above, and to increase the maximum amplitudes reached by the ions, a frequency modulation shaking can be used. In this method the variation of ω_0/ω is mainly due to the variation of the shaking frequency ω, including in the process also the slow ions (like the ones trapped in localized pockets). In order to be more efficient, the variation of ω must be like a descending saw-tooth. For a given ion, ω_0/ω is initially small (large ω), is then adiabatically increased leading to arbitrarily large ion amplitudes (see figure 1), and then suddenly reduced (ω is increased to its top value). This sudden (non-adiabatic) variation, assures that the large amplitudes ions will remain in that state.

Frequency modulation was also tested in the CERN AA, this time without much success (at least, the efficiency did not attain the level of the fixed frequency shaking). This was mainly because it was used the low-power shaker (even if near a betatron side-band). A systematic study of this procedure should be done in the Fermilab accumulator (as well as in the CERN AA) with a high-power shaker. A study of the range of rates of variation of the shaking frequency which insures adiabaticity has also to be done.

References

[1] J. Marriner and A. Poncet, *Neutralization Experiments with Protons and Antiproton Stacks — Ion Shaking,* $\bar{p}$-Note 481, Fermilab Internal Note, 1989.

[2] J. Marriner, *Longitudinal and Transverse Density of the Accumulator Anti-proton Stack,* "Physics at Fermilab in the 1990's - Collected Reports of the Accelerator and Beam Line Working Groups", E. Malamud and G. Dugan, Eds, Fermilab, 1990.

[3] J. B. Rosenzweig and P. Zhou, *Coherent Beam-Ion Instabilities in the Fermilab Antiproton Accumulator,* these proceedings.

[4] J. Marriner, D. Möhl, Y. Orlov, A. Poncet and S. van der Meer, *Experiments and Practice in beam Shaking,* CERN/PS/89-48 (AR) and "Proceedings of the XIVth International Conference on High Energy Accelerators", Tsukuba, Japan, 1989.

[5] R. Alves Pires, D. Möhl, Y. Orlov, F. Pedersen, A. Poncet and S. van der Meer, *On The Theory Of Coherent Instabilities Due To Coupling Between A Dense Cooled Beam And Charged Particles From The Residual Gas,* "Proceedings of the 1989 Particle Accelerators Conference", F. Benett and J. Kopta, Eds., 800 (IEEE 1989).

[6] Y. Orlov, *The Suppression of Transverse Instabilities Caused by Trapped Ions in the AA by shaking of the $\bar{p}$ beam,* "Workshop on Crystalline Ion Beams", Darmstadt, 1988.

[7] R. Alves Pires, R. Dilão, *On The Theory Of Shaking,* to be published.

[8] A. Poncet, private communication.

[9] C. Bovet, R. Gouiran, I. Gumowski and K.H. Reich, *A Selection of Formulae and Data Useful for the Design of A.G. Synchrotrons,* CERN/MPS-SI/Int. DL/70/4, 1970.

[10] L. Thorndahl, private communication.

Ion Trapping in Tevatron with Separated Orbits

P. Zhou and J.B. Rosenzweig
*Fermi National Accelerator Laboratory**
P. O. Box 500, Batavia, Illinois 60510

August 15, 1990

1 Introduction

With the Fermilab upgrade plan, Tevatron in its 1991 and the following collider runs will have separated proton and anti-proton orbits. The average separation is greater than 5σ[1]. The electric force due to proton beam, which acts as a clearing force to ions, is greatly reduced and therefore leaves the possibility of having ions trapped around the anti-proton orbit. Here we investigate using the upgrade performance parameters whether there will be trapped ions in Tevatron and and if so where and under what circumstances this will happen.

2 Tevatron performance parameters

Listed here are the parameters for collider run III, IV and V, that are of concern in the following calculation, under the Fermilab upgrade plan.

*Operated by the Universities Research Association under contract with the U. S. Department of Energy

Run #		III	IV	V
Number of bunches		6	18 (36)	18 (36)
Bunch spacing (RF buckets)		185 186	$5 \times 42 + 161$ $(11 \times 21 + 140)$	$5 \times 42 + 161$ $(11 \times 21 + 140)$
# of particles/Bunch (10^{10})	proton	7 – 10	10 – 15	33 – 50
	pbar	7.2	3.4 (1.7)	7.3 (3.7)
Transverse emittance (95%, π mm-mrad)	proton	15	15	30
	pbar	14	19	22
Momentum spread (rms, 10^{-4})	proton	1.2	1.2	1.2
	pbar	1.2	0.38	0.27

3 Ion stability theory

Because of the presence of residual gas in the vacuum chamber positive ions are constantly created by collisions with beam particles. When there is only negatively charged DC beam present positive ions created at rest are always stable. They undergo oscillations in the electric field of beam. The strength of the beam only affects the oscillation frequencies of ions. If the beam is bunched, then ions experience time varying focusing force. The beam bunches can be viewed, in the simplest model, as focusing elements acting on ions[2][3]. The effect of these "focusing elements" on ion motion depends on the beam transverse distribution and the bunch spacing scheme[4].

The fields of an ultra-relativistic beam are almost purely transverse. In this limit the transverse electric field due to a Gaussian bunch with rms size in horizontal and vertical direction being σ_x and σ_y respectively is[5]

$$\begin{pmatrix} E_x \\ E_y \end{pmatrix} = Ze\frac{2\lambda\sqrt{\pi}}{\sqrt{2(\sigma_x^2-\sigma_y^2)}} \times \begin{pmatrix} Im \\ Re \end{pmatrix} \left\{ W\left(\frac{x+iy}{\sqrt{2(\sigma_x^2-\sigma_y^2)}}\right) - e^{-\frac{1}{2}\left(\frac{x^2}{\sigma_x^2}+\frac{y^2}{\sigma_y^2}\right)} W\left(\frac{x\frac{\sigma_y}{\sigma_x}+iy\frac{\sigma_x}{\sigma_y}}{\sqrt{2(\sigma_x^2-\sigma_y^2)}}\right) \right\}$$

where Z is the ion charge state, r_p the classical radius of proton and λ the particle line density, and W is the complex error function.

If the beam pulse length is short compared to an ion oscillation time in general we can neglect the motion of ions during the time the beam bunch

passes by them and treat the kick from the beam as δ-function like impulse at the time when the center of bunch passes ions i.e. using thin lens approximation. Only ion velocity is changed by the kick in this approximation, not its position. In Tevatron $\sigma_z = 40$cm. Taking $L = 2\sigma_z = 80$cm as bunch length and simplifying the bunch as longitudinally uniform and transversely round, the analogue to the linear focusing strength in lattice theory is then (see Section 3.1), $K = \frac{ZNr_p}{A\sigma^2 L}$, where N is the number of particles per bunch and r_p the classical radius of proton. The thin lens approximation requires $\sqrt{K}L \ll 1$. For Tevatron the average transverse beam size is $\sim 0.5cm$ and in the above simplification $\sqrt{K}L \approx 0.6\sqrt{\frac{Z}{A}}$ for the biggest antiproton bunch density in the upgrade. Thus the thin lens approximation is only valid for ions with $\frac{A}{Z} \gtrsim 4$.

In this approximation we can write the change in transverse velocity of the ion due to the Gaussian bunch as

$$\begin{pmatrix} \Delta x' \\ \Delta y' \end{pmatrix} = \frac{Z}{A}\frac{2Nr_p\sqrt{\pi}}{\sqrt{2(\sigma_x^2-\sigma_y^2)}} \times \begin{pmatrix} Im \\ Re \end{pmatrix} \left\{ W\left(\frac{x+iy}{\sqrt{2(\sigma_x^2-\sigma_y^2)}}\right) - e^{-\frac{1}{2}\left(\frac{x^2}{\sigma_x^2}+\frac{y^2}{\sigma_y^2}\right)} W\left(\frac{x\frac{\sigma_y}{\sigma_x}+iy\frac{\sigma_x}{\sigma_y}}{\sqrt{2(\sigma_x^2-\sigma_y^2)}}\right) \right\}$$

where N is the total number of particles per bunch, A the ratio of ion to proton mass and

$$x' = \frac{1}{c}\frac{dx}{dt}$$

$$y' = \frac{1}{c}\frac{dy}{dt}$$

3.1 Linear theory

For small amplitude ion oscillation ($x \ll \sigma_x$, $y \ll \sigma_y$) the transverse electric field can be linearized to give

$$E_x = \frac{2Ze\lambda}{(\sigma_x+\sigma_y)}\frac{x}{\sigma_x}$$

$$E_y = \frac{2Ze\lambda}{(\sigma_x+\sigma_y)}\frac{y}{\sigma_y}$$

Use s_b for the distance between two consecutive bunches and L for bunch length, the ion motion can be described by the following transfer matrices M_x, M_y from the passage of one bunch to the next one:

$$\begin{pmatrix} x \\ x' \end{pmatrix}_{n+1} = M_x \begin{pmatrix} x \\ x' \end{pmatrix}_n$$

where

$$M_x = \begin{pmatrix} 1 & s_b - L \\ 0 & 1 \end{pmatrix} \begin{pmatrix} \cos(\sqrt{K}L) & \frac{1}{\sqrt{K}}\sin(\sqrt{K}L) \\ -\sqrt{K}\sin(\sqrt{K}L) & \cos(\sqrt{K}L) \end{pmatrix}$$

and the similar for M_y in the vertical direction.

In the thin lens approximation the equations above simplifies to

$$\Delta x' \equiv a_x x = \frac{2ZNr_p}{A(\sigma_x + \sigma_y)} \frac{x}{\sigma_x}$$

$$\Delta y' \equiv a_y y = \frac{2ZNr_p}{A(\sigma_x + \sigma_y)} \frac{y}{\sigma_y}$$

and

$$M_x = \begin{pmatrix} 1 & s_b \\ 0 & 1 \end{pmatrix} \begin{pmatrix} 1 & 0 \\ -a_x & 1 \end{pmatrix}$$

If the bunches are equally spaced, and the fluctuation in bunch to bunch density and revolution frequency are neglected, then the stability of ions requires that $TrM_x < 2$ and $TrM_y < 2$. It then leads to a critical mass such that ions with mass greater than critical will be stable and smaller than critical unstable. The critical mass is thus set by the higher of $TrM_x = 2$ and $TrM_y = 2$. Explicitly we have

$$A_c = \frac{ZNs_b r_p}{2(\sigma_x + \sigma_y)} \cdot \frac{1}{\min(\sigma_x, \sigma_y)}$$

As can be seen here the most possible place for ion trapping is where the beam size is big i.e. large beta functions. In Tevatron this corresponds to sections of beta function bump around the colliding points.

The variation in the spacing between bunches and in bunch to bunch density will introduce stop bands in the otherwise stable region of ion mass.

In general if we have n different bunch spacing $s_1, \ldots, s_n$ and bunch density $a_1, \ldots, a_n$ that repeats itself, then ion stability will be determined by the transfer matrix

$$M = M_1 \cdot M_2 \ldots M_i \ldots M_n$$

where

$$M_i = \begin{pmatrix} 1 & s_i - L \\ 0 & 1 \end{pmatrix} \begin{pmatrix} \cos(\sqrt{K_i}L) & \frac{1}{\sqrt{K_i}}\sin(\sqrt{K_i}L) \\ -\sqrt{K_i}\sin(\sqrt{K_i}L) & \cos(\sqrt{K_i}L) \end{pmatrix}, i = 1 \ldots n$$

and in general we will have n stable bands in ion mass.

3.2 Nonlinear effects

The electric field expressed at the beginning of this section is very nonlinear when the distance is greater or comparable to the beam's rms size. If we want to consider also the stability of large amplitude ions, or the effect of proton beam from a separated orbit when we have two beams in the ring then we have to work with the nonlinear force. First when ions are far enough from the beam center this force becomes locally defocusing. The consequence of this is that the stability for large amplitude ions are almost solely determined by the longest gap between any two consecutive bunches. Secondly it introduces coupling between horizontal and vertical directions.

Calculation is not as simple as in the linear case any more. We have to track the motion of ions to test their stability. A computer code was developed to do both linear calculation and nonlinear tracking of ions. To avoid the extremely time consuming numerical integration the code uses thin lens approximation, which means it's not applicable to very light ions. The effect due to the fluctuations in bunch density is ignored. The code also track ion motion inside a dipole magnet. Caution has to be taken here. In Tevatron the magnetic field of dipole magnets is 3.8 T and the corresponding proton cyclotron frequency is $\omega = \frac{eB}{m_p} = 0.36GHz$. The rotation angle of a proton during the 3 ns beam bunch passage time is 60 degrees, therefore the range of thin lens approximation in the nonlinear calculation should be $A \gtrsim 20$, regardless of bunch density.

4 Calculations and results

Fig. 1 shows the Tevatron lattice functions in the collider mode. There are two typical parts of it. One includes the regular cells and the other the low beta insertions. Linear calculations, ignoring the proton beam, for one representative regular lattice point $s = 320$, Fig. 2-1 shows the stable mass bands for all three operational modes. In this and all following calculations we will only pay attention to ions with $\frac{A}{Z} = 1, 2, 4, 28$ which corresponds to singly ionized H, H_2, He, N_2, CO and most fully ionized ion species. For comparison we also show the results for cases of 18 and 36 bunches Fig. 2-2, but with the bunches distributed in almost periodical fashion, i.e. instead of $(5 \times 42 + 161)$ in 18 bunch case we use $(5 \times 62 + 61)$, and instead of $(11 \times 21 + 140)$ we use $(11 \times 31 + 30)$. The comparison is unambiguous — the big gap (abort gap), greatly destablizes ions. Also by doing tracking on cases where linear calculation predicts stable motion in both horizontal and vertical direction for different initial amplitudes ($< \sigma$), we verified the observation made in the previous section that because of the accumulation of the nonlinear effect, except for very small amplitude oscillations, these narrow stable bands virtually don't exist.

From the stability plot we can see that in the mass range of our concern the stable bands are all very narrow. This means even very small amplitude ions are barely stable. Adding the proton beam to the nonlinear calculations, with reasonable separations, we find that ions are knocked out almost immediately. This can be easily explained using the following argument. The average force from proton beam is $\propto \frac{N_p}{R}$ where R is the separation between proton and antiproton beam, and the maximum focusing force from antiproton beam is $\propto \frac{N_{\bar{p}}}{\sigma_{\bar{p}}}$. So when $\frac{N_p}{N_{\bar{p}}} > \frac{R}{\sigma_{\bar{p}}}$ no ions are stable. When this is not satisfied the proton beam field contributes to driving the ions out of the linear antiproton beam force region and into unstable motion.

This leaves our concern only to the high beta sections around colliding points, which according to linear theory are the most possible places to trap ions.

Linear and nonlinear calculations have been done at $s = 2040$ which has $\beta_x \sim 87m, \beta_y \sim 390m$. Fig. 3-1, 3-2 show the linear calculation result. This should be the most favorable place for ion trapping because β_y is close to its maximum and it is inside a dipole magnet and thus horizontal motion is

Figure 1. Tevatron Beta Functions

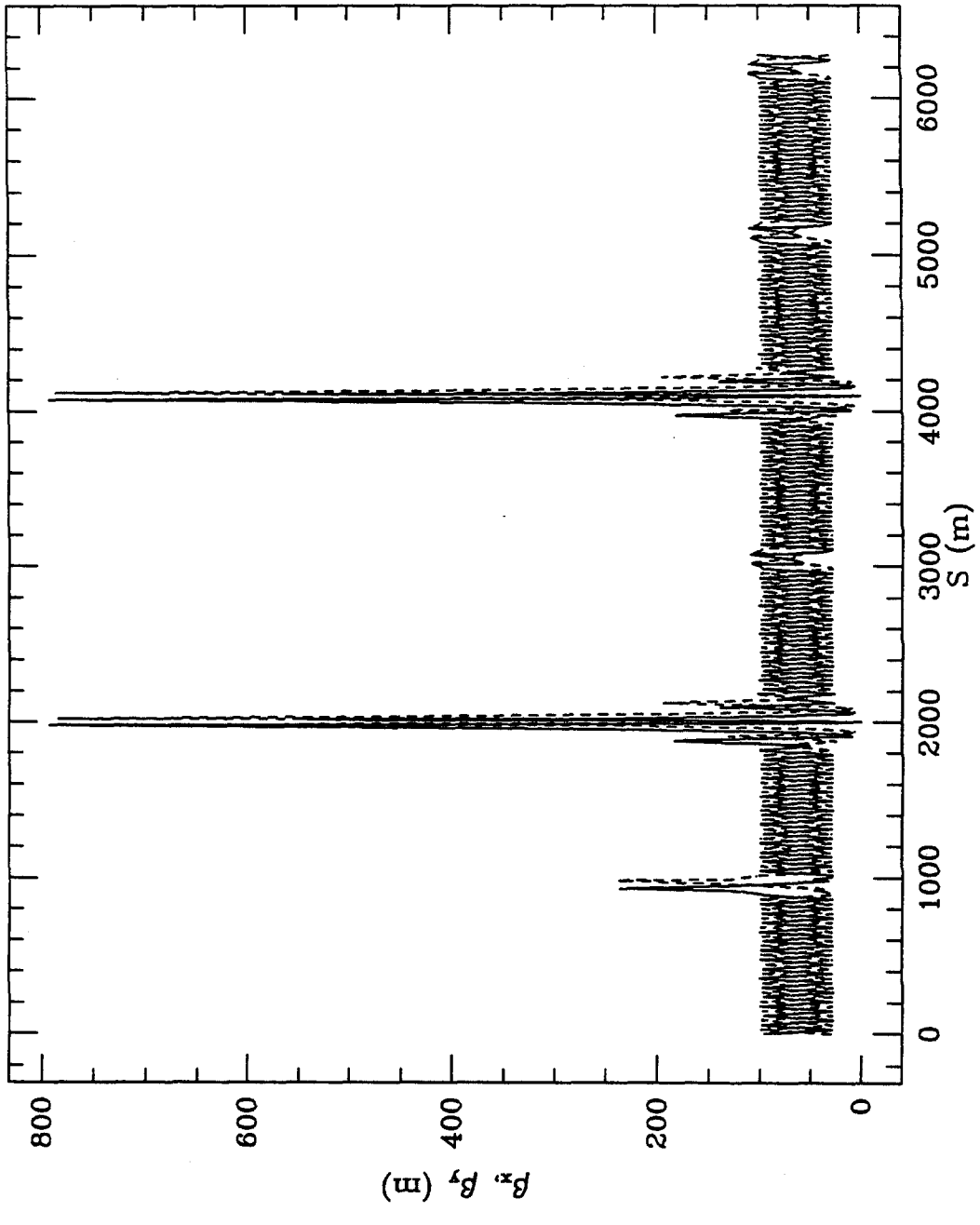

Figure 2-1. Linear Stability Plot at S=320m

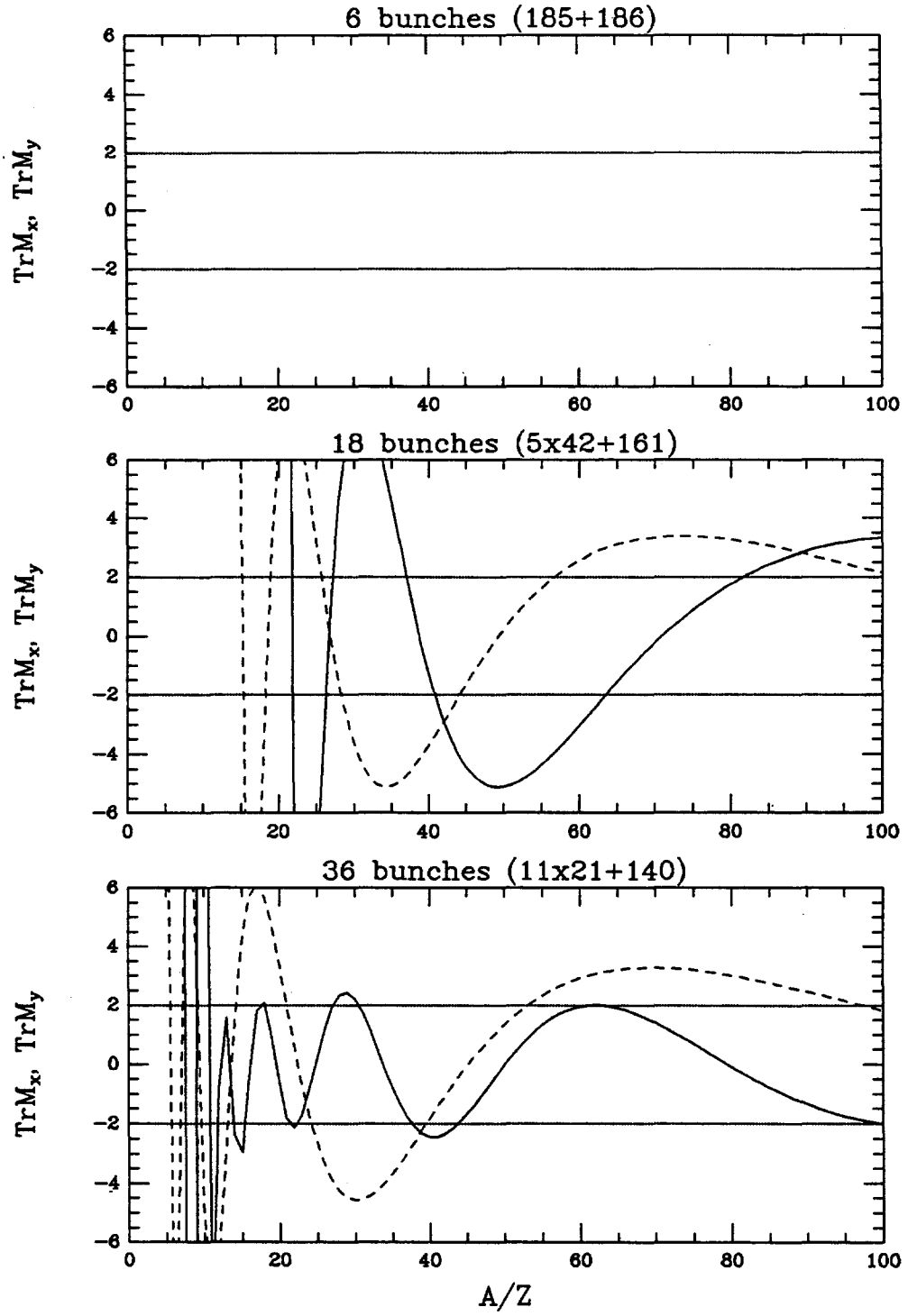

Figure 2-2. Linear Stability Plot at S=320m

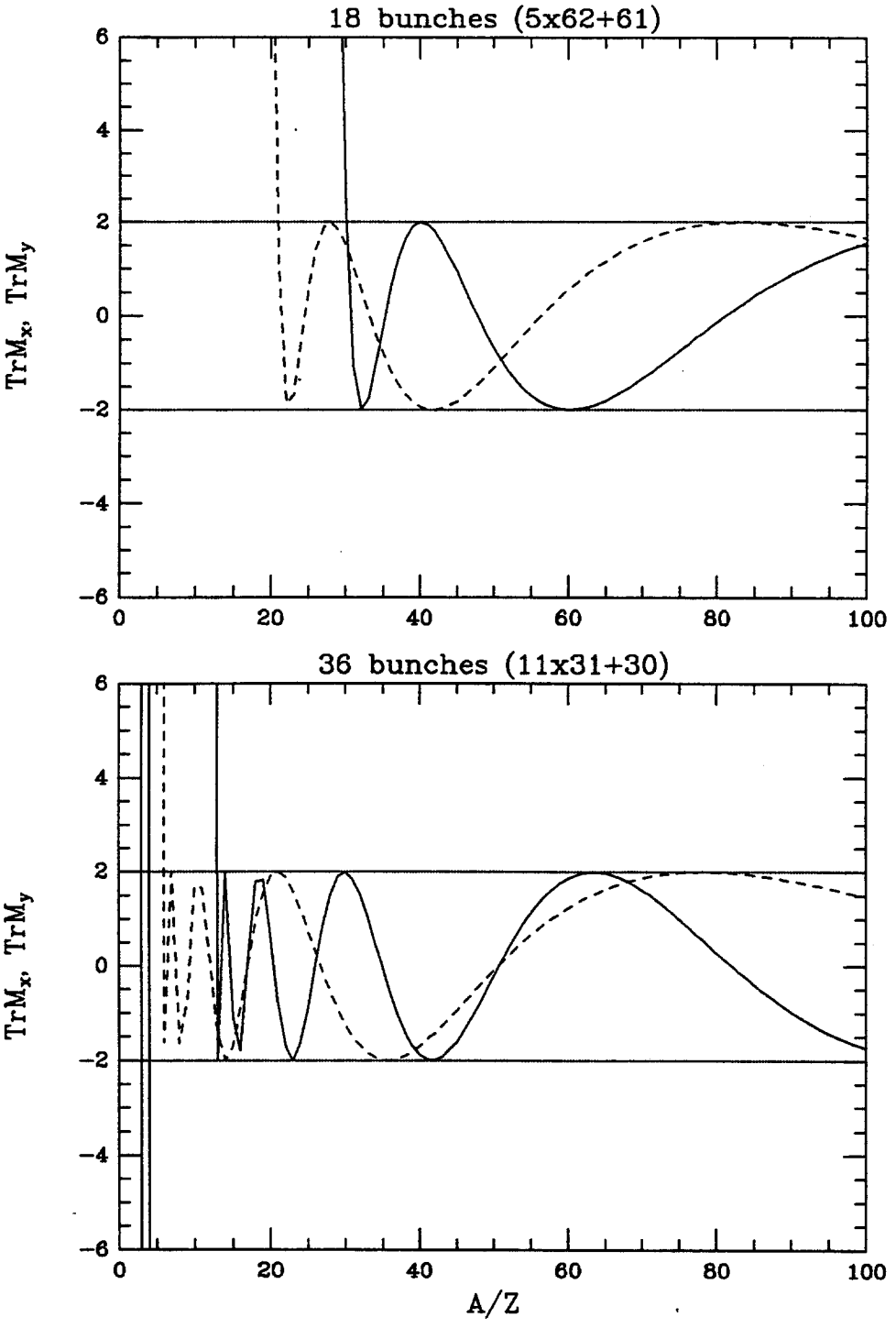

Figure 3-1. Linear Stability Plot at S=2040m

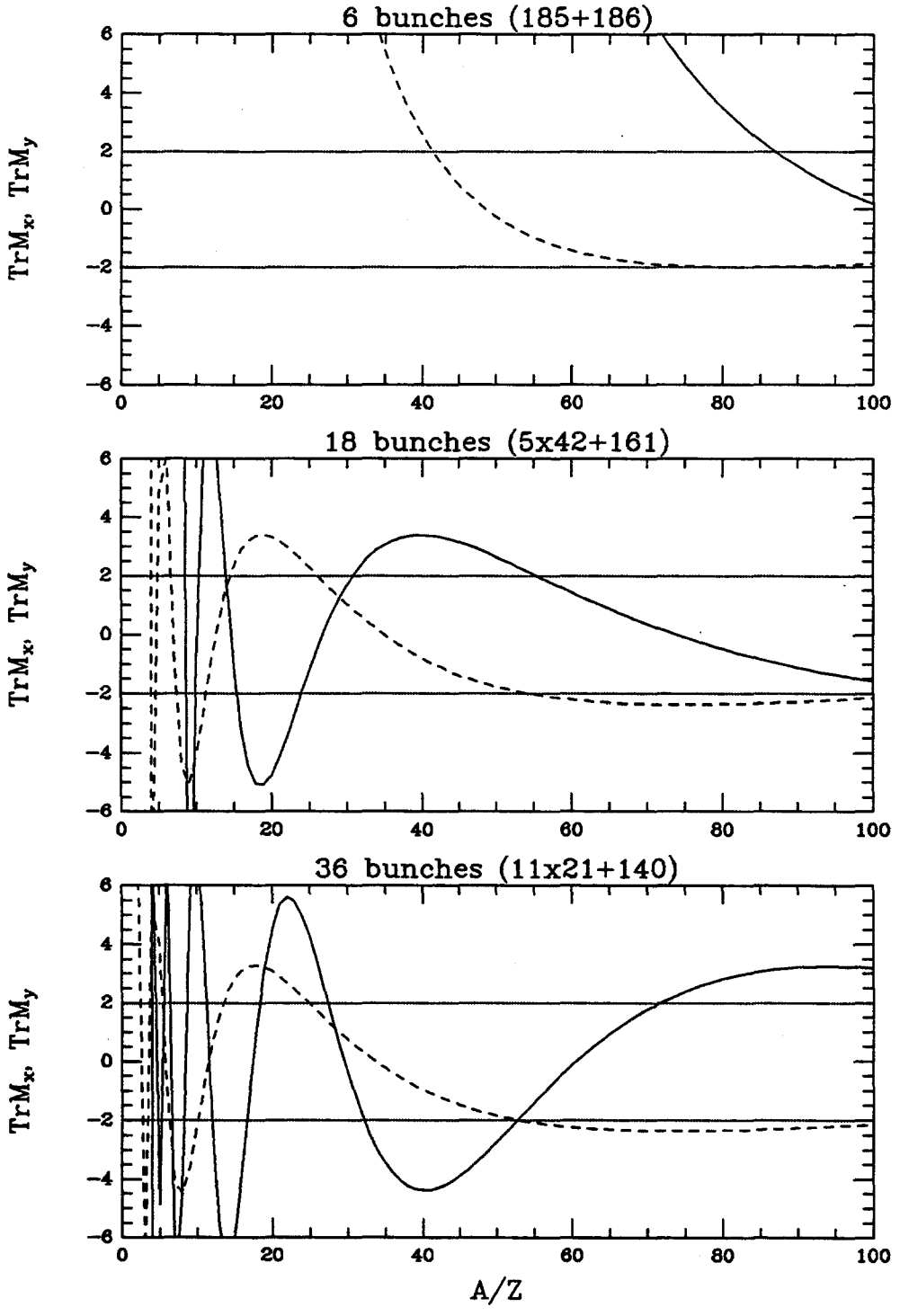

Figure 3-2. Linear Stability Plot at S=2040m

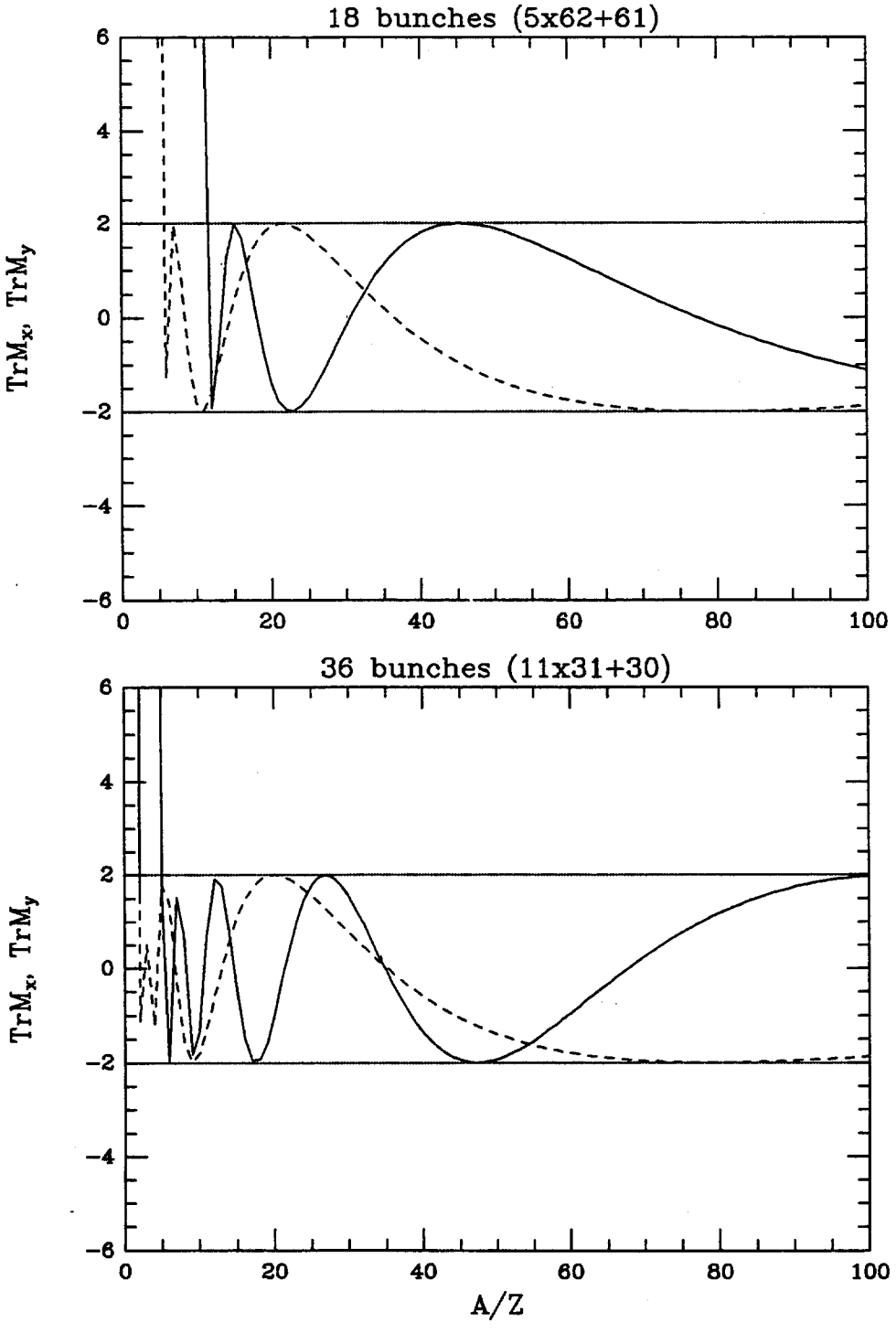

automatically stable. The cycloidal motion due to crossed $\vec{E}$ and $\vec{B}$ fields results in a secular longitudinal (z) drift. Stable ions drift towards the ends of dipole magnet and accumulate there. In our simulation we neglect the effect of this drift on the bunch passing time because the drift is usually $\lesssim 1m$ in the time scale of our simulation compared to the length in one RF bucket $\sim$ 5.6m and the length of dipole magnets $\sim$ 6m. In Fig. 4 we show a sample Poincare plot of a stable motion for $A = 28$ with only anti-proton beam. In all three modes light ions are unstable as can be seen from linear stability plot, but for the two multi bunch modes with only antiproton beam ions with $A = 28$ and $A = 44$ are stable and, this stability only occurs inside the dipole magnetic field. Adding the proton beam with the design density, in all the listed operation modes, clears ions out except when the two beams are very close to purely horizontally separated. There will be both horizontal and vertical separators between the colliding point and the dipole magnet in consideration according to the proposed separator locations[1], and the separation between proton and antiproton beam is only 2–3σ around this point. These conditions exclude the possibility of trapping ions here.

5 Conclusion

To summarize, in Tevatron, there won't be any light ions trapped with or without proton beam. With the planned intensity proton beam present ions of concern are not likely to be trapped either. If there is only antiproton beam in the ring then trapping is possible for ions like CO, N_2 and CO_2, but almost exclusively in dipole magnets. Inside superconducting magnets residual gas is composed of mostly light ions and very few heavy ions, and additionally as these heavy ions get further ionized they will become unstable trapped ions will likely not have any effect on stored beams. Therefore it is safe to say that in collider runs III, IV and V ion trapping will not be a problem for Tevatron.

References

[1] A.D. Russell "Assignment of Separator Locations", Fermilab Internal Note, July 12, 1989

[2] C.J. Bocchetta and A. Wrulich, "The Trapping and Clearing of Ions in ELETTRA", *ST/M-88/26,* Trieste Internal Note, November 1988

[3] Y. Baconnier and G.B. Brianti, "The Stability of Ions in Bunched Beam Machines", *CERN/SPS/80-2(DI),* CERN Internal Note, 1980

[4] W. Marsh, "Ion Trapping", *Physics at Fermilab in the 1990's – Collected Reports of the Accelerator and Beam Line Working Groups,* E. Malamud and G. Dugan, Eds. Fermilab, 1990

[5] M. Bassetti and G. Erskine, *CERN-ISR-TH/80-06,* CERN Internal Note, 1980.

Ion Clearing Using Cyclotron Shaking

P. Zhou and J.B. Rosenzweig

October 3, 1990

1 Introduction

Accumulation of ions has been a limiting factor in the performance of antiproton accumulators. Besides the direct clearing method using clearing electrodes, beam shaking has been proven very effective in further clearing ions[1] and reducing the neutralization level (ratio of ion charge to beam charge) in the machine. In the so called "resonant shaking"[2] a driving voltage with frequency close to that of the ion oscillatory motion in the beam's electric field (bounce frequency) and slightly lower than a betatron side-band is applied to the beam, which responds by shaking generating an oscillating transverse electric field which in turn drives transverse ion motion. Ions traversing different beam sizes, and thus bounce frequencies, through slow longitudinal motion will be locked-on to larger amplitudes due to the hysteresis effects found in these driven nonlinear oscillations; in this way the neutralization effects can be reduced[3]. The same or better results should be achievable through modulation of the driving frequency[4], which is called frequency modulation shaking. This way the process is controllable and does not rely on the ions' longitudinal motion. To distinguish from what we are going to describe here we call this kind of shaking bounce shaking because it is the ion bounce motion that is being driven.

An interesting and important experimental fact is that the bounce shaking described above doesn't work well in horizontal plane. A plausible explanation is as follows. While ions in straight sections are much easier to be cleared by the clearing electrodes, ions inside dipole magnets cannot be easily cleared, because there are no clearing electrodes inside magnets due to the physically tight space there, and the only clearing mechanisms are through

Coulomb heating and the longitudinal drift, which is much smaller than the unimpeded thermal motion in the magnetic field-free regions. As a result the neutralization level inside the magnets is much higher than the rest of the machine and ion effects are most likely caused mainly by the ions in dipoles (in Fermilab antiproton accumulator dipole magnets count as nearly a quarter of the total length of the ring). The strong magnetic field inside magnets leads to cyclotron motion of ions in the horizontal plane. This makes the horizontal ion oscillation frequency much different from that of the bounce motion, and therefore the bounce shaking is not effective in the horizontal plane. This explanation leads us to the possibility of shaking close to ion cyclotron frequency, which we call cyclotron shaking, on which we present a preliminary analysis here.

2 Theory of Shaking

The theoretical analysis for cyclotron shaking is exactly parallel to that of bounce shaking[4], which uses the averaging technique originally developed by Krylov and Bogoliubov[5][6]. For completeness we reproduce the detailed method of analysis here.

Let x be the transverse coordinate of ion in the horizontal plane and z the longitudinal coordinate, then, ignoring the space charge of the ions themselves, the equations of motion for the ion are,

$$\begin{aligned} \frac{d^2x}{dt^2} &= -\omega_c \frac{dz}{dt} + \frac{q}{m} E_x(x - x_0 \cos \omega t) \\ \frac{d^2z}{dt^2} &= -\omega_c \frac{dx}{dt} \end{aligned}$$

where q and m are the charge and mass of ion respectively, and ω_c is the cyclotron frequency. For a round Gaussian beam the form of radial electric field is

$$E_r(r) = \frac{2\lambda}{r}(1 - e^{-\frac{r^2}{2\sigma^2}})$$

where λ is the beam line density.

The displacement of the ion from the beam center $\tilde{x} = x - x_0 \cos(\omega t)$ is

then described by

$$\frac{d^2\tilde{x}}{dt^2} = -\omega_c^2\tilde{x} - \omega_b^2 f(\tilde{x}) - A(\omega_c^2 - \omega_b^2)\cos(\omega t)$$

where $\omega_b = \sqrt{q\lambda/m\sigma^2}$ is the ion bounce frequency, $A = x_0/\sigma$ and $f(\tilde{x}) = 2[1 - \exp(-\frac{1}{2}\frac{r^2}{\sigma^2})]$.

Seeking the equilibrium solution of the form

$$\begin{aligned} \tilde{x} &= a(t)\cos(\omega t + \theta(t)) \\ \frac{d\tilde{x}}{dt} &= -\omega a(t)\sin(\omega t + \theta(t)) \end{aligned}$$

leads to the following equations:

$$\begin{aligned} \frac{da}{dt} &= \frac{1}{\omega}[(\omega_c^2 - \omega^2)a\cos\phi - \omega_b^2 f(a\cos\phi) + A(\omega_c^2 - \omega^2)\cos\omega t]\sin\phi \\ \frac{d\theta}{dt} &= \frac{1}{a\omega}[(\omega_c^2 - \omega^2)a\cos\phi - \omega_b^2 f(a\cos\phi) + A(\omega_c^2 - \omega^2)\cos\omega t]\cos\phi \end{aligned}$$

where $\phi = \omega t + \theta(t)$. For equilibrium solutions we assume that $a(t)$ and $\theta(t)$ change slowly relative to the oscillation period. Averaging over a period yields equations for the oscillation amplitude and phase function:

$$\begin{aligned} \frac{da}{dt} &= \frac{(\omega_c^2 - \omega^2)}{2\omega}A\cos\theta \\ \frac{d\theta}{dt} &= \frac{(\omega_c^2 - \omega^2)}{2\omega}[1 - \frac{A}{a}\sin\theta] + \frac{\omega_b^2}{2\omega}G(a^2) \end{aligned}$$

where $G(a^2) = \frac{4}{a^2}[1 - e^{(-\frac{a^2}{4})}I_0(\frac{a^2}{4})]$. The maximum amplitude satisfies $da/dt = d\theta/dt = 0$, therefore we have an implicit relation between the driving frequency and equilibrium ion amplitude:

$$\frac{\omega^2 - \omega_c^2}{\omega_b^2} = \frac{G(a^2)}{1 \pm \frac{A}{a}}$$

Setting $\omega_c = 0$ gives the relation for bounce shaking.

3 Simulation and Results

Simulation study was done for the Fermilab antiproton accumulator with its upgrade parameters[7]. For simplicity we assumed round beam with rms

size of 0.22 cm. The amplitude of the motion of beam center was taken to be 0.01 mm and all calculations were done for proton motion. For comparison both bounce shaking and cyclotron shaking were investigated.

In order to get the amplitude of equilibrium motion as calculated in the previous section we put in very small viscosity term in the equations of motion to damp out the portion of the oscillation connected to the initial conditions. The results, shown in Fig. 1, agree remarkably well with the analytical theory.

The modulation of frequency, in both shaking schemes, is shown to be very effective by simulation. As shown in Fig. 1, large amplitude of ion oscillation can only be achieved by starting with relatively high frequency and slowly reducing it. The level of amplitude that can be achieved is limited by two factors. First, as the rate of frequency change has to be slow, a larger frequency range would require longer time to complete a cycle of modulation and therefore reduce the efficiency of ion clearing which is the ultimate goal. Secondly, ions inevitably have deviations in their amplitudes from the equilibrium ones, and when the two curves in Fig. 1 get close enough at some large amplitude the deviation will cause ion motion to enter the unstable region and their amplitudes to drop sharply. Fig. 2 shows a few examples of modulated frequency shaking with different frequency modulation ranges and rates.

4 Discussion

As can be seen above cyclotron shaking and bounce shaking are very similar in many aspects. The equilibrium amplitudes can be described by the same plot and hence both have the same hysteresis "lock on" effect which is crucial in reducing neutralization effects[3][8]. However because of the very different frequencies of the cyclotron and bounce motion, the two ways of shaking do have different properties. The cyclotron frequency ω_c, at least in our case, is much higher than the bounce frequency ω_b. The correspondence of $\sqrt{(\omega^2 - \omega_c^2)/\omega_b^2}$ in cyclotron shaking and ω/ω_b in bounce shaking implies the corresponding frequency spread in cyclotron shaking will be a factor of $\omega_c/\omega_b = 15$ smaller than that in bounce shaking. The period of frequency modulation for cyclotron shaking should be the same as that for bounce shaking to achieve the same effect. This is because one must frequency mod-

Fig. 1 Equilibrium Ion Oscillation Amplitude vs. Shaking Frequency

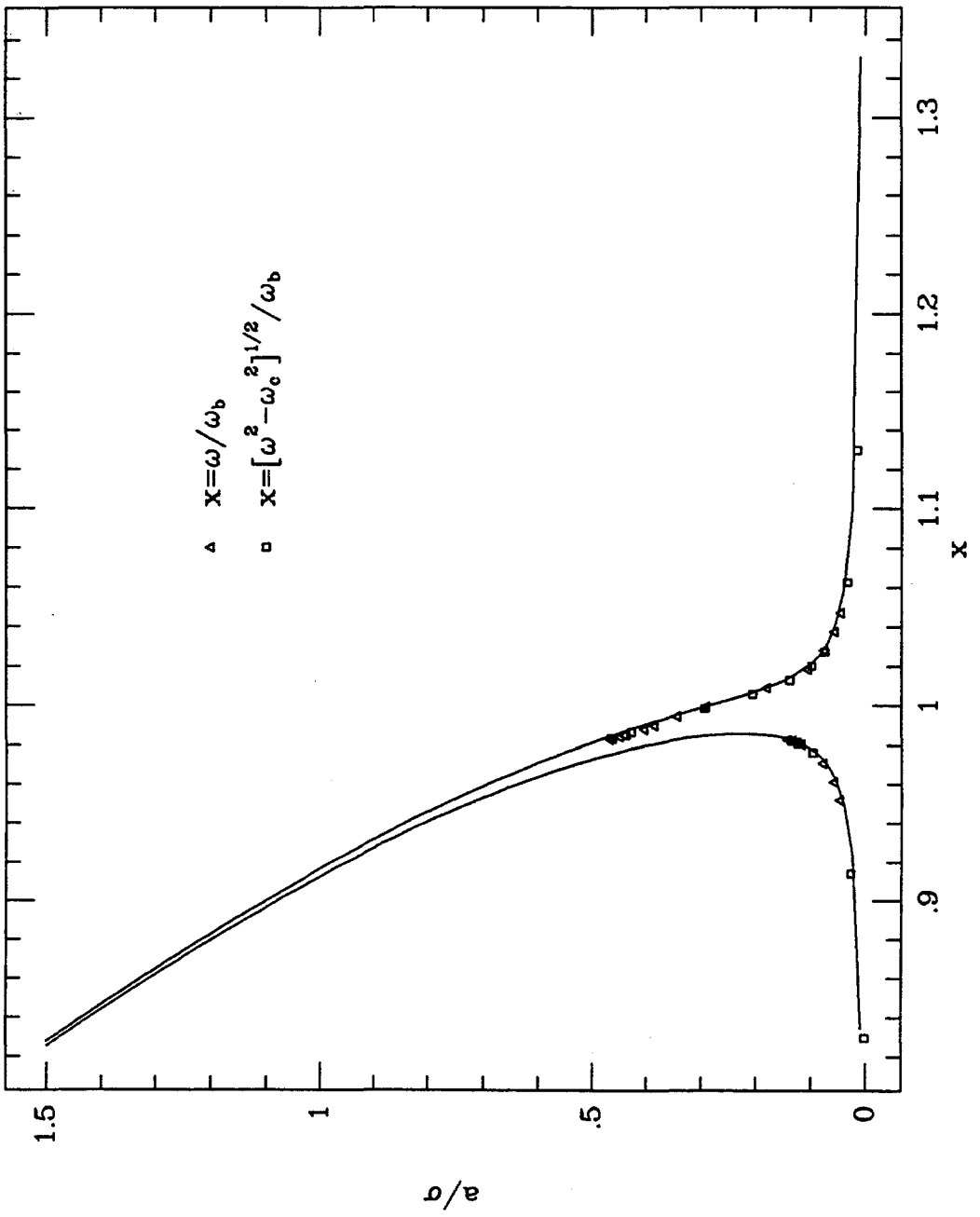

Fig. 2-1 Frequency modulated bounce shaking.

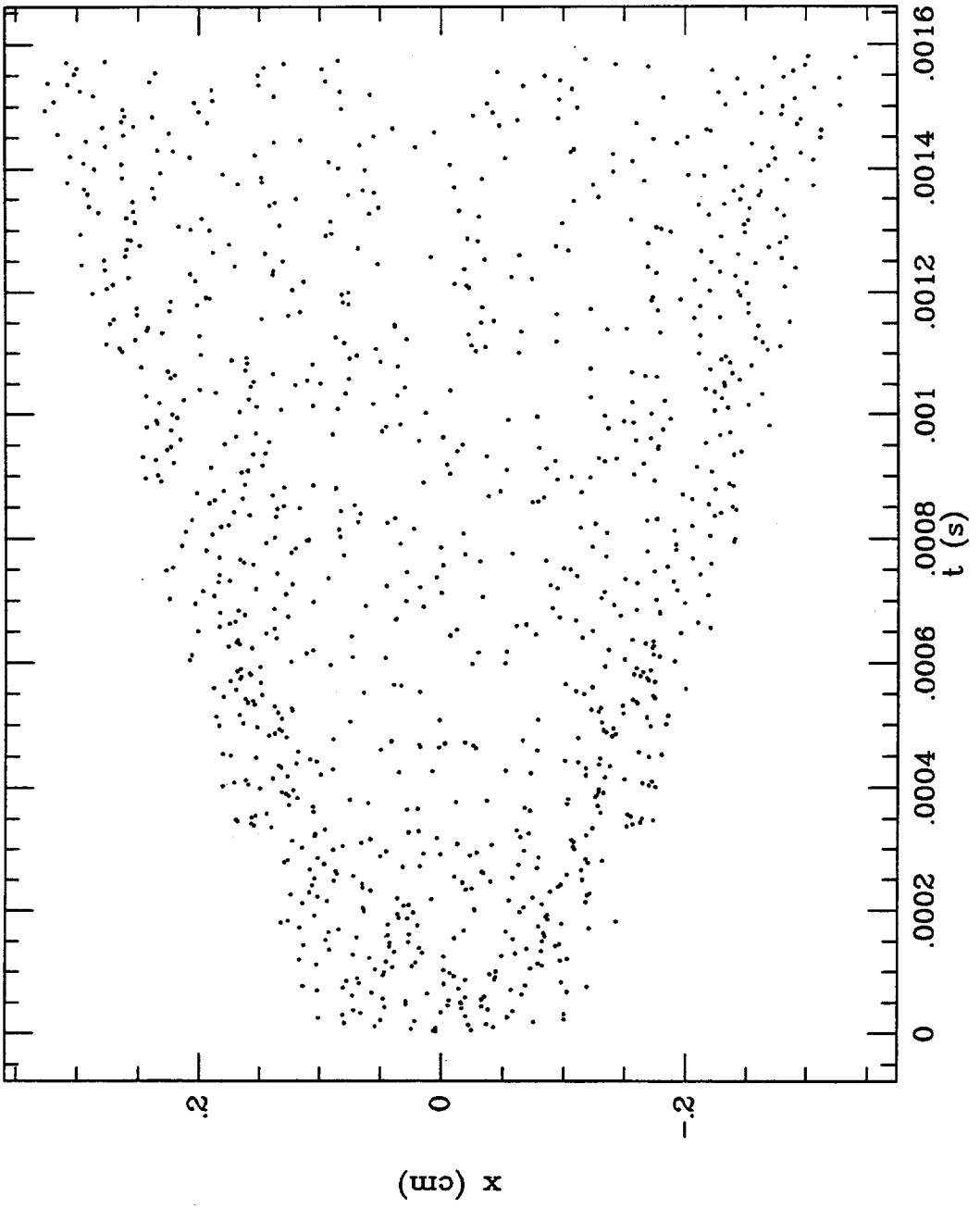

Fig. 2-2 Frequency modulated cyclotron shaking.

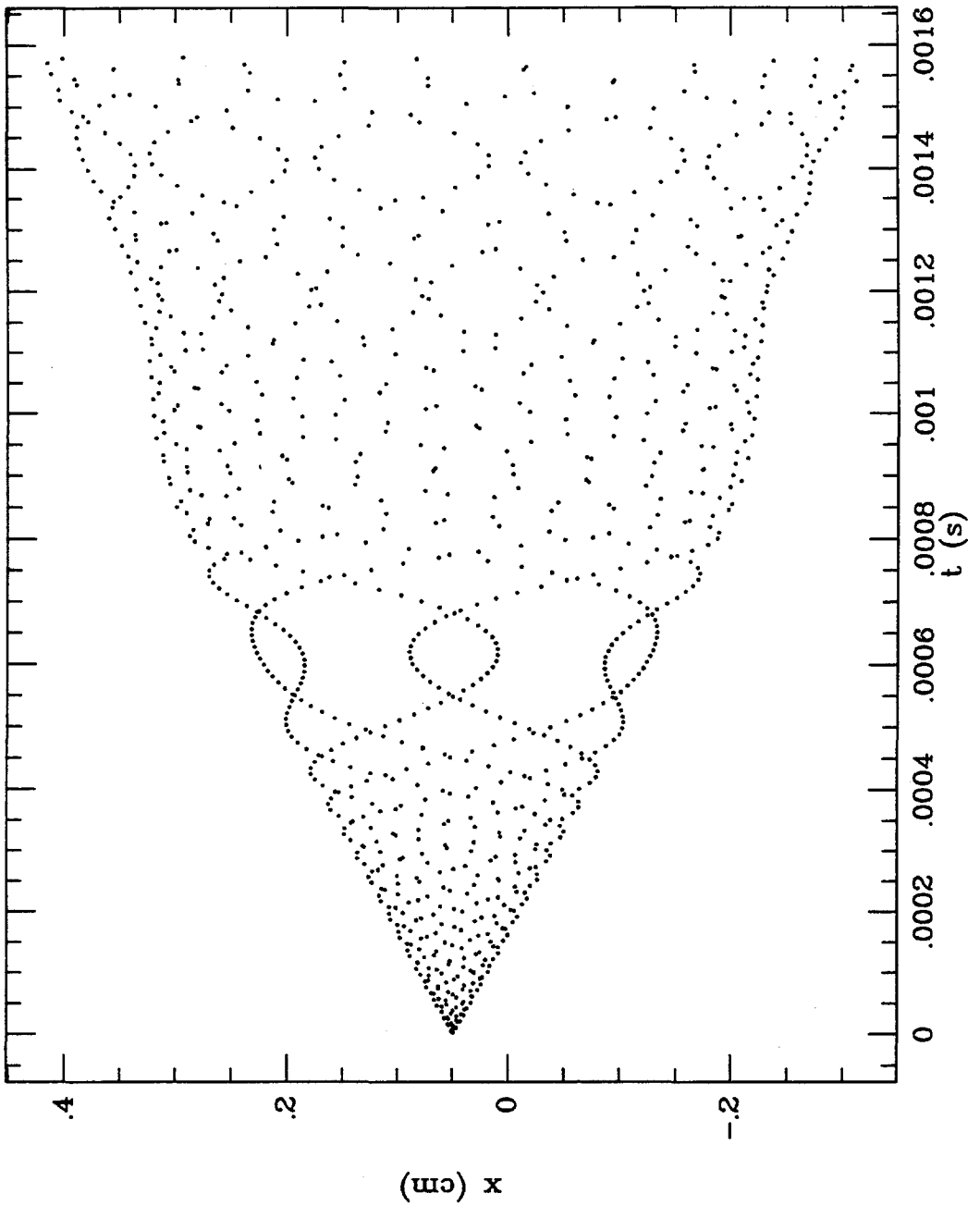

Fig. 2-3 Frequency modulated cyclotron shaking.
(with higher starting frequency and longer time)

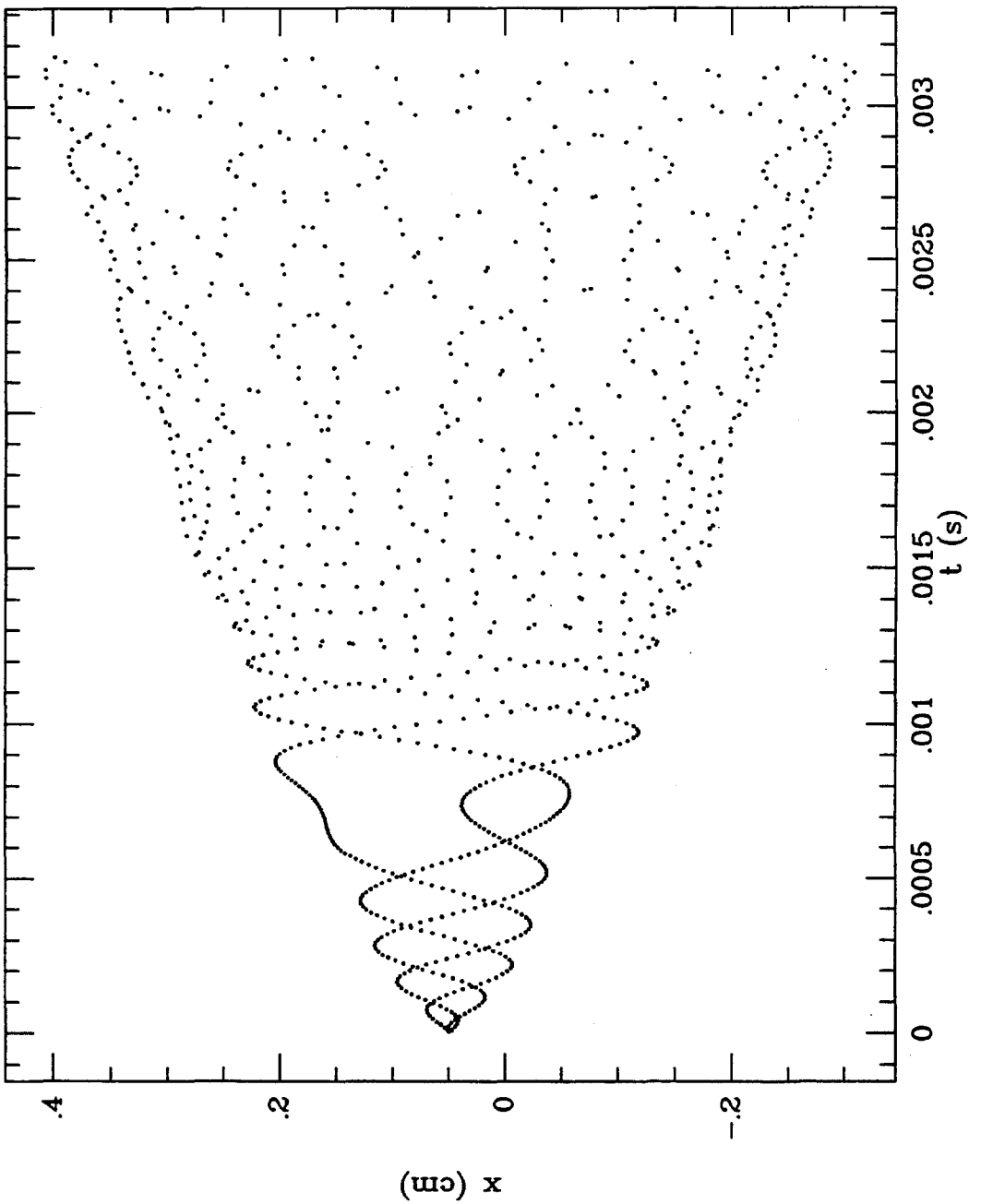

ulate through the narrower cyclotron resonance band slower than the bounce resonance band by a factor of the ratio of the band widths. However, this only applies for locking-on of the equilibrium amplitudes, and the simulation shows that the longer lasting transient in the cyclotron case causes near loss of lock-on even though the modulation in this case is twice as slow as for the modulated bounce shaking. It should be noted that the transient in this case is the worst that can exist, as the ion is initially motionless at the beam center. Some level of transient effect is always expected, however, and, thus it will take slightly longer to complete a modulation cycle. If one clears slower, the equilibrium neutralization will be larger.

The long transient from a "cold start" in the ion motion in the case of driving cyclotron resonant motion is easily understood by noting that there is a lot more kinetic energy in a cyclotron orbit than in a bounce orbit of the same horizontal amplitude. For the cases shown in Figure 2, the cyclotron kinetic energy is $E_k = (x_m\omega_c)^2 m/2 \simeq 500$ eV, and the maximum bounce kinetic energy is smaller by a factor of $(\omega_b/\omega_c)^2$, or 2.2 eV. At the end of the magnets, when a bounce-shaken ion has exited through its $\mathbf{E} \times \mathbf{B}$ drift motion, removal of the ion is still predicated on adequate clearing voltages, which may not always be provided. If the ion is cyclotron-shaken, however, it can by virtue of its large energy easily escape the beam potential well and clear completely. In addition, inside the magnet, if the cyclotron-shaken ion has an elastic collision with an ion, a neutral, or a beam particle which redirects even 5% of its energy into the vertical plane, it will escape the beam entirely. Preliminary calculations indicate that this beneficial phenomenon may occur at a nonnegligible rate in the Fermilab antiproton accumulator.

All the analysis above assumed the constant beam center oscillation amplitude. As shown in Fig. 3, this amplitude has a big impact on the ion response. This is effect is worrisome in the case of frequency modulation, because the beam response to the actual driving voltage depends strongly on the frequency. To write out this response explicitly, in the linear lattice theory,

$$x_0 = \frac{F}{(\nu - n)^2 - \nu_\beta^2}$$

$$F = \frac{eE_0\Delta s}{2\pi R m_p \gamma \omega_0^2}$$

where $\nu = \omega/\omega_0$, ω_0 is the beam revolution frequency, ν_β is betatron tune,

Fig. 3 Comparison of different driving amplitudes.

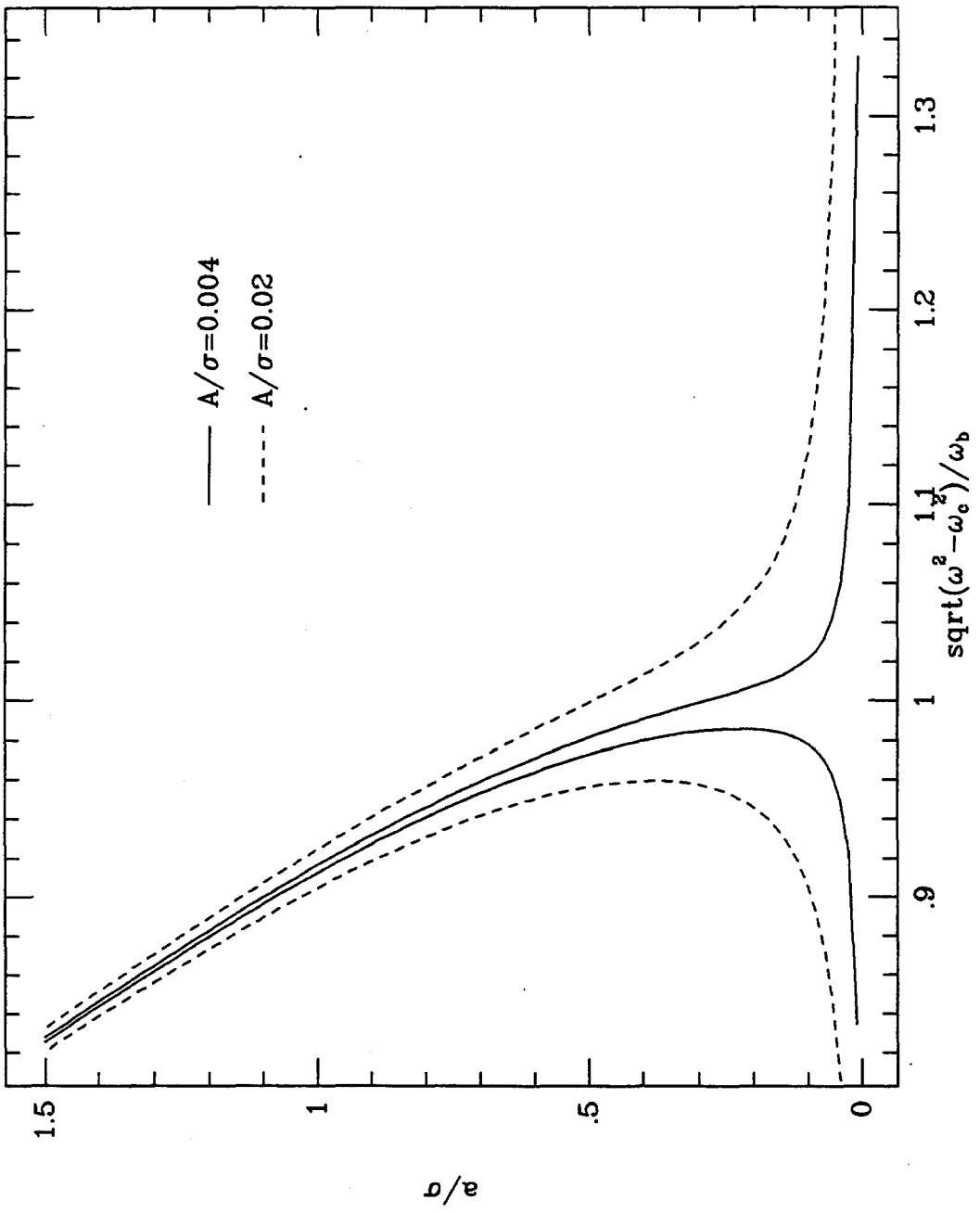

and F is the measure of shaker strength, where R is the average radius of the ring, and $eE_0\Delta s$ is the maximum integrated kick from the shaking field. If the driving frequency is not close to any betatron sideband the response is a superposition of several of the above.

As can seen above, the beam response to the driving voltage varies rapidly around betatron sidebands. If in the process of frequency modulation the beam responds too fast and wildly, transients are generated and the ions could loose the lock-on and fall off onto the bottom stable curve on the low frequency side of the resonance, as shown in Fig. 1. This could limit the effectiveness of modulated frequency shaking. The small frequency range of cyclotron shaking helps in stabilizing the beam response in the whole process of frequency change. In the case of Fermilab accumulator, $\omega_0 = 3.97 \times 10^6 s^{-1}$, the fractional tune is about 0.621 which corresponds to a difference of $1.5 \times 10^6 s^{-1}$ from the closest multiple of ω_0. The ion bounce frequency ω_b corresponding to 2×10^{12} total number of antiprotons and beam size $\sigma = 0.23$ cm is $1.05 \times 10^7 s^{-1}$. To raise the ion amplitude to 1.5σ at any point in the ring by bounce shaking requires frequency modulation of $10^7 s^{-1}$, while the corresponding required cyclotron shaking range is $6 \times 10^5 s^{-1}$. We can see that the frequency must cross a betatron sideband and thus cause the beam response to change wildly in the case of bounce shaking, while the beam response should not vary much over the band necessary for cyclotron shaking if the cyclotron frequency is not close to a betatron side band. Note that if the cyclotron frequency falls very near a betatron side band, a beam-ion instability may be excited. This subject will be analyzed in a future paper.

In short we conclude that the cyclotron shaking is less susceptible to the change of beam response to external driving voltage and therefore may be more effective in reducing ion neutralization effects. In addition, the large energy associated with exciting cyclotron orbits of radii on the order of the beam size may aid significantly in final removal of the ions from the beam. More detailed theoretical and experimental study is needed, and is presently being pursued.

References

[1] J. Marriner and A. Poncet, "Neutralization Experiments with Proton and Antiproton Stacks – Ion Shaking", Pbar-note 481, Fermilab Internal Note, March 1989.

[2] R. Alves Pires, "Beam Shaking for the Fermilab Antiproton Accumulator", Proceeding of the Fermilab III Instability Workshop, 1990

[3] Yuri Orlov, "The Suppression of Transverse Instabilities in the CERN AA by Shaking the $\bar{p}$ Beam", *CERN PS/89-01(AR),* 1989.

[4] R. Alves Pires and R. Dilão, "On the Theory of Shaking", to be published

[5] N. Krylov and N. Bogoliubov, *Introduction to Nonlinear Mechanics* (Princeton University Press, Princeton, N.J., 1943)

[6] Ronald E. Mickens, *Introduction to Nonlinear Oscillations* (Cambridge University Press, 1981)

[7] G. Dugan *et al,* "Report of the Accelerator and Beam Line Options Working Group", *Physics at Fermilab in the 1990's – Collected Reports of the Accelerator and Beam Line Working Groups,* E. Malamud and G. Dugan, Eds. Fermilab, 1990

[8] R. Alves Pires, *et al,* "On the Theory of Coherent Instabilities due to Coupling Between a Dense Cooled Beam and Charged Particles from the Residual Gas", *IEEE Trans. on Nucl. Sci.,* **NS-36** (1989) p. 800

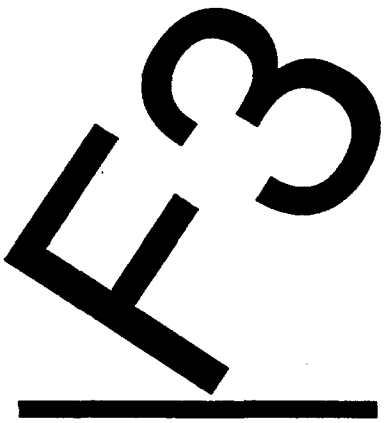

LONGITUDINAL INSTABILITIES AND IMPEDANCES

Outlook

D. Boussard
CERN

Dedicated presentations of the longitudinal aspects of the various machines (Booster, Main Injector, Accumulator and Tevatron) were organized within the framework of the longitudinal group. The most critical points emerged from these presentations and discussions. The workshop participants focused their attention on these particular points, the results of which are described in the following papers. Some of these contributions have been already formulated during the workshop, others which require simulation or experiments were added at a later stage.

Although they have not specifically been addressed during the workshop, some rather general aspects are worth mentioning. It was not possible during the short time available to analyze the aspects of impedance estimates and impedance budgets in the various machines. The impedance measurement activities already existing at FNAL can only be encouraged. Estimates of parasitic resonances in the various machine components, as well as their broadband impedance should be made available using the well established wire measurement technique. This should lead to a better evaluation of the overall machine impedance. For the existing machines and especially for the Tevatron, beam measurements with single bunches should be carried out in order to obtain a better estimate of the inductive wall impedance. Quadrupole mode measurements are best suited for this purpose. In the following we have taken the existing data or the assumed values of the ring impedances.

In reviewing the various machines it turned out that three types of problems deserve particular attention: the longitudinal instabilities, bunch coalescing, and beam loading problems.

Coupled Bunch Instabilities

With the very dense beams considered, natural Landau damping is lost almost anywhere in the chain of accelerators. This is particularly clear in the case of the Booster and Tevatron (*cf.* next paper). Consequently bunch-to-bunch instabilities, with many modes present at the same time dominate the scene. The resulting blow-up of bunches is uncontrolled and therefore difficult to predict with a good degree of confidence if the intensity is to be substantially increased. The group felt that a project of the scope of Fermi III should be based on controllable parameters and therefore recommended solutions to avoid instabilities. The lowest instability modes (dipole and possibly quadrupole) are to be damped by active feedback systems. The higher order modes which will unavoidably develop if the emittance stays too low must be cured by controlled blow-up of the longitudinal emittance. Papers III and IV cover the particular case of the Booster. Possible feedback parameters (paper III)

and a controlled blow-up scenario are given (paper IV). For the Tevatron in colliding mode the shorter bunch distance with 36 bunches will require a new design of the bunch-by-bunch damping system. In the fixed target mode, Landau damping will almost certainly be lost at high intensity. If one does not want to run with almost filled buckets, which could restore Landau damping, it might be necessary to use a harmonic Landau cavity to significantly increase the synchrotron frequency spread without reducing the RF bucket size.

Tests of a feedback system for the Booster have already been done. They should be pursued with a more powerful kicker and improved electronics and detectors. This might give as an additional benefit a better understanding of the instability, its most unstable modes, etc.

Bunch Coalescing

This is a critical RF manipulation in the Main Injector, especially at high energy. The present performance in the Main Ring is totally inadequate for the Fermi III upgrade. At the expected intensity the measured efficiency is only 45% whereas it should be close to 100%.

Two problems are of concern: control of RF voltage down to very low values in the presence of a significant beam loading and microwave instabilities at the end of the "debunching" of the 53 MHz bunches. The first problem clearly depends on details of the RF hardware and control circuitry. Simulation of microwave instability is in progress (J.MacLachlan): the first results with a single bunch in an almost full bucket are impressive and give a good hope that a full simulation of the coalescing process will lead to very significant results.

The quality of the coalescing process is directly linked to the cleanliness of the quasi-debunched bunches, just prior to rotation. It was suggested to debunch a set of 53 MHz bunches in the Tevatron, which has a significantly lower Z/n than the Main Ring. In this way one can better evaluate the future situation in the Main Injector and possibly discriminate between microwave instability and RF beam loading effects.

Another, more radical, solution has been looked at (paper VI). It avoids coalescing at high energy where η is very small, with a new low frequency RF system in the Main Injector. Coalescing would be completely avoided for antiprotons and replaced by some low energy (8 GeV) "merging" for the protons. Transition crossing at a much slower rate than foreseen will have to be carefully evaluated.

Beam Loading

In the high intensity, fixed target mode of operation, ordinary beam loading of the RF cavities is large. The critical parameter here is the ratio of beam to generator current, which for the Tevatron RF system will be about three in the upgrade scenario. It is known, from the work of F. Pedersen that beam loading factors larger than one or two should be avoided if a conventional RF control system, with independent tuning, amplitude, and phase loops is employed. The well established solution to this problem is to reduce the effective cavity impedance by RF feedback. For the fixed frequency Main Ring and Tevatron RF systems, this is a perfectly applicable solution (paper VII) provided the peak power capability of the final RF amplifiers is adequate.

Longitudinal Stability in the Booster and Tevatron

T. P. R. Linnecar, CERN
J. MacLachlan, Fermilab
R. A. Schill, Jr., University of Illinois - Chicago

Booster

The data used to calculate the frequency shifts and synchrotron tune spreads is taken from the slides of the presentation given at F3IW[1] and corresponds to the 8 GeV cycle with 16 cavities. This data is reproduced in Table I. Information about the D magnets of the Booster is also available;[2] these apparently are the dominant source of impedance in the machine.

Comparison of space charge Z/n and magnet Z/n

The space charge impedance is capacitive and of amplitude

$$Z/n = \frac{g_\circ Z_\circ}{2\beta\gamma^2} \ ,$$

where $Z_\circ = 377\ \Omega$, β and γ are usual Lorentz parameters, and $g_\circ$ is a coupling parameter taken here as 4; calculations made previously[2] have used $g_\circ = 6$. Table II gives this quantity through the Booster cycle. It starts at 638 Ω dropping to 12 Ω. Figure 1 shows the impedance data on the magnets which have an inductive Z/n of approximately 70 Ω. (There is also a resistive Z/n component of approximately 100 Ω, the effect of which should be studied.) The inductive impedance is constant to about 30 MHz and then falls rapidly to 120 MHz becoming capacitive afterwards.

We assume a bunch area of 0.05 eVs which gives the bunch lengths along the cycle as in Table I. These bunch lengths are such that they probe frequencies much higher than 30 MHz except at injection where the space charge impedance is very high. To first order we assume that the inductive effect is small compared to the space charge effect all through the cycle. We assume that there are no other significant sources of impedance.

Calculation of the shift of incoherent particle frequencies

The formula to calculate this quantity is given in many references, *e. g.* ref. [3]. The constant depends on assumed particle distribution, but it varies by less than a factor 2. We use

$$\frac{\Delta\omega_{sh}}{\omega_\circ} = \frac{3}{2\pi^2}\frac{I_\circ}{h^2\hat{V}\cos\phi_s\,\beta^2}\left(\frac{2\pi R}{ct}\right)^3\left|\frac{Z}{n}\right|$$

Table I: Booster Parameters Used for $\Delta\omega_{sh}$ and $\Delta\omega_{sp}$

cycle time [ms]	β	γ	$\hat{V}$ [kV]	ϕ_s [deg]	bucket area [eVs]	bucket length [ns]	bunch length [ns]
5	0.663	1.336	600	15	0.06	20	15
10	0.904	2.34	750	35	0.07	10	7.5
15	0.95	3.2	750	50	0.08	6	3.9
20	1	4	750	55	0.17	5	2.2
25	1	6	700	50	0.15	6	2.76
30	1	7	500	35	0.2	8	3.12
35	1	8	300	5	0.6	15	3.3

Table II: Space Charge Z/n and Incoherent Frequency Shift

cycle time [ms]	$\frac{g_o Z_o}{2\beta\gamma^2}$	$\frac{\Delta\omega_{sh}}{\omega_o}$
5	638	0.009
10	152	0.008
15	77.6	0.034
20	47	0.116
25	21	0.032
30	15.4	0.014
35	11.8	0.013

Table III: Frequency Spread and Comparison $\Delta\omega_{sp}$ to $\Delta\omega_{sh}$

cycle time [ms]	bunch length [ns]	$\sin\phi_s$	$\frac{\Delta\omega_{sp}}{\omega_o}$	$\frac{\Delta\omega_{sp}}{\Delta\omega_{sh}}$
5	15	0.259	0.187	20.8
10	7.5	0.574	0.120	15.9
15	3.9	0.766	0.069	2.02
20	2.2	0.819	0.034	0.29
25	2.76	0.766	0.04	1.25
30	3.12	0.574	0.027	1.93
35	3.3	0.09	0.017	1.31

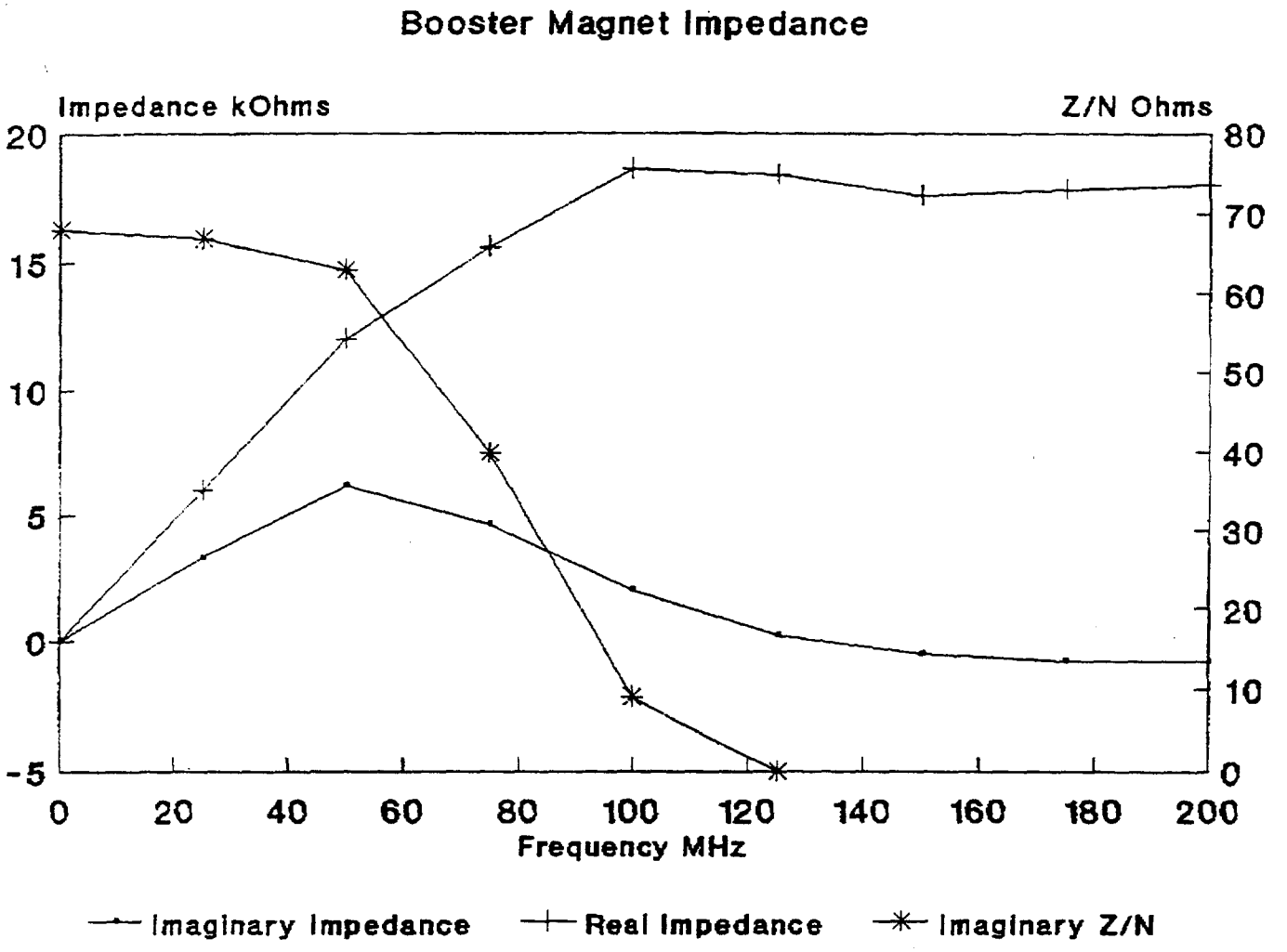

Figure 1: Booster magnet impedance

$$\frac{Z}{n} = -\frac{g_o Z_o}{2\beta\gamma^2} + \left(\frac{Z}{n}\right)_{\text{ind}}$$

with parameters

R	machine radius	76	m
h	harmonic number	84	
I_o	mean beam current	varies	A
$\hat{V}$	peak rf voltage	varies	V
c	velocity of light	$2.998 \cdot 10^8$	m/s
t	bunch length	varies	s
ω_o	revolution frequency	varies	s^{-1}

We take A = 0.05 eVs and injection current $I_o = 0.13$ A, the present situation, and use the corresponding values in the tables. In the formula we assume all h buckets are filled. The calculated value of $\Delta\omega_{sh}/\omega_o$ as a function of time in the cycle is given in Table II and plotted in Fig. 2.

Calculation of frequency spread in the bunch

We are interested in comparing the frequency shift with the spread of particle frequencies. Using standard tables[6] this shift can be found as a function of bunch length and bucket parameters. The results are given in Table III, and $\Delta\omega_{sp}/\omega_o$ is plotted in Fig 2.

Comparison of $\Delta\omega_{sh}/\omega_o$ and $\Delta\omega_{sp}/\omega_o$

A rule of thumb for stability is that $\Delta\omega_{sp}/\Delta\omega_{sh} > 4$. More precise calculations are possible; these depend on the distribution but also give information about higher modes. Besnier, quoted in ref. [4], gives the following:

$$\Delta\omega_{sp}/\Delta\omega_{sh} > K_m$$

m	1	2	3	4
K_m	3.4	1.6	0.9	0.65

The ratio is plotted in Fig. 3 with the Besnier limits for dipole and quadrupole modes.

Discussion

a. Damping is clearly lost for the 0.05 eVs bunch at this intensity at around 15 ms in the cycle; the second mode is probably stable. At three times the intensity, *i. e.* in the upgraded Booster, higher modes will be above the threshold, but stability will probably still be lost at roughly the same time in the cycle. The worst region is around 15 to 25 ms.

b. The shift scales as t^{-3} and the frequency spread as t^2, so the ratio scales as t^5. In principle, small increases in bunch length quickly stabilize the bunch. As a rough calculation

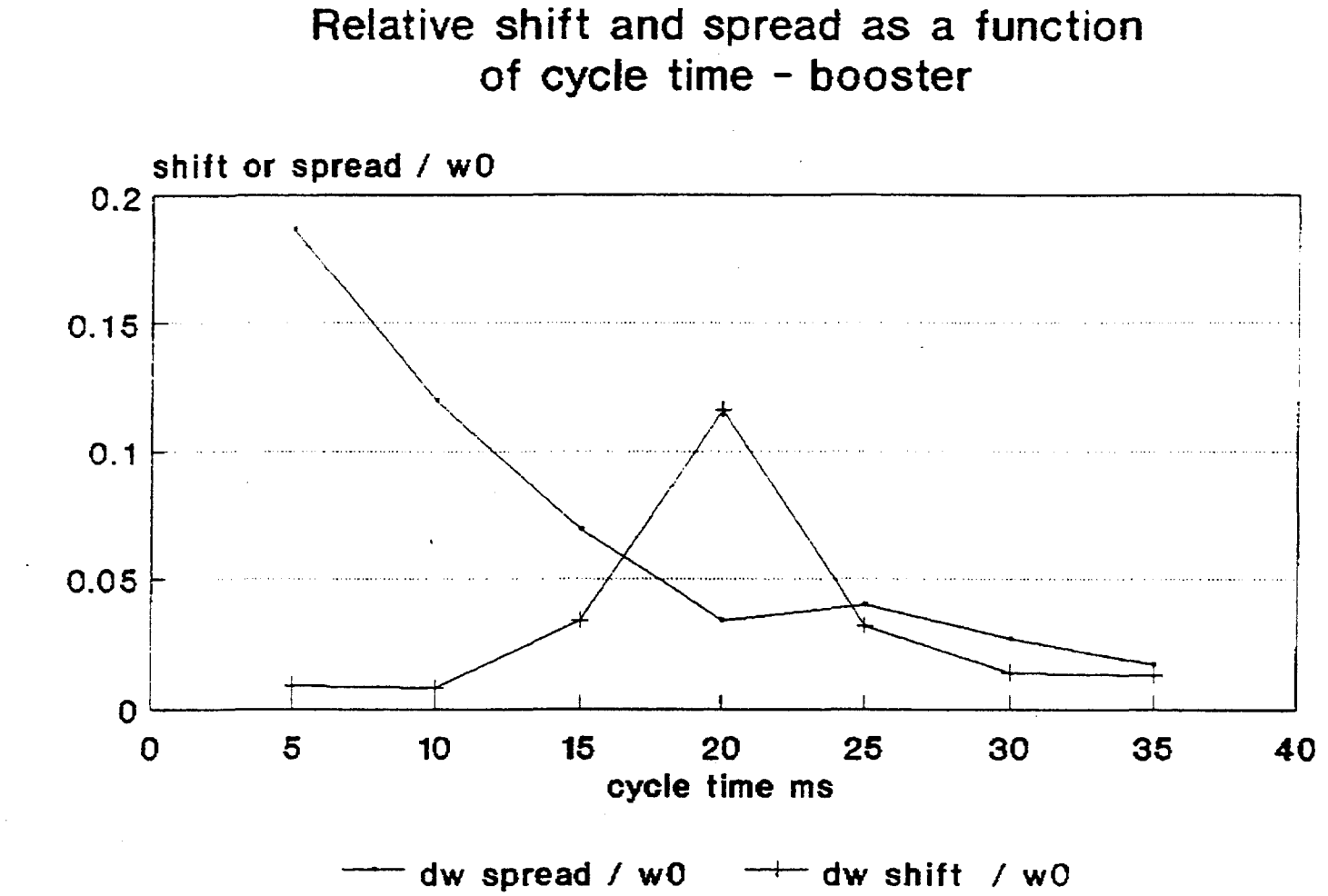

Figure 2: $\Delta\omega_{sp}/\omega_o(\cdot)$ and $\Delta\omega_{sh}/\omega_o(+)$ *vs.* time in Booster

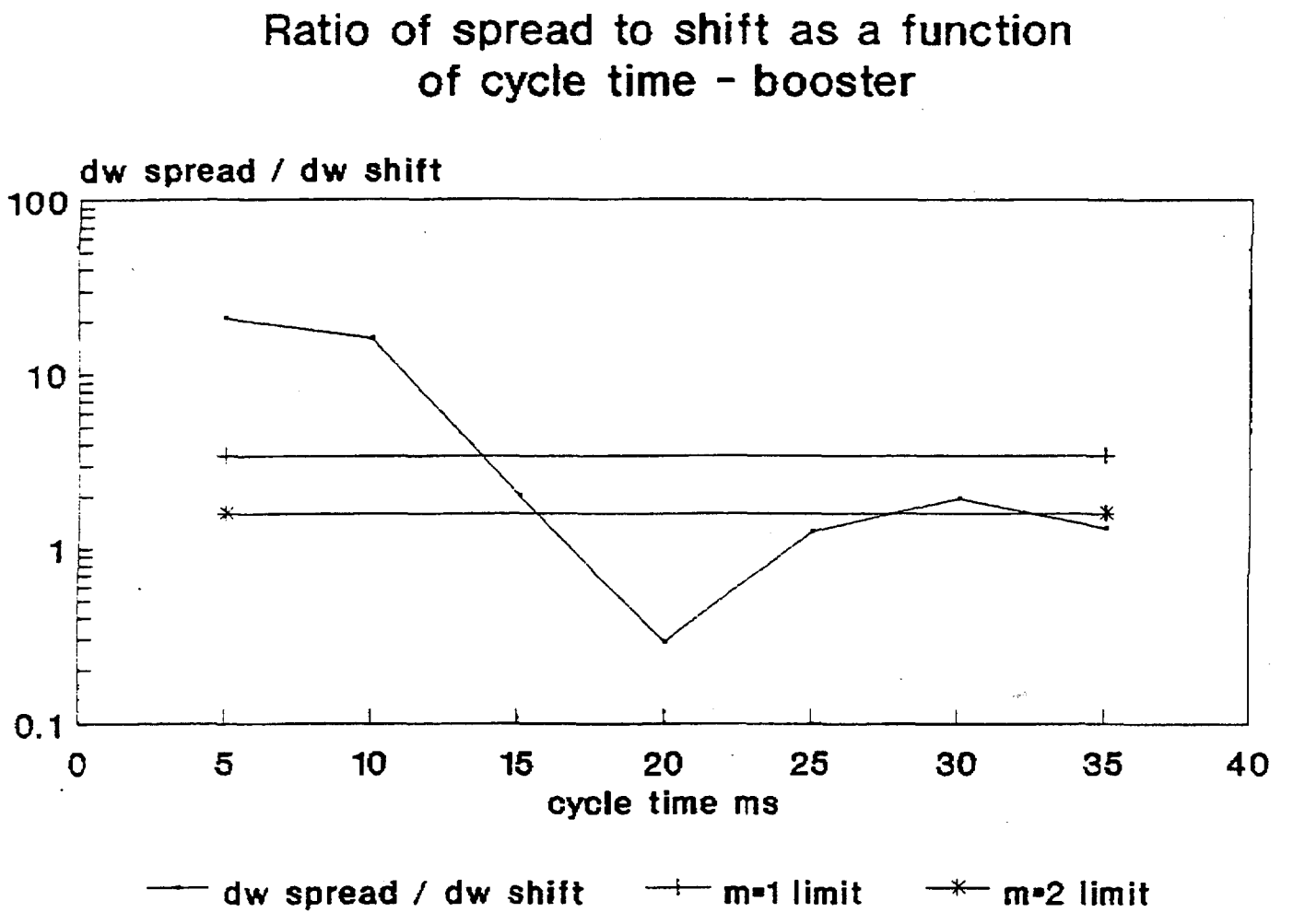

Figure 3: Ratio $\Delta\omega_{sp}/\Delta\omega_{sh}$ *vs.* time in Booster

we can say that the bunch area scales as t^2 and therefore $\Delta\omega_{sp}/\Delta\omega_{sh}$ scales as $A^{2.5}$. In the present Booster situation an increase in this ratio of 10 times should be sufficient to ensure stability; *i. e.*, the bunch emittance should be 2.5 times higher or 0.125 eVs. (The bucket parameters *etc.* would have to change which would slightly affect the result). It might be possible to blow up the bunches to this value just before transition to stabilize the beam, but in the short time available in the cycle this seems difficult. The same projection for the upgraded Booster requires a 30 times increase in ratio, *i. e.*, four times the present emittance. Bunches with $A = 0.2$ eVs should be stable if nothing else is done.

c. A very rough argument to predict the bunch emittance at extraction of the beam for the higher intensity upgraded Booster, if nothing is done and assuming the instabilities that develop are fast growing, supposes that

$$\begin{aligned} \text{Initial emittance} \times \text{Final emittance} &= (\text{Max stable emittance})^2 \\ (0.05 \text{ eVs}) \times (?\ eVs) &= (0.2 \text{ eVs})^2 \end{aligned}$$

This suggests a final emittance of the order of 0.8 eVs.

Conclusion for the Booster

A feedback system is required; this should probably act on at least dipole and quadrupole modes if nothing else is done. This may be a difficult problem for a fast cycling booster. A higher harmonic cavity might also help. Both of these possibilities have already been examined in ref. [5]. With the 400 MeV injection proposed it is worth examining whether the resulting cycle allows enough bucket area for a preventive blow-up from injection.

Tevatron

Stability calculation (fixed target)

The problem is attacked slightly differently for the Tevatron.[4] The expression for frequency shift due to machine impedance is as before. In the Tevatron the space charge contribution is negligible and the inductive impedance due to the broad band wall impedance is assumed dominant. The spread in bunch frequencies is given by an approximate formula which is valid for bunch lengths small compared to the bucket length:

$$\frac{\Delta\omega_{sp}}{\omega_o} = \frac{(ct)^2}{64}\left(\frac{h}{R}\right)^2 .$$

Taking $\beta = 1$ and $\phi_s = 0$ in our previous expression for $\Delta\omega_{sp}/\omega_o$ and dividing the above by it we obtain

$$\frac{\Delta\omega_{sp}}{\Delta\omega_{sh}} = \frac{\hat{V}}{768\pi}\frac{h^4}{R^5}\frac{(ct)^5}{I_o Z/n} .$$

With $h = 1113$, $\hat{V} = 1$ MV, and $R = 1000$ m we obtain

$$\frac{\Delta\omega_{sp}}{\Delta\omega_{sh}} = \frac{1.48 \cdot 10^{42} t^5}{I_o Z/n} ,$$

where, remember, t is the bunch length in s. This is plotted in Fig. 4 for two values of $Z/n \times I_o$. The first is for the present Tevatron with $I_o = 0.167$ A and $Z/n = 0.8\ \Omega$ and the second for the upgraded Tevatron where $I_o = 0.5$ A and Z/n degrades to 2 Ω because of the separators.

Discussion

Present operating conditions use a large bucket, 4 eVs, with small bunches, 0.4 eVs, to restrict particle loss during ramping in the Tevatron. This implies a bunch length of 4.8 ns. From the graph this bunch should be stable under the present conditions but on the verge of instability in the upgraded Tevatron.

If, as appears to be the case, the bunch is un-damped in the existing situation, oscillations due to injection errors *etc.* remaining throughout the ramp, then it is perhaps advisable to re-examine the situation and verify the present Tevatron broad band impedance.

References

[1] Kathy Harkay, Fermilab, presentation at this workshop

[2] Data supplied by Jim Crisp, Fermilab, priv. comm.

[3] S. Hansen *et al.*, "Effects of Space Charge and Reactive Wall Impedance on Bunched Beams", IEEE Trans. on Nucl. Sci., **NS-22**, No. 3(1975)

[4] J. Gareyte,"Ultimate Longitudinal Particle Density in High Energy Proton Bunches", CERN internal report CERN SPS/80-I/DI

[5] M. Cornacchia, "Observation and Computations of Higher Energy Collective Effects in the Fermilab Booster", Lawrence Berkeley Laboratory internal report LBL-22978

[6] S. Ohnuma, "The Beam and the Bucket", Fermilab internal report TM-1381

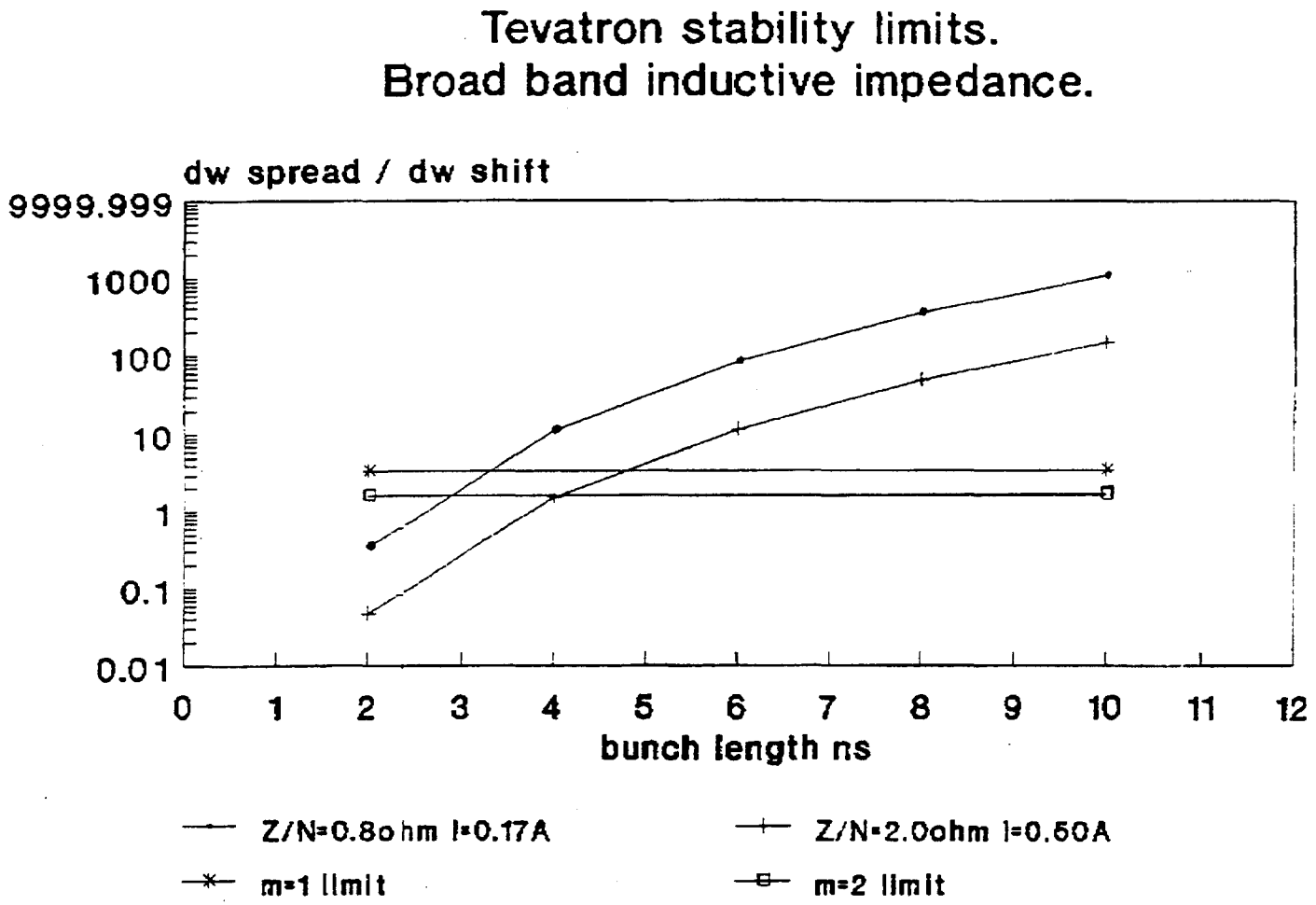

Figure 4: $\Delta\omega_{sp}/\Delta\omega_{sh}$ for $Z/n = 0.8\ \Omega$ (·) and $2.0\ \Omega$ (+). Also shown, the Besnier limits for mode 1 (*) and mode 2 (□)

Parameters of a Feedback Against Longitudinal Instabilities in the Booster

D. Boussard
CERN

Growth Rate Estimates

The mountain range display of Fig. 1 shows a clean instability when the γ_T-jump is in use. We measure the e-folding time

$$\tau \approx 4 \text{ ms}$$

at an intensity of $1.5 \cdot 10^{10}$/bunch. Extrapolating to the future Booster intensity ($6 \cdot 10^{10}$/bunch) we expect

$$\tau = 1 \text{ ms} = 1/\Delta\omega$$

and therefore

$$\Delta\omega/\omega_s = 0.06 \quad (f_s = 2500 \text{ Hz}) \ .$$

Required Power

a Phase measurement

The required power is given by the detection error of the phase measurement (assuming that the injection transients have completely died out when the instability starts). Assuming an error of one tenth of the total bunch length, *i. e.* 5° of RF phase one obtains with

$$V_f = 2\frac{\Delta\omega}{\omega_s} V \cos\phi_s \, \delta\phi \ ,$$

where V_f is the feedback voltage, V the RF voltage, and $\delta\phi$ the phase error the following:

$$V_f = 5.2 \text{ kV}$$

with

$$V \cos\phi_s = 500 \text{ kV} \ .$$

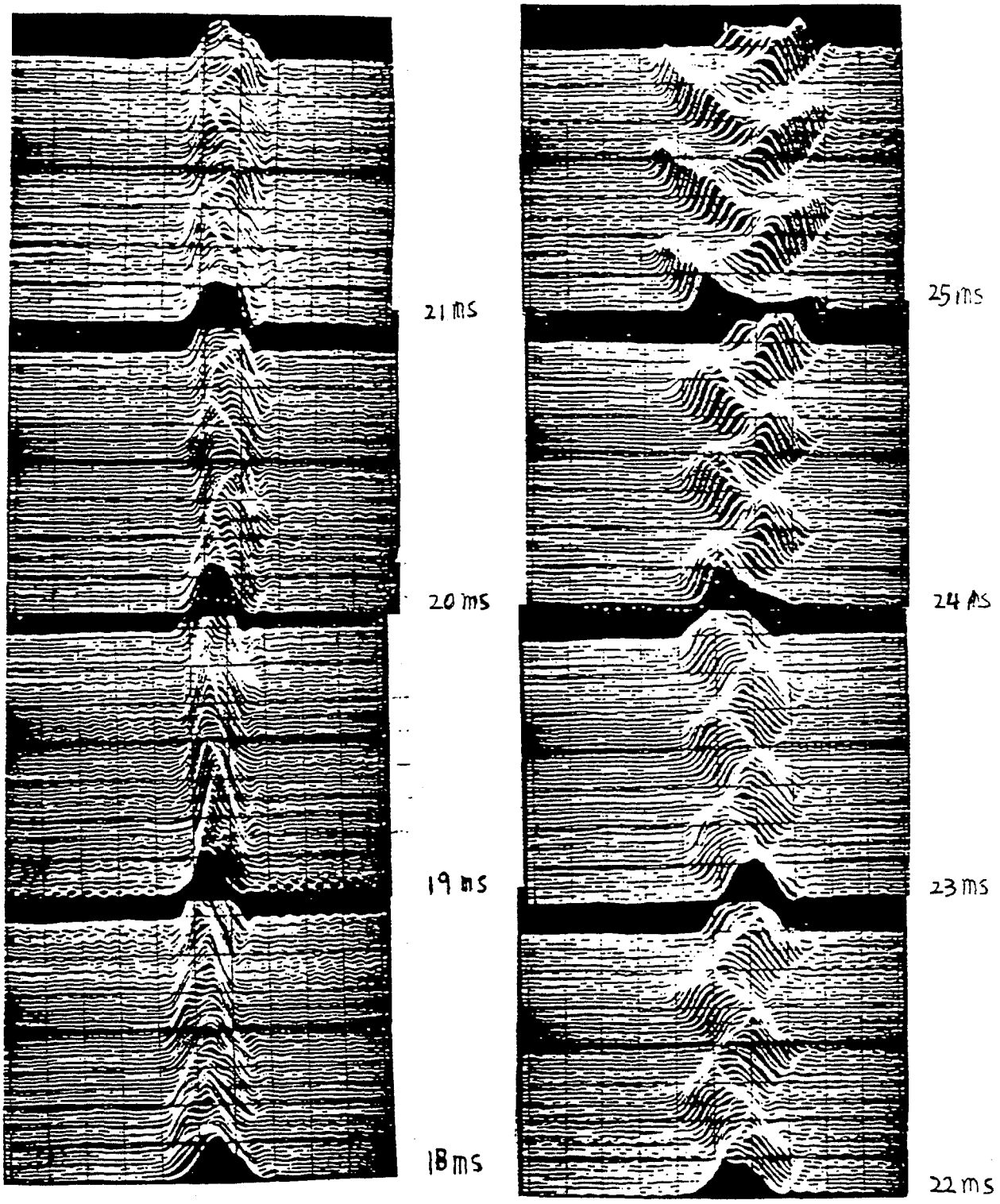

Figure 1: Mountain range of Booster bunch with γ_T-jump active

b Radial measurement

The formula in this case is the following

$$V_f = 2\Delta\omega_s\beta^2\frac{E}{f_o}\gamma_T^2\frac{\Delta R}{R}$$

for a radial pick-up located at a region of average dispersion. For the Booster at 8 GeV one obtains with $\Delta R = 5$ mm (including closed orbit displacement at the pick-up)

$$V_f = 55.5 \text{ kV} \ .$$

Clearly this solution is far less interesting than that with phase detection. To better reject the closed orbit components (or f_{rev} lines) would require programmable notch filters with a negligible phase shift at the synchrotron satellites. This seems difficult taking into account the fast sweeping rate of the Booster.

A Possible Architecture *(Fig. 2)*

Individual bunch phase measurements are made through a broad band filter in the phase pick-up chain. The phase information of each bunch is stored via a sample and hold circuit and digitized with a fast flash ADC. The digital notch filter and delay are clocked at the RF frequency to ensure the correct location of notches and the correct delay throughout the cycle.

This scheme automatically rejects the nf_o lines which otherwise would saturate the amplifier. It provides the necessary quadrature component as the f_s side bands fall on the skirts of the notches.

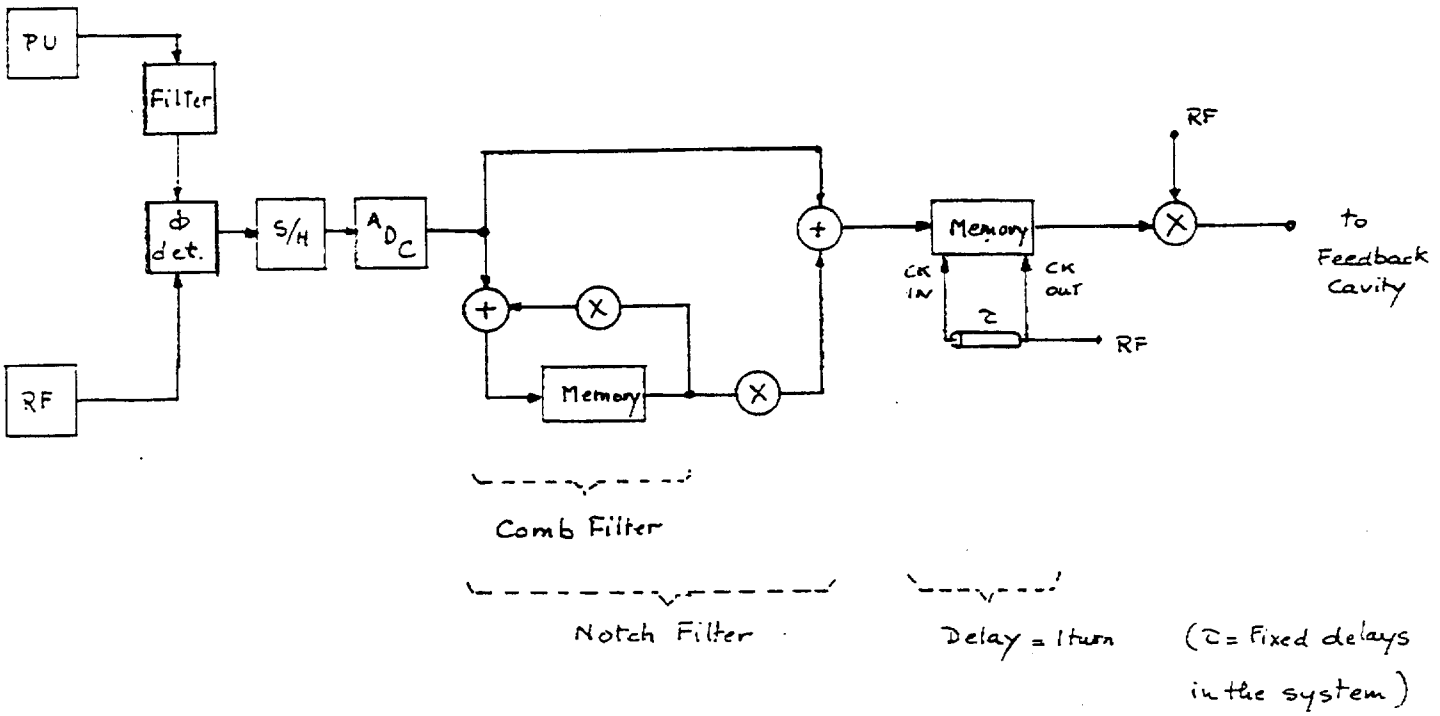

Figure 2: Block diagram of a wide band longitudinal phase feedback system for the Booster

Controlled Blow-Up in the Booster

D. Boussard
CERN

Following the examples of the CERN-PS and the Brookhaven AGS, one can try to evaluate the parameters of a possible high frequency blow-up cavity for the booster. Using the model which gives a good fit to the CERN-PS experimental results, the blow-up rate can be estimated from the formula[1]

$$\frac{\langle \Delta x \rangle}{\Delta t} = \frac{\pi^2}{4} f_s \left(\frac{V_1}{V_o}\right)^2 \frac{f_o}{f_1} \left(\frac{1+2x}{\hat{\phi}}\right) \quad ,$$

where

x is the bunch to bucket areas ratio (x = 1 at the separatrix)
f_s is the unperturbed synchrotron frequency
V_1, V_o, f_1, f_o are the amplitudes and frequencies of the blow-up and normal cavities respectively.

The relation has been verified only for a stationary bucket, $\phi_s = 0$. In the absence of a better estimate, we apply it in the case of the Booster ($\phi_s \neq 0$) and assume, as in the case $\phi_s = 0$ that the value of the bracket $((1+2x)/\hat{\phi})$ is approximately equal to unity.

Experience has shown that the frequency f_1 should be such that several wavelengths occur within the bunch length. We propose tentatively $f_1 = 400$ MHz and therefore $f_o/f_1 = 1/8$. With $V_1/V_o = 0.2$ (100 kV at 400 MHz, 500 kV at 53 MHz) and $f_s = 2500$ Hz one obtains

$$\frac{\langle \Delta x \rangle}{\Delta t} = 30.84 \quad .$$

If dipole and quadrupole modes are suppressed by feedback the required emittance for stability can be estimated to be about 0.07 eVs (paper I). For a bucket area just after transition of 0.15 eVs, the blow-up parameter x is of the order

$$(0.07 \text{ eVs} - 0.05 \text{ eVs})/0.15 \text{ eVs} = 0.13$$

The time needed for controlled blow-up would be

$$\Delta t = 4.2 \text{ ms} \quad ,$$

which seems just feasible taking into account the very short Booster cycle time.

The high frequency cavity would have to have a large enough bandwidth to accommodate the frequency swing during its 4.2 ms of operation. A quality factor of 500 seems adequate for this purpose. Assume two cavities, each with an R/Q of 200 Ω. The total required power (at the edges of the band) would be

$$P = 2 \times \frac{(50\ \text{kV})^2}{2 \times 200 \times 500} = 25\ \text{kW} \quad .$$

References

[1] D. Boussard, "The RF Noise Theory Applied to the PS Longitudinal Controlled Blow-Up", CERN internal report CERN SPS/ARF 85-7

Limits to Coalescing and Bunch Rotation for $\bar{p}$ Production Resulting from Microwave Instability

J. A. MacLachlan
Fermilab

Abstract

Bunch narrowing by shape oscillation in a miss-matched bucket and adiabatic debunching for bunch coalescing are two beam manipulations used in the present scheme of collider operation which reduce the momentum spread of the beam substantially below the normal operating conditions. Therefore, microwave instability is a potential difficulty in extending these techniques to higher intensity. Bunch narrowing takes place on a much faster time scale than the coalescing process, so only conditions well above the instability threshold will produce emittance growth of practical importance. For bunch coalescing, however, microwave instability sets a significant fundamental limit on efficiency. These processes have been modeled with parameters characteristic of the Main Ring and the Main Injector. Interim results are reported and the status of related calculations to eliminate or evaluate the contribution of numerical artifacts is described.

Introduction

There are two particular steps in the procedures now used for colliding beam operation in which the momentum spread of the beam in Main Ring is reduced far below its values anywhere else in the cycle, *viz.*, the debunching/coalescing process for protons and antiprotons at 150 GeV and the proton bunch narrowing process for $\bar{p}$ production at 120 GeV. As the intensity is raised toward the goals of Fermilab III, these steps may become obstacles because of emittance dilution caused by microwave instability, that is, the bunching and deceleration of part of the beam by beam-induced voltage at frequencies several times the rf fundamental. This instability is occasionally called "self-trapping instability", but there are special features implied by the microwave instability label. Basically, all of these features derive from the source of the bunching voltage being a wall impedance with bandwidth extending over essentially all harmonics of the beam circulation frequency up to the microwave cutoff of the vacuum chamber. The phenomena are qualitatively distinguishable from those of beam interaction with a high-Q resonance.

The instability threshold is given[1] by the variously named Keil-Schnell-... criterion as written for bunched beam

$$|Z/n| \leq F \frac{\beta^2 E|\eta|}{e\hat{I}} \left(\frac{\Delta p}{p}\right)^2_{\text{FWHM}} ,$$

where Z/n is the longitudinal impedance $Z_{\|}(\omega)$ divided by the harmonic of the beam circulation frequency, F is a form factor chosen so that the growth time is less than a synchrotron period, and $\hat{I}$ is the peak value of the beam current. F has a value of about 0.65 for a typical, *e. g.* elliptical, phasespace distribution. For the Main Ring Z/n has been estimated to be in the range 9–20 Ω, and for the Main Injector the design criterion is 5 Ω. For proton bunch coalescing in the Main Ring the idealized (zero dilution) process requires total debunching of the 53 MHz bunches into a 2.5 MHz bucket produced by a few volts. Using numbers similar to current conditions, $S_b = 0.2$ eVs and $n_b = 3 \cdot 10^{10}$ protons/bunch, one finds that the ideal process requires $Z/n \sim 1\ \Omega$.

It is hard to get much information from analysis about the emittance dilution to be expected during a manipulation which may pass the threshold for some period with various time scales of parameter variation. Therefore, it is interesting to know the feasibility of numerical modeling. This note gives interim results of simulations of both debunching and bunch narrowing made with ESME.[2] It discusses some test cases examined for artifacts of the numerical methods like, for example, number of macroparticles, number and frequency separation of selected fourier components of the beam current, and parameters of the longitudinal impedance model. Despite reservations because the work is incomplete, even the interim results are clearly relevant to Main Injector design choices. It will be shown that bunch narrowing should not be disturbed by any plausible $Z_{\|}$; on the other hand, even at current intensity, bunch coalescing will be significantly degraded by microwave instability if more gross effects having to do with narrow band impedances[3] and control of small rf voltage can be cured. This observation suggests that one might want to consider circumventing the coalescing process entirely, the subject of another contribution to the longitudinal instabilities group.[4] The matter of microwave instability in the transition crossing process is not developed in this report although it is amenable to a similar approach. It will be considered as an aspect of an alternative transition crossing scheme to be described elsewhere.[5]

Numerical Methods

In the same fashion that tracking is carried out for transverse degrees of freedom, the evolution of a distribution of phase-energy coordinates in a synchrotron beam can be followed by iterating single-turn or partial-turn maps interspersed with non-linear energy kicks representing accelerating cavities, spacecharge, high-Q resonators, and broadband longitudinal coupling impedance. The tracking code ESME employs this approach although it differs from familiar tracking codes like TEAPOT in using non-linear maps containing higher order terms in the kinematics.[6]

Roland Garoby used ESME several years ago[7] to do the first modeling of bunch coalescing in the Main Ring including effects of wall impedance at high frequency. His object was to investigate what was happening with parameters comparable to those in use at the time rather than to test microwave instability limits to an otherwise ideal process. He used a cutoff of 2 GHz and Z/n of 9.5 and 19 Ω as representative values. His results unmistakably demonstrate qualitative features of the onset and development of microwave instability, and they are qualitatively consistent with observation. However, it is not obvious that his model

is sufficiently faithful to the physics. For example, his choice to use only 32 bins for the fourier analysis of the charge distribution was motivated by desire to reduce computing time and keep reasonable statistics, but he therefore ignored all contribution above 850 MHz. With only 16 fourier components of the beam current it is difficult to believe that the microstructure developed in the bunch could be very realistic. The earliest steps in the work leading to the results reported below were attempts to check Garoby's work.

Parameters of the impedance model

No attempt will be made to examine the model for the wall coupling impedance critically. This note assumes the validity of the broadband model which represents the net effect of smooth chamber resistive wall, bellows, beam pickups, kickers, *etc.* as a Q=1 resonance at the microwave cutoff frequency of the vacuum chamber. The R_{shunt} of the resonance is chosen for the particular machine; Z/n can be a few ohms when special care has been taken to keep the vacuum chamber smooth to more than 100 Ω where there are many discontinuities in the chamber. If there are significant particular impedances effective below the microwave regime, they can be handled explicitly, but for three octaves or so below cutoff $Z_{||}(\omega)$ is typically smooth, inductive, and growing with frequency like the model. It is important to remember that the cutoff frequency is also an important parameter affecting the amount of voltage the beam develops at high frequency. In the principal results reported later, a value of 1.7 GHz was used for the cutoff, which is probably more representative than the 2.0 GHz used by Garoby, but may still be a bit high.

Check with un-bunched beam

The microwave instability for un-bunched coasting beam is somewhat more straightforward to analyze both mathematically and numerically. To check that the program was performing correctly, one of the tests was to compare observed with predicted instability threshold for un-bunched beam with a gaussian energy distribution. The Keil-Schnell threshold relation is

$$|Z/n| = \frac{\mathrm{F}\beta^2 E|\eta|}{eI_{\mathrm{beam}}}\left(\frac{\Delta p}{p}\right)^2_{\mathrm{FWHM}} ,$$

where now $\mathrm{F} \approx 1$ and I_{beam} is the average beam current. The runs made looked at 0.2 eVs in 1/1113 of the ring with $n_b = 10^{10}$ for which the coasting beam threshold is 4.88 Ω. To compare with Garoby, the peak of the resonance was set at 2 GHz, but 64 fourier components of the beam current were taken and 40,000 macroparticles were used instead of 10,000. With Z/n = 5 Ω there is little visible change in the phasespace distribution in the 42 ms tracked, but the rms energy spread increased. When the growth rate of an instability is calculated from the linearized Vlasov equation, it is the rate of growth of the perturbation amplitude. However, in the tracking results, even at very early times in the instability growth, many different modes are involved and as the instability develops the dominant modes move to lower frequency. From a practical standpoint the quantity of interest is the longitudinal emittance ε_l. Figure 1a shows ε_l *vs.* time for the 9.5 Ω case. The beam phase space at 42 ms is represented by the scatter plot shown in Fig. 1b. To quote a growth rate the quantity

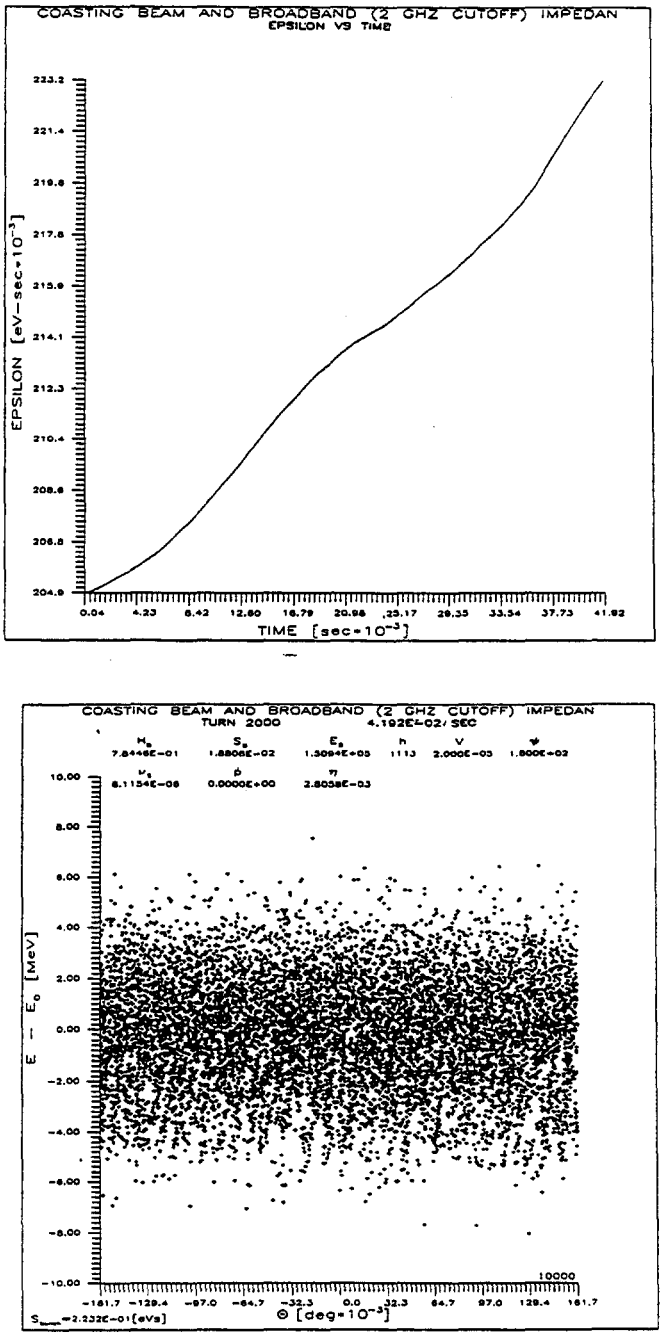

Figure 1: Microwave instability in a coasting beam with $I_{\text{beam}} = 85$ mA at Z/n = 9.5 Ω (a) ε_l *vs.* time (b) phase space plot of Δ E *vs.* azimuth (1113-th of circumference)

$\dot{\varepsilon}/\varepsilon$ averaged over the first 5.2 ms is used. For Z/n = 5 Ω the growth rate is 0.067 s^{-1} and for a low-side estimate of Main Ring Z/n of 9.5 Ω the growth rate is 0.236 s^{-1} and clear microstructure develops in the bunch in 42 ms. These growth rates are rather low, but the small-amplitude synchrotron period for a full 0.2 eVs h=1113 bucket is 0.42 s, and the growth rate will of course be higher for more intense beam. One may also, therefore, anticipate trouble in bunched beam of comparable emittance, at least at the higher Z/n. For Z/n of 3.3 Ω no growth is observable in 42 ms.

Initial phase space distribution

Proton bunches have a reasonably localized phase space distribution without long tails. An elliptical distribution is used for the examples treated. It is appropriate to bunches originating from capture from, say, a parabolic or elliptical energy distribution. It does not have a discontinuity at the boundary which would produce an unrealistic space charge potential, and the local threshold for microwave instability is constant everywhere across the bunch.[8] The choice of bunch shape does influence the initial beam current spectrum, but, because the microwave instability is essentially the same phenomenon in either bunched or coasting beam, the details of the bunch shape should not influence the results in a fundamental way. The principal difference between the bunched and coasting beam cases is that the instability threshold is raised because the growth time must be less than a synchrotron period.

Momentum spread

The momentum spread appearing in the Keil-Schnell criterion is the local momentum spread at the same azimuth that the peak current is evaluated, not necessarily the bunch height. So, for example, in the bunch narrowing process for $\bar{p}$ production the bunch approaches threshold as it debunches with rf off even though the total momentum spread does not change (much) during this phase of the procedure. ESME runs were made to demonstrate that the simulation showed this characteristic; an interesting example showed that this behavior is still evident when neighboring bunches are fully overlapped, as predicted by Ng.[9]

Periodicity and number of rotation harmonics in current spectrum

The particular harmonics of the beam circulation frequency present in the beam current spectrum depend on how regularly the buckets are filled. However, for a cutoff frequency of 1.7 GHz the log decrement of the wake field from a Q = 1 resonator is

$$\tau_D = 2Q/\omega \approx 0.19\ ns\ .$$

Thus, it is necessary to carry out the calculation only for a single bunch, and it can not make any difference how the ring is filled. The power in the high frequency spectrum will depend on the bunch charge and shape; with the resonance covering many circulation harmonics it matters little how that power divides between neighboring circulation harmonics. Therefore, one can certainly assume that the buckets are filled regularly and calculate for a single

bunch with periodic boundary conditions at $\pm\pi/h$. Then the beam current contains only harmonics of the rf frequency and a modest number of fourier components span the range to the beampipe cutoff. This is why Garoby got reasonable results with only sixteen harmonics. To get from 53 MHz to 1.7 GHz for either Main Ring or Main Injector takes $\sim$ 32 harmonics. Runs made with 512 and 64 harmonics gave very similar results.

Number of particles to track

To evaluate n amplitudes and phases of the beam current corresponding to a bunch, the azimuth interval $2\pi/h$ is divided into 2 n bins. The bunch itself might span somewhat fewer bins, but for the debunching process all bins will ultimately have some contents. The spectrum is found by doing a finite fourier transform (FFT) of the bin population. One can see by thinking of the evaluation of coefficients for a fourier series as an integration $\int f(x) \sin mx \, dx$ that the highest frequency component comes essentially from the sum of differences between adjacent bins. A rough statistical argument for the number of macroparticles required for the tracking follows from the proposition that the statistical error of the bin population should be less than the systematic difference between bins. For N_B bins the difference between bins should be $\mathcal{O}(N_B^{-1})$. The statistical error for the i-th bin is $\mathcal{O}(n_i^{-1/2})$ where n_i is the bin population. The bin population is itself $\mathcal{O}(N_p/N_B)$, where N_p is the number of macroparticles used for the tracking. Requiring the systematic difference to be greater than the expected error one finds

$$\left(\frac{N_B}{N_p}\right)^{\frac{1}{2}} < \frac{1}{N_B} \Rightarrow N_p > N_B^3 \ .$$

Therefore, for 32 harmonics one needs 2^6 bins and should take $\sim 2^{18} \approx 2.6{\cdot}10^4$ macroparticles. Calculation on this scale is practicable, but computer runs take significant time. For the FPS 164 it takes something like $8 \cdot 10^{-5}$ s/particle-turn for typical parameters. Because the debunching for coalescing takes almost a second, simulations run several hours.

Main Injector Calculations

Several calculations were made in the process of developing the understanding of the fundamentals described in the preceding section, but with these established one is equipped to calculate directly the effect of microwave instability on beam manipulations in the Main Injector. The examples reported below are given with parameters taken from the nominal values in the conceptual design report.[10] They may not be the optimum parameters for the particular process. The parameters important for the the calculations are collected in the table.

Main Injector Parameters for RF Calculations

Mean radius (R_{eq})	528.302	m
Transition gamma (γ_T)	20.4	
Energy for $\bar{p}$ production	120.	GeV
Energy for bunch coalescing	150.	GeV
RF harmonic number (h)	588	
Maximum rf amplitude ($\hat{V}_{max}$)	4.	MV
Longitudinal emittance (ε_l)	0.5	eVs
Longitudinal coupling impedance (Z/n)	5.	Ω
Protons per bunch (n_p)	6	$\times 10^{10}$
Beampipe cutoff (f_{co})	1.7	GHz

Bunch rotation for $\bar{p}$ production

The bunch narrowing process consists of drifting proton bunches with the rf off followed by recapture in a large bucket for just over a quarter of a synchrotron oscillation period before extraction at minimum bunch width. The momentum spread is at its minimum shortly after recapture when the miss-matched bunch has rotated full-down, but it doesn't remain there very long because the recapture voltage is high. The process is illustrated in Figs. 2–5. Figure 2 shows a scatterplot of the drifted bunch after 2.7 ms; there is no sign of high frequency structure on the bunch. Figure 3 shows the bunch after it has rotated upright in a bucket produced by 4 MV rf. The momentum spread is less than 0.6 % FW, and the time spread is about 1.1 ns. A slightly shorter drift might reduce the tails seen in Fig. 3 sufficiently to get the time spread under one ns. The plot of rms energy spread *vs.* time shown in Fig. 4 characterizes the whole process fairly well. Figure 5 gives the ε_l *vs.* time. There is no emittance growth until the tails are produced during the rotation.

Just for assurance that something could be seen, the calculation was repeated with Z/n raised to 50 Ω. Figure 5 shows small signs of high-frequency bunching in the drifted bunch. The plot of E_{rms} *vs.* time given in Fig. 6 shows some growth of the energy spread during the drift. This results from a wakefield deceleration of the front of the bunch and acceleration of the tail rather than a deceleration of micro-bunches out of the main bunch. The momentum spread is above threshold, but the whole process takes place too fast for much disruption of the bunch.

Debunching for coalescing

In contrast to bunch narrowing, the debunching prior to coalescing is a slow process so that even a slowly growing instability can cause significant emittance growth. Again nominal Main Injector parameters are used although the optimum values of intensity and bunch area could be rather different for both proton and $\bar{p}$ bunch coalescing.

Debunching as now executed in the Main Ring is inherently a diluting process quite apart from the practical difficulties of multi-bunch wakefields pointed out at this workshop

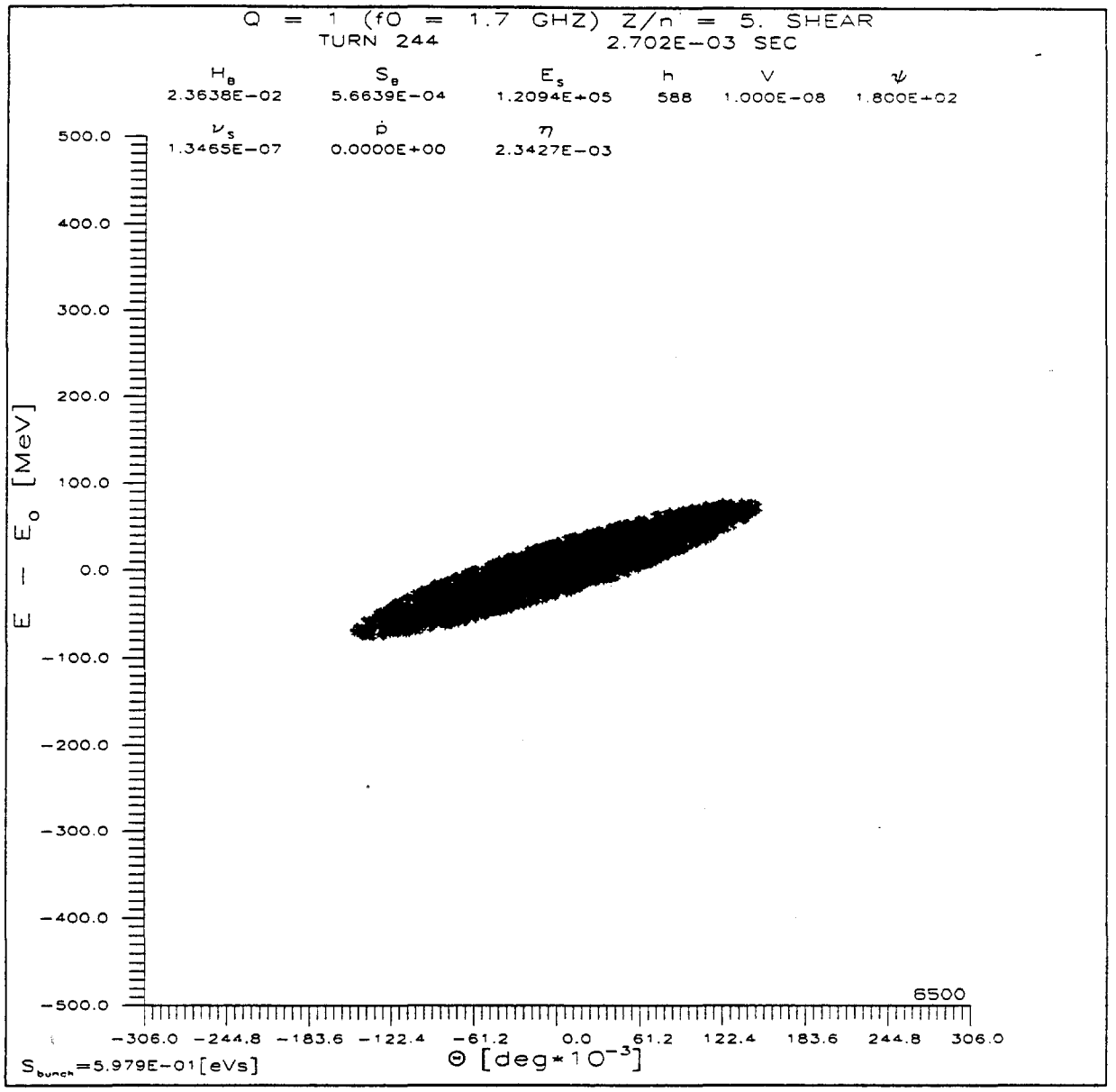

Figure 2: Drifting bunch of 0.5 eVs with $6 \cdot 10^{10}$ protons and Z/n = 5 Ω for $\bar{p}$ production. Δ E *vs.* azimuth (588-th of circumference)

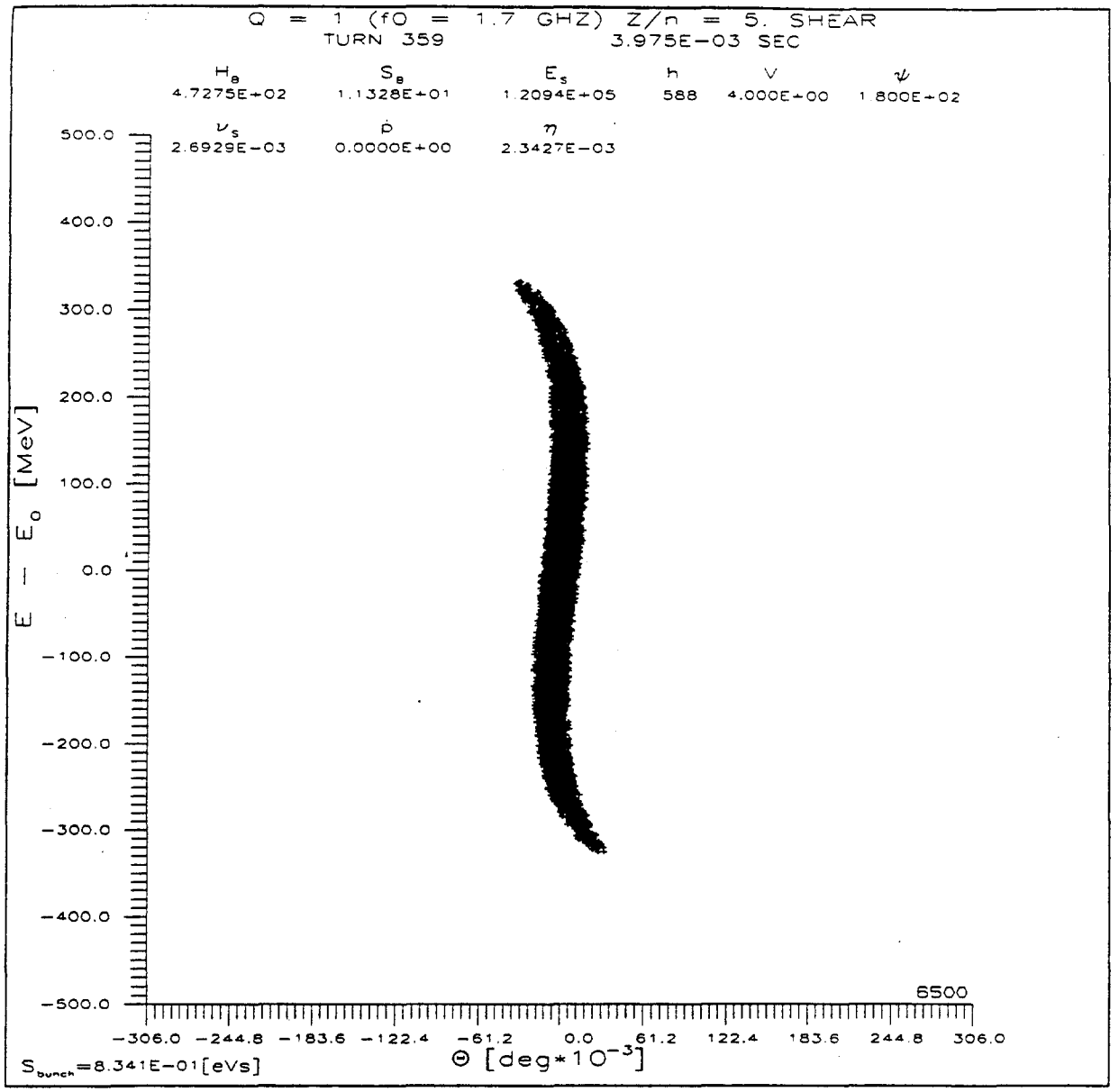

Figure 3: Rotated bunch (following conditions of Fig. 2). Δ E *vs.* azimuth (588-th of circumference)

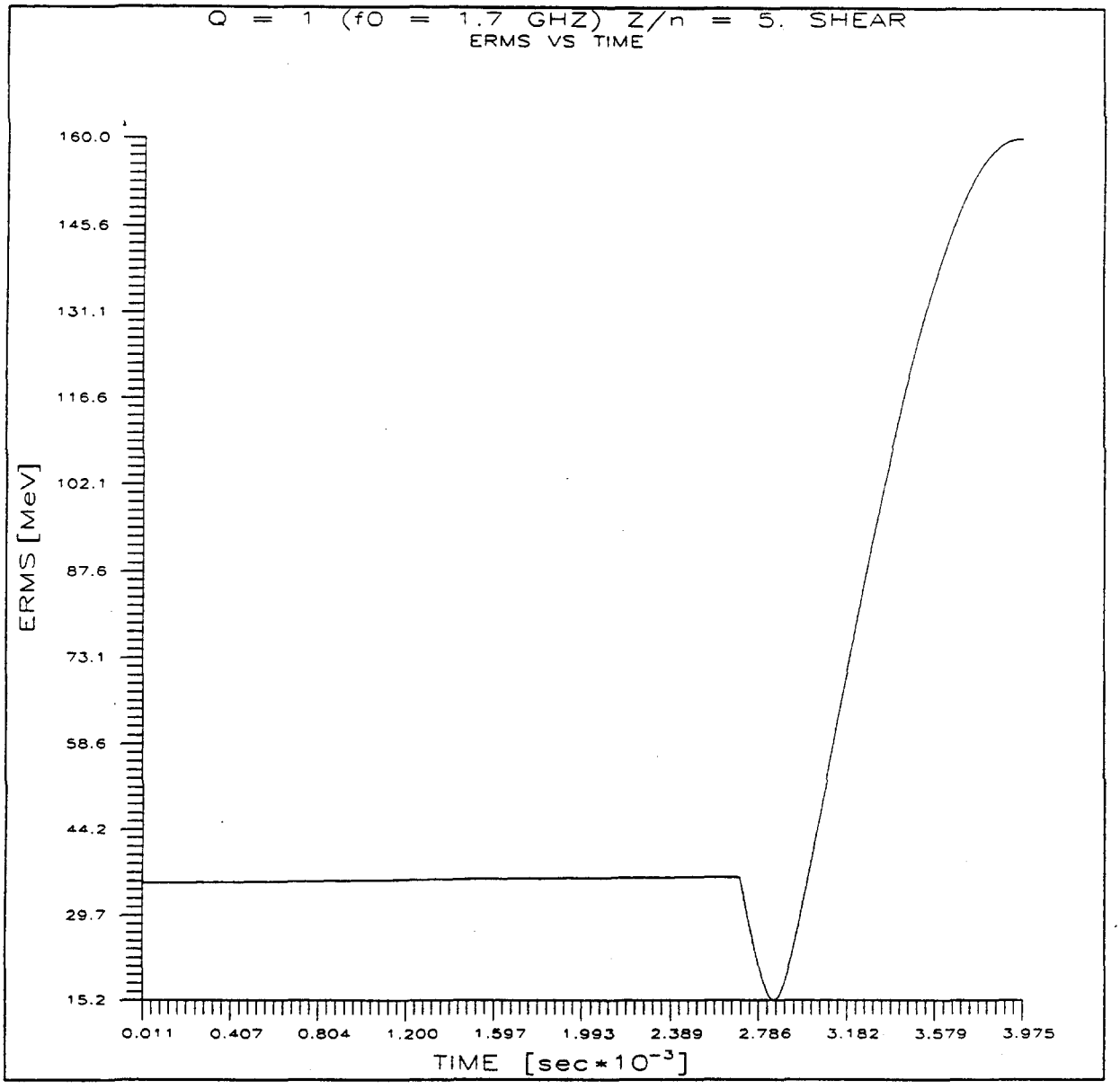

Figure 4: Bunch shearing and rotation for $\bar{p}$ production. rms energy spread *vs.* time. (see Figs. 2–3)

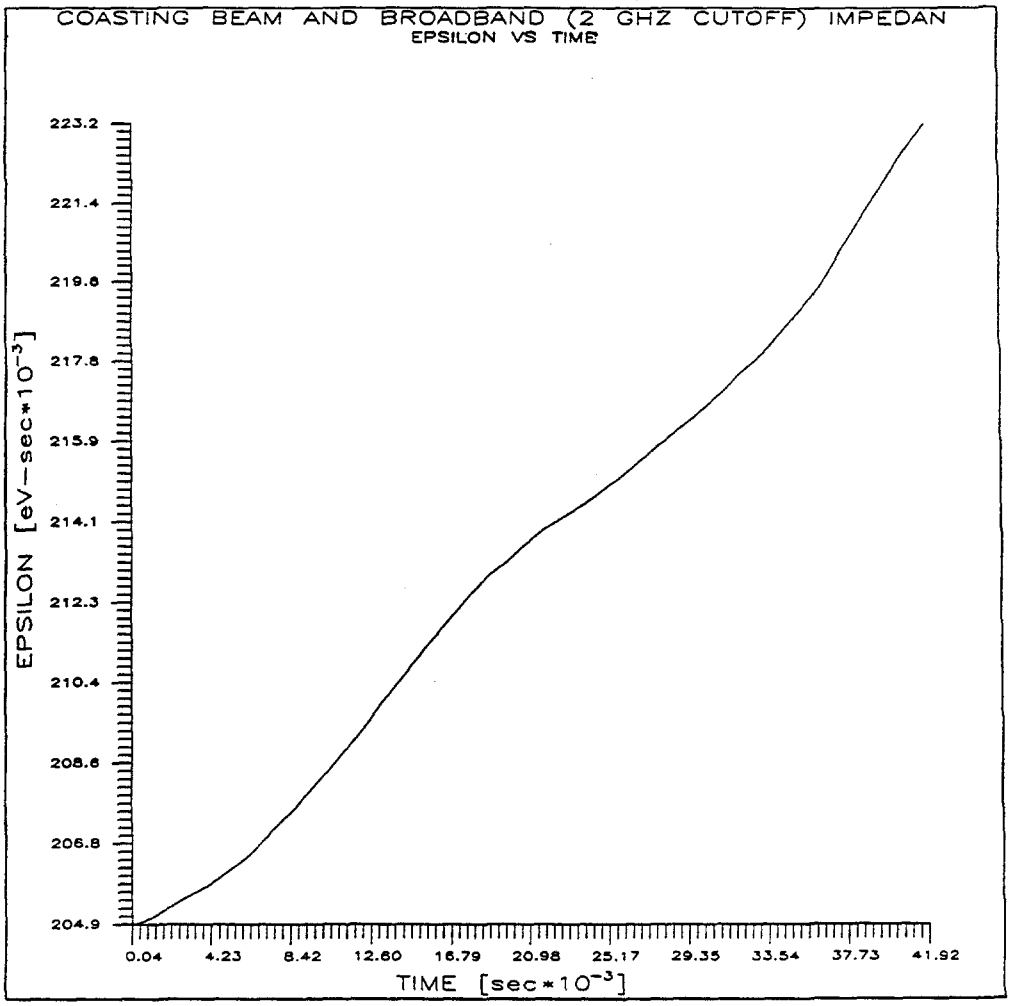

Figure 5: Bunch shearing and rotation for $\bar{p}$ production. ε_l *vs.* time. (see Figs. 2–3)

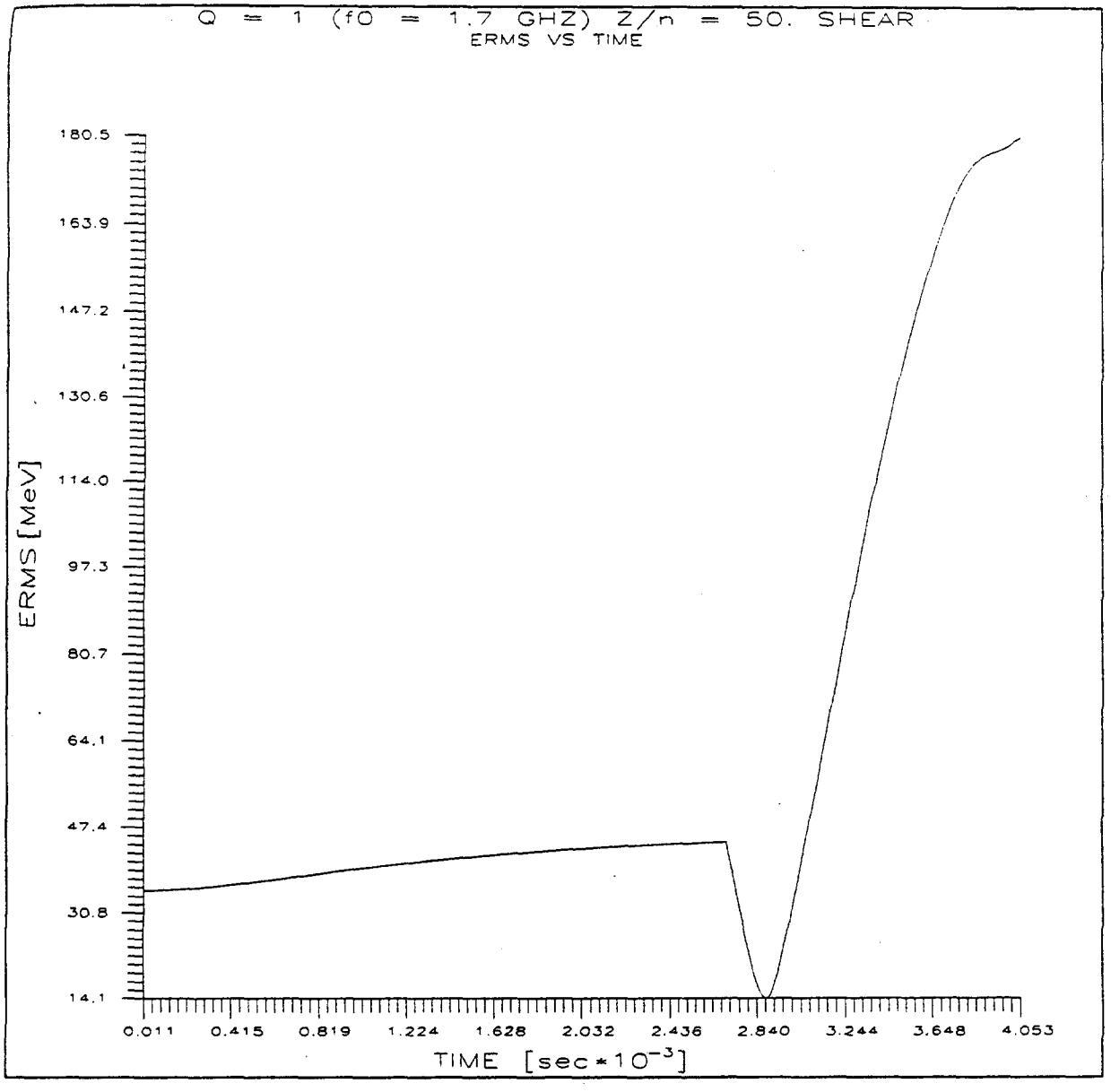

Figure 6: Bunch shearing and rotation for $\bar{p}$ production, Z/n = 50 Ω. rms energy spread *vs.* time. (compare Fig. 4)

by Martin[3] and Griffin[4] because the debunching is carried out only until the high frequency buckets (h=1113, 53 MHz) are full. As a next step the low frequency rotating bucket (h=53, 2.5 MHz) is turned on. However, if the beam is fully debunched from the high frequency bucket into a matched low frequency bunch, the process in principle can conserve the original bunch area perfectly.[11] This idealized version is difficult to realize because it requires control of both the 53 MHz and 2.5 MHz voltages to very low amplitudes (hundreds and tens of volts respectively), the momentum spread is even less, and the time for adiabatic debunching is about one second. However, if one could manage the low voltages, one might choose to go for extra beam brightness by pushing the coalescing process toward fundamental limits. Therefore, the case chosen for demonstration is that of proton coalescing where debunching proceeds somewhat beyond full buckets. The low frequency bucket is not included in the simulation, but, since periodic boundary conditions at $\pm 180°$ of rf phase are used to give the effect of a full ring, the phase space flow is practically the same as for the middle bunches of an ensemble coalescing into a low frequency bunch.

Figure 7 is a plot of the rms energy spread *vs.* time during debunching of a 0.5 eVs bunch as the voltage is lowered from 10 to 3.5 kV over 0.3 s with neither space charge nor wall coupling impedance forces. Figure 8 shows the same curve for $6 \cdot 10^{10}$ protons with a longitudinal coupling impedance $Z/n = 5\ \Omega$. There is some difference in the expected direction, but it is not of practical significance. Looking at the phase space scatter plot in Fig. 9 one sees none of the obvious self-trapping in evidence in the un-bunched beam example. However, if Z/n should be somewhat higher than designed one could get results like those shown in Fig. 10 where $Z/n = 10\ \Omega$ has been assumed.

Conclusions

One may conclude that the Z/n specified in the Main Injector conceptual design is sufficiently low that microwave instability does present significant practical limits to the operations of bunch rotation for $\bar{p}$ production and proton bunch coalescing at the intensities foreseen. This is not to imply that there are not other beam loading/self trapping problems at lower frequency. However, Z/n can not be much greater than the design value before microwave instability leads to significant loss of beam brightness in the coalescing process, and to improve significantly beyond brightness of 10^{11} per eVs will require greater refinement of the coalescing procedure and further reduction of the longitudinal coupling impedance.

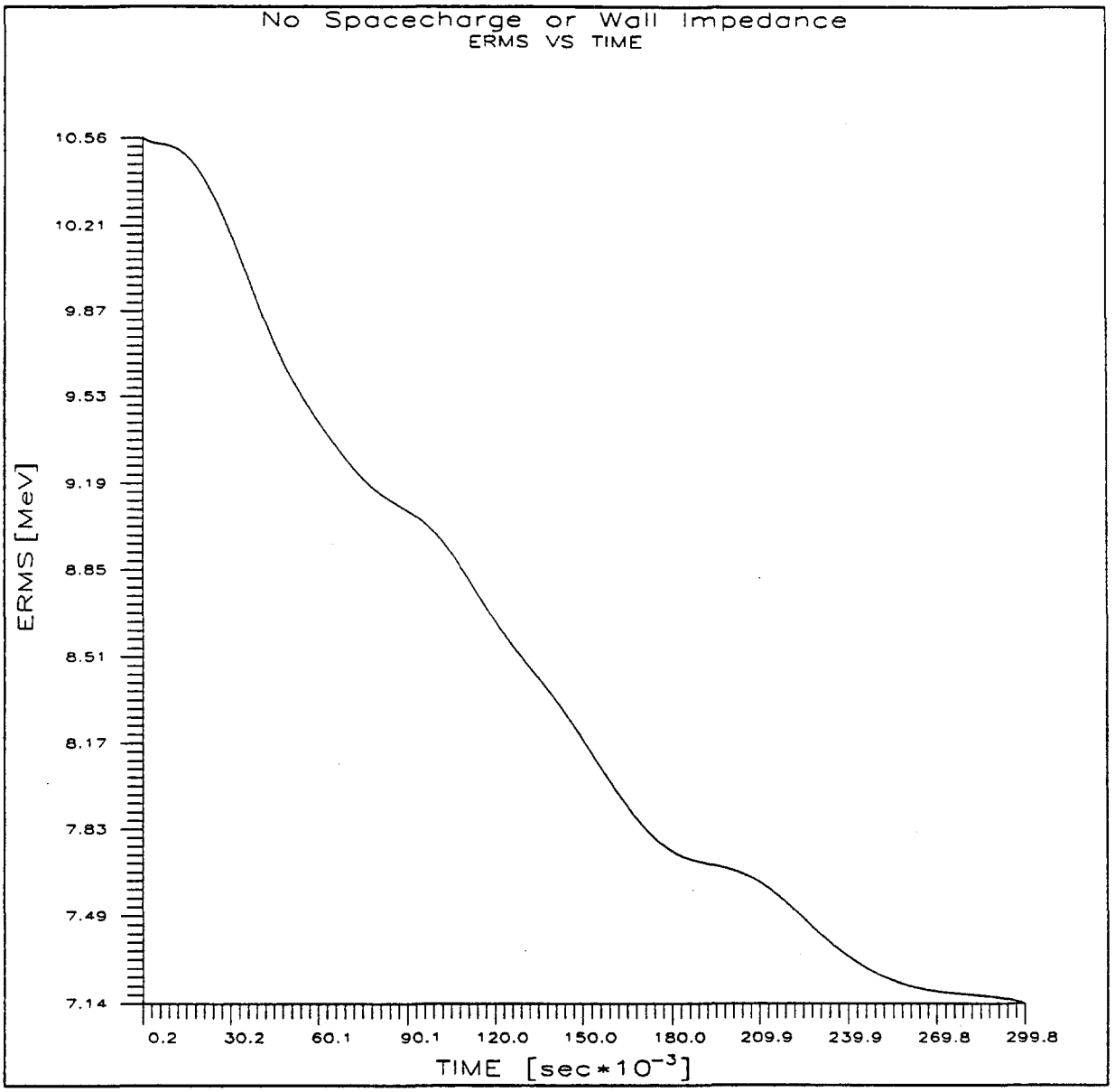

Figure 7: Debunching for proton bunch coalescing — 0.5 eVs, no space charge or longitudinal coupling impedance. E_{rms} *vs.* time.

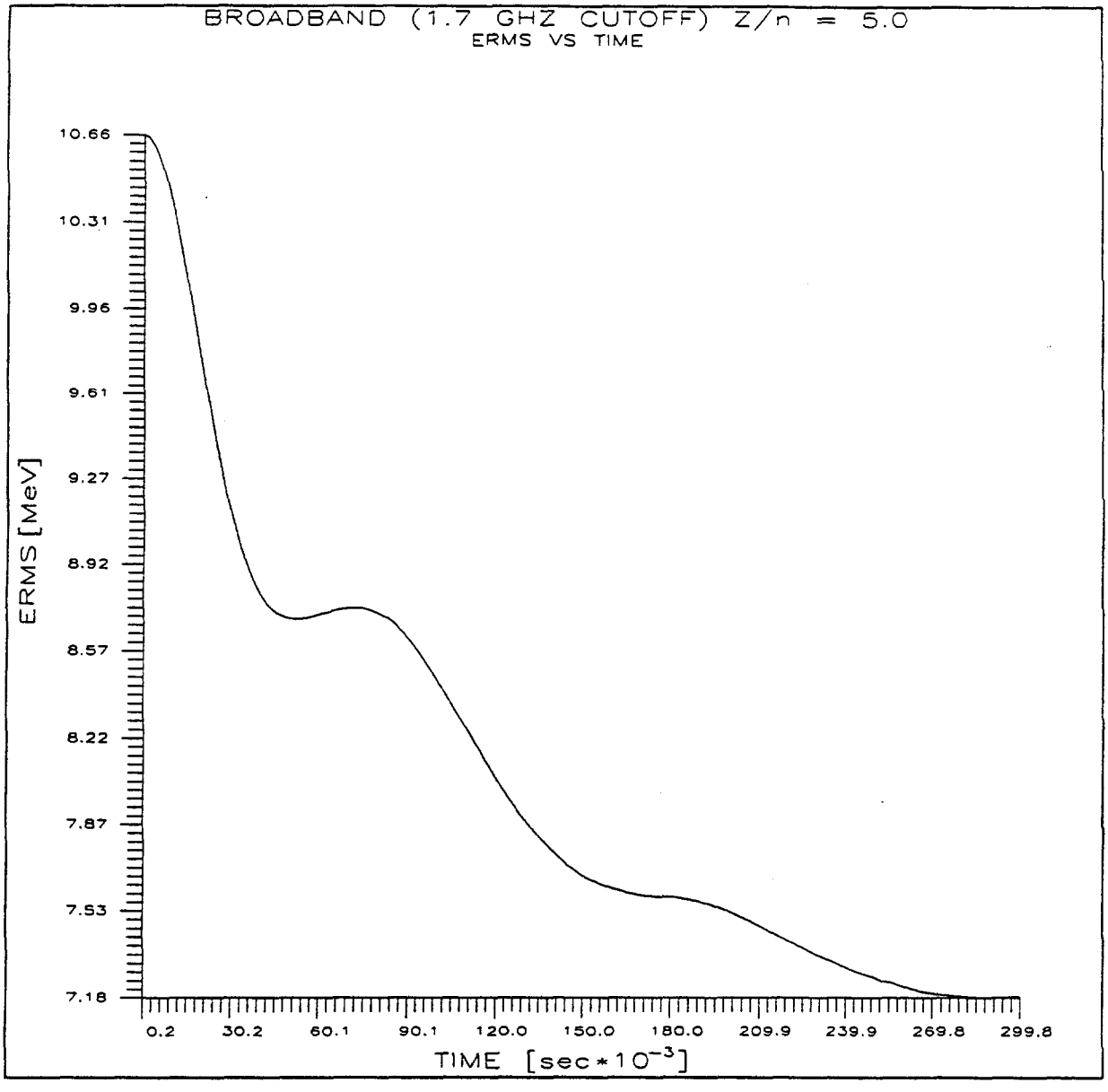

Figure 8: Debunching for proton bunch coalescing — Z/n = 5 Ω, $6 \cdot 10^{10}$ protons. E_{rms} *vs.* time.

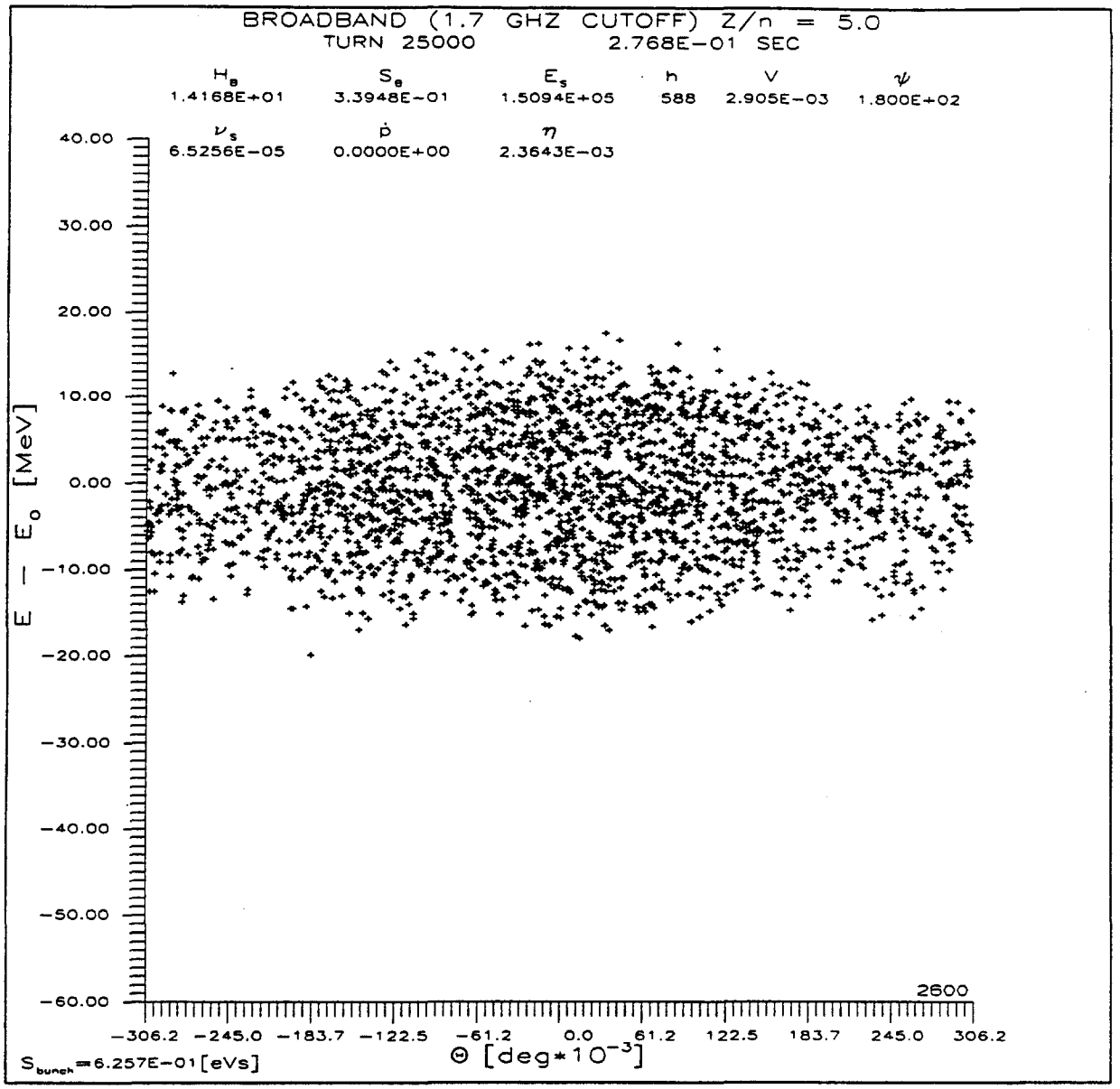

Figure 9: Debunching for proton bunch coalescing — Z/n = 5 Ω, $6 \cdot 10^{10}$ protons. Δ E *vs.* azimuth (588-th of circumference)

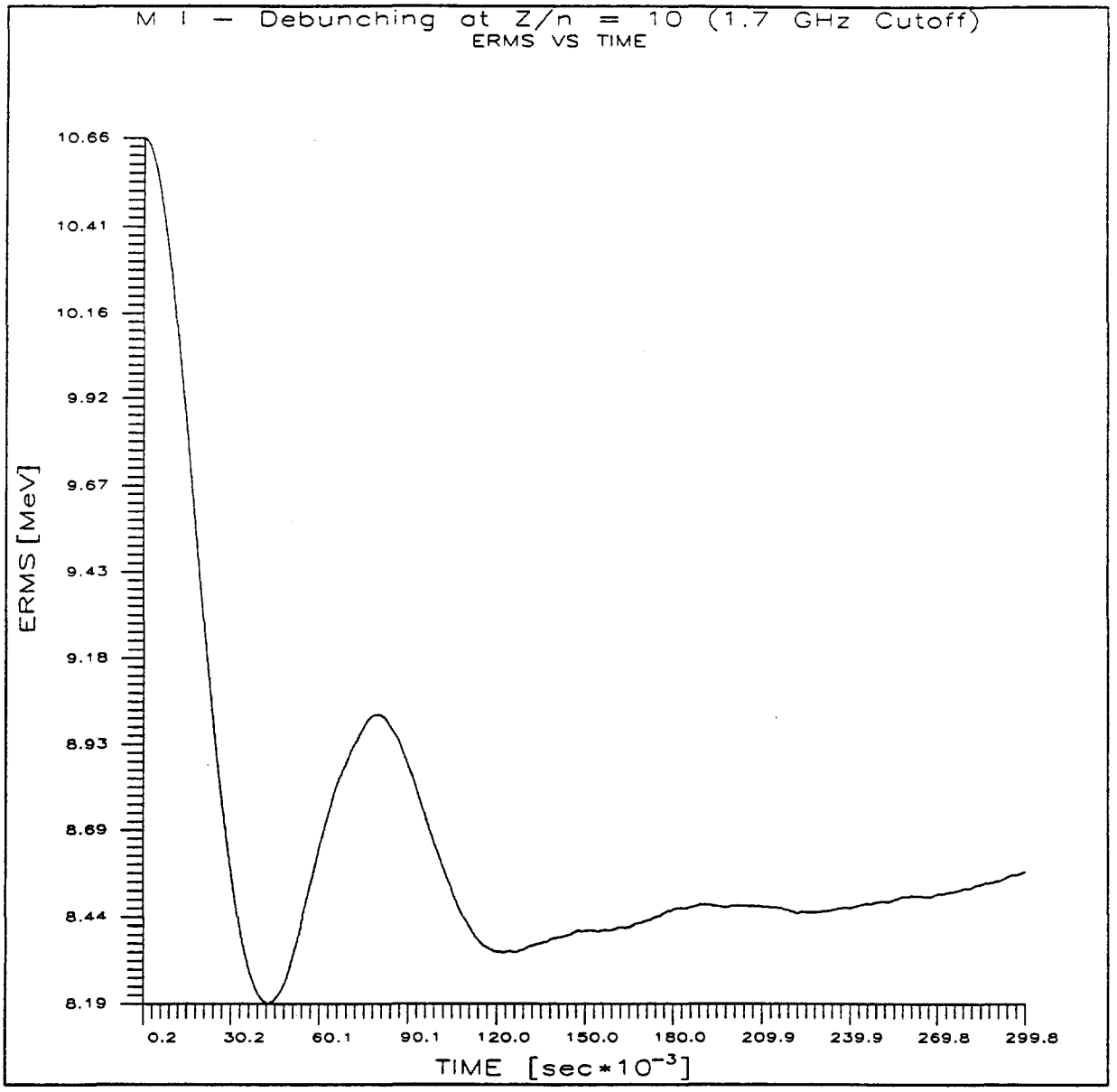

Figure 10: Debunching for proton bunch coalescing — Z/n = 10 Ω, $6 \cdot 10^{10}$ protons. E_{rms} *vs.* time. (compare Figs. 7 and 8)

References

[1] A. Hofmann, "Longitudinal Instabilities" in " Theoretical Aspects of the Behavior of Beams in Accelerators and Storage Rings", CERN 77-13(19 July 77)139ff

[2] S. Stahl and J. MacLachlan, "User's Guide to ESME v. 7.1", Fermilab internal note TM-1650(26 February 90)

[3] P. Martin, remarks at this workshop on coalescing problems.

[4] J. Griffin, "Bunch Coalescing", contribution to longitudinal instabilities working group

[5] J. Griffin and J. MacLachlan, (title uncertain) avoiding beam loss and emittance growth in crossing synchrotron transition with high intensity beam, to be published

[6] J. MacLachlan, "Difference Equations for Longitudinal Motion in a Synchrotron", Fermilab note FN-529(15 December 89)

[7] R. Garoby, "Simulation of Bunches Coalescing in the Main Ring in the Presence of a High-Frequency, Wide-Band Resonator", Fermilab internal notes TM-1495(4 December 86) and TM-1495-rev(4 December 86)

[8] A. Hofmann and F. Pedersen, "Bunches with Local Elliptic Energy Distributions", IEEE Trans. on Nucl. Sci., **NS-26** No. 3(June 1979)3526ff

[9] K.-Y. Ng, "Microwave Instability for Overlapped Bunches", Fermilab note FN-432(May 86)

[10] "**Fermilab Upgrade: Main Injector** Conceptual Design Report", Revision 2.3, Fermilab(April 90)

[11] J. A. MacLachlan and J. E. Griffin, "Debunching into a Bucket of Lower Harmonic Number", Fermilab internal note TM-1504 (9 Dec 87)

Bunch Coalescing

J. E. Griffin
Fermilab

Introduction

At a very early stage in the development of the colliding beam program (TeV 1) it became clear that in order to achieve acceptable intensity it would be necessary to inject single bunches of protons and antiprotons containing greater than 10^{11} particles into the Tevatron. Since there was no easy way to create proton bunches of that intensity in the Booster, and even if there had been it would not have been likely that they could have been accelerated through transition in the Main Ring intact, it became necessary to invent a way to create such bunches at high momentum. In 1980 the idea of accelerating an ensemble of smaller bunches to 150 GeV where they could be combined, or coalesced, emerged. The first coalescing was done using the h=159 sub-harmonic spanning seven h=1113 buckets. Four adjacent bunches were successfully coalesced.[1] Shortly thereafter the sub-harmonic was reduced to h=53, spanning 21 standard buckets, so that a larger number of bunches could be coalesced within a reasonably linear region of the synchrotron motion. Linearization of the motion was further improved by the addition of a second harmonic component to the h=53 sinewave.[2] The coalescing procedure has been refined extensively during the intervening years[3] and must be considered an integral part of a successful colliding beam program. Even so there may arise serious problems in extending the process to the levels anticipated for the future.

Status and Potential Problems

The Main Injector will be expected to produce coalesced bunches of substantially larger numbers of protons than the Main Ring is presently producing. Also it is expected that five or six ensembles of proton bunches will be coalesced simultaneously at 150 GeV in the Main Injector. It will be useful, therefore, to examine the present Main Ring coalescing performance with a view toward understanding any existing problems and proposing, if possible, improved or alternative ways of proceeding.

It has been observed that the coalescing efficiency deteriorates seriously as the total number of protons in the ensemble is increased. In Fig. 1 it is apparent that for a total Main Ring intensity of $2.5 \cdot 10^{11}$ protons in an ensemble the coalescing efficiency is about 50 %, nearly independent of the number of Booster turns used to create the initial bunches. A contributing factor to this loss in efficiency is shown in Fig. 2. As the 53 MHz rf voltage

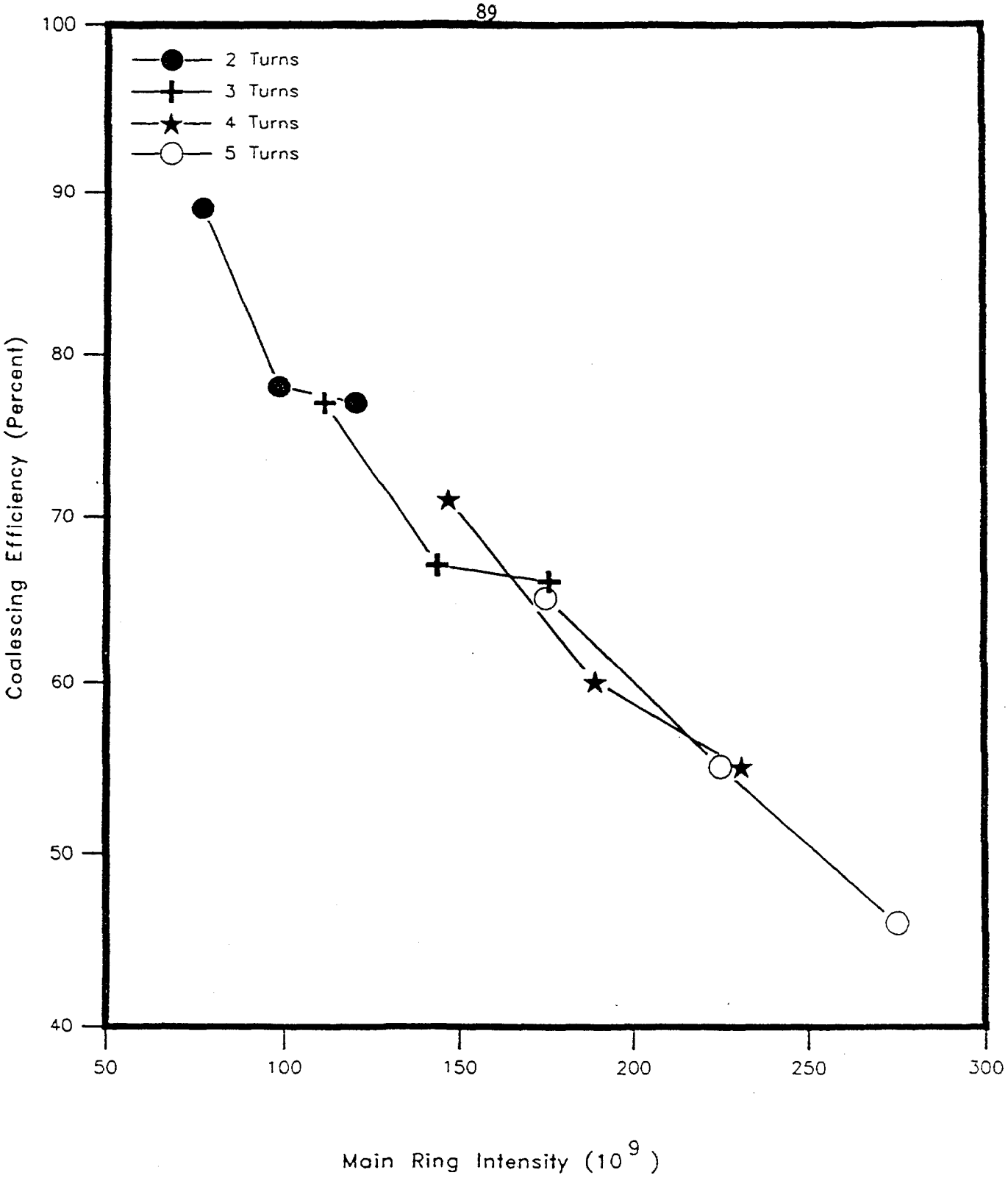

Figure 1: Coalescing efficiency in the Main Ring *vs.* beam intensity

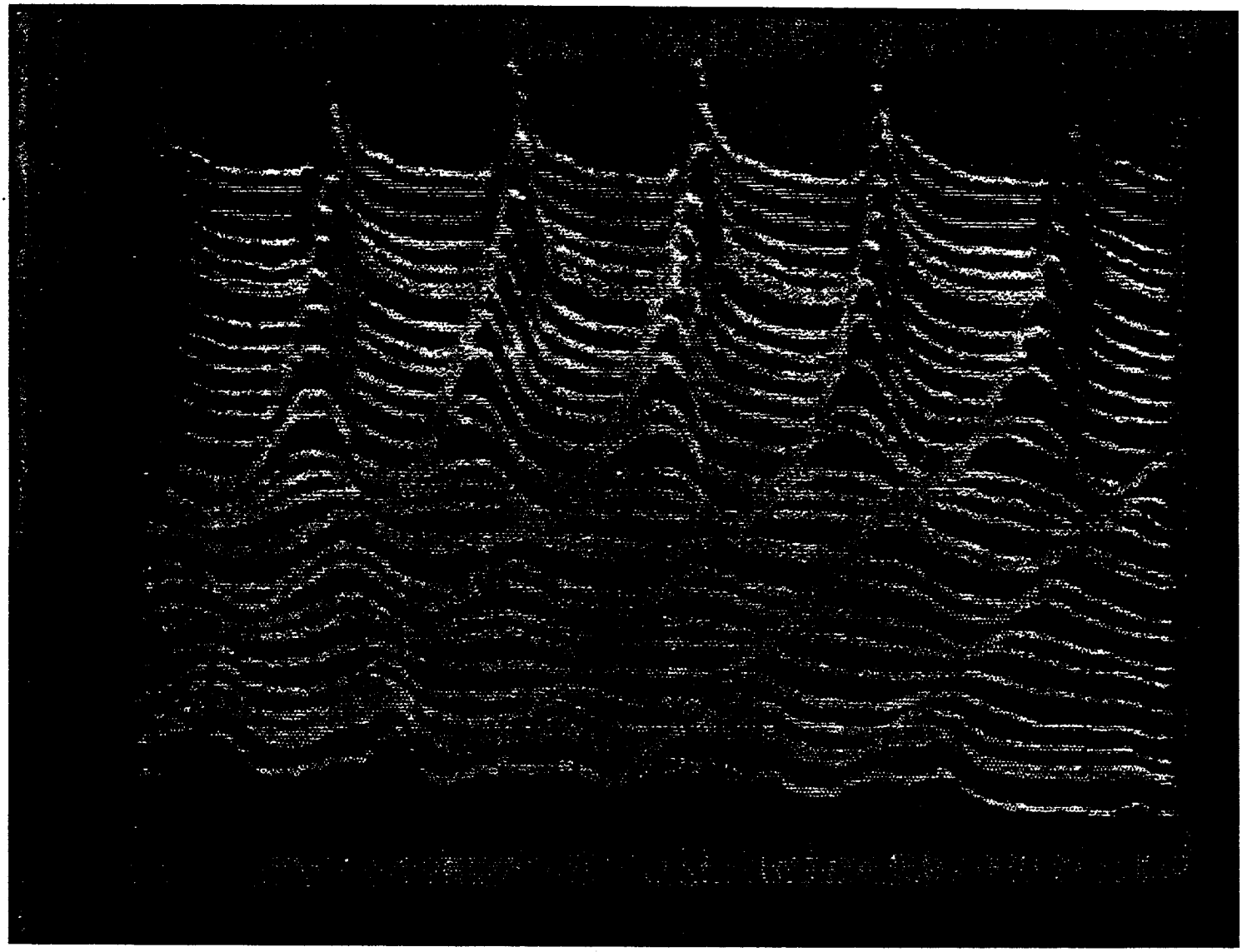

Figure 2: h=1113 bunches during coalescing in the Main Ring showing later buckets (toward right) losing charge as voltage is lowered. The traces progressing from top to bottom are successively later turns.

is reduced adiabatically to a level where the buckets should be substantially full prior to bunch rotation, it is observed that charge from bunches which arrive at later times in the ensemble is spilling out of the buckets. This effect grows more pronounced as the bunch number in the ensemble increases. Charge from these buckets is observed to move toward earlier time, indicating (since the system is above transition) that these charges are being selectively decelerated. Since this charge is at anomalously lowered momentum it cannot be successfully rotated into the final single 53 MHz bucket separatrix.

Various attempts to change the location of this charge loss toward the earlier buckets by adjusting the relative phase and amplitude of the counter-phasing rf phasors has been unsuccessful. This is interpreted to mean that the effect is not caused by beam loading of the 53 MHz rf cavities. Beam induced voltage in the h=53 (2.5 MHz) rf system has been measured during coalescing to be only tens of volts, not sufficient to caused the observed effect.

Low Frequency Low Q Resonator Hypothesis

The beam loss from the last few buckets in the ensemble described above suggests that on each turn the charge ensemble is exciting a very low frequency resonator (or a combination of several such resonators) in such a way that the (decelerating) voltage rises monotonically (perhaps approximately linearly) during the passage of the ensemble. The time constant of the putative resonator should be large with respect to the total ensemble period (188 ns) but small with respect to the rotation period (20.9 μs). The voltage is developed each turn but decays to zero before the ensemble returns on the next turn. In this way the first bunch sees essentially no voltage while the later bunches see increasing decelerating voltage on each turn. A time constant of order 1 μs would be about right. The natural period of the resonator should be large with respect to the ensemble time, so a resonant frequency from a few hundred kHz to a few MHz is indicated.

As an example, assume that we intend to coalesce ten bunches each containing $2.5 \cdot 10^{10}$ protons and longitudinal emittance 0.24 eVs. The total charge in the ensemble is $4 \cdot 10^{-8}$ C and the average beam current within the ensemble is 0.21 A. The rf voltage should be reduced adiabatically to 3.5 kV at which point the bucket area should be equal to the bunch area and the buckets full. But during this period the later bunches are seeing an additional decelerating voltage, assumed here to reach a maximum of 1 kV. Because the process is adiabatic these bunches will move to a synchronous phase angle such that they receive a corresponding accelerating voltage from the applied rf. When the applied rf voltage reaches 7 kV the generated bucket area A(0) is 0.35 eVs, but the synchronous phase angle reaches 8.2° resulting in a moving bucket factor $\alpha(\Gamma)$ of 0.74. This reduces the bucket area to 0.25 eVs, and for further voltage reduction the bucket area for late bunches will be smaller than the the bunches so beam will spill out of the buckets as observed.

What sort of resonator is required? Assume, for example, that a single lumped RLC resonator at 1 MHz is the culprit. For excitation time short with respect to the period, the voltage developed is essentially the charge deposited on the capacitor. (We assume a series

LR in parallel with a capacitor C. Initially the inductor prevents current from passing down that leg.) The image charge of the ensemble, deposited on the capacitor during passage, causes the voltage to rise almost linearly during passage. For a maximum voltage of 1 kV and a total charge of 400 nC the capacitor must be 40 pF. With these assumptions, the Q of the circuit is π, the series resistance R is 1266 Ω, and the effective shunt resistance ($R_{sh} = Q^2R$) is 12.5 kΩ. Can such an object (or objects) be found in the Main Ring?

Surprisingly, the stretched wire measurements (described elsewhere at this workshop) on two (of six installed) cells of the C48 kicker show a broad resonance near 650 kHz with Q $\approx$ 1.5 and R_{sh} = 11 kΩ. This remarkable agreement is probably not correct because the impedance matching cones in the stretched wire system are far from effective at such a low frequency. Nevertheless the result is suggestive.

The geometry of the kicker is shown in Fig. 3. It is a window frame ferrite structure with current carrying busses passing inside the ferrite along each side of a ceramic beam tube. Current enters one side of the structure, passes through the bus to the end of the three cells, each about 1 m long, then crosses over to the opposite bus and to a point opposite the entry point. Here the bus is terminated in a 10 mΩ resistance to ground. The ferrites are encased in metallic jackets which are connected longitudinally by very small resistances and by the outer conductors of the coaxial cables (RG220) which carry the bus current from cell to cell. This structure can be thought of as a coaxial transmission line, the inner conductor of which is the two bus bars in parallel and the outer conductor the outer shell. The line is dielectrically and magneticly loaded by the properties of the ferrite. The resulting velocity is about $8.5 \cdot 10^6$ m/s. Estimates of inductance and capacitance per unit length indicate a characteristic impedance of about 97 Ω. Further measurements on the two cell structure, made externally with a vector impedance meter, indicated a characteristic impedance of 71 Ω and a Q about 40. Measurement at the open end of the two cells with the opposite end terminated in a 25 Ω resistance, simulating the damping resistance which is actually installed, showed a broad resonance near 3 MHz with Q about 2.5. These measurements were made without the crossover connections in place. The crossover connection consists of two 1.5 m lengths of RG220 coaxial cable in parallel. The capacitance per unit length is of this cable is about 100 pF per meter, so at low frequency the crossover looks like a 300 pF capacitor.

The model which emerges is a lumped RLC resonator consisting of the crossover capacitance in parallel with the inductance of the kicker cells, damped to low Q by the 25 Ω damping resistor. Using the measured value and Z_o we calculate a total inductance for three cells of 25 μH. This gives a resonant frequency of 1.8 MHz.

The kicker acts much like the example given above except that the capacitance is 7.5 times larger. This means that the beam induced voltage will be only about 133 V per turn. But there are two cells per kicker and two such kickers in the ring so the total decelerating voltage reaches 530 V per turn from these kickers alone. There are four or five additional kickers in the ring, probably C-frame style, whose properties should be examined in this context.

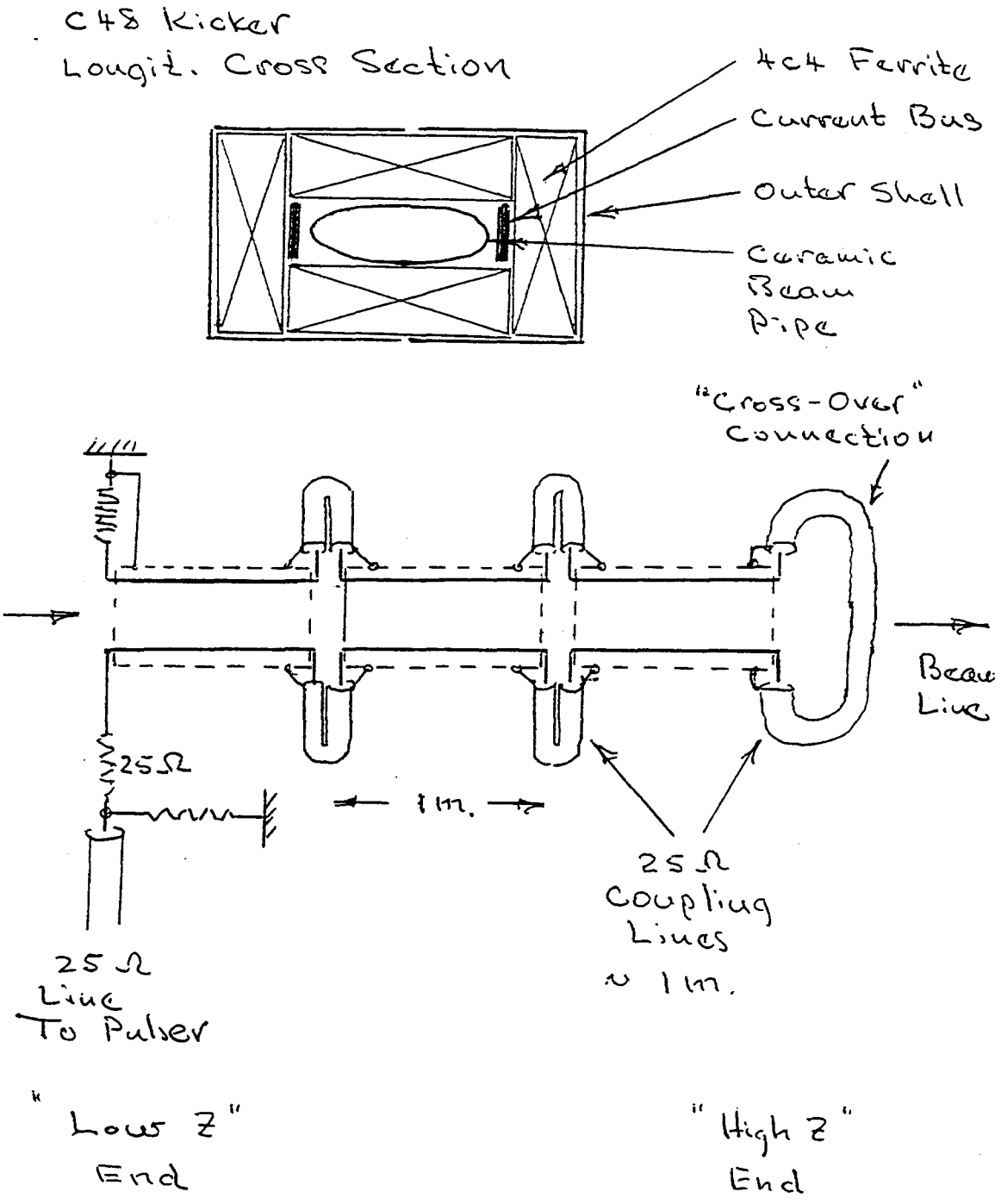

Figure 3: Sketch of the configuration of the C48 kicker from the Main Ring

Can Coalescing be Eliminated in the Main Injector?

Bunch coalescing has always been an expedient made necessary by limitations inherent in the Booster and Main Ring. With design of an entirely new ring it may be advantageous to consider elimination of bunch coalescing as it is presently done. I propose here a scheme which, with appropriate modifications, may result in intense bunches with higher longitudinal emittance density than has been possible heretofore. This would result in shorter bunches in the Tevatron, a possible advantage in an era of tighter low β insertions.

For antiprotons the scheme is relatively straightforward. We assume a cooled core of antiprotons with longitudinal emittance density $1.5 \cdot 10^{11}$ per eVs and that we require antiproton bunches containing $5 \cdot 10^{10}$ particles. All stated bunch areas are 95 % of the total occupation.

Establish normal buckets at h=4 (2.514 MHz) with area 0.33 eVs in the cooled core in the Accumulator, either suddenly or adiabatically. Each bucket should contain $5 \cdot 10^{10}$ particles. These four bunches are accelerated to the extraction momentum, just as is done now. The rf voltage required to create the stationary bucket is 7 V. This process can be done with the ARF1 system with minor low level modification. With bunches on the extraction orbit the h=4 rf voltage is raised to about 550 V (possibly using a slightly modified ARF2 system) causing the bunches to have a full length of 100 ns. The energy spread goes to ± 2.23 MeV with $\delta p/p = 2.5 \cdot 10^{-4}$. These four bunches are extracted and delivered to matched buckets in the Main Injector at h=84 (7.542 MHz). The bunches in the Main Injector are separated by two empty buckets. The matched buckets require an rf voltage of 740 V and the synchrotron frequency at this time is 8.9 Hz. (This is a bit of a tight squeeze. The bucket to bunch area ratio could be increased substantially without an alarming increase in momentum spread, but at the expense of a much larger bunching voltage in the Accumulator, or, perish the thought, bunch rotation in the Accumulator prior to extraction.)

At this point these four bunches can be accelerated in the Main Injector at h=84, bunch rotated at 150 GeV into matched h=588 (53.104 MHz) buckets, and injected into the Tevatron. Alternatively, the bunches can remain in stationary buckets at 8 GeV in the Main Injector until additional groups of four bunches are extracted from the Accumulator and larger multiples of four can be accelerated simultaneously. The antiproton bunches are spaced every seventh h=1113 bucket, and this sets the ultimate bunch spacing in the Tevatron, 131.8 ns.

For protons we still have the Booster configuration to deal with. We assume that the goal is to create bunches containing $5 \cdot 10^{11}$ protons with the smallest possible longitudinal emittance, spaced in the Tevatron exactly as the antiprotons are.

We start by accelerating normally in the Booster 84 bunches with total intensity $2 \cdot 10^{12}$ ($2.2 \cdot 10^{10}$ protons per bunch). This is a reasonable intensity for the Booster and we assume here that the extracted bunches have longitudinal emittance 0.1 eVs. No phase locking will be required prior to extraction from the Booster so the rf voltage could be reduced substantially or bunch rotation could be employed to reduce the extracted beam momentum spread. The extracted beam could reasonably have an energy spread of 1.5 MeV.

The extracted Booster beam is injected into the Debuncher ring, which is not occupied at the moment and is patiently at the correct momentum. The protons are easily prevented from spreading into the additional circumference by the barrier bucket system. The total

longitudinal phase space area occupied by the injected beam will be 16 eVs. The beam can now be momentum cooled by a factor of at least two giving a total emittance of 8 eVs. Now this uniformly debunched and cooled beam can be captured adiabatically in four 2.515 MHz buckets with each bunch having a longitudinal emittance of 2 eVs. Of course this frequency is not an integral harmonic of the rotation frequency (588.781 kHz) so this rf wave must be generated with a broadband "isolated bucket" system with h=4.286. If this system were required to bunch each of the 2 eVs to a full length of 100 ns adiabatically, a voltage of 5 kV would be required. This is not practicable. Using bunch rotation from $\pm 120°$ the voltage is reduced to 1 kV. Even this is beyond the capability of existing systems, but it is a buildable system, requiring a 10 kW broadband amplifier (or perhaps a system operating at an impedance larger than 50 Ω).

It may turn out that intrabeam scattering in the Tevatron will largely negate any benefit derived from cooling proton bunches in the debuncher. In such a case the considerable time spent in cooling would be wasted. In this case the protons can be adiabatically captured into four bunches of four eVs each, as described above, but it would be technically impracticable to narrow the bunches sufficiently so that they could be matched to h=84 buckets in the Main Injector. However, they can be injected into matched buckets at h=28 in the Main Injector and narrowed by bunch rotation prior to acceleration. This would relax the voltage requirement in the Debuncher to about 500 V and require an additional small rf system in the Main Injector at 2.5 MHz.

One or the other of these processes is repeated as required to fill the Tevatron with intense proton bunches, essentially using the Debuncher to coalesce and possibly to to cool protons. It may be useful in this process to cool the protons in the betatron dimensions also.

This proposal requires some internal modifications to the Debuncher ring and some beam lines which do not presently exist. But, of course, the Main Injector does not exist either, and it seems prudent to examine any geometry which would enhance the quality of the colliding beam program.

Large rf systems operating near 7 MHz require large quantities of ferrite and lots of rf power. Since this system is to be used perhaps only once a day for a few cycles there is no need for a very short acceleration cycle. The required rf voltage might reasonably limited to 100 kV. This implies an acceleration time of about 28 s. Since this proposal eliminates the need for a sub-harmonic bunch coalescing system it may be possible to use the existing PPA cavities for the accelerating system. This would require reverting them to a condition similar to their operating condition, but with reduced tuning range and ferrite biassing current. Figure 4 is a representative rf voltage curve providing bucket area ranging upward from 4.5 eVs at injection.

The objection has been raised that it may be difficult to accelerate these large bunches through transition at the slow rate proposed. This problem is being carefully considered and it appears that it may be solved. This will be the subject of future presentations.

The propensity for the intense proton bunches to suffer from microwave instability must be examined throughout the cycle. A quick check at 15 GeV with bunch length 50 ns gives a threshold value of $Z/n = 33\ \Omega$, which is no problem. Simulations of the transition crossing using the scheme alluded to above have shown a very minor suggestion of instability near

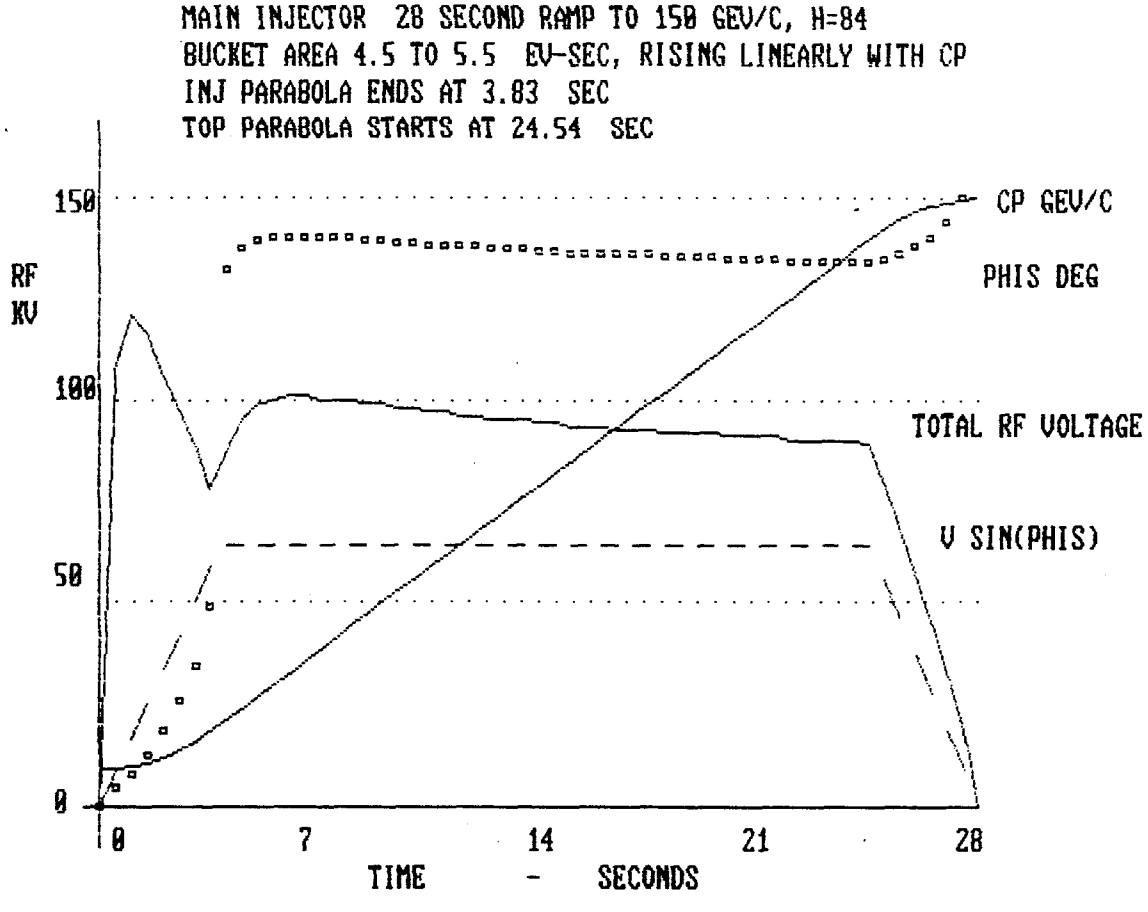

Figure 4: RF voltage curve for h=84 acceleration of bunches of $5 \cdot 10^{10}$ antiprotons or $5 \cdot 10^{11}$ protons

transition, but no bothersome blow-up using a 2 GHz broadband Z/n of 5 Ω.

Conclusions

It appears promising that some of the problems presently plaguing bunch coalescing in the Main Ring may be due to kicker impedances. If this is verified a simple solution presents itself. The crossover point in window frame kickers can relatively easily be terminated, thus eliminating the resonant property of such kickers. C-magnet kickers should be examined to determine whether they may have similar hidden propensity for low frequency resonance.

An entirely different proposal for creating high intensity bunches required for future high luminosity colliding beam physics has been described. While it may have its own problems, the proposal eliminates bunch coalescing as we now know it. The old scheme seemed like a good idea at the time, and it has served us well. But it should not be allowed to become so entrenched that it stands in the way of potentially better procedures.

References

[1] J. E. Griffin *et al.*, "Preparation of Bunches Containing 10^{11} Protons in the Fermilab Main Ring", IEEE Proc. Nucl. Sci., **NS-28** No. 3 (1981)2037

[2] J. E. Griffin *et al.*, "RF Exercises Associated with Acceleration of Intense Antiproton Bunches at Fermilab", IEEE Proc. Nucl. Sci., **NS-30** No. 4(1983)2627

[3] P. S. Martin *et al.*, "Improvements in Bunch Coalescing in the Fermilab Main Ring", IEEE Proc. Part. Accel. Conf. 1987, p1527

Parameters of RF Feedback in the Tevatron

D. Boussard
CERN

In the fixed target mode, the Tevatron DC beam current amounts to 0.5 A or about 1 A RF in the case of very short bunches. The beam loading voltage in each cavity (assumed unloaded by the power amplifier) would be of the order of 1 MV, *i. e.* much larger than the operating voltage of 360 kV. Beam loading problems are therefore to be expected.

The most efficient way to deal with beam loading is to use RF feedback around the power amplifier. In the case of a gridded tube, without circulator, the tube capability is given by

$$P = \frac{1}{2} V I_b \ ;$$

$$P = 100 \text{ kW per cavity} \ .$$

This is smaller than the Eimac Y567B tube capability of 200 kW. The minimum impedance which can be achieved with RF feedback is given by

$$R_{\min} = 4\tau \frac{R}{Q} f_{\mathrm{RF}} \ ,$$

where τ is the overall delay in the feedback chain. With $f_{RF} = 53$ MHz, $R/Q = 160\ \Omega$, and $\tau \approx 300\ \mu$s one obtains

$$R_{\min} = 10 \text{ k}\Omega \ ,$$

which is perfectly adequate. The overall loop gain would be of the order of 40 dB at most. At fixed frequency this should not pose any special problems.

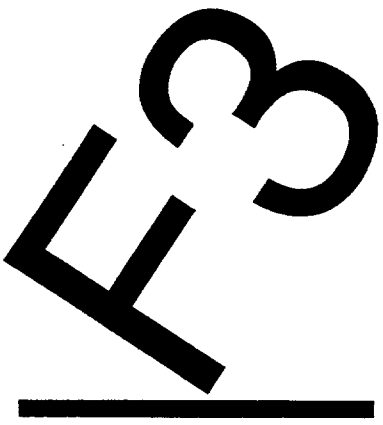

TRANSITION CROSSING INSTABILITIES

Summary Report on the Transition Crossing for the Main Injector

S.Y. Lee*
Brookhaven National Laboratory
Accelerator Development Department
Upton, NY 11973

Group Members: King Yuen Ng – Secretary
Alex Bogacz
Ioanis Kourbanis
Keith Meisner
Steve Peggs
Dejan Trbojevic
Jie Wei

Abstract

The working group evaluates the problems related to transition energy crossing in the main injector for Tevatron at Fermilab. We found that the dominant problem arises from the nonlinear synchrotron motion and the microwave instability at the transition energy region. γ_T jump such that $\dot{\gamma}_T \geq 1500$ sec^{-1} seems sufficient to obtain satisfactory transition energy crossing. To avoid longitudinal and transverse microwave instability, the maximum tolerable broad–band impedances can be derived. A possible imaginary γ_T lattice has also been studied. Some possible further studies are suggested.

The main injector (MI) for Tevatron is designed to accelerate p or $\bar{p}$ from 8 GeV to 150 GeV. In a medium energy range accelerator, the transition energy crossing is an important, longitudinal beam–dynamical problem. There are two possible scenarios for the lattice design, i.e. transition crossing lattice or transitionless lattice. There are many accelerators such as AGS, CPS, JPS, Fermilab Booster, etc., where the transition energy crossing is a routine operation. To avoid longitudinal bunch dilution and beam loss, CPS and Fermilab Booster have γ_T jump schemes. The working group evaluates the problem related to the transition crossing in the main injector design. Here I summarize problems and solutions to the γ_T crossing.

I. Beam Dynamics at γ_T Region

It is known that the synchrotron motion of particles at the transition energy is dominated by the microwave instability and nonlinear dependence of the phase slip factor, η.

* Work performed under the auspices of the U.S. Department of Energy.

These phenomena can be described by two times scales, i.e. the characteristic time and the nonlinear time. For the main injector, the characteristic time[1] and the nonlinear time[2] are respectively given by[4]

$$\tau_c \simeq 2\left(\frac{V_{\rm rf}\cos\phi_0}{2.78[\mathrm{MV}]\cos[37.6^\circ]}\right)^{-1/3} \text{ ms} \tag{1}$$

$$\tau_{\rm NL} \simeq \frac{(\alpha_1+\frac{3}{2})\gamma_T}{\dot\gamma}\sqrt{6}\,\sigma_\delta \simeq 2.7 \text{ ms} \tag{2}$$

where the Johnsen's nonlinear momentum compaction factor has been assumed to be $\alpha_1 \sim 1$ for uncorrected natural chromaticity. Within the characteristic time around the transition energy region, the bunch synchrotron motion is frozen. The bunch is then sensitive to microwave instability. Besides, particle motion in the bunch may experience defocusing synchrotron motion due to the nonlinear dependence of phase slip factor η on the momentum.

Particle tracking simulation[3] indicates that particle loss will be about 20% and the emittance growth[3,4] can be a factor of $2 \sim 3$. Thus γ_T jump is inevitable (careful analysis shows that the dependence of the transition energy on the betatron amplitude due to space charge,[3,4] sextupole, octupole, etc. is not important).

II. γ_T Jump

A γ_T jump scheme has been proposed for the MI. The γ_T jump scheme[5] can be summarized in the following,

$$\Delta\gamma_T = -0.069\left(\int G d\ell[\mathrm{KG}]\right)^2 \tag{3}$$

$$\hat{X}_p = 2.2 + 4.8(\Delta\gamma_T)^{1/2} \text{ [meters]} \tag{4}$$

With $\Delta\gamma_T = 1$, the maximum dispersion will be 7 m. The corresponding momentum width is

$$\sigma_\delta = 2.45\times10^{-3}\left(\frac{S}{0.4 \text{ eV-sec}}\right)^{1/2}\Delta\gamma_T^{-1/4}\left(\frac{V_{\rm rf}\cos\phi_0}{2.78[\mathrm{MV}]\cos[37.6^\circ]}\right)^{1/4} \tag{5}$$

Thus the required momentum aperture is about 40 mm. Transverse phase space tracking calculation at the transition energy region for $500 \sim 1000$ turns will be important to define the available dynamical aperture.[6]

The minimum transition energy jump is $\Delta\gamma_T \geq \max(2\dot\gamma\tau_c, 3\dot\gamma\tau_{\rm NL})$. The maximum $\Delta\gamma_T$ is determined by the dynamical aperture limitation, which corresponds to maximum

$\hat{X}_p = 8.5$ m. These two conditions give us $1.72 \geq \Delta\gamma_T \geq 1.3$. The minimum number of turns N_a, for the γ_T jump which minimizes transverse phase space area growth is given by[7]

$$\frac{\Delta\hat{X}_p}{N_a} \cdot \sigma_\delta \ll A_\beta \tag{6}$$

where A_β is the rms betatron amplitude at maximum beta $\hat{\beta} = 57$ m. One expects, for $\Delta\gamma_T = 1$ and normalized 95% transverse emittance of 20π mm-mr, the minimum number of turns should be about 39 or the minimum jumping time should be about 0.43 ms which gives 1% nonadiabatic change in transverse phase space. Thus one obtains $\dot{\gamma}_T \geq 2340\ \text{sec}^{-1}$, which is about 14 times larger than the nominal $\dot{\gamma}$. Numerical simulation[3] shows that a jump of

$$\Delta\gamma_T \cong 1.5 \left(\frac{S}{0.4\ \text{eV-sec}}\right)^{1/2} \geq 3\dot{\gamma}\tau_{\text{NL}} \simeq 3\gamma_T\hat{\delta} \tag{7}$$

in 1 ms is sufficient to maintain the bunch area. Here $\hat{\delta} = \sqrt{6}\ \sigma_\delta$. Thus the nonlinear effect dictates longitudinal beam dynamics at the transition energy crossing.

III. Longitudinal and Transverse Microwave Instabilities After γ_T Jump

After the transition γ_T jump, the microwave instability threshold may still be small due to small $|\eta|$, where

$$|\eta| \simeq \frac{\Delta\gamma_T}{\gamma_T^3} \tag{8}$$

The longitudinal and transverse impedance threshold is given by,[8]

$$\left|\frac{Z_\parallel}{n}\right| \leq 10\ [\Omega] \left(\frac{S}{0.4\ \text{eV-sec}}\right)^{3/2} \left(\frac{V\cos\delta_0}{2.78[\text{MV}]\cos[37.6°]}\right)^{1/4} \left(\frac{N}{6\times10^{10}}\right)^{-1} \Delta\gamma_T^{3/4} \tag{9}$$

$$|Z_\perp| \leq 2.3 \left[\frac{\text{M}\Omega}{\text{m}}\right] \left(\frac{S}{0.4\ \text{eV-sec}}\right) \left(\frac{N}{6\times10^{10}}\right)^{-1} |(n-\nu)\eta - \xi\nu| \tag{10}$$

Thus the impedance budget is still important even when γ_T jump schemes is used.

IV. Imaginary Transition Lattice

Recently Trbojevic et al.[9] worked out a lattice with imaginary transition γ_T. The lattice has regular lattice properties. However, the following lists of problems should be worked out.

a) Chromatic correction scheme

b) Off-momentum behavior of the lattice, i.e. $\gamma_T(\delta)$, $Q_{x,y}(\delta)$, $\beta_{x,y}(\delta)$, $\hat{X}_p(\delta)$ etc.

c) Tunability

d) Slow extraction efficiency

e) Tolerance to error

f) Tracking of dynamical aperture.

Items (a), (b) and (c) have been studied by Trbojevic and myself. The tunability and off-momentum behaviors of the lattice are good. Items (d), (e) and (f) are yet to be studied.

V. Experiments to Test the Longitudinal Beam-Dynamics

Most of the analysis in the workshop are carried out through the particle tracking calculations. It is important to test the validity of the tracking program. Several experiments were carried out recently in Fermilab.[10]

VI. Conclusion

The working group has worked out the requirement of γ_T jump criteria for main injector. With appropriate γ_T jump, transition energy will not be the performance limitation. We have also obtained the criteria for the betatron phase space adiabaticity in the γ_T jump. We obtain then the maximum achievable $\dot{\gamma}_T$. We found that the γ_T jump can enhance the transition energy crossing by a factor of 10, i.e. $\dot{\gamma}_T \simeq 10\dot{\gamma}$. Depending on $\Delta\gamma_T$, the impedance threshold should be carefully controlled after γ_T jump.

Several beam dynamical experiments has been contemplated and reported in the proceeding of the workshop.

References

1) S.Y. Lee and J.M. Wang, IEEE Transactions on Nucl. Science, NS 32, 2323 (1985).

2) S.Y. Lee and J. Wei, *Nonlinear Synchrotron Motion Near Transition Energy in RHIC*, EPAC proceedings p. 764 (1988).

3) A. Bogacz, *Transition Crossing in the Main Injector ESME Simulation*, these proceedings.

J. Wei, *Transition Crossing in the Main Injector*, these proceedings.

I. Kourbanis and K.Y. Ng, *Main Ring Transition Crossing Simulations*, these proceedings.

4) K.Y. Ng, *Some Estimation Concerning Crossing Transition of the Main Injector*, FNAL-TM1670, also these proceedings.

5) S. Holmes, *Main Injector Transition Jump*, Fermilab Internal Report MI-0008, 1989.

6) A. Bogacz, F. Harfoush, and S. Peggs, *A Comparison of Matched and Unmatched γ_T-jump Schemes in the Main Injector*, these proceedings.
A. Bogacz and S. Peggs, *Comments on the Behavior of α_1 in the Main Injector γ_T-jump Schemes*, these proceedings.

7) S. Peggs, *Betatron Adiabaticity During a γ_T Jump*, these proceedings.
K.Y. Ng, *Transverse Emittance Growth During γ_T Jump*, these proceedings.

8) S.Y. Lee and K.Y. Ng, *Longitudinal and Transverse Instabilities Around a γ_T Jump*, these proceedings.

9) D. Trbojevic and S.Y. Lee, *Examination of the Imaginary γ_T Lattice Stability*, these proceedings.

10) I. Kourbanis, K. Meisner, and K.Y. Ng, *Experimental Study of the Main Ring Transition Crossing*, these proceedings.

Transition Crossing in the Main Injector

*J. Wei**

Accelerator Development Department

Brookhaven National Laboratory

Upton, New York 11973

Abstract

This report summarizes the study of various longitudinal problems pertaining to the transition-energy crossing in the proposed Fermi Lab Main Injector. The theory indicates that the beam loss and bunch-area growth are mainly caused by the chromatic non-linear effect, which is enhanced by the space-charge force near transition. Computer simulation using the program TIBETAN shows that a "γ_T jump" of about 1.5 unit within 1 ms is adequate to achieve a "clean" crossing in the currently proposed h=588 scenario.

*Work performed under the auspices of the U.S. Department of Energy.

1. Introduction

The transition-energy crossing is characterized by a time scale T_c during which the particle motion is non-adiabatic,[1-4]

$$T_c = \left(\frac{\pi E_s \beta_s^2 \gamma_T^3}{qe\hat{V}|\cos\phi_s|\dot{\gamma}_s h\omega_s^2} \right)^{\frac{1}{3}}, \tag{1}$$

where the subscript s represents the synchronous particle, γ_T is the transition energy, h is the harmonic number, and ϕ_s, ω_s, $\beta_s c$, $E_s = m_0 c^2 \gamma_s$, and $\dot{\gamma}_s$ are the synchronous phase, revolution frequency, velocity, energy, and acceleration rate, respectively.

Problems related to transition crossing can mainly be divided into two categories: single- and multi-particle. In the former category, we study the effect of chromatic non-linearities which impel particles of different momenta to cross transition at different times; while in the latter, we study the bunch-shape mismatch and microwave instability induced by low- and high-frequency self fields, respectively. Theoretical estimates are presented in the first part of section 2; results of computer simulation are addressed in the second part. Compensation methods and requirements are discussed in section 3.

2. Problems at Transition Energy

A. Theoretical Estimates

Chromatic non-linear effect

Particles of different momenta traverse closed orbits of different lengths L. The difference may be expressed in terms of the momentum deviation ($\delta \equiv \Delta p/p$) as

$$\frac{L}{L_s} = 1 + \frac{\delta}{\gamma_T^2}\left(1 + \alpha_1\delta + O(\delta^2)\right). \tag{2}$$

The so-called "frequency-slip factor" η can thus be written as

$$\eta = \eta_0 + \eta_1\delta + \cdots,$$

where

$$\eta_0 = \frac{1}{\gamma_T^2} - \frac{1}{\gamma_s^2}, \quad \text{and} \quad \eta_1 \approx \frac{2}{\gamma_s^2}\left(\alpha_1 + \frac{3\beta_s^2}{2}\right).$$

The two terms in η_1 correspond respectively to the differences in circumference and velocity for particles of different momenta at the first non-linear order. The effect of η_1 on the particle motion is important only near the transition energy ($\gamma_s = \gamma_T$) when η_0 approaches zero. Define[4-6] the "non-linear time" T_{nl} during which $\left|\eta_1 \hat{\delta}(0)\right|$ is larger than $|\eta_0|$,

$$T_{nl} = \frac{|(\alpha_1 + \frac{3}{2}\beta_s^2)\hat{\delta}(0)\ \gamma_T|}{\dot{\gamma}_s}, \tag{3}$$

where

$$\hat{\delta}(0) = \frac{2^{1/2}\omega_s \left(hAqe\hat{V}|\cos\phi_s|T_c\right)^{1/2}}{3^{2/3}\pi^{1/2}\Gamma(2/3)E_s\beta_s^2}$$

is the maximum momentum spread at transition, $\Gamma(2/3) \approx 1.354$, and A is the bunch area before transition. The effective increase in the bunch area during the crossing depends on the ratio of T_{nl} to T_c (eqs. 4.25 and 4.27 in ref.4),

$$\frac{\Delta A}{A} \approx \begin{cases} 0.76\ \dfrac{T_{nl}}{T_c}, & \text{for } T_{nl} \ll T_c; \\ \\ e^{\frac{4}{3}\left(\frac{T_{nl}}{T_c}\right)^{3/2}} - 1, & \text{for } T_{nl} \geq T_c. \end{cases} \tag{4}$$

Beam loss occurs if the effective bunch area $A + \Delta A$ after transition is larger than the bucket area.

It is assumed[7] for the Main Injector that $\gamma_T = 20.4$, $\omega_s = 566.78\text{s}^{-1}$, $h = 588$, $\hat{V} = 2.78\text{MV}$, $\phi_s = 37.6°$ and $\alpha_1 = 1$. With these parameters, it can be shown that $T_c \approx 2.0\text{ms}$, $\hat{\delta}(0) \approx 8.5 \times 10^{-3}$, and $T_{nl} \approx 2.7\text{ms}$. According to eq. 4, the phase-space area occupied by particles near the edge of the bunch is much larger than the bucket area after transition. Therefore, beam loss is expected to occur. Quantitatively, the amount of beam loss depends on the particle distribution in the phase space.

Bunch-shape mismatch

Both reactive and resistive impedances cause mismatch[8-9] in the nominal bunch shape at the time the synchronous phase is switched at transition. A reactive impedance changes

the focusing force of the rf system differently below and above transition. The amount of mismatch is then proportional to the ratio of the self field to the rf field provided by the accelerating cavities. In addition to the mismatch, a resistive impedance causes energy dissipation which compensates part of the rf acceleration. Because this compensation induces a shift in the synchronous phase (ϕ_s), the amount of synchronous phase ($\pi - 2\phi_s$) to be switched at transition is changed accordingly.

Quantitatively, the amount of mismatch again depends on the particle distribution in phase space. For a parabolic distribution, the effective increase in the bunch area due to the mismatch, induced by a coupling impedance $|Z_L/n|$ at low frequency range, is (eq. 5.18 in ref.4)

$$\frac{\Delta A}{A} = \frac{2h\hat{I}\,|Z_L/n|}{\hat{V}|\cos\phi_s|\;\hat{\phi}^2(0)}, \tag{5}$$

where

$$\hat{I} = \frac{3hN_0qe\omega_s}{4\hat{\phi}(0)}$$

is the peak current, and

$$\hat{\phi}(0) = 3^{1/6}\Gamma(2/3)\left(\frac{2hA}{\pi qe\hat{V}|\cos\phi_s|T_c}\right)^{1/2}$$

is the maximum phase spread of the bunch at transition. If the resistive impedance at low frequency is $\mathcal{R}$, the shift in synchronous phase can also be shown as (eq. 5.22 in ref.4)

$$\Delta\phi_s = \frac{\hat{I}\mathcal{R}}{\hat{V}|\cos\phi_s|} \tag{6}$$

for $\Delta\phi_s$ much smaller than 1.

The effective impedance of the space charge below the cutoff frequency is

$$\frac{Z}{n} = \frac{ig_0Z_0}{2\beta_s\gamma_s^2},$$

where g_0 is a geometric factor, and $Z_0 = (\varepsilon_0 c)^{-1} = 377\Omega$. Taking $g_0 = 4.5$, this corresponds to a capacitive impedance of about 2Ω at transition. With an intensity of $N_0 = 6 \times 10^{10}$ per bunch, the increase of bunch area due to the corresponding bunch-shape mismatch is about 10%.

Microwave instability

Near the transition energy, the frequency spread which provides Landau damping vanishes along with the vanishing phase stability and the decreasing synchrotron-oscillation frequency. Both the reactive and the resistive components of the coupling are likely to induce instability. However, since particles cross transition with a non-zero acceleration rate, the synchrotron-oscillation frequency defined by the time derivative of the angle variable (canonically conjugate with the action variable J) of the system Hamiltonian, is also non-zero at transition. Consequently, the threshold for microwave instability to occur at transition becomes (eq. 5.58 in ref.4) for the parabolic distribution

$$\frac{8h\hat{I}\,|Z_H/n|}{3\hat{V}|\cos\phi_s|\;\hat{\phi}^2(0)} \geq 1, \tag{7}$$

where $|Z_H/n|$ refers to the coupling impedance at microwave frequency range. Again, the coefficient in eq. 7 may differ for different particle distribution.

With a beam intensity of 6×10^{10} per bunch, the threshold impedance is of the order of 10Ω. Since the space-charge impedance is only 2Ω, it is not likely to induce microwave instability at transition.

The theoretical estimates indicate that the primary concern at transition is due to the chromatic non-linear effect. The development of the "non-linear tails" after the synchronous-phase switch over is further enhanced by the space-charge force. Computer simulation is needed to understand more precisely the various mechanisms and to quantitatively determine the crossing efficiency.

B. Results of computer simulation

The computer program TIBETAN was originally developed in the Brookhaven National Laboratory to study the transition process in the proposed RHIC collider. The program simulates the longitudinal motion of a particle beam by tracking a collection of macro-particles in phase space. It constructs the self fields directly in the time (phase) domain. The bin length used for the construction of the self fields is chosen in accordance

with the cutoff frequency of the vacuum pipe.

This program has been used to simulate the transition process in the Main Injector. Beam-induced fields are calculated every turn with 3600 macro-particles. Before transition, the bunch is assumed to have a Gaussian-like distribution in longitudinal phase space with a 95% area of 0.4eV·s. Fig. 1 shows the phase-space diagram after transition at γ_s=22. With $\alpha_1 = 1$, the chromatic non-linear effect results a beam loss of about 15%. For a bunch with 6×10^{10} protons, the enhancement of the beam loss due to longitudinal space charge is less than 1%.

The transition-crossing efficiency is defined as the ratio of the total number of particles inside the rf bucket when the synchronous energy is far above the transition energy, to the one when it is far below. The solid line in fig.2 shows the crossing efficiency as a function of the bunch area before transition. With a smaller bunch area, beam loss due to the non-linear effect is reduced. However, the effect of beam-induced fields becomes more important.

3. Compensation Methods

An effective way to cure both the beam-induced and the chromatic non-linear effect is to increase the transition-crossing rate of the beam. This can be accomplished either by temporarily adjusting the lattice to achieve a "γ_T jump", or by manipulating the synchronous phase and the voltage of the accelerating rf system.

A. Crossing by an acceleration rate increase

Particle motion is non-adiabatic during the transition time T_c. If the magnetic-field ramping rate can be adjusted or the momentum aperture is adequate at transition, the synchronous phase may be switched from ϕ_s to 90° during this period to temporarily increase the acceleration rate.

The dash line in fig 2 indicates the crossing efficiency achieved by this technique. The synchronous phase is switched from 37.6° to 90° for 4 ms at transition. Effectively, $\dot{\gamma}_s$ is increased by a factor of 1.7. With the bunch area 0.4eV·s, the beam loss is reduced from

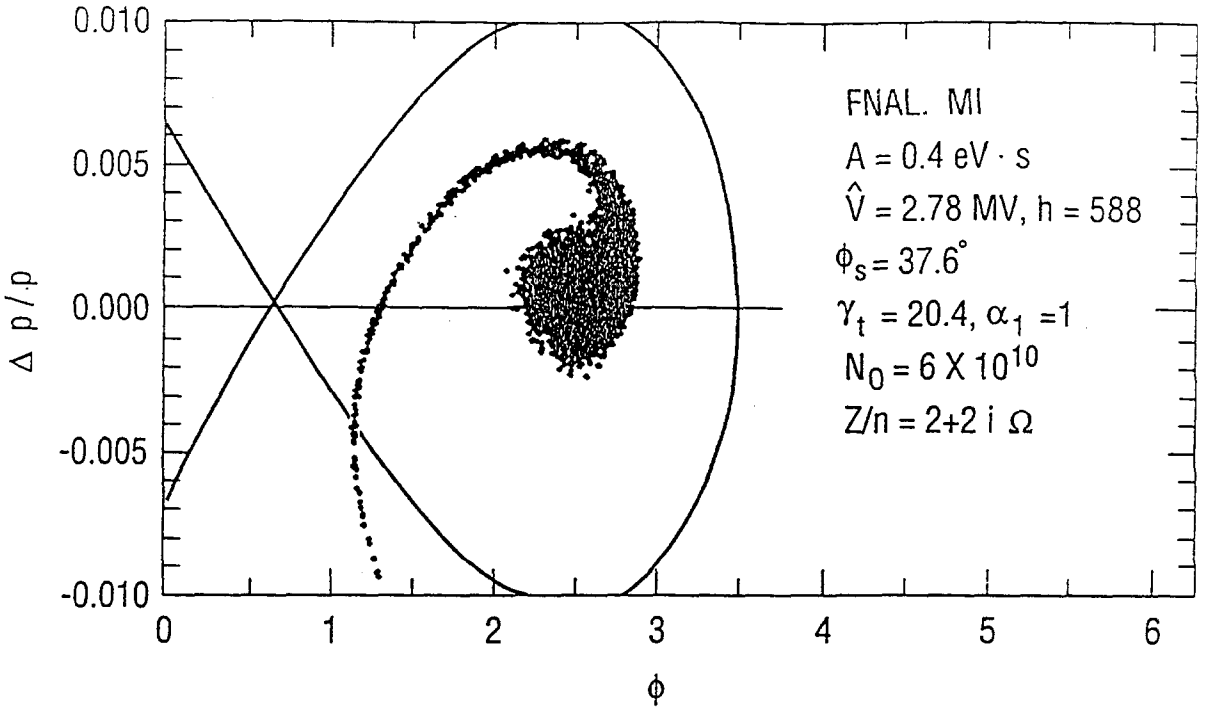
0.010
0.005
0.000
-0.005
-0.010
Δ p/p
0
1
2
3
4
5
6
ϕ
FNAL. MI
A = 0.4 eV · s
V̂ = 2.78 MV, h = 588
ϕs = 37.6°
γt = 20.4, α1 = 1
N0 = 6 X 10^10
Z/n = 2+2 i Ω

Fig. 1

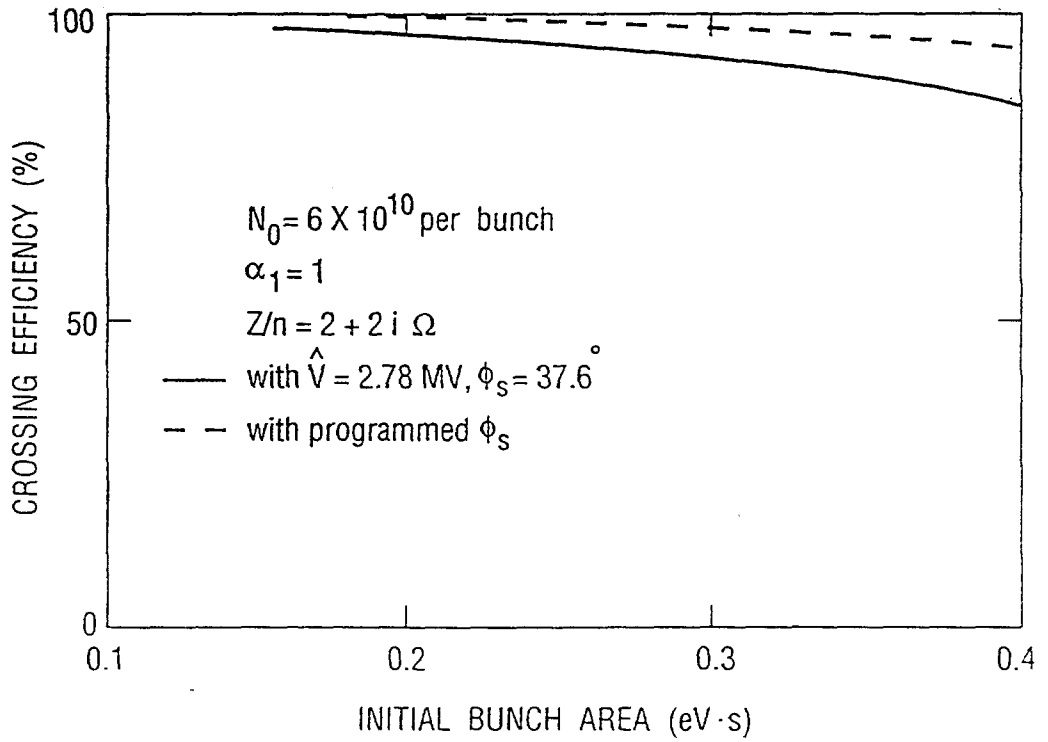
100
50
0
CROSSING EFFICIENCY (%)
N0 = 6 X 10^10 per bunch
α1 = 1
Z/n = 2 + 2 i Ω
with V̂ = 2.78 MV, ϕs = 37.6°
with programmed ϕs
0.1
0.2
0.3
0.4
INITIAL BUNCH AREA (eV·s)

Fig. 2

15% to 5%.

B. Crossing by a "γ_T jump"

Compared with the method addressed above, "γ_T jump" often provides a larger crossing-rate enhancement without causing severe mismatch at transition. In the case that the non-linear effect is dominating, the amount of $\Delta\gamma_T$ needed to eliminate the un-desired beam loss and bunch-area growth is

$$\Delta\gamma_T \sim 2\ \dot{\gamma}_s\ (2T_{nl}) \sim 1.5,$$

with both $\dot{\gamma}_s$ and T_{nl} taking the original values. Fig. 3 shows the phase-space diagram after transition ($\gamma_s = 22$) with a γ_T jump of 1.5 unit in 1ms. The crossing rate is enhanced by a factor of 9. The crossing efficiency is 100%, while the bunch-area growth is negligible.

For a given α_1, the amount of $\Delta\gamma_T$ needed is proportional to the momentum spread and, therefore, the square root of the bunch area. This relation is shown in fig. 4.

Typically, the γ_T jump should be centered at the moment that the synchronous phase is switched at transition. However, in the case that the space-charge effect is appreciable, the "non-linear tails" are enhanced after this moment. Therefore, jumping with the center shifted after the transition center (say, by 0.4ms) might be helpful if the desired amount of $\Delta\gamma_T$ is not achievable.

Acknowledgment

I am grateful to Dr. S.Y. Lee for the valuable discussion. I would like to thank Dr. K.Y. Ng for the important correction and discussion. I would also like to thank Dr. A.G. Ruggiero for reading the manuscript and for the comments.

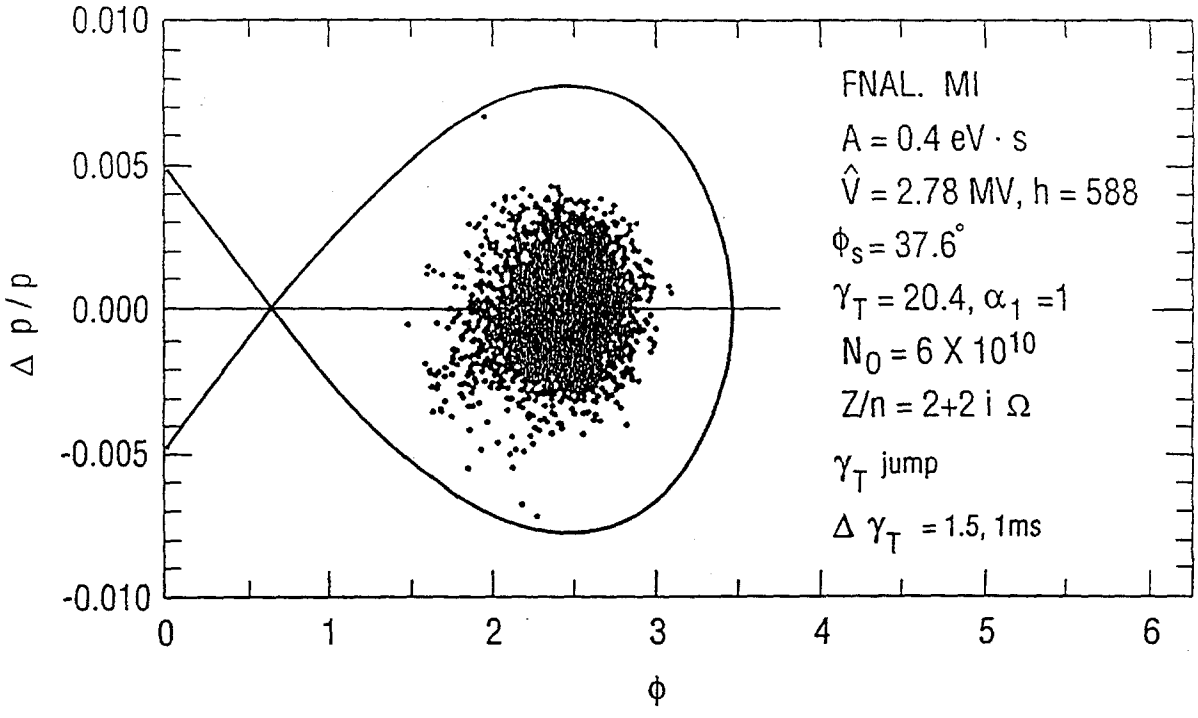
0.010
0.005
0.000
-0.005
-0.010
Δ p / p
0
1
2
3
4
5
6
ϕ
FNAL. MI
A = 0.4 eV · s
V̂ = 2.78 MV, h = 588
ϕs = 37.6°
γT = 20.4, α1 =1
N0 = 6 X 10^10
Z/n = 2+2 i Ω
γT jump
Δ γT = 1.5, 1ms

Fig. 3.

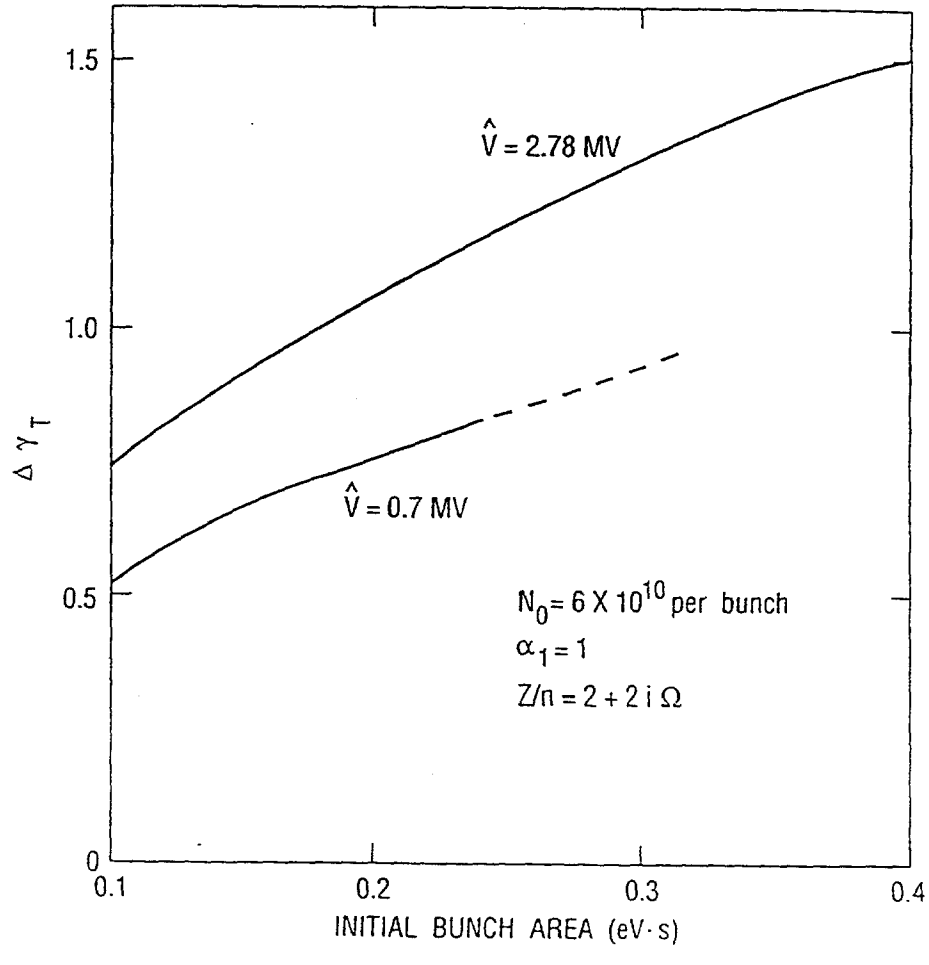
1.5
1.0
0.5
0
Δ γT
0.1
0.2
0.3
0.4
INITIAL BUNCH AREA (eV·s)
V̂ = 2.78 MV
V̂ = 0.7 MV
N0 = 6 X 10^10 per bunch
α1 = 1
Z/n = 2 + 2 i Ω

Fig. 4.

REFERENCES

1. E.D. Courant and H.S. Snyder, Ann. Phys. **3**, 1 (1958).

2. J.C. Herrera, Particle Accelerators **3**, 49 (1972).

3. S.Y. Lee and J.M. Wang, IEEE Trans. Nucl. Sci. **NS-52**, 2323 (1985).

4. J. Wei, *Longitudinal Dynamics of the Non-Adiabatic Regime on Alternating-Gradient Synchrotrons*, Ph.D thesis, State University of New York at Stony Brook, 1990.

5. K. Johnsen, Proceedings of CERN Symposium on High-Energy Accelerators and Pion Physics (Geneva, 1956), Vol.1, p.106.

6. S.Y. Lee and J. Wei, Proceedings of European Particle Accelerator Conference (Rome, 1988), p.764.

7. K.Y. Ng, TM-1670, Fermi Lab.

8. A. Sørenssen, Proceedings of 6th International Conference on High-Energy Accelerators (Cambridge, Mass., 1967), p.474.

9. J. Wei and S.Y. Lee, Particle Accelerators **28**, 77 (1990).

FIGURE CAPTIONS

Fig. 1. Longitudinal phase-space diagram of a proton bunch after transition at $\gamma_s = 22$. The crossing efficiency is about 85%.

Fig. 2. Transition-crossing efficiency as a function of the bunch area before transition.

Fig. 3. Similar to fig. 1, but with a γ_T jump of 1.5 unit in 1ms. The crossing efficiency is 100%.

Fig. 4. The amount of $\Delta\gamma_T$ needed to eliminate the un-desired effects at transition.

TRANSITION CROSSING IN THE MAIN INJECTOR – ESME SIMULATION

S.A. Bogacz

Accelerator Physics Department, Fermi National Accelerator Laboratory*,

P.O. Box 500, Batavia, IL 60510, USA.

August 1990

A longitudinal phase-space tracking code (ESME) is used to model transition crossing in the Main Injector. The simulation is aimed at various collective and single particle effects contributing to the longitudinal emittance blowup. Our model takes into account the longitudinal space-charge force (bunch length oscillation), the transverse space-charge (the Umstätter effect) and finally the dispersion of the momentum compaction factor (the Johnsen effect). As a result of this simulation one can separate relative strengths of the above mechanisms and study their individual effects on the longitudinal phase-space evolution, especially filamentation of the bunch and formation of "galaxy-like" patterns. Finally, a simple scheme of γ_t-jump is implemented. Comparison of both cases (slow and fast transition crossing) points out that the above scheme can be very useful in suppressing beam loss and the emittance blowup at transition.

* Operated by the Universities Research Association under contract with the U.S. Department of Energy

Introduction

This study is motivated by the longitudinal phase-space dilution effects induced by the transition crossing. Here we employ ESME[1] as an effective tool to simulate transition crossing in the Main Injector. One of the obvious advantages of the simulation compared to existing analytic formalisms, e.g. based on the Vlasov equation[2], is that it allows us to consider the collective effects in a self-consistent manner with respect to the changing accelerating conditions. Furthermore this scheme enables us to model nonlinearities of the longitudinal beam dynamics, which are usually not tractable analytically[3].

Implemented in the simulation are both intensity dependent coherent forces (the longitudinal and transverse space charge) and single-particle kinematic effects due to the explicit momentum offset dependence of the momentum compaction factor, α. Their individual contributions to the longitudinal emittance blowup across transition are studied here. The transition crossing time for the synchronous particle is identified as a zero synchrotron tune point on the history plot, Fig. 1.

Longitudinal Phase Space Tracking with the Space Charge

The tracking procedure used in ESME consists of turn-by-turn iteration of a pair of Hamilton-like difference equations describing synchrotron oscillation in θ–ε phase-space ($0 \le \theta \le 2\pi$ for the whole ring and $\varepsilon = E - E_o$, where E_o is the synchronous particle energy). Knowing the particle distribution in the azimuthal direction, $\rho(\theta)$, and the revolution frequency, ω_o, after each turn, one can construct the longitudinal wake field induced by the coherent space charge force[4]

$$V_i(\theta) = e\omega_o \sum_{n=-\infty}^{\infty} \rho_n Z_{s\text{-}c}(n\omega_o) e^{in\theta}, \qquad (1)$$

where

$$Z_{s\text{-}c}(n\omega_o) = \frac{nZ_o}{2\beta\gamma^2} \left\{ 1 + 2 \ln \frac{b}{a} \right\} .$$

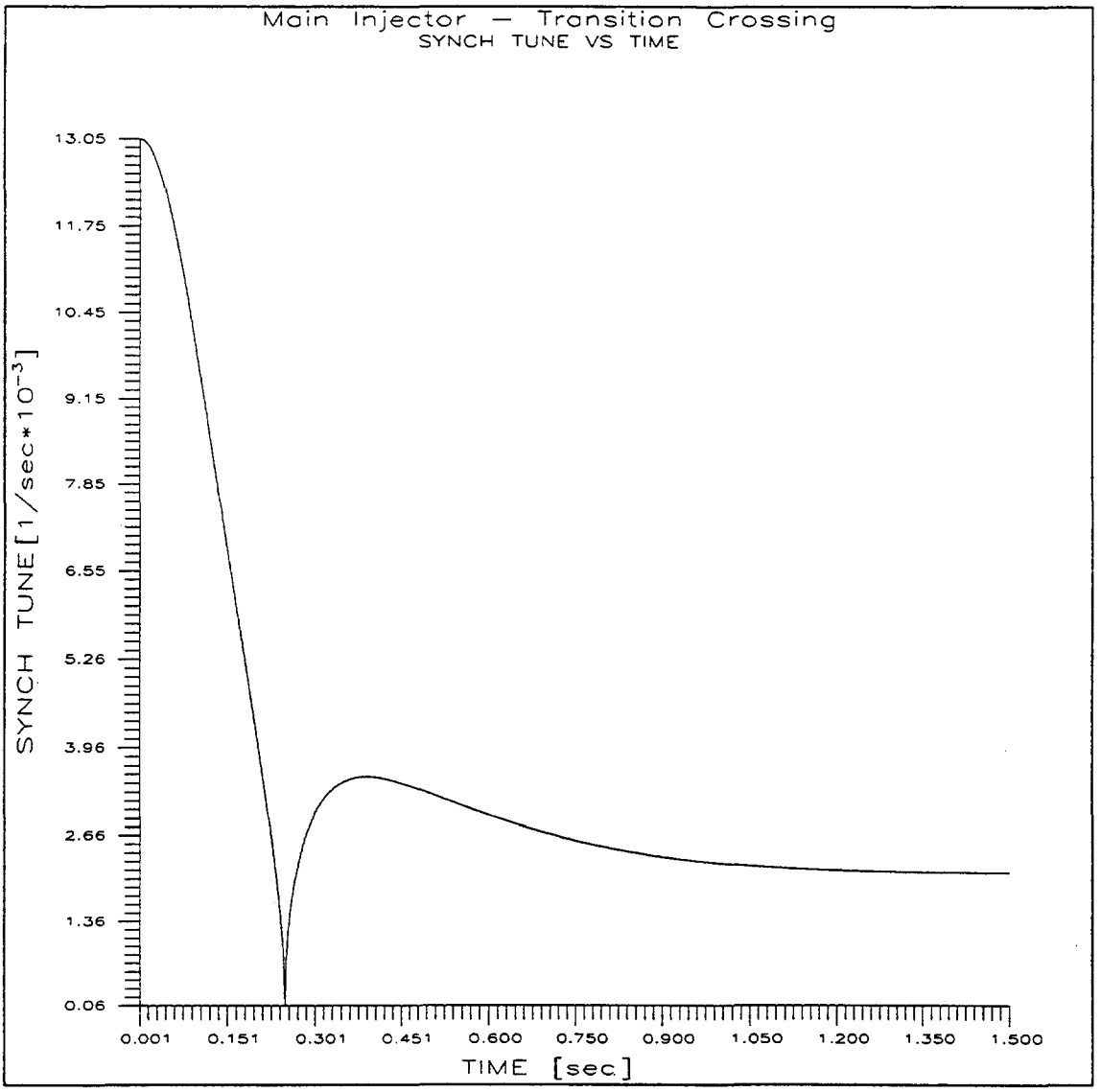
Main Injector – Transition Crossing
SYNCH TUNE VS TIME
SYNCH TUNE [1/sec*10^-3]
13.05
11.75
10.45
9.15
7.85
6.55
5.26
3.96
2.66
1.36
0.06
0.001
0.151
0.301
0.451
0.600
0.750
0.900
1.050
1.200
1.350
1.500
TIME [sec]

Fig. 1

Here, a and b are the radii of the beam and the smooth vacuum pipe, respectively.

The above force is defocusing below and focusing above the transition. Therefore it corrects the equilibrium bunch length to be longer below and shorter above the transition (compare to the case without any space charge). This yields bunch length oscillation above the transition set off by nonlinear bunch length overshoot[5]. This phenomenon can be clearly observed by looking at the history of θ_{rms} or simply by watching "mountain range" evolution of the azimuthal bunch profile (see Figs. 7 and 12).

Implementation of the Umstätter and Johnson Effects, γ_t-jump Scheme

As a result of the transverse space charge forces each particle suffers a horizontal betatron tune shift, which is proportional to the particle density, $\rho(\theta)$, at the given longitudinal position θ. This tune shift translates directly into the change of γ_t. Close to the transition, when η goes through zero, even very small corrections to γ_t play dominant role and they govern the longitudinal beam dynamics. One of the features of ESME code is that each particle has its own γ_t, which allows us for straightforward implementation of the Umstätter effect (described above). Similarly, to account for the dispersion of the momentum compaction factor (Johnsen effect), different parts of the bunch (particles with different momentum offset) are allowed to cross transition at different times. Both contributions to the γ_t shift are summarized below[6]

$$\Delta\left(\frac{1}{\gamma_t}\right)^2 = 2hr_p R \frac{1}{\beta^2\gamma^7 a^2}\rho(\theta) - \alpha_1 \frac{\Delta p}{p} - 2j(t)\frac{1}{\gamma^3} \qquad (2)$$

The last term in the above equation represents some external γ_t-jump accomplished by firing a pulsed quadrupole magnet. One purposely taylors j(t), so that the transition crossing happens much faster and no significant emittance blowup has time to develop. For the purpose of this simulation the last γ_t ma-

nipulation is implemented according to a simple η-program presented in Fig. 2. Here the rate of transition crossing is boosted by the factor of four (see Fig. 2)

ESME Simulation

As a starting point for our simulation a single bucket in θ–ε phase-space is populated with 5000 macro-particles according to a bi-Gaussian distribution matched to the bucket so that 95% of the beam is confined within the contour of the longitudinal emittance of 0.4 eV–sec. Each macro-particle is assigned an effective charge to simulate a bunch intensity of 6×10^{10} protons.

The first set of results, Fig.3-7, corresponds to the situation when only intensity dependent coherent forces are present ($\alpha_1 = 0$). The simulation is carried out over a symmetric (with respect to the transition) time interval of 2700 turns. Fig. 3 represents a sequence of the longitudinal phase space snap-shots taken every 400 turns. One can clearly see dilutions effects leading to extensive filamentation of the beam at transition. Fig. 4 illustrates longitudinal emittance blowup (100%) and beam loss (5%) at transition. The same characteristics for faster transition crossing are collected for comparison in Figs. 5 and 6. Here the emittance blowup reaches only 12% with no beam loss.

To visualize the position and shape of individual bunches as they evolve in time one can compose a "mountain range" diagram[4] by plotting θ-projections of the bunch density in equal increments of revolution number and then stacking the projections to imitate the time flow. The resulting mountain range plots for both cases are compared in Fig. 7.

The second set of simulations incorporates in addition to previously discussed coherent space charge forces also the Johnsen effect. The dispersion of the momentum compaction factor, α_1, is assigned a value of 5×10^{-3} and all three features described by Eqs. (1) and (2) are used in the simulation. Again, the phase-space snap shots, Figs. 8 and 9, refer to slower transition crossing, while Figs. 10 and 11 describe the scenario with γ_t-jump. Figs. 8 and 9 illustrate catastrophic beam loss at transition (50% loss); one can see very sharp tails made of particles rapidly steaming out of the bucket to the unstable region of the phase-

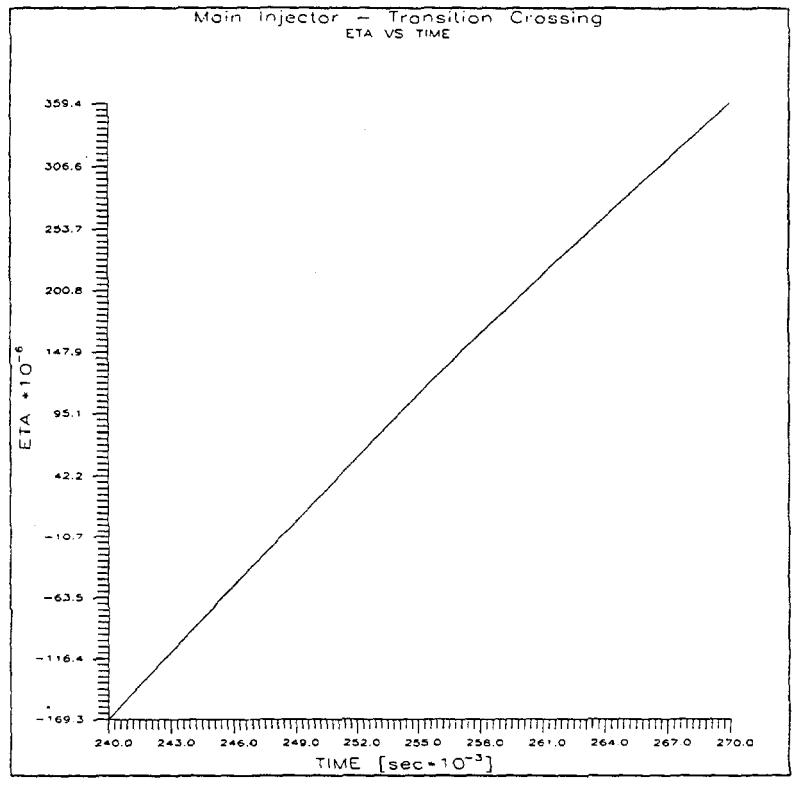
Main Injector – Transition Crossing
ETA VS TIME
359.4
306.6
253.7
200.8
147.9
95.1
42.2
-10.7
-63.5
-116.4
-169.3
ETA *10^-6
240.0 243.0 246.0 249.0 252.0 255.0 258.0 261.0 264.0 267.0 270.0
TIME [sec*10^-3]

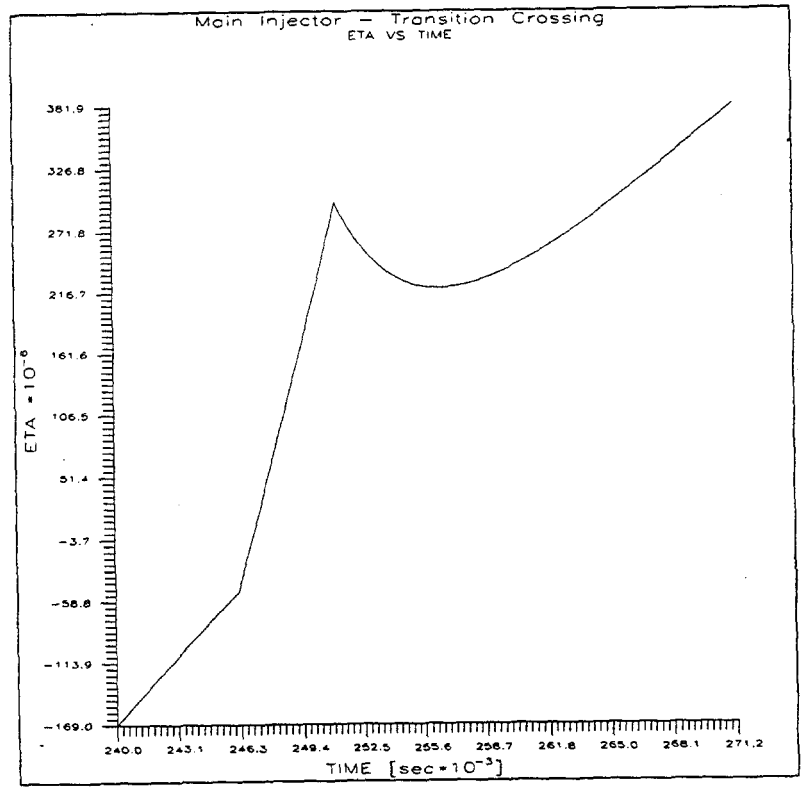
Main Injector – Transition Crossing
ETA VS TIME
381.9
326.8
271.8
216.7
161.6
106.5
51.4
-3.7
-58.8
-113.9
-169.0
ETA *10^-6
240.0 243.1 246.3 249.4 252.5 255.6 258.7 261.8 265.0 268.1 271.2
TIME [sec*10^-3]

Fig. 2

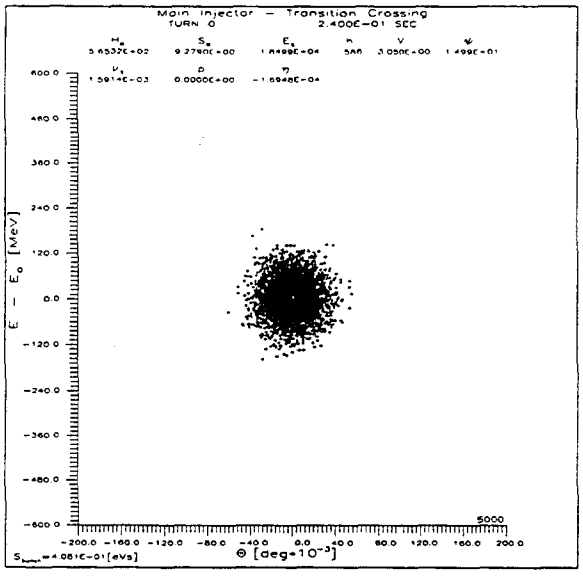
Main Injector – Transition Crossing
TURN 0
2.400E-01 SEC
E – E0 [MeV]
Θ [deg·10⁻³]

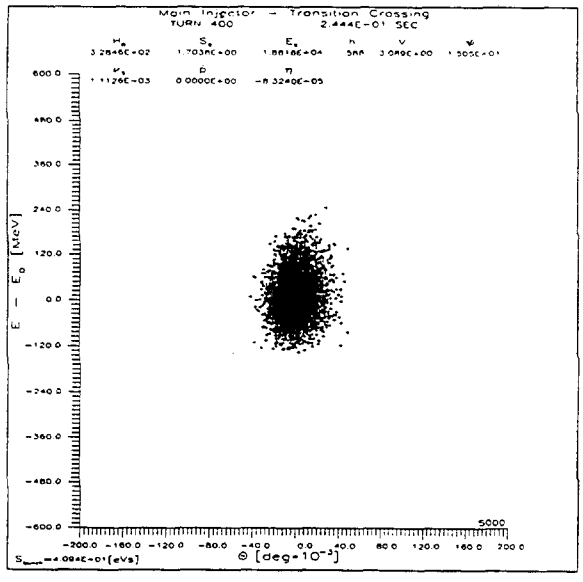
Main Injector – Transition Crossing
TURN 400
2.444E-01 SEC
E – E0 [MeV]
Θ [deg·10⁻³]

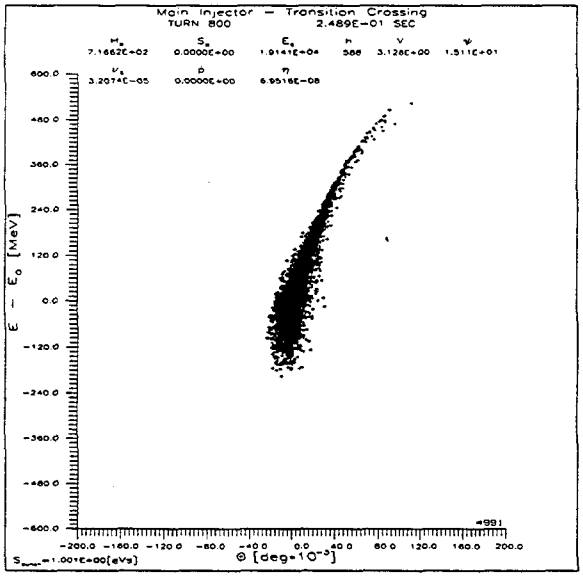
Main Injector – Transition Crossing
TURN 800
2.489E-01 SEC
E – E0 [MeV]
Θ [deg·10⁻³]

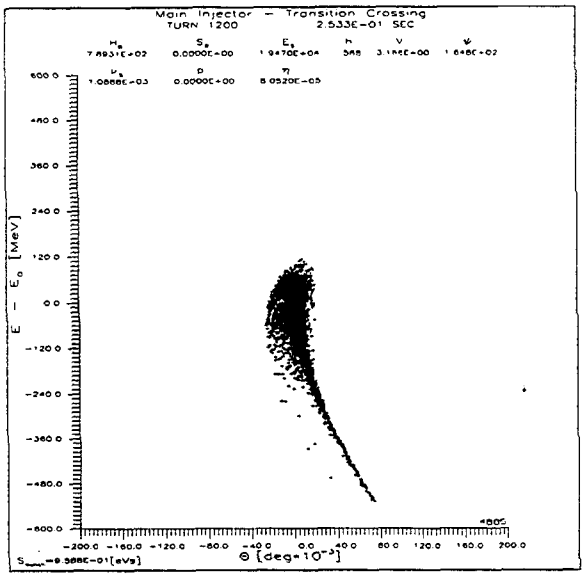
Main Injector – Transition Crossing
TURN 1200
2.533E-01 SEC
E – E0 [MeV]
Θ [deg·10⁻³]

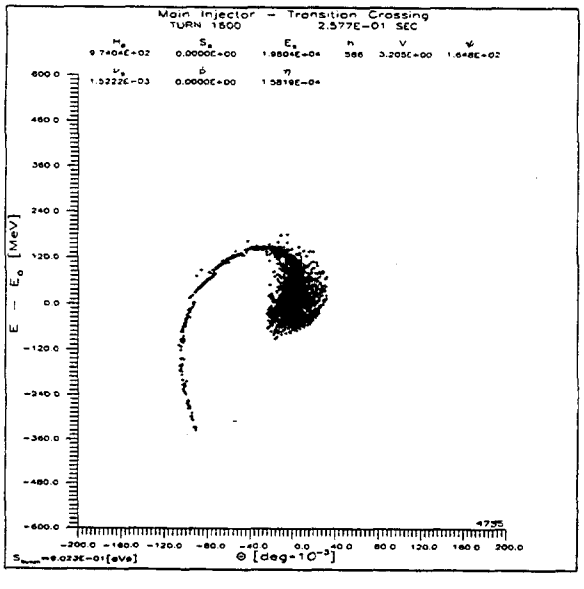
Main Injector – Transition Crossing
TURN 1600
2.577E-01 SEC
E – E0 [MeV]
Θ [deg·10⁻³]

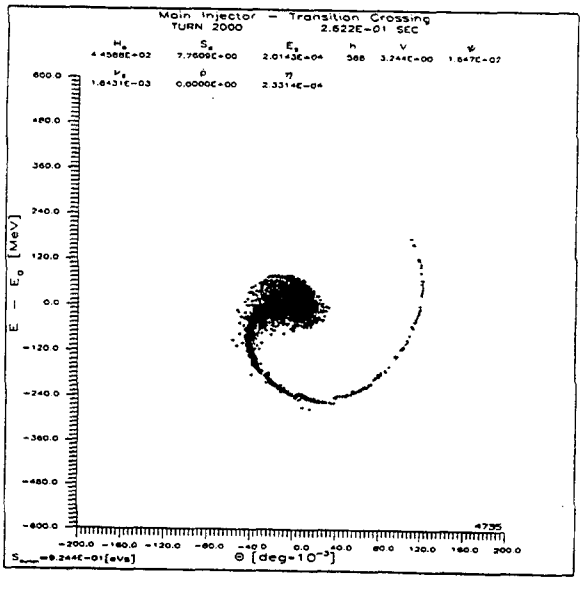
Main Injector – Transition Crossing
TURN 2000
2.622E-01 SEC
E – E0 [MeV]
Θ [deg·10⁻³]

Fig. 3

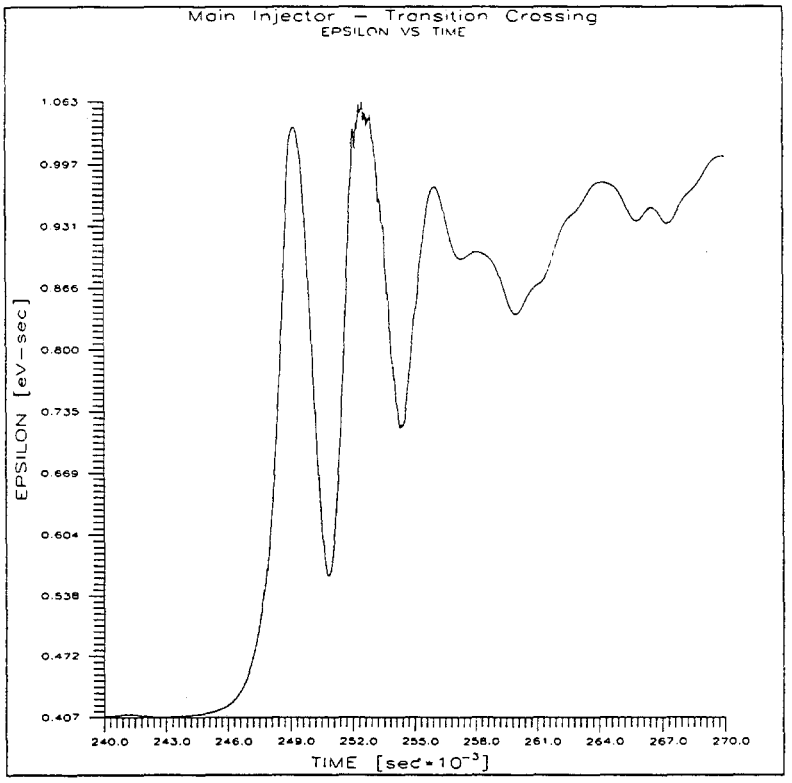
Main Injector – Transition Crossing
EPSILON VS TIME
EPSILON [eV-sec]
1.063
0.997
0.931
0.866
0.800
0.735
0.669
0.604
0.538
0.472
0.407
240.0 243.0 246.0 249.0 252.0 255.0 258.0 261.0 264.0 267.0 270.0
TIME [sec*10^-3]

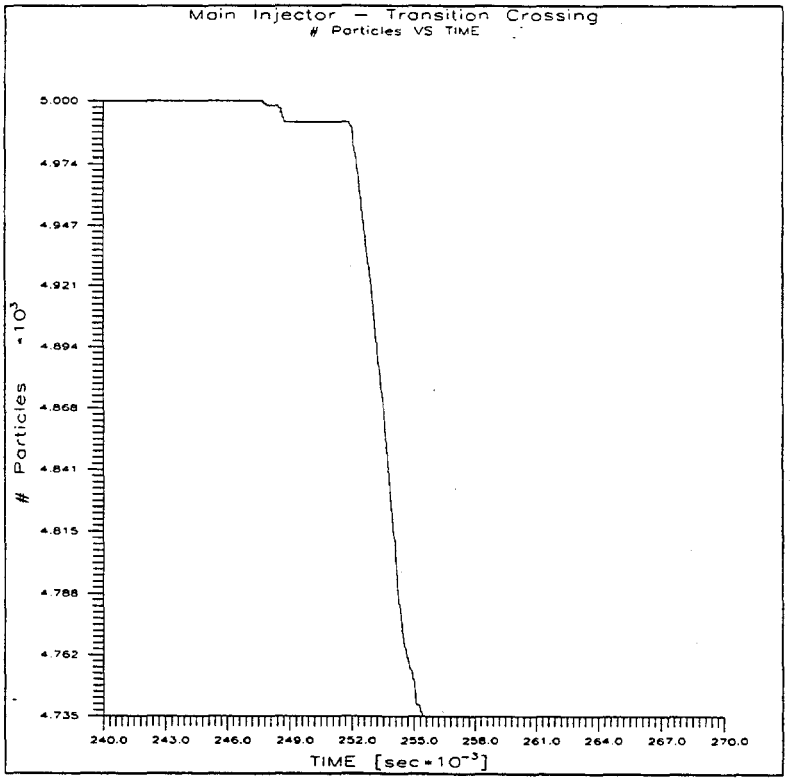
Main Injector – Transition Crossing
Particles VS TIME
Particles *10^3
5.000
4.974
4.947
4.921
4.894
4.868
4.841
4.815
4.788
4.762
4.735
240.0 243.0 246.0 249.0 252.0 255.0 258.0 261.0 264.0 267.0 270.0
TIME [sec*10^-3]

Fig. 4

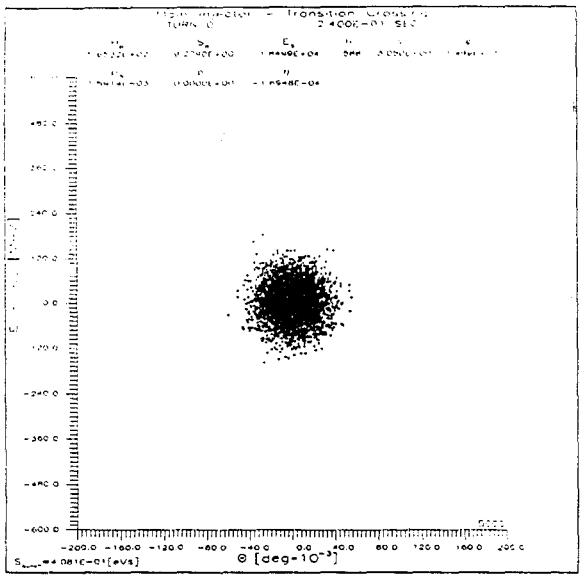

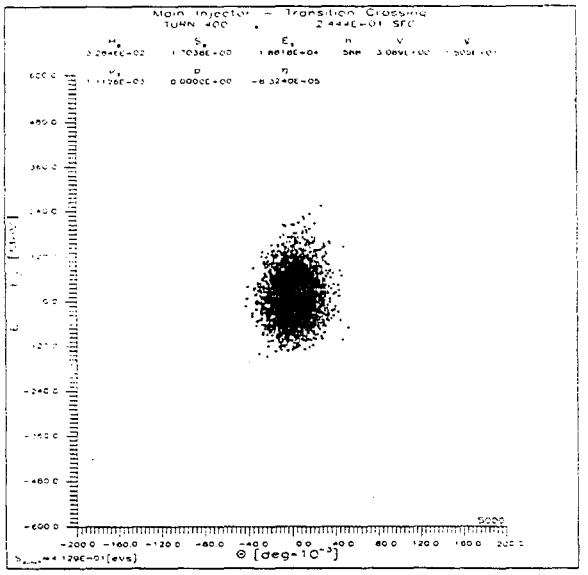
Main Injector – Transition Crossing
TURN 400
2.444E-01 SEC
Θ [deg-10⁻³]

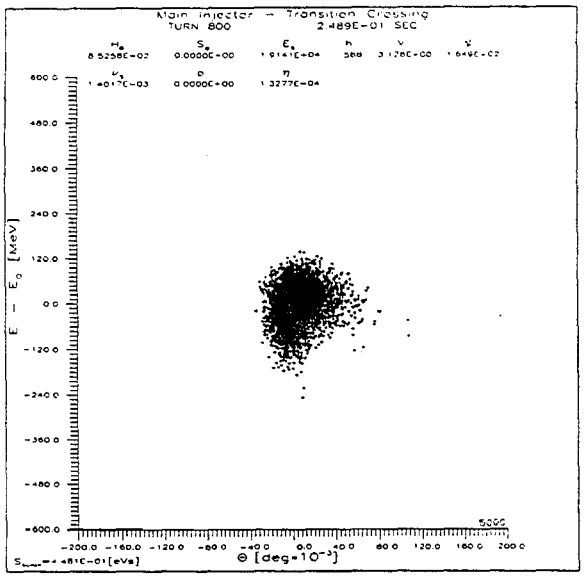
Main Injector – Transition Crossing
TURN 800
2.489E-01 SEC
E – E₀ [MeV]
Θ [deg-10⁻³]

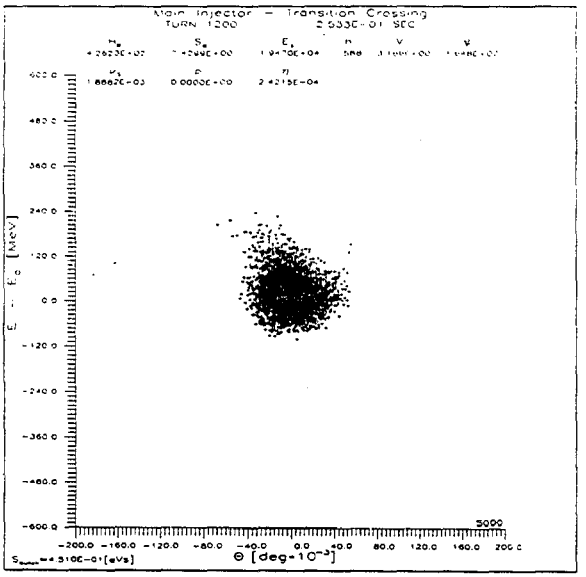
Main Injector – Transition Crossing
TURN 1200
2.533E-01 SEC
E – E₀ [MeV]
Θ [deg-10⁻³]

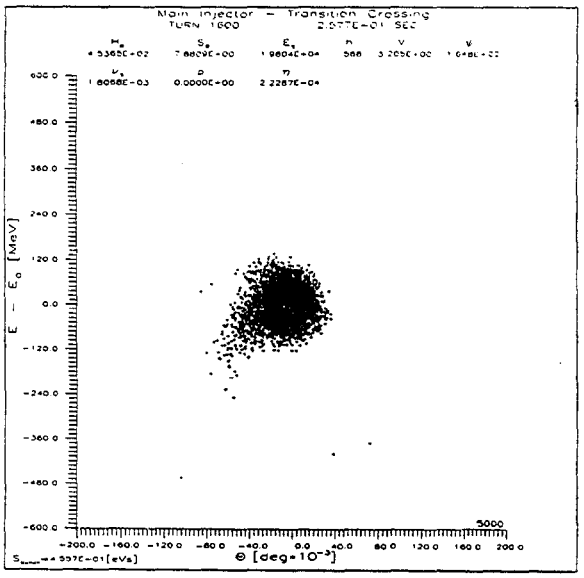
Main Injector – Transition Crossing
TURN 1600
2.577E-01 SEC
E – E₀ [MeV]
Θ [deg-10⁻³]

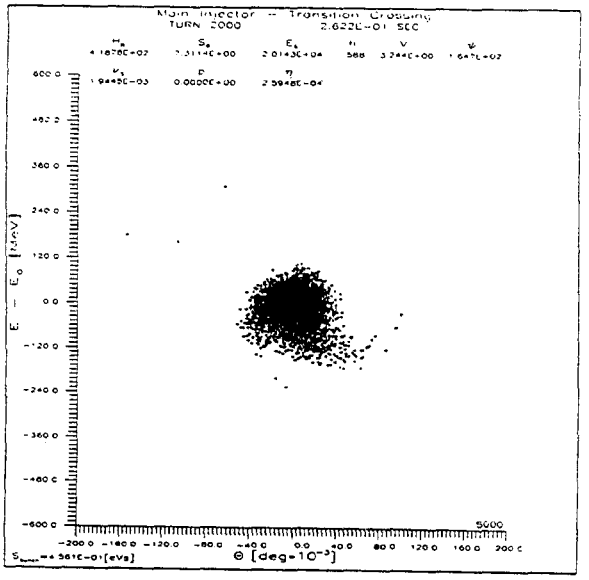
Main Injector – Transition Crossing
TURN 2000
2.622E-01 SEC
E – E₀ [MeV]
Θ [deg-10⁻³]

Fig. 5

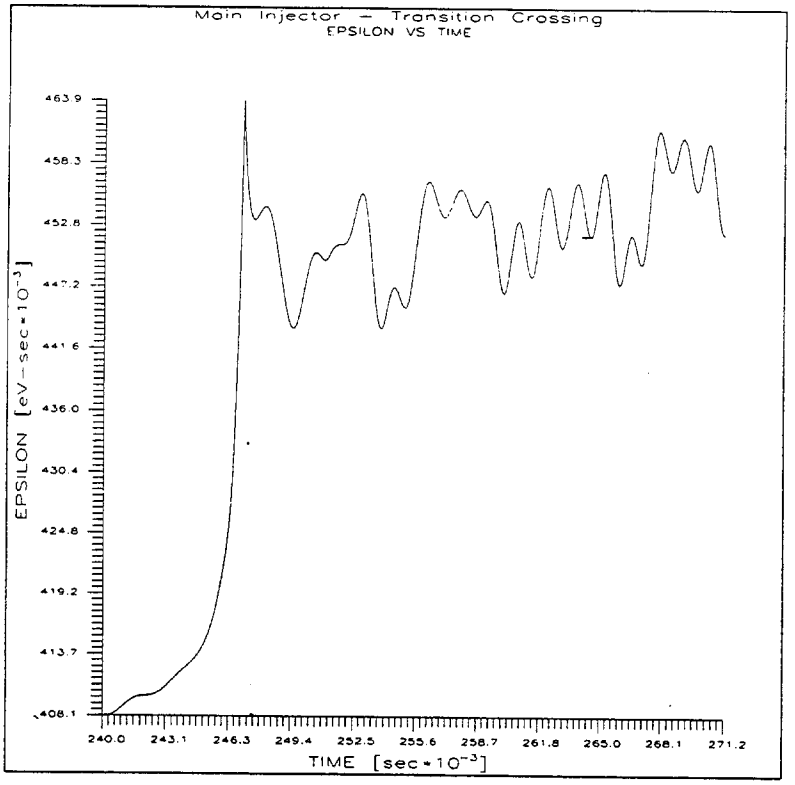
Main Injector – Transition Crossing
EPSILON VS TIME
EPSILON [eV-sec*10^-3]
463.9
458.3
452.8
447.2
441.6
436.0
430.4
424.8
419.2
413.7
408.1
240.0
243.1
246.3
249.4
252.5
255.6
258.7
261.8
265.0
268.1
271.2
TIME [sec*10^-3]

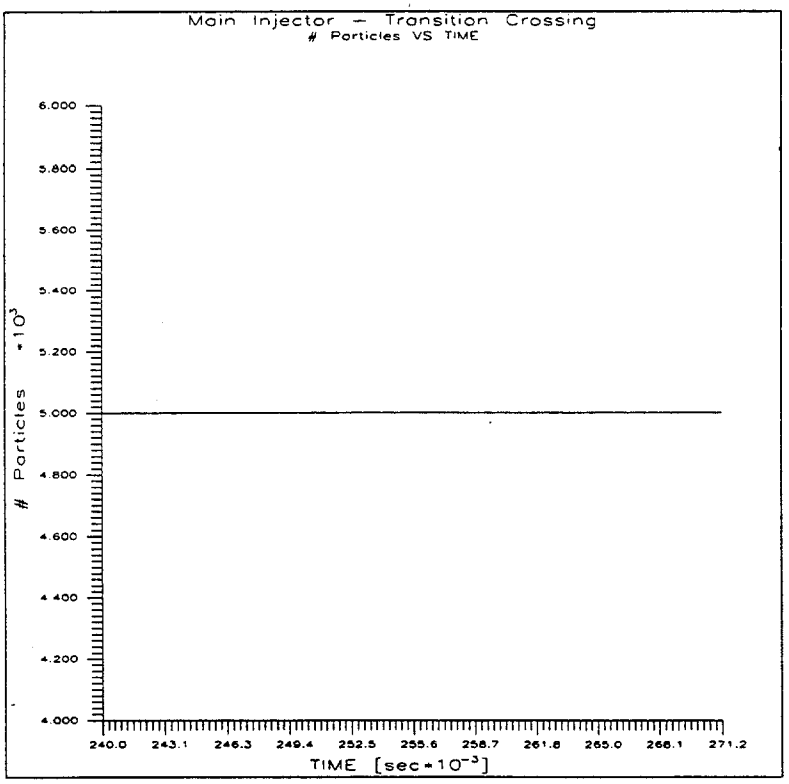
Main Injector – Transition Crossing
Particles VS TIME
Particles *10^3
6.000
5.800
5.600
5.400
5.200
5.000
4.800
4.600
4.400
4.200
4.000
240.0
243.1
246.3
249.4
252.5
255.6
258.7
261.8
265.0
268.1
271.2
TIME [sec*10^-3]

Fig. 6

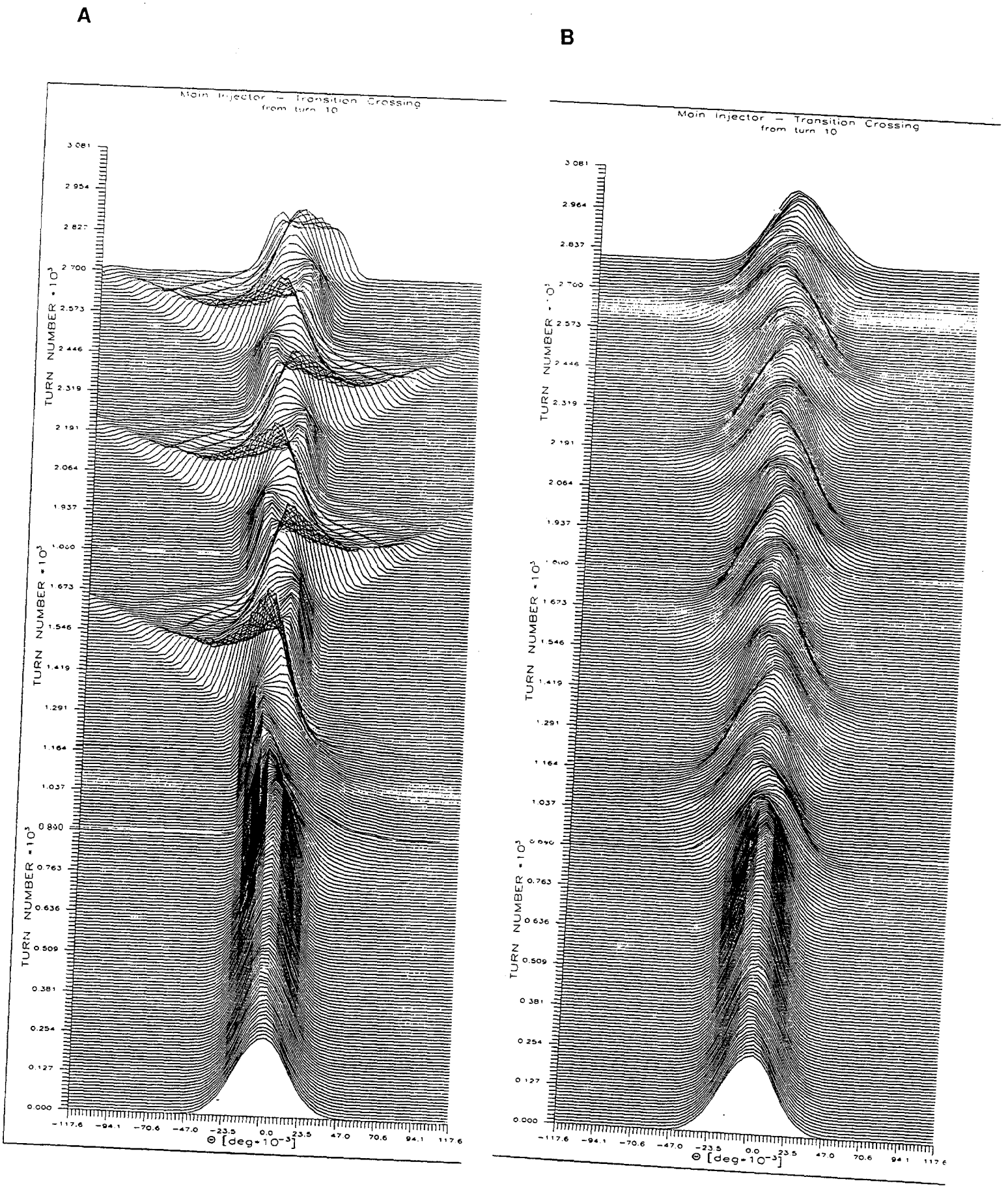
A
B
Main Injector – Transition Crossing
from turn 10
TURN NUMBER *10³
Θ [deg*10⁻³]

Fig. 7

space. When the γ_t-jump is applied (see Figs. 10 and 11) the development of tails is much slower and the transition is successfully crossed with about 75% emittance blowout and about 6% beam loss. Finally, the mountain range plots for the case without and with the γ_t-jump (labeled by A and B) are summarized in Fig.12.

Conclusions

One can see from our simulation that the presence of large α_1 has crucial impact on beam degradation at transition. One can look at the Johnsen effect using simple physical picture of instantaneous phase space configurations. Particle with large positive momentum offset cross transition sooner than the synchronous particle and they end up "seeing" unstable phase-space region long before the synchronous phase is "snapped" ($\phi_s \rightarrow \pi - \phi_s$ at the transition crossing for the synchronous particle). They follow unstable orbits in phase space and eventually leave the bucket (long tail formation). Similarly, for particles with large negative momentum offset transition crossing is delayed with respect to the synchronous particle. After the synchronous phase "snap" they are still below transition and drifting into unstable region, which contributes to formation of the second tail (see Figs. 3, 5, 8 and 10). However by speeding up the transition crossing one can easily recover from substantial emittance blowup and beam loss. Therefore the γ_t-jump scheme should be given serious consideration in the context of Main Injector lattice design.

References

[1] J.A. MacLachlan, FERMILAB TM-1274 (1984)

[2] S. Krinsky and J.M. Wang, Particle Accelerators, **17**, 109 (1985)

[3] S. Stahl and S.A. Bogacz, Phys. Rev. D, **37**, 1300 (1988)

[4] J.A. MacLachlan, FERMILAB FN-446 (1987)

[5] S.A. Bogacz and K-Y Ng, Phys. Rev. D, **36**, 1538 (1987)

[6] A. S ørenssen, Particle Accelerators, **6**, 141 (1975)

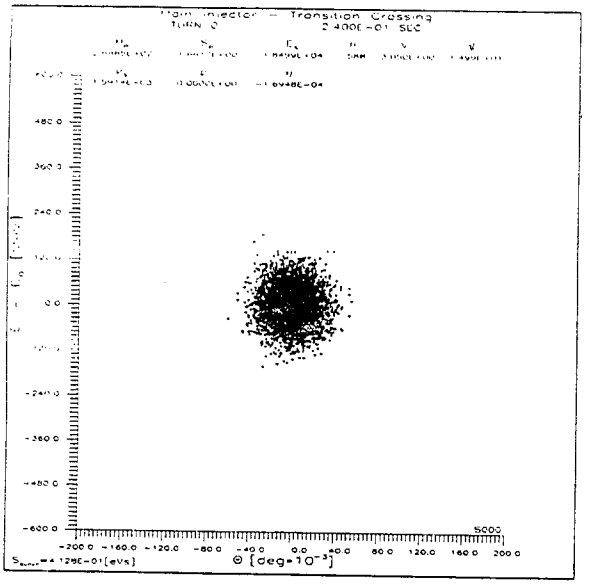
Main Injector – Transition Crossing
TURN 0
2.400E-01 SEC
E − E0 [MeV]
Θ [deg-10^-3]

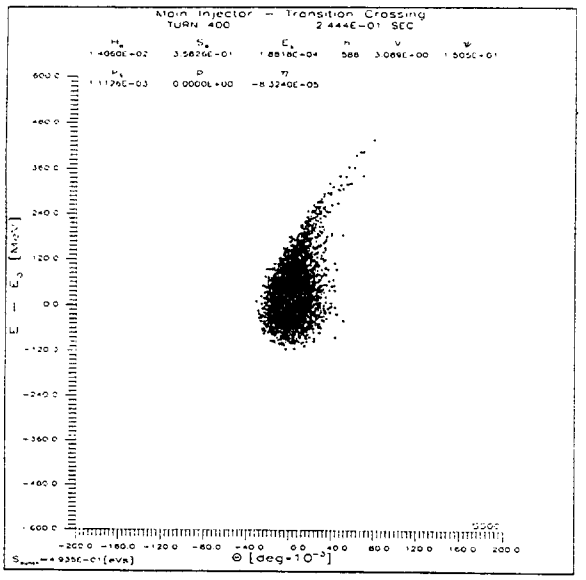
Main Injector – Transition Crossing
TURN 400
2.444E-01 SEC
E − E0 [MeV]
Θ [deg-10^-3]

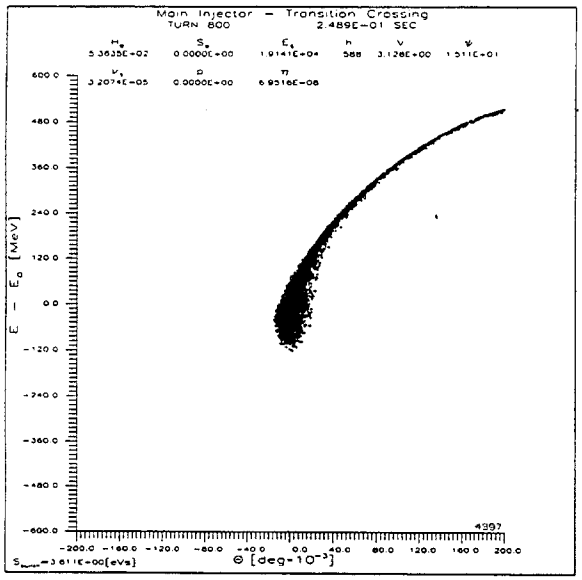
Main Injector – Transition Crossing
TURN 800
2.489E-01 SEC
E − E0 [MeV]
Θ [deg-10^-3]

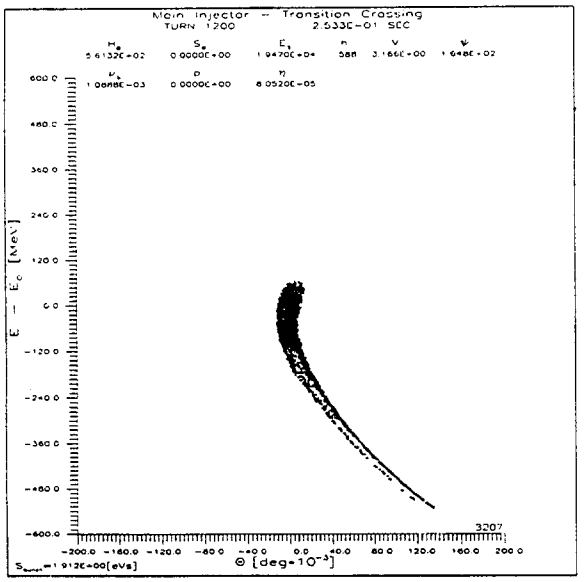
Main Injector – Transition Crossing
TURN 1200
2.533E-01 SEC
E − E0 [MeV]
Θ [deg-10^-3]

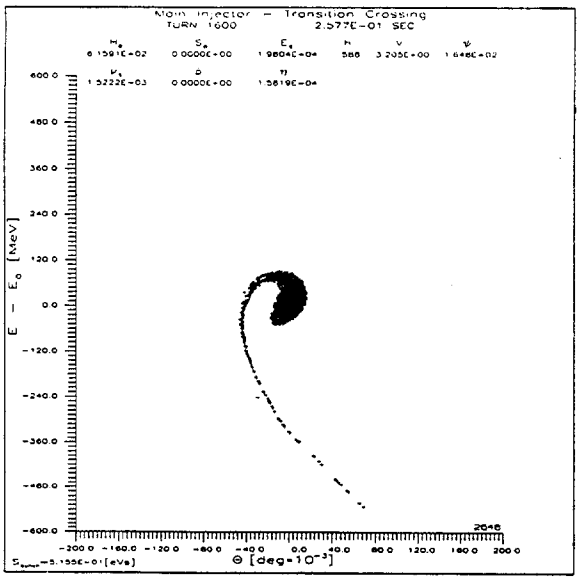
Main Injector – Transition Crossing
TURN 1600
2.577E-01 SEC
E − E0 [MeV]
Θ [deg-10^-3]

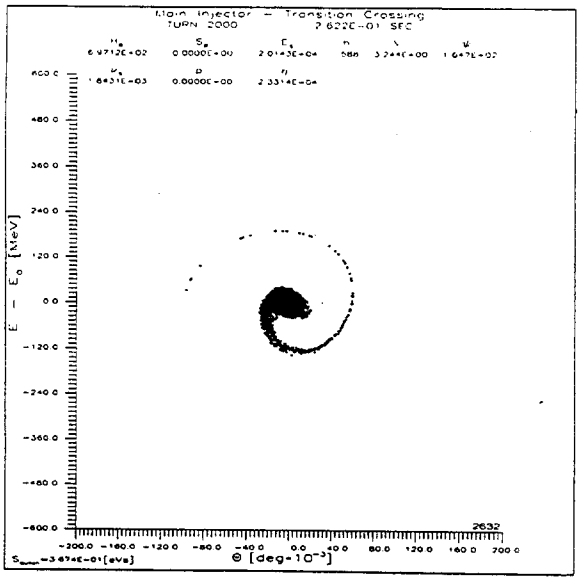
Main Injector – Transition Crossing
TURN 2000
2.622E-01 SEC
E − E0 [MeV]
Θ [deg-10^-3]

Fig. 8

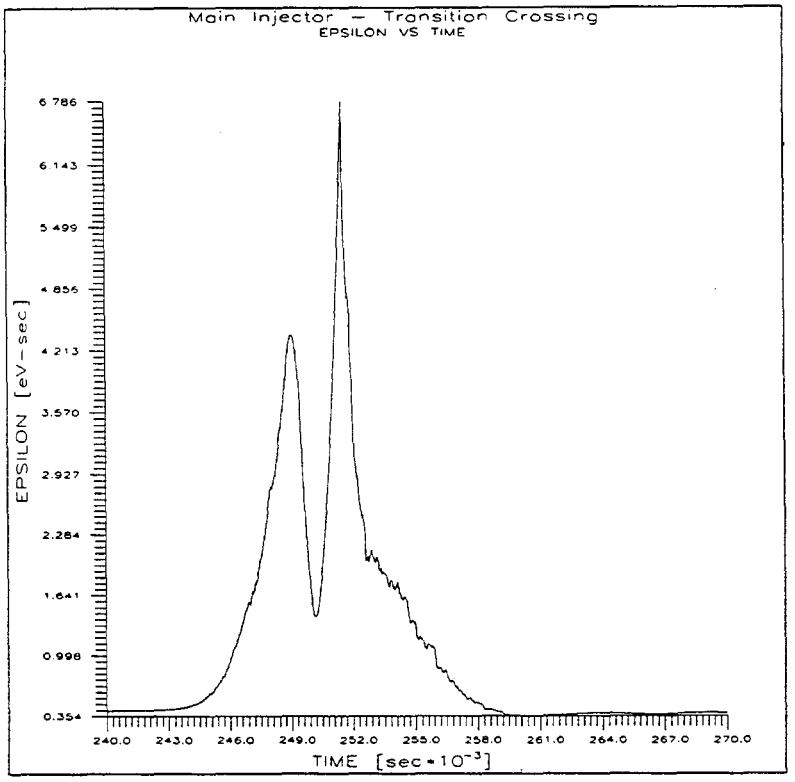
Main Injector – Transition Crossing
EPSILON VS TIME
EPSILON [eV-sec]
6.786
6.143
5.499
4.856
4.213
3.570
2.927
2.284
1.641
0.998
0.354
240.0 243.0 246.0 249.0 252.0 255.0 258.0 261.0 264.0 267.0 270.0
TIME [sec*10^-3]

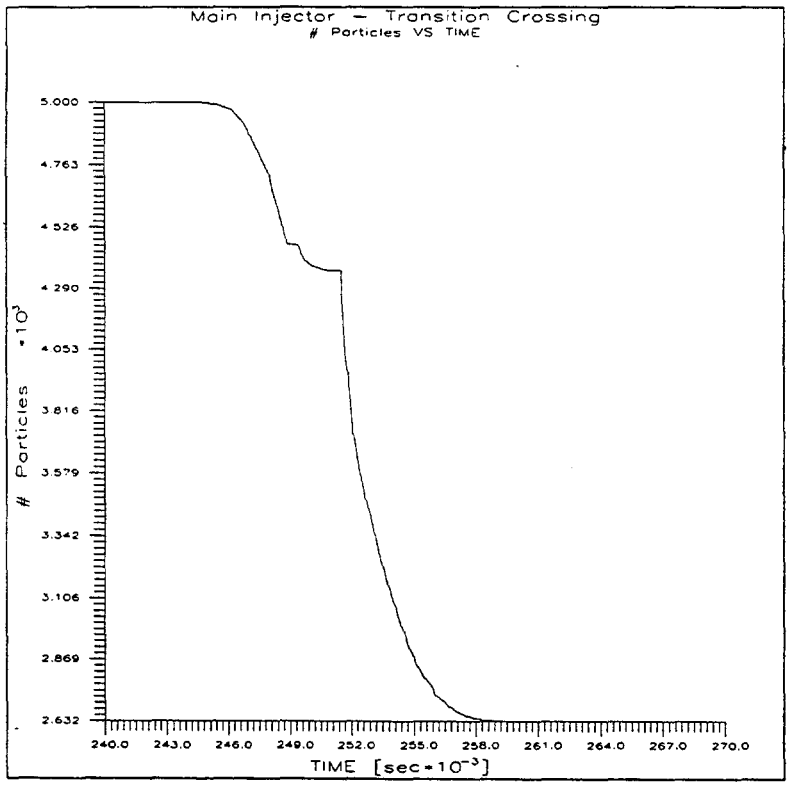
Main Injector – Transition Crossing
Particles VS TIME
Particles *10^3
5.000
4.763
4.526
4.290
4.053
3.816
3.579
3.342
3.106
2.869
2.632
240.0 243.0 246.0 249.0 252.0 255.0 258.0 261.0 264.0 267.0 270.0
TIME [sec*10^-3]

Fig. 9

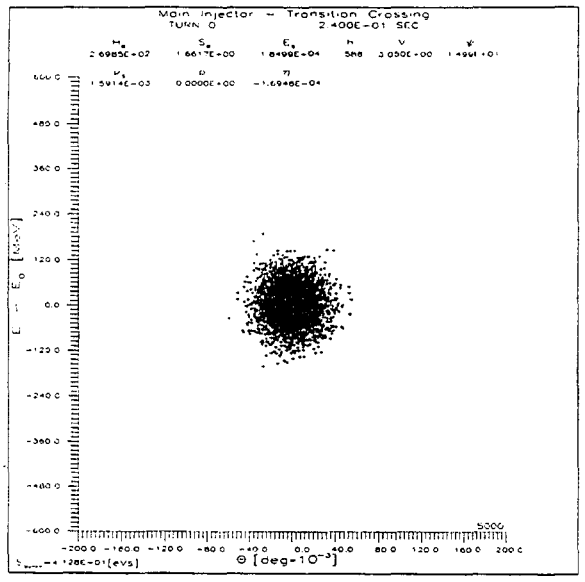
Main Injector - Transition Crossing
TURN 0
2.400E-01 SEC
E - E0 [MeV]
Θ [deg-10^-3]

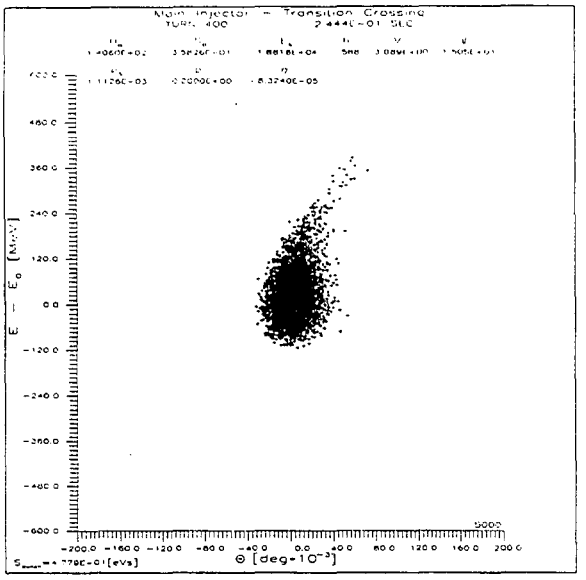
Main Injector - Transition Crossing
TURN 400
2.444E-01 SEC
E - E0 [MeV]
Θ [deg-10^-3]

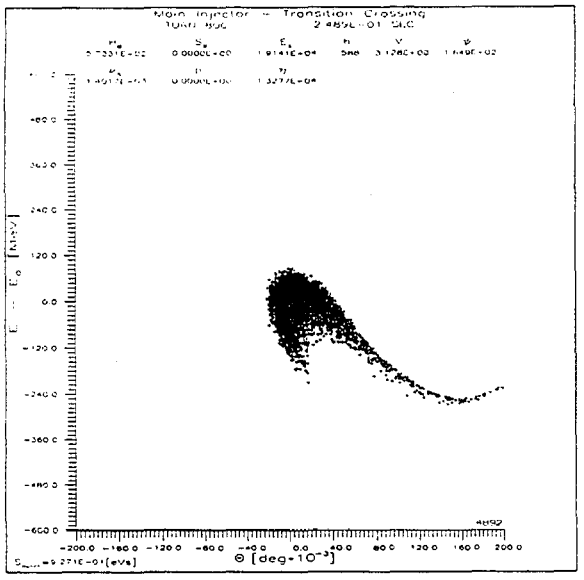
Main Injector - Transition Crossing
TURN 800
2.489E-01 SEC
E - E0 [MeV]
Θ [deg-10^-3]

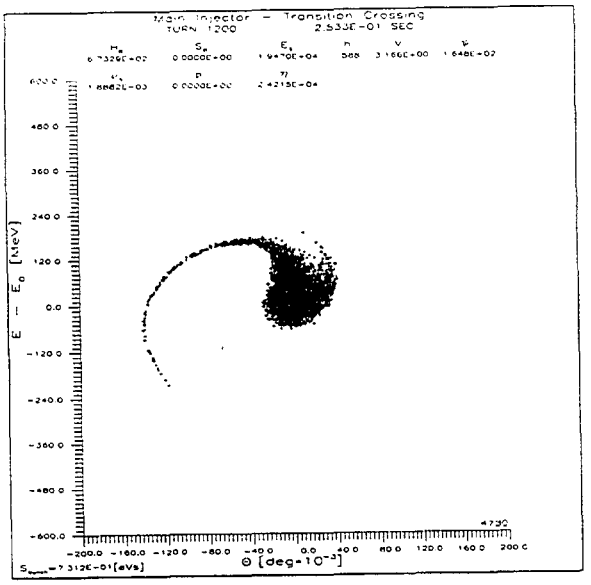
Main Injector - Transition Crossing
TURN 1200
2.533E-01 SEC
E - E0 [MeV]
Θ [deg-10^-3]

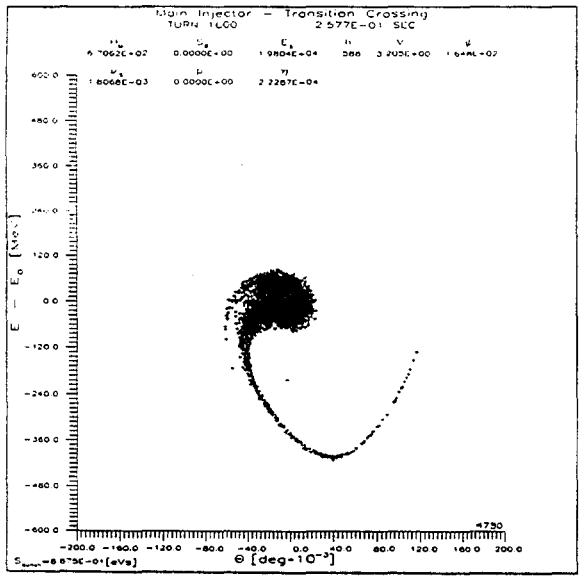
Main Injector - Transition Crossing
TURN 1600
2.577E-01 SEC
E - E0 [MeV]
Θ [deg-10^-3]

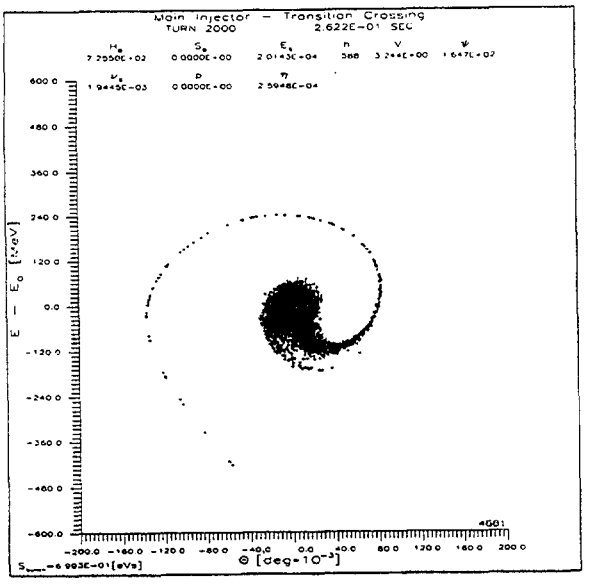
Main Injector - Transition Crossing
TURN 2000
2.622E-01 SEC
E - E0 [MeV]
Θ [deg-10^-3]

Fig. 10

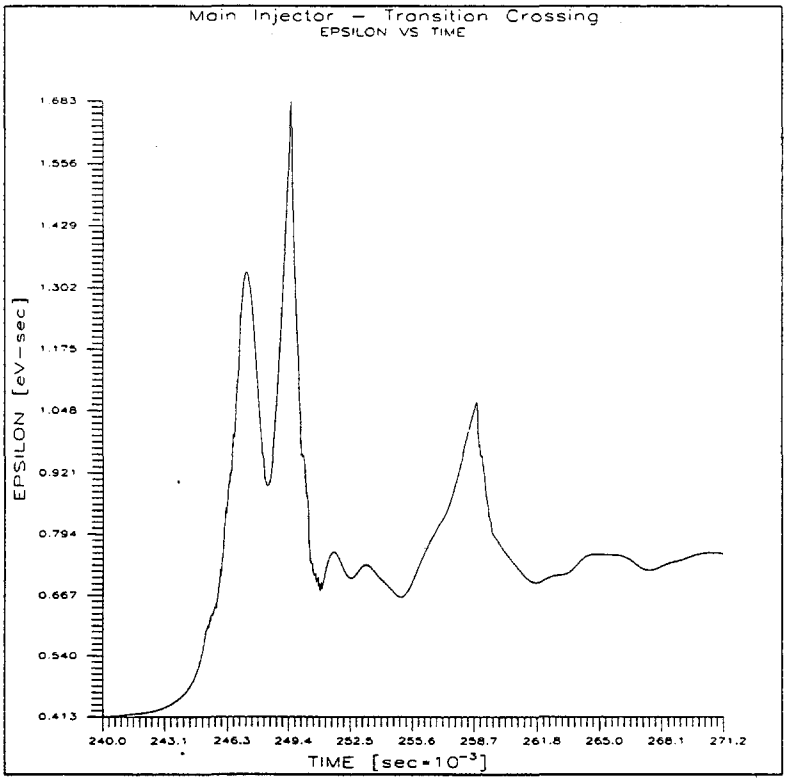
Main Injector – Transition Crossing
EPSILON VS TIME
EPSILON [eV-sec]
1.683
1.556
1.429
1.302
1.175
1.048
0.921
0.794
0.667
0.540
0.413
240.0 243.1 246.3 249.4 252.5 255.6 258.7 261.8 265.0 268.1 271.2
TIME [sec*10^-3]

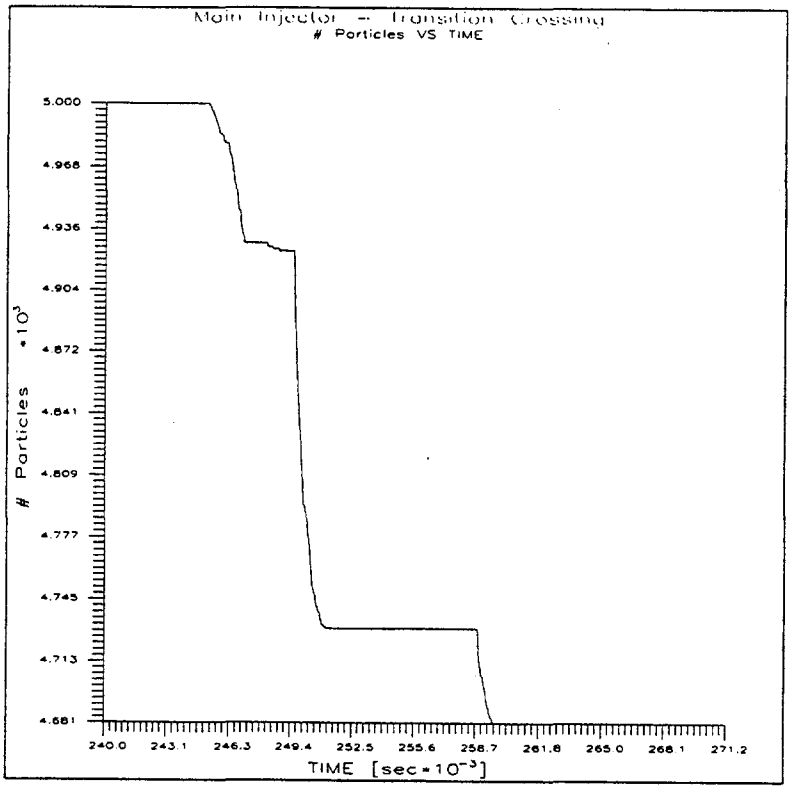
Main Injector – Transition Crossing
Particles VS TIME
Particles *10^3
5.000
4.968
4.936
4.904
4.872
4.841
4.809
4.777
4.745
4.713
4.681
240.0 243.1 246.3 249.4 252.5 255.6 258.7 261.8 265.0 268.1 271.2
TIME [sec*10^-3]

Fig. 11

A

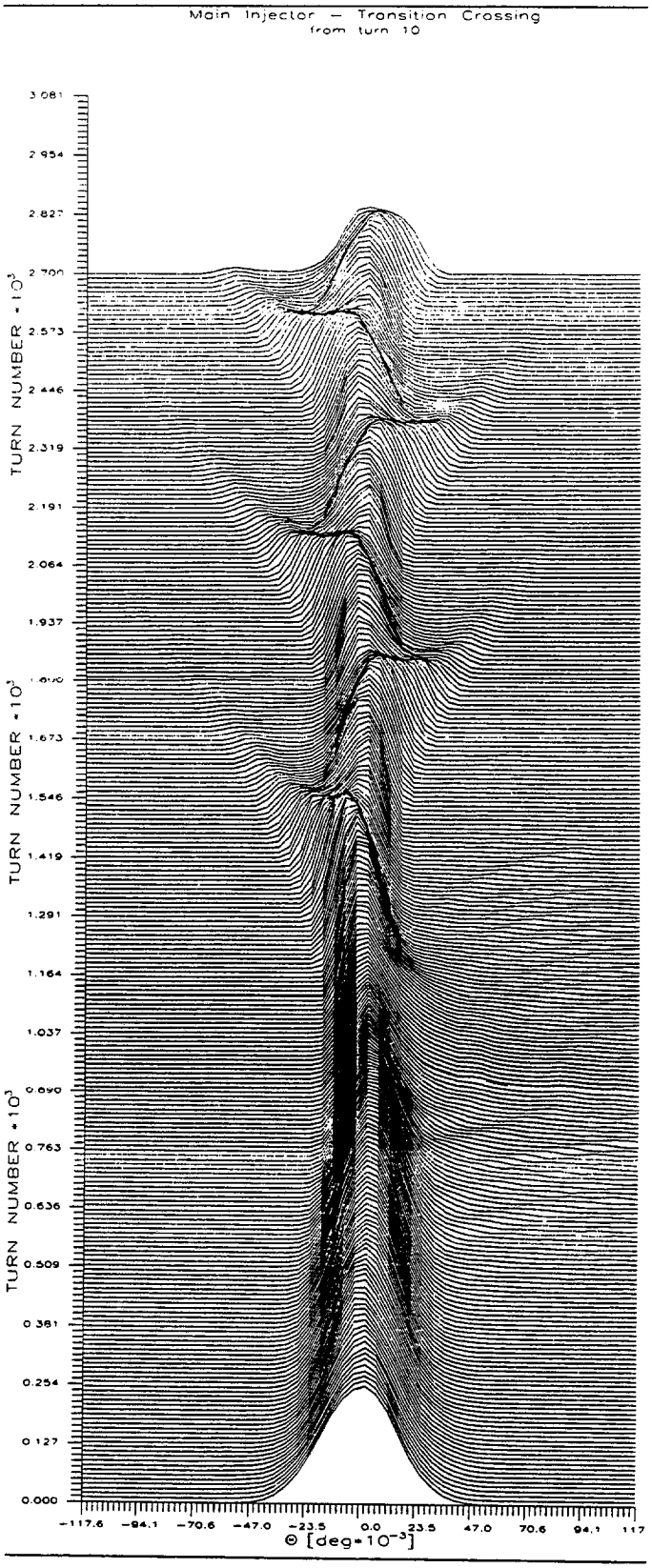
Main Injector – Transition Crossing
from turn 10
TURN NUMBER • 10³
3.081
2.954
2.827
2.700
2.573
2.446
2.319
2.191
2.064
1.937
1.673
1.546
1.419
1.291
1.164
1.037
0.890
0.763
0.636
0.509
0.381
0.254
0.127
0.000
−117.6 −94.1 −70.6 −47.0 −23.5 0.0 23.5 47.0 70.6 94.1 117
Θ [deg•10⁻³]

B

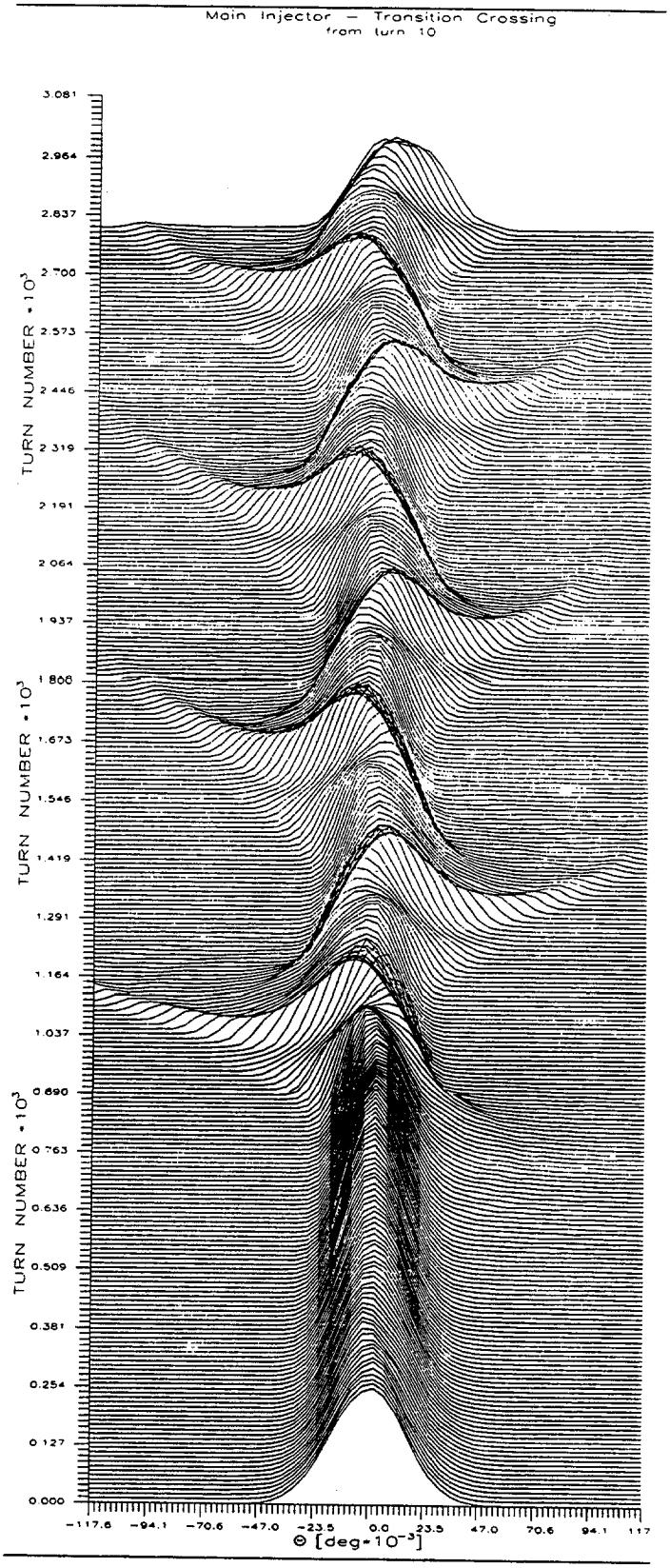
Main Injector – Transition Crossing
from turn 10
TURN NUMBER • 10³
3.081
2.964
2.837
2.700
2.573
2.446
2.319
2.191
2.064
1.937
1.806
1.673
1.546
1.419
1.291
1.164
1.037
0.890
0.763
0.636
0.509
0.381
0.254
0.127
0.000
−117.6 −94.1 −70.6 −47.0 −23.5 0.0 23.5 47.0 70.6 94.1 117
Θ [deg•10⁻³]

Fig. 12

TM-1670

MI-30

SOME ESTIMATION CONCERNING CROSSING TRANSITION OF THE MAIN INJECTOR

King-Yuen Ng

Fermi National Accelerator Laboratory, Batavia, IL 60510, U.S.A.*

(June, 1990)

*Operated by the Universities Research Association, Inc., under contract with the U.S. Department of Energy.

I. INTRODUCTION

We estimate some parameters pertaining to the transition crossing of the Main Injector. These include the nonadiabatic time, bunch length and bunch height at transition, the microwave growth across transition driven by a longitudinal impedance, and the parameters that govern the Umstätter's and the Johnsen's effects.

II. BUNCH LENGTH AND HEIGHT AT TRANSITION

At time T_c before and after transition, the bucket changes so rapidly that the bunch is not able to follow it. We call this region the nonadiabatic region. This characteristic time is given by[1,2]

$$T_c = \left[\left(\frac{\pi \beta_t^2 \gamma_t^4}{h \omega_0^2 \dot{\gamma}_t} \right) \left(\frac{E_0/e}{V_{\rm rf} \cos \phi_0} \right) \right]^{\frac{1}{3}} , \tag{2.1}$$

where

$$\begin{aligned} E_0 &= 0.93827 \text{ GeV, rest energy of proton,} \\ \gamma_t &= 20.4 = \left(1 - \beta_t^2\right)^{-1/2} \text{, transition gamma,} \\ \omega_0 &= 566.78 \text{ kHz, angular revolution frequency,} \\ h &= 588 \text{, rf harmonic number,} \\ V_{\rm rf} &= 2.78 \text{ MV, rf voltage,} \\ \phi_0 &= 37.6^\circ \text{ rf phase,} \end{aligned} \tag{2.2}$$

and

$$\dot{\gamma}_t = \frac{\omega_0 e V_{\rm rf} \sin \phi_0}{2\pi E_0} = 163.1 \text{ sec}^{-1} \tag{2.3}$$

is the rate of change of γ at transition. We find $T_c = 1.96$ ms. If every particle crosses transition at exactly the same time, the evolution of the bunch can be computed easily. At transition, the bunch ellipse in the longitudinal phase space is tilted. The *maximum* rms bunch length (not at zero momentum offset) is given by

$$\sigma_\tau = \frac{2}{3^{5/6}\Gamma(1/3)} \left(\frac{A T_c^2 e V_{\rm rf} \dot{\gamma}_t}{E_0 \beta_t^2 \gamma_t^4} \right)^{\frac{1}{2}} = 0.371 \text{ ns} , \tag{2.4}$$

where $\Gamma(1/3) = 2.678939$ is the gamma function and the bunch area $A = 0.4$ eV-sec has been assumed. The *maximum* rms energy spread is

$$\sigma_E = \frac{\Gamma(1/3)}{3^{2/3}2\pi}\left(\frac{A\beta_t^2\gamma_t^4 E_0}{T_c^2\dot{\gamma}_t}\right)^{\frac{1}{2}} , \tag{2.5}$$

or $\sigma_E/E = 3.45 \times 10^{-3}$. Note that here $6\pi\sigma_E\sigma_\tau$ is not equal to the bunch area A because the ellipse is tilted.

III. MICROWAVE GROWTH

The growth of microwave amplitudes across transition is unavoidable because, for a certain time interval, the frequency-slip parameter $\eta = 1/\gamma_t^2 - 1/\gamma^2$ is too small to provided enough frequency spread for Landau damping. It has been shown by Courant and Synder[1,2] as well as by Herrera[3] that, if one assumes η/E to be a linear function of time in that interval, the invariant of the the longitudinal phase space can be solved analytically in terms of Bessel function and Neumann function of order 2/3. A dispersion relation can be set up and the growth rate can then be solved numerically.[4] If we further assume that Z/n is real and the bunch is gaussian in shape, the problem can be solved approximately resulting in a handy formula.[5] The total growth across transition is $\exp(S_b + S_a)$, where

$$S_{b,a} = \int \mathcal{I}m\,\Delta\Omega dt\Big|_{\mathcal{I}m\,\Delta\Omega>0} \tag{3.1}$$

represent the integrated growth rate $\mathcal{I}m\,\Delta\Omega$ before and after transition. The handy formula gives

$$\frac{S_b}{n} = \frac{S_a}{n} = \frac{F_1\left[eN(Z/n)\gamma_t^2\right]^2}{V_{\rm rf}\sin\phi_0}\frac{(E_0/e)^2\,\sigma_\tau}{(A/e)^3} , \tag{3.2}$$

where N is the number of particles of charge e per bunch, n is the harmonic of the microwave frequency, and $F_1 = 8.735$ is a numerical constant. In the above, σ_τ is the rms time spread of the bunch at time $-t_0$ when stability is lost before transition or at time t_0 when stability is regained after transition. This time t_0 and time spread σ_τ are found to be

$$t_0 = \frac{F_2 eN(Z/n)\gamma_t^4}{\omega_0 V_{\rm rf}\sin\phi_0}\frac{(E_0/e)^2\sigma_\tau}{(A/e)^2} , \tag{3.3}$$

$$\frac{\sigma_\tau}{T_c} = \begin{cases} \dfrac{2}{3^{1/3}\Gamma(1/3)} \left(\dfrac{AeV_{rf}\omega_0 \sin\phi_0}{6\pi E_0^2 \beta_t^2 \gamma_t^4}\right)^{\frac{1}{2}} \left(1 + 0.6859\dfrac{t_0}{T_c}\right) & \dfrac{t_0}{T_c} \ll 1 \ , \\ \left(\dfrac{AeV\omega_0 \sin\phi_0}{6\pi^2 E_0^2 \beta_t^2 \gamma_t^4}\right)^{\frac{1}{2}} \left(\dfrac{t_0}{T_c}\right)^{\frac{1}{4}} & \dfrac{t_0}{T_c} \gtrsim 1 \ . \end{cases} \tag{3.4}$$

Assuming that $(NZ/n) \gtrsim 10$ ohms, we obtain

$$\begin{aligned} t_0 &= 0.0705 \left(N\frac{Z}{n}\right)^{4/3} \text{ ms} \ , \\ \sigma_\tau &= 0.176 \left(N\frac{Z}{n}\right)^{1/3} \text{ ns}, \\ \frac{S_{b,a}}{n} &= 1.44 \times 10^{-7} \left(N\frac{Z}{n}\right)^{7/3} \ , \end{aligned} \tag{3.5}$$

where N is in 10^{10} and Z/n in ohms. An illustration is given in Table I. The growth of the microwave amplitude in the last row was computed by assuming a broad band centered at 1.5 GHz corresponding to $n = 16629$. One has to bear in mind that the actual growth is usually less than indicated because nonlinear effect may come in eventually to suppress the growth rate. The growth of the microwave amplitude will dilute the bunch area and lead to a growth of the bunch area. However, the relation between the two growths is not known.

The longitudinal space-charge force will help stability before transition but help instability after transition. It leads to the shortening of t_0 before transition and lengthening of t_0 after transition. Nevertheless, its contribution will not affect the estimation in Table I by very much.

IV. UMSTÄTTER'S EFFECT

The transverse space-charge force will lower the betatron tune of those particles at the transverse edge of the bunch near the center, and therefore lower the transition γ. These particles will cross transition at a time earlier than the synchronous particle.[6] This effect is called the Umstätter's effect. Roughly, the depression of γ_t is given by

$$2\gamma_t \Delta\gamma_t = -\varepsilon\lambda(0) \ . \tag{4.1}$$

$N\frac{Z}{n}$	10 Ω	20 Ω	30 Ω
t_0	1.52 ms	3.83 ms	6.57 ms
σ_τ	0.380 ns	0.478 ns	0.547 ns
$\frac{S_{b,a}}{n}$	3.11×10^{-5}	1.57×10^{-4}	4.04×10^{-4}
$e^{S_b+S_a}$	2.81	13.5	820

Table I: Microwave growth across transition

where

$$\lambda(0) = \frac{N}{\sqrt{2\pi}\sigma_\tau h\omega_0} \tag{4.2}$$

is the linear particle density at the center of the bunch and

$$\varepsilon = \frac{4hr_pR}{\beta_t^2\gamma_t^3}\left[\frac{1}{a(a+b)} - \frac{\epsilon_1}{h_v^2}\right], \tag{4.3}$$

with a and b the half-width and half-height of the beam, $r_p = 1.535 \times 10^{-18}$ m the classical proton's radius, $R = 528.30$ m the ring radius, $\epsilon_1 = 0.172$ the electrostatic image coefficient corresponding to rectangular 2" by 4" beam pipe, and h_v the half-height of the vacuum chamber. Assuming a normalized transverse emmitance of the beam 20π mm mr and a minimum beta-function 11.6 m, we get $a = b = 6.74$ mm and therefore $\varepsilon = 2.52 \times 10^{-12}$. Using $\sigma_\tau = 0.380$ ns and $N = 5.10 \times 10^{10}$ from Section II, we get for the maximum linear density $\lambda(0) = 16.0 \times 10^{10}$. This leads to a maximum depression of $\Delta\gamma_t = 0.00995$. From Eq. (2.2), the rate of acceleration is $\dot{\gamma}_t = 163.1$. Therefore, some particles at the center of the bunch will cross transition at a time $\Delta T = \Delta\gamma_t/\dot{\gamma}_t = 0.583$ ms earlier than the synchronous particle. Since this time is much less than the adiabatic time $T_c = 1.96$ ms, Umstätter's effect should be negligible.

V. JOHNSEN'S EFFECT

Each particle inside a bunch has momentum slightly different from the syn-

chronous momentum p_0. It travels along a different closed orbit and has a different momentum compaction factor. If the momentum deviation is Δp, its orbit length is given by

$$L = L_0 \left[1 + \alpha_0 \frac{\Delta p}{p_0} \left(1 + \alpha_1 \frac{\Delta p}{p_0} \right) \right] , \tag{5.1}$$

where L_0 is the synchronous orbit length and α_0 is the momentum compaction factor of the synchronous particle. Obviously, this off-momentum particle will have a different γ_t and crosses transition at a time ΔT earlier. It can be shown that ΔT, which is also called the *nonlinear time*, is given by[7]

$$\Delta T \approx \frac{(\alpha_1 + 3/2)\gamma_t}{\dot{\gamma}_t} \left(\frac{\Delta E}{E} \right) , \tag{5.2}$$

where $\Delta E/E$ is approximately equal to the relative height of the bunch if every particle crosses transition at exactly the same time (or $\alpha_1 = -1.5$). From Section II, $\sigma_E/E = 3.45 \times 10^{-3}$ at transition, we have maximum $\Delta E/E \sim 8.45 \times 10^{-3}$. This gives

$$\Delta T|_{\max} \sim 1.057(\alpha_1 + 1.5) \text{ ms} . \tag{5.3}$$

If one assumes a perfect FODO-cell structure of phase advanced φ_c with two sets of sextupoles at, respectively, the F-quads and D-quads canceling a fraction f of the natural chromaticity, α_1 can be derived readily to give[8]

$$\alpha_1 = \frac{1 + s_c/12 - f}{1 - s_c/12} , \tag{5.4}$$

where $s_c = \sin \varphi_c/2$. If the sextupoles are not turned on, $f = 0$. The Main Injector consists of 90°-cells. Therefore $\alpha_1 = 25/23$. Thus, we obtain maximum $\Delta T = 2.7$ ms or maximum $\Delta T/T_c = 1.4$. the growth of bunch area due to Johnsen's effect will be appreciable.[9] On the other hand, if there is a complete cancelation of chromaticity, $f = 1$ and $\alpha_1 = 1/23$. Then, $\Delta T/T_c = 0.84$. The growth in bunch area will be much less. The detail will be discussed elsewhere.

REFERENCES

1. E.D. Courant and H.S. Synder, Annals of Physics **3**, 1 (1958).

2. G.K. Green and E.D. Courant, Hanbuch der Physik, Vol. XLIV, edited by S.

Flügge, p. 218 (1959).

3. J.C. Herrera, Particle Accelerators **3**, 49 (1972).

4. S.Y. Lee and J.M. Wang, IEEE Transaction on Nuclear Science **NS32**, 2323 (1985).

5. K.Y. Ng, Fermilab Report TM-1383, 1986.

6. A. Sørenssen, Particle Accelerators **6**, 141 (1975).

7. K. Johnsen, Proc. of CERN Symposium on High Energy Accelerators and Pion Physics, Geneva, 1956, Vol. 1, p. 106.

8. S. Peggs, Fermilab Internal Report AP Note 90-004, 1990.

9. J. Wei, *Longitudinal Dynamics of the Non-Adiabatic Regime on Alternating-Gradient Synchrotrons*, Thesis, State University of New York at Stony Brook, May 1990.

EXPERIMENTAL STUDY OF THE MAIN RING TRANSITION CROSSING

Ioanis Kourbanis, Keith Meisner, and King-Yuen Ng

Fermi National Accelerator Laboratory, P.O. Box 500, Batavia, IL 60510*

1. Introduction

A number of different experiments were proposed as part of the Fermilab III Instabilities Workshop in order to study the transition crossing in the Main Ring. Due to time limitations and operational restrictions only one of the experiments was actually performed. The results and analysis presented here are preliminary. We used an injection mismatch to deliberately blow up the longitudinal emittance in the MR 29 cycles, and measured the increase in bunch emittance and the particle loss through transition as functions of the initial bunch emittance. The experiment was repeated for different intensities (2, 4 booster turns) and for different rf voltages around transition. The purpose of the experiment was to distinguish the mechanism that is responsible for emittance growth and particle loss across transition.

Two mechanisms can lead to the growth of bunch emittance and particle loss across transition. The first one is nonlinearity, which is due to the nonlinear terms in the expansion of the momentum compaction factor or the orbit length as a power series in the momentum spread. With these nonlinear terms, particles of different momenta cross transition at different times. The spread in crossing time is called the *nonlinear time*,[1] which is proportional to the momentum spread and depends on the Johnsen's nonlinear coefficient[2] in the momentum compaction factor. After those particles with larger momenta than the synchronous particle cross transition and before the rf phase is switched, they are outside the accelerating bucket and drift away forming a tail in the longitudinal phase space. Those particles with lower momenta than the synchronous particle also develop into a tail after the rf phase is switched because they cross transition much later. These tails can lead to emittance growth and particle loss. The second mechanism is microwave instability because the

*Operated by the Universities Research Association, Inc., under contract with the U.S. Department of Energy.

phase-slip parameter $\eta = 1/\gamma_T^2 - 1/\gamma^2$ is vanishingly small near transition and therefore cannot provide enough Landau damping to stabilize the growth of the microwave amplitudes. However, these two mechanisms are very different.

If nonlinear effect dominates at transition crossing, we expect the effect to increase with initial bunch emittance ϵ_L and the rf voltage $V_{\rm rf}$ at transition. This is because a bigger ϵ_L or a bigger $V_{\rm rf}$ at constant $\dot{\gamma}_T$ implies larger momentum spread, which enhances the time difference between the fastest particle and the synchronous particle in crossing transition. In fact, according to Ref. 1, we have

$$\frac{\Delta\epsilon_L}{\epsilon_L} \propto \epsilon_L^{\frac{1}{2}} V_{\rm rf}^{\frac{2}{3}} \ . \tag{1}$$

On the other hand, if microwave instability dominates at transition crossing, we expect its effect to decrease with initial bunch emittance and rf voltage at transition. This is because both larger ϵ_L and $V_{\rm rf}$ imply larger momentum spread near transition, which in turn provides more Landau damping for stabilization. We obtain from Refs. 3 and 4 that

$$\frac{\Delta\epsilon_L}{\epsilon_L} \propto \epsilon_L^{-3} V_{\rm rf}^{-1} \ . \tag{2}$$

When the bunch emittance is sufficiently small, the dominant effect should be microwave instability. However, when the bunch emittance is sufficiently large, nonlinearity should dominate. As a result, we expect to see the variations of emittance growth and particle loss as functions of initial bunch emittance to follow curves as indicated in Fig. 1. Also microwave effect is intensity dependent while nonlinear effect is not.

2. Preparation and setup

We found that the most effective way to increase the emittance at injection in the MR was through phase mismatch. We started with 0° phase error and tuned the rf voltage at injection so as to minimize the bunch length oscillations measured by the BLMON, a bunch-length monitor which is not well-calibrated. A picture of BLMON, rf voltage RFSUMT, rf phase PHIS, and radial beam position RPOSP at injection after the tuning is shown on Fig. 2. The absence of synchrotron oscillations before transition was checked by taking mountain range pictures at 0.32 sec into the cycle

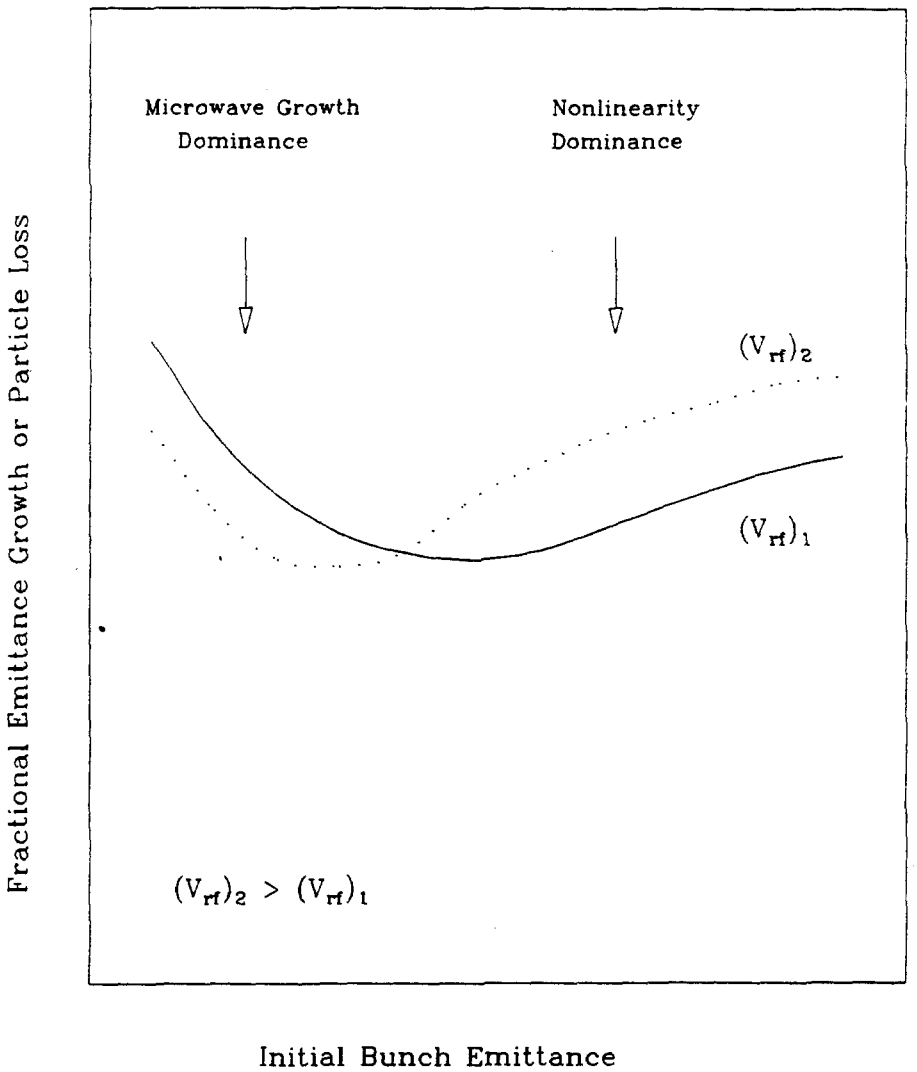

Figure 1

Schematic plot of fractional growth of bunch emittance and particle loss across transition versus initial bunch emittance at different transition rf voltages.

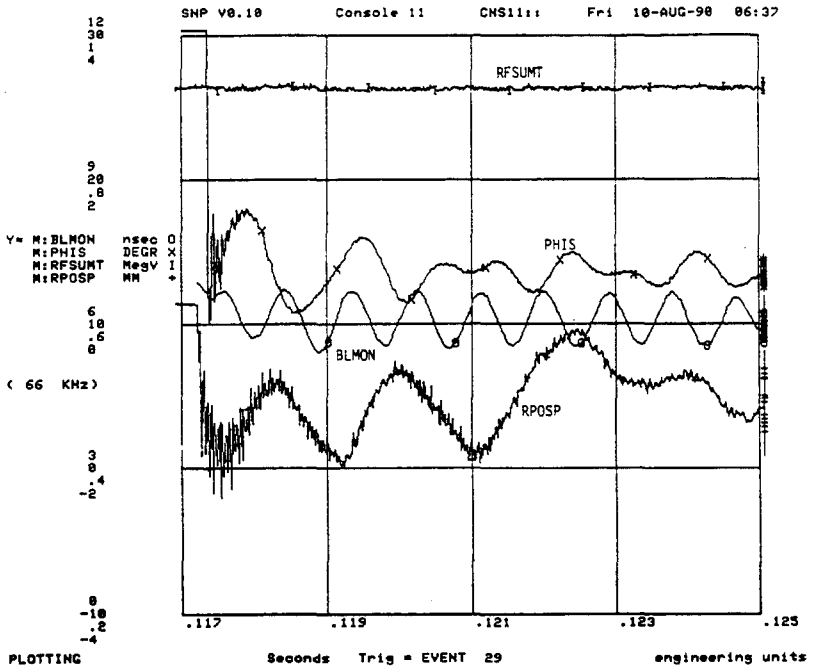

Figure 2

Typical bunch length oscillations, rf voltage synchronous phase and radial position at injection in a 29 cycle (4 booster turns no phase error).

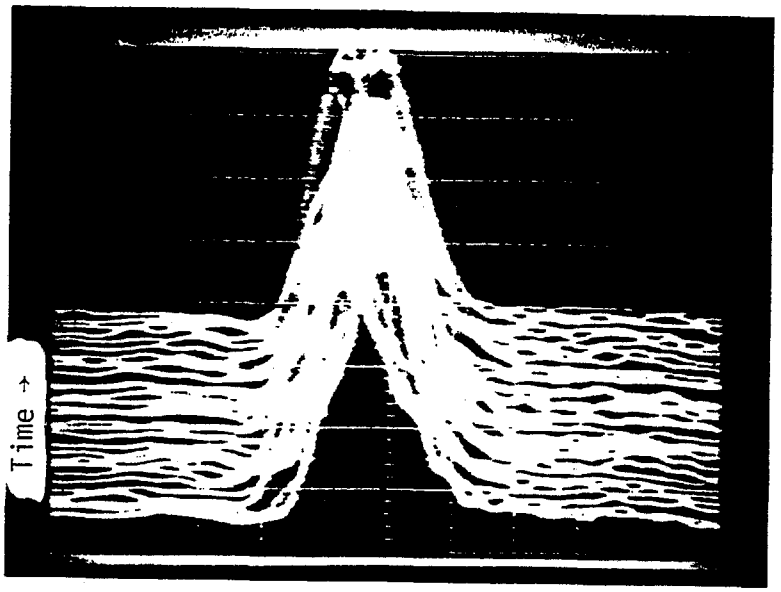

Figure 3

Typical mountain range picture before transition (30 traces 10 turns or 0.2 msec apart).

i.e., 60 ms before transition. Fig. 3 shows a typical mountain range picture taken during our studies. It shows 30 traces 10 turns (0.2 ms) apart.

The longitudinal emittance was calculated by measuring the bunch length (from mountain range pictures), the rf voltage and the rf phase at two places before transition (60, 30 ms) and at two places after transition (60, 150 ms). Figure 4 shows a picture of two beam profiles before and two after transition for 2 booster cycles and 150° phase mismatch. The particle loss through transition was measured with the intensity monitor IBEAMM.

Figure 5 shows a typical picture of the rf voltage RFSUMT, the beam intensity IBEAMM, the radial position RPOSP and the phase angle PHIS in the time interval we took our measurements. An injection phase error was then introduced and the measurements were repeated. The phase error varied between 0° and 40°. As mentioned before, measurements were taken at two different intensities, i.e., for 2, 4 booster turns corresponding to 0.9×10^{10} and 1.6×10^{10} ppb respectively.

Efforts had also been made to blow up the bunch emittance by introducing a rf-voltage mismatch, but the blowup was not as efficient as the phase mismatch. The bunch spreader had also been used. In this case, the output bunch shape became so irregular that the bunch length was unable to be defined.

3. Results and Conclusions

The results of our experiment are summarized in Figs. 6 and 7, where we have plotted the growth in bunch area and particle loss through transition as functions of the initial emittance for two different intensities and two transition voltages. The errors indicate mainly the uncertainty in estimating the the bunch length.

Figures 6(a), 6(b), 7(a), and 7(b) show clearly that both the fractional growth in emittance and particle loss increase with V_{rf} at transition. As a result, we conclude that nonlinear effect dominates the Main Ring at transition.

We see from Figs. 6(b) and 7(b) that particle loss also increases with the initial bunch emittance ϵ_L as expected in a nonlinear-effect dominance. However, a closer look at Figs. 6(a) and 7(a) reveals that the fractional growth in emittance stays roughly constant with the initial bunch emittance at $V_{rf} = 2.0$ MV for 4-booster-turn

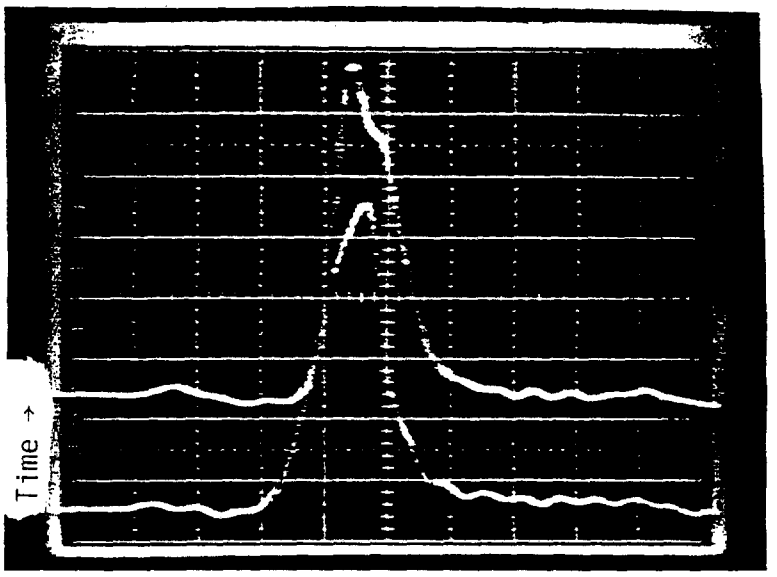

Figure 4(a)

Beam profile 60 ms and 30 ms before transition for 2 booster cycles and 150° phase mismatch.

Figure 4(b)

Beam profile 60 ms and 150 ms after transition for 2 booster cycles and 150° phase mismatch.

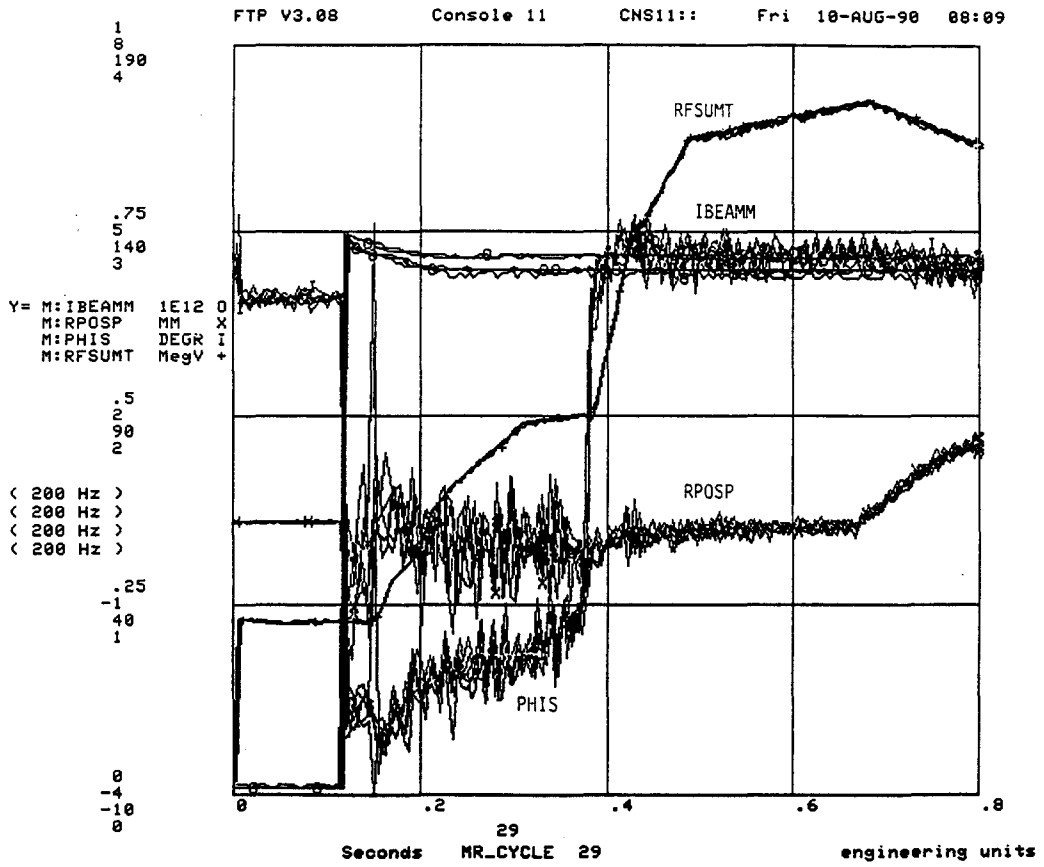

Figure 5

Typical picture of the beam intensity IBEAMM, rf voltage RFSUMT, radial position RPOSP, and synchronous phase PHIS versus time in a 29 cycle during our measurements.

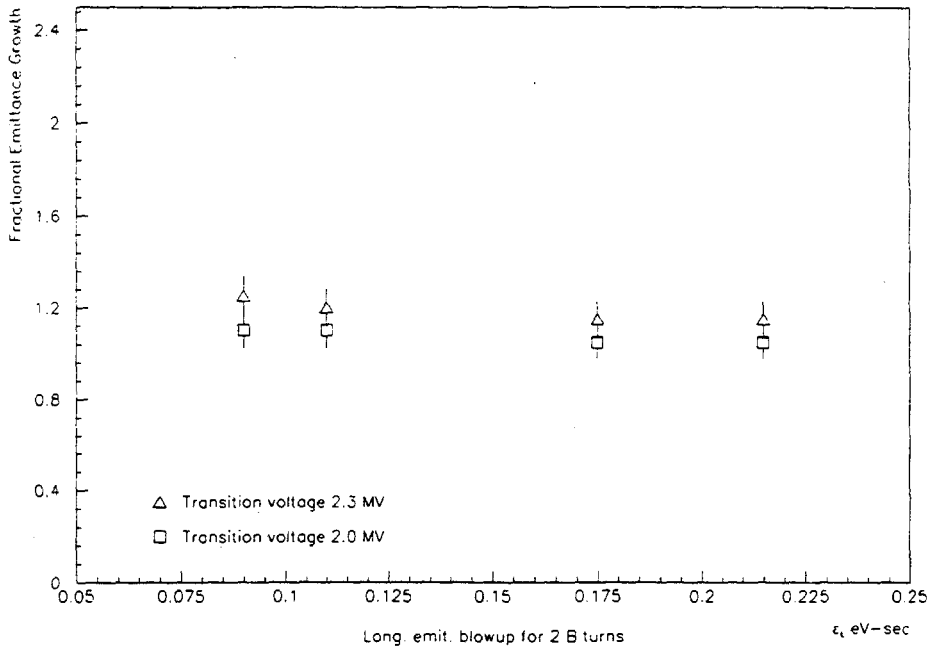

Figure 6(a)

Change in bunch area as a function of initial bunch emittance for 2 booster turns.

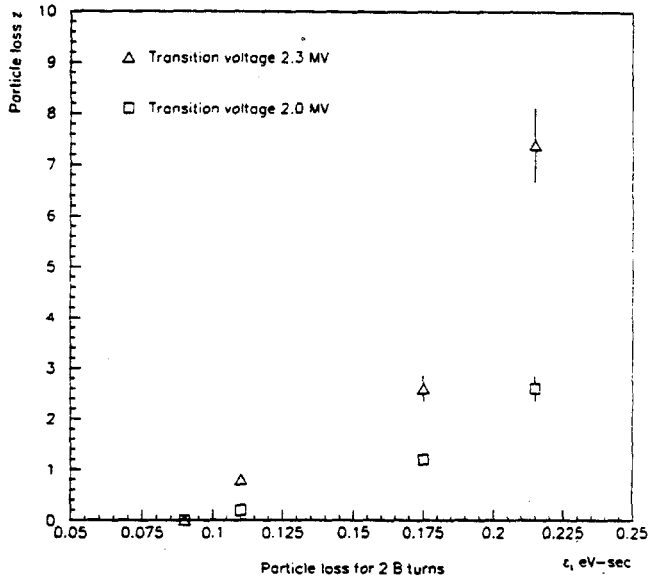

Figure 6(b)

Particle loss through transition versus initial bunch emittance for 2 booster turns.

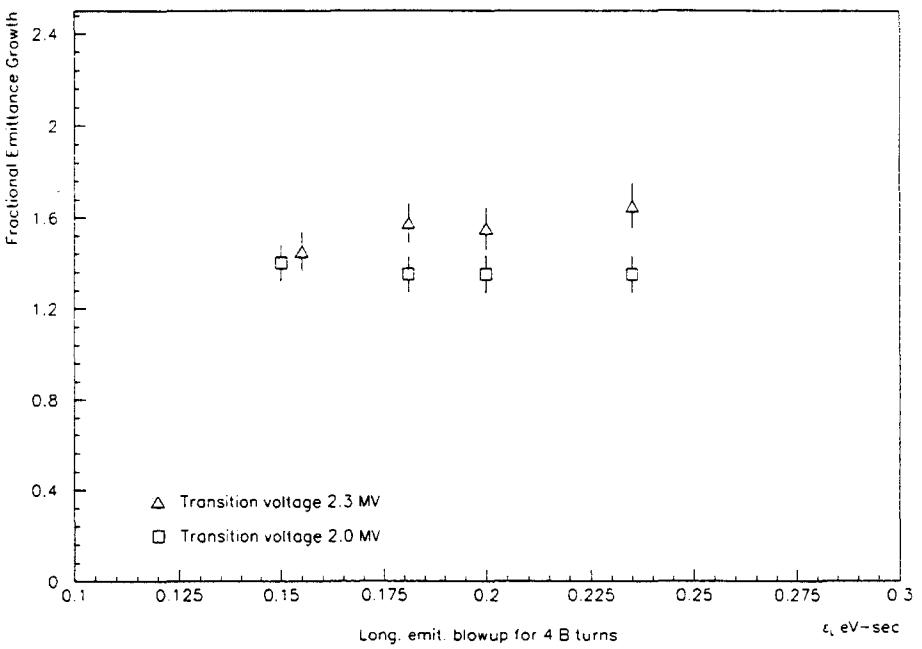

Figure 7(a)

Change in bunch area as a function of initial bunch emittance for 4 booster turns.

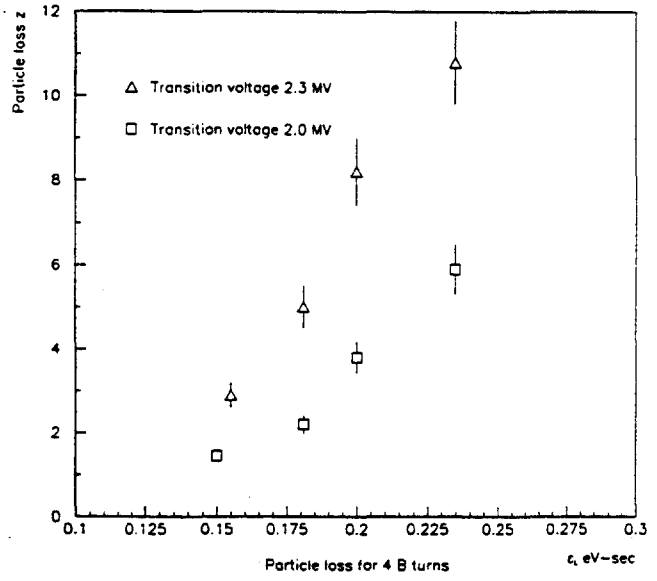

Figure 7(b)

Particle loss through transition versus initial bunch emittance for 4 booster turns.

injection, and even decreases slightly with ϵ_L at both V_{rf} = 2.0 MV and 2.3 MV for 2-booster-turn injection. The 4-booster-turn results are understandable. A $\Delta\epsilon_L/\epsilon_L$ constant with ϵ_L at V_{rf} = 2.0 MV implies that there is some contribution from microwave instability. At V_{rf} = 2.3 MV, the bunch becomes much more microwave stable and therefore $\Delta\epsilon_L/\epsilon_L$ increases with ϵ_L due to nonlinear effect in the region 0.15 eV-sec $< \epsilon_L <$ 0.23 eV-sec. In the same ϵ_L region and at the same V_{rf}, a 2-booster-turn (lower intensity) bunch should be much less affected by microwave growth than a 4-booster-turn bunch. We should expect more nonlinearity dominance so that the fractional growth of emittance should increase more rapidly with ϵ_L than the 4-booster-turn results. However, as depicted in Fig. 6(a) the fractional growth of emittance decreased slightly with ϵ_L instead. This contradiction may arise from errors in the measurement.

Quantitatively, we find that for 2-turn fixed intensity (0.9×10^{10} ppb) the growth of bunch area was about 10% and did not change much when the voltage around transition varied from from 2.0 to 2.3 MV. For the larger intensity (1.6×10^{10} ppb), the bunch area growths were about 40% and 60%, respectively, for the two rf voltages. The particle loss followed an exponential increase and grew must faster for larger transition voltage. Numerical fittings gives

$$\% \text{ Particle Loss} = \begin{cases} 0.0139e^{24.7\epsilon_L} & \text{2 turn at 2.0 MV ,} \\ 0.0765e^{20.9\epsilon_L} & \text{2 turn at 2.3 MV ,} \\ 0.178e^{14.3\epsilon_L} & \text{4 turn at 2.0 MV ,} \\ 0.482e^{13.1\epsilon_L} & \text{4 turn at 2.3 MV .} \end{cases} \tag{3}$$

REFERENCES

1. J. Wei, *Transition Crossing in the Main Injector*, these proceedings.

2. K. Johnsen, *Effects on Nonlinearities on Phase Transition*, CERN, Symposium on High Energy Accelerators, Geneva, 1956, Vol. 1, p.106.

3. S.Y. Lee and J.M. Wang, IEEE Tranc. Nucl. Sc. **NS 32**, 2323 (1985).

4. K.Y. Ng, *Some Estimation Concerning Crossing Transition of the Main Injector*, FNAL-TM1670, 1990, also these proceedings.

MAIN RING TRANSITION CROSSING SIMULATIONS

Ioanis Kourbanis and King-Yuen Ng

Fermi National Accelerator Laboratory, P.O. Box 500, Batavia, IL 60510*

I. INTRODUCTION

We used ESME[1] to simulate transition crossing in the Main Ring (MR). For the simulations, we followed the MR 29 cycle used currently for $\bar{p}$ production with a flat top of 120 GeV. In Sect. II, some inputs are discussed. In Sect. III, we present simulations with space charge turned off so that the effect of nonlinearity can be studied independently. When space charge is turned on in Sect. IV, we are faced with the problem of statistical errors due to binning, an analysis of which is given in the Appendices. Finally in Sects. V and VI, the results of simulations with space charge are presented and compared with the experimental measurements.

II. SOME INPUTS

1. Rf voltage and acceleration

The typical rf high voltage curve in Fig. 1 was reproduced as accurately as possible by breaking it down into many segments. The rf phase was chosen automatically by following the acceleration curve in Fig. 1.

2. Initial bunch area and number per bunch

Since the longitudinal emittance (bunch area) at injection in the MR depends strongly on the intensity of the beam, i.e., the number of booster-turn injection from the linac, actual measurements were made and the results are compiled in Table I. The numbers in this table were used as input to ESME for the initial bunch emittance and the number of particles per bunch in order to simulate the performance of the MR as closely as possible.

*Operated by the Universities Research Association, Inc., under contract with the U.S. Department of Energy.

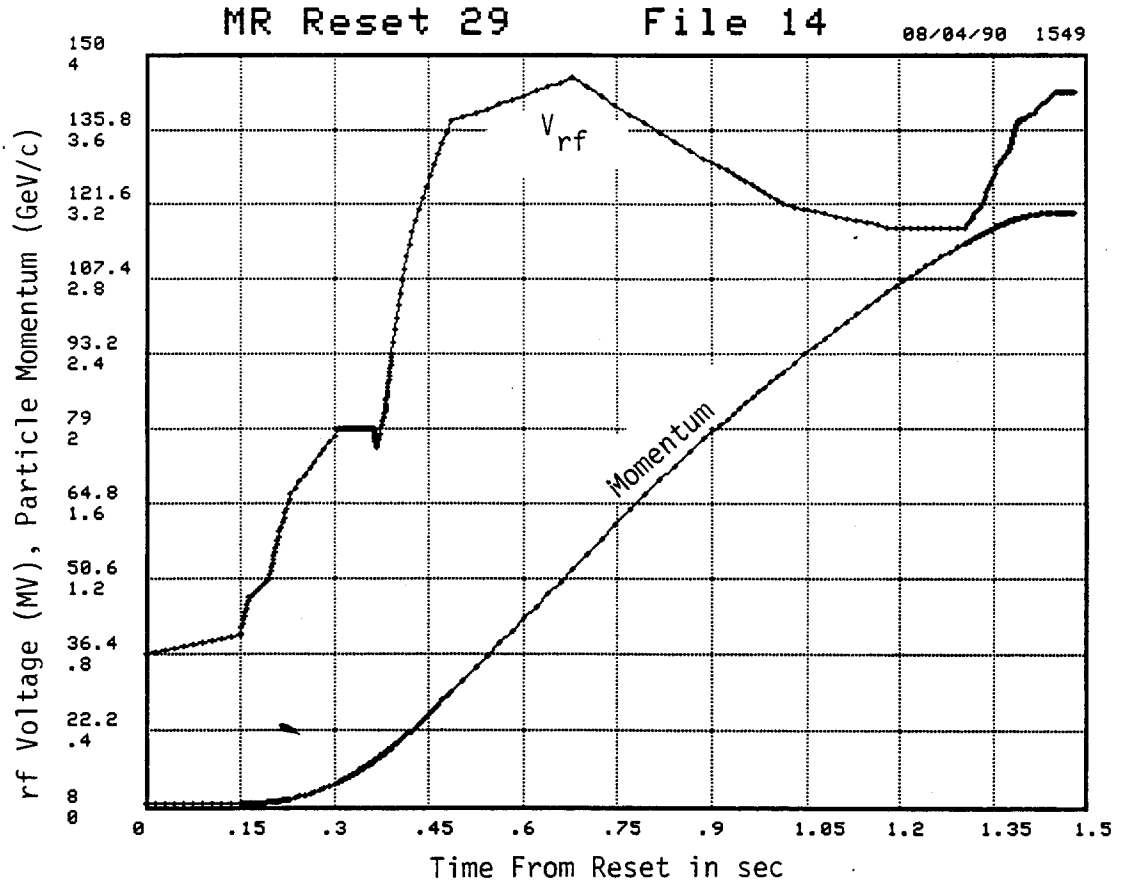

Fig. 1. RF Voltage and Momentum as a function of time in a 29-MR cycle.

No. of Booster Turns	Bunch Area ϵ_L (eV-s)	No. Particle per Bunch ($\times 10^{10}$)
2	0.09	0.9
3	0.10	1.3
4	0.12	1.6
5	0.16	1.8

Table I: Bunch area and number per bunch for different booster cycles.

3. Nonlinear phase-slip

The phase-slip parameter η is defined as

$$\eta = \alpha_p - \frac{1}{\gamma^2} , \tag{2.1}$$

where the momentum compaction factor α_p is not a constant. At momentum p, it can be expanded about the synchronous momentum p_0 as

$$\alpha_p(p) = \alpha_0^E + \alpha_1^E \delta + \alpha_2^E \delta^2 + \cdots , \tag{2.2}$$

where

$$\delta = \frac{p - p_0}{p_0} . \tag{2.3}$$

Here,

$$\gamma_T = \frac{1}{\sqrt{\alpha_0}} \tag{2.4}$$

is the transition gamma of the synchronous particle, and α_i^E with $i = 1, 2, \cdots$ are called the nonlinear coefficients of the momentum compaction factor. In these simulations, only the lowest nonlinear coefficient α_1^E is included. The α_i^E defined in Eq. (2.2) (the same in ESME) are different from the nonlinear coefficients α_i^J in the power-series expansion of orbit length defined originally by Johnsen.[2] In fact, the lowest- and first-order coefficients† are related by

$$\alpha_0^E = \alpha_0^J \equiv \alpha_0 ,$$

† Actually α_1^J is called α_2 in Johnsen's paper.

$$\alpha_1^E = \alpha_0(1 + 2\alpha_1^J - \alpha_0) \ . \tag{2.5}$$

Without turning on any sextupoles to correct for the natural chromaticity, $\alpha_1^J \approx 1$. For the MR, $\alpha_0 = 0.002844$ corresponding to $\gamma_T = 18.75$. In the actual MR 29 cycle, natural chromaticity is mostly corrected and $\alpha_1^J \approx 0$. Thus $\alpha_1^E \approx \alpha_0$. In our simulations, we took $\alpha_1^E = 3.0 \times 10^{-3}$.

4. Space charge

The longitudinal space charge can be included in ESME by a longitudinal space-charge impedance

$$\frac{Z_{sc}}{n} = i\frac{Z_0 g}{2\beta\gamma^2} \ , \tag{2.6}$$

where $Z_0 = 377\ \Omega$ is the free-space impedance and the geometric factor g is

$$g = 1 + 2\ln\frac{b}{a} \tag{2.7}$$

with b and a denoting, respectively, the radius of the beam pipe and the radius of the beam. In the simulations with space charge, $g = 6.5$ was used.

The transverse space-charge force will lower the betatron tune and therefore the transition γ of those particles near the axial center of the bunch by a larger amount than those particles at the transverse edge. Thus, particles near the center will cross transition at an earlier time than those at the edge. This effect, known as the Umstätter's effect,[3] is very similar to the Johnsen's nonlinear effect,[2] with the exception that it is intensity dependent. Following the estimation performed in Ref. 4, assuming a transverse beam half-width and half-height of 5 mm, a γ_T depression of $\Delta\gamma_T \sim 0.025$ is obtained. With $\dot{\gamma} \sim 100$/sec, some particles at the center of the bunch will cross transition at a time $\Delta T = \Delta\gamma_T/\dot{\gamma}_T \sim 0.25$ ms earlier. Since this time is much less than the nonadiabatic time $T_c = 2.97$ ms for the MR and Umstätter's effect is not presently incorporated in ESME, transverse space charge has not been included in our simulations.

III. SIMULATIONS WITHOUT SPACE CHARGE

The simulation of the MR 29 cycle was first performed with space charge turned off and with $\alpha_1^E = 3.0 \times 10^{-3}$. No other impedances were imposed. The effect of

transition crossing is therefore intensity independent and only the effect of nonlinearity is important. By nonlinearity, we mean a nonzero dynamic nonlinear coefficient α_1^J and a nonzero (actually 1.5) kinematic coefficient in Eq. (3.1) below, which imply that particles with different momenta cross transition at different times. The spread in crossing time is called the *nonlinear time*,[5] and is defined as

$$T_{\rm NL} = \left(\alpha_1^J + \frac{3}{2} - \frac{\alpha_0}{2}\right) \frac{\gamma_T}{\dot{\gamma}_T} \frac{\Delta p}{p_0} , \tag{3.1}$$

where $\dot{\gamma}_T$ is the rate of change of γ at transition and $\Delta p/p_0$ is the fractional half-spread of momentum.

We performed the simulations with five thousand macro-particles per bunch at different initial bunch emittances. No particle loss was observed across transition when the initial bunch emittance was below $\epsilon_L = 0.18$ eV-sec, which corresponded to 5 booster-turn injection. We started to see a loss of 1.5% when the initial bunch emittance reached $\epsilon_L = 0.24$ eV-sec. The growth in bunch area as a function of initial bunch emittance is shown in Fig. 2(a) and the particle loss at transition as a function of initial emittance is shown in Fig. 2(b). For pure nonlinear effect,[6] the fractional increase in bunch emittance is proportional to the square root of the initial bunch emittance, or

$$\frac{\Delta \epsilon_L}{\epsilon_L} \propto \sqrt{\epsilon_L} . \tag{3.2}$$

We see that the results in Fig. 2(a) agree with such a dependency. We also see from Fig. 2(b) that the number of particles lost across transition increases rapidly with the initial bunch emittance. This is a typical consequence of the nonlinear effect, because a bigger ϵ_L implies a larger momentum spread in the beam and therefore a bigger nonlinear time.

IV. PROBLEMS ASSOCIATED WITH SPACE-CHARGE SIMULATION

The actual performance of the MR was simulated. As a result, the emittance and particles per bunch in Table I was followed with space charge turned on.

The first thing observed was a blowup of bunch emittance and a loss of particles even before transition. For example, for 5 booster-turn injection, the bunch emittance

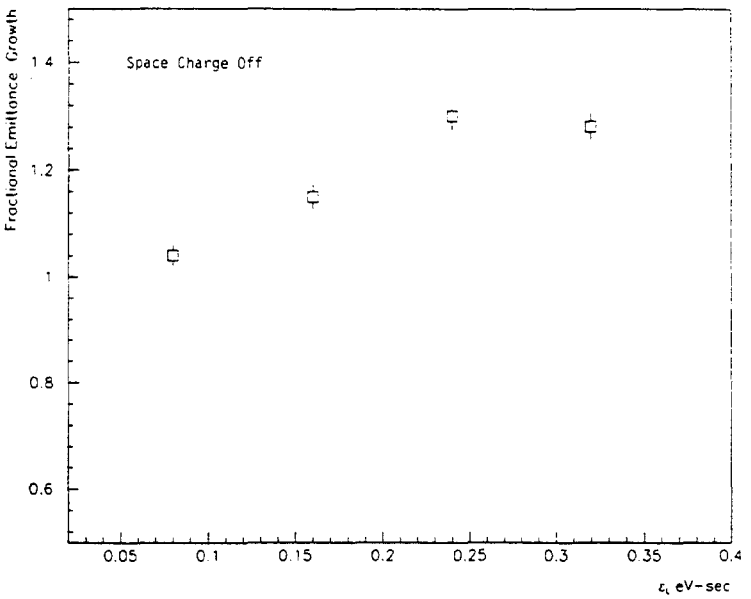

Fig. 2(a). Change in bunch area as a function of initial bunch emittance without space charge.

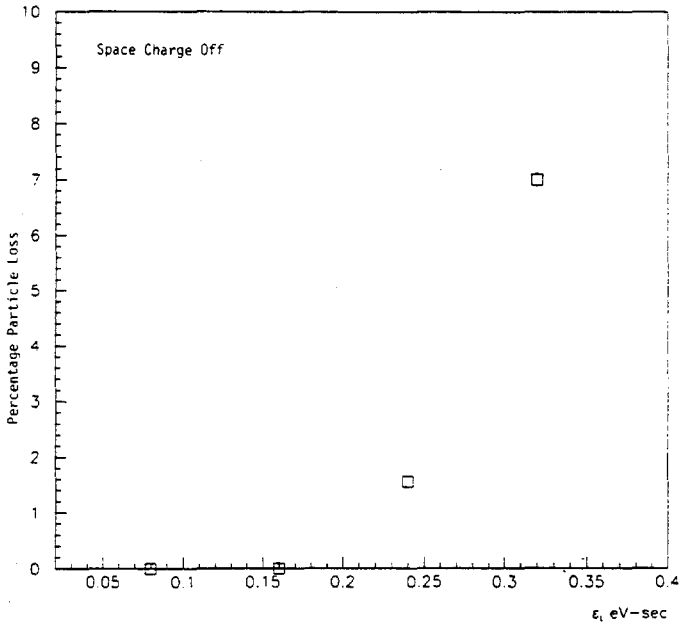

Fig. 2(b). Particle loss through transition versus initial bunch emittance without space charge.

grew by a factor of about three from 0.164 eV-sec to 0.483 eV-sec as shown in Fig. 3(a), accompanied by a particle loss of 7.7% before transition in the simulation as shown in Fig. 3(b). The total particle loss was 20.5%. However, the bunch emittance did not grow further across transition, in contradiction to Eq. (3.2) if nonlinearity were the dominating effect. Closer study of the simulation revealed that the growth had been limited by the bucket area which shrunk to a minimum of 0.49 eV-sec only after transition. As a result, we saw a big particle loss instead. Note that bucket area is the actual area of the bucket, whereas bunch emittance is defined here as 6π multiplied by the product of the rms bunch length and rms energy spread of the bunch. In this simulation, $N_t = 2000$ macro-particles were tracked, $N_b = 512$ bins were used for a rf wavelength, and $\alpha_1^E = 1.0 \times 10^{-3}$ was assumed.

The growth of bunch area and particle loss before transition were in fact unphysical. There are two possible reasons for this artifact. They are the unmatched bunch shape and the incorrect binning.

1. Unmatched bunch shape

In ESME, we populate a bunch according to a certain form of distribution and a certain bunch emittance to fit the rf bucket *without* the consideration of space charge. As space charge is turned on in the tracking, the rf potential will be altered. The initial bunch will no longer fit the space-charge modified bucket. It tumbles inside the bucket and results in a growth of bunch emittance. If the bunch is big enough to start with, the space-charge loaded bucket may not be big enough to hold it, and particle loss will occur.

There have been many different proposals and ideas of how to eliminate these artificial effects due to the sudden turn on of space charge. The best suggestion, of course, is to turn on space charge adiabatically (increasing it in many turns). Then the bunch emittance must be conserved. However, this option is not available in ESME at the moment. Another method is to start with a smaller emittance and hope that the emittance would blowup to the desired value before transition after turning on space charge suddenly. This method is pretty difficult, because it is hard to know what emittance to start with.

Fortunately, the mismatch is not big. If we assume an rms bunch length of $\sigma_\phi =$

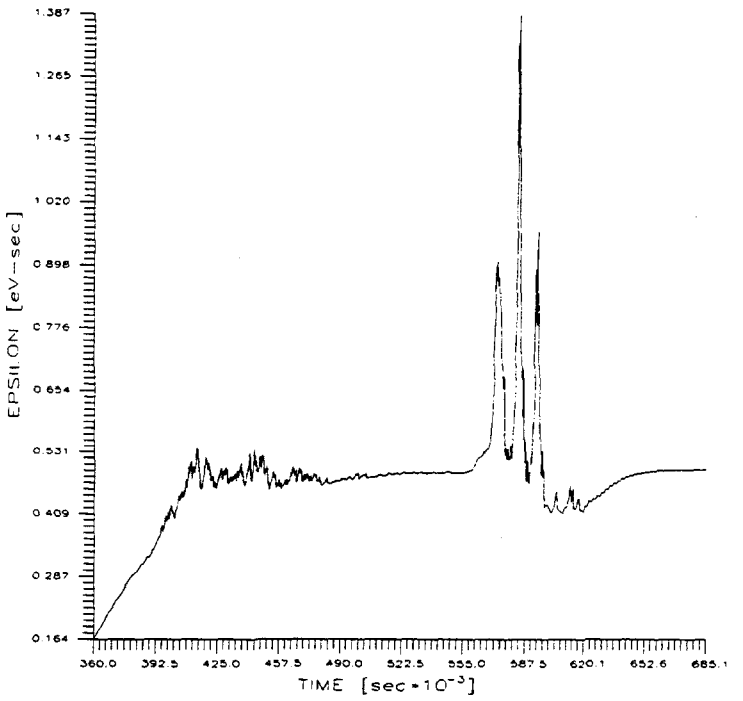

(a)

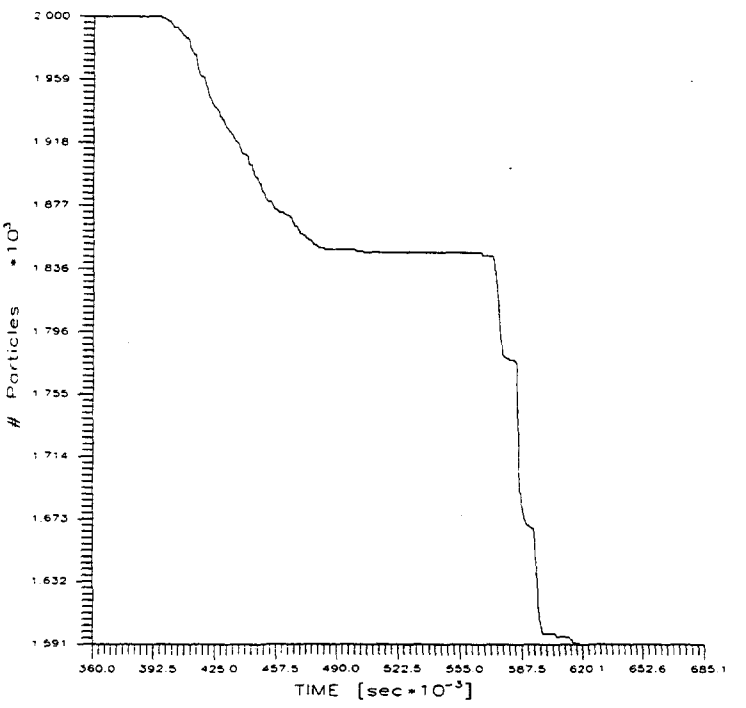

(b)

Fig. 3. Simulation with space charge for 5-booster turns with $N_t = 2000$, $N_b = 512$, MSC = 1, $\alpha_1^E = 1.0 \times 10^{-3}$. (a) Longitudinal emittance versus time. (b) Percentage particle loss versus time.

$\pi/9$ rf rad, for a 5-turn beam intensity of $N_0 = 1.8 \times 10^{10}$ per bunch, the maximum space-charge potential per turn is only

$$E_{sc} = e^2 h^2 \omega_0 \frac{gZ_0}{2\beta\gamma^2} \frac{N_0}{\sqrt{2\pi}} \frac{e^{-1/2}}{\sigma_\phi^2} = \begin{cases} 28.8 \text{ keV} & \text{at injection } \gamma = 9.5 \text{ ,} \\ 7.45 \text{ keV} & \text{at transition } \gamma = 18.75 \text{ ,} \end{cases} \tag{4.1}$$

where $h = 1113$ is the rf harmonic and $\omega_0/2\pi \sim 47.7$ kHz is the revolution frequency. A Gaussian bunch has been assumed. This amounts to only $\sim 3\%$ ($\sim 0.7\%$) of a 1 MV rf.

2. Incorrect binning

In ESME, after each turn, the voltage seen by a particle is computed by convoluting the bunch spectrum with the coupling impedance. To obtain the bunch spectrum, the rf wavelength is divided into N_b equal bins and a fast Fourier transform is performed. As is shown in Appendix A, the statistical rms error in the space-charge voltage is

$$\Delta E_{sc} = e^2 h^2 \omega_0 \frac{gZ_0}{2\beta\gamma^2} \frac{N_0}{2\pi\sqrt{6}} \sqrt{\frac{N_b^3}{N_t}} \ . \tag{4.2}$$

This "cubic rule" was first derived by Wei.[5] It is clear that a small bin number N_b is crucial in reducing the error of computation. However, we do not want to sacrifice the high-frequency details of the simulations. With a beam pipe radius of 3.5 cm, we need at least 61.7 waves in a rf wavelength in order to cover up to the first propagating TM wave. In a fast Fourier transform of N_b bins, we can only obtain up to $N_b/2$ waves because the other $N_b/2$ higher frequency components are just a repetition of the lower frequency components. For this reason, the smallest number of bins used can only be $N_b = 128$. If we track $N_t = 5000$ macro-particles, the fractional error per turn is still 67%. Further increase in the number of macro-particles increases the computer time by very much. Nevertheless, as shown in Fig. 4(a) and (b), the fractional growth in bunch emittance before transition has drastically reduced to 1.1% with no particle loss.

In ESME, we can introduce space-charge MSC times per particle revolution by changing the input parameter MSC. This can also help in reducing the space-charge statistical error by a factor of $\sqrt{\text{MSC}}$ if the errors in successive applications of space charge are random. The analysis is given in Appendix B. We find that this is indeed

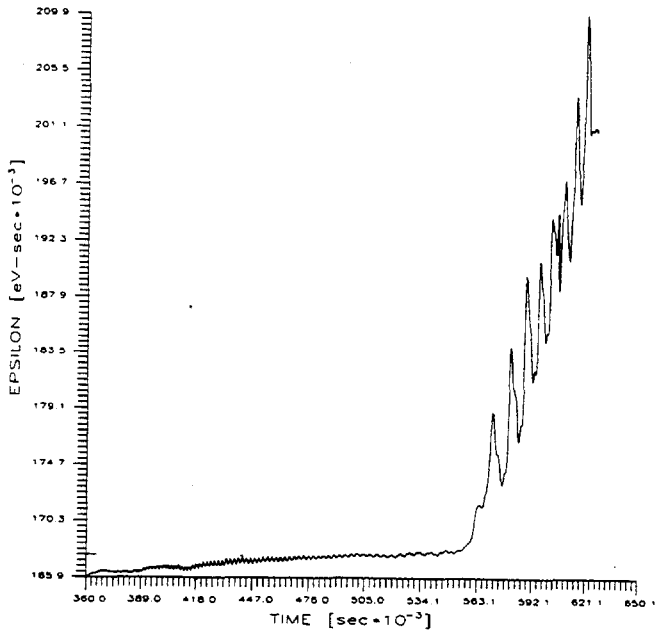

(a)

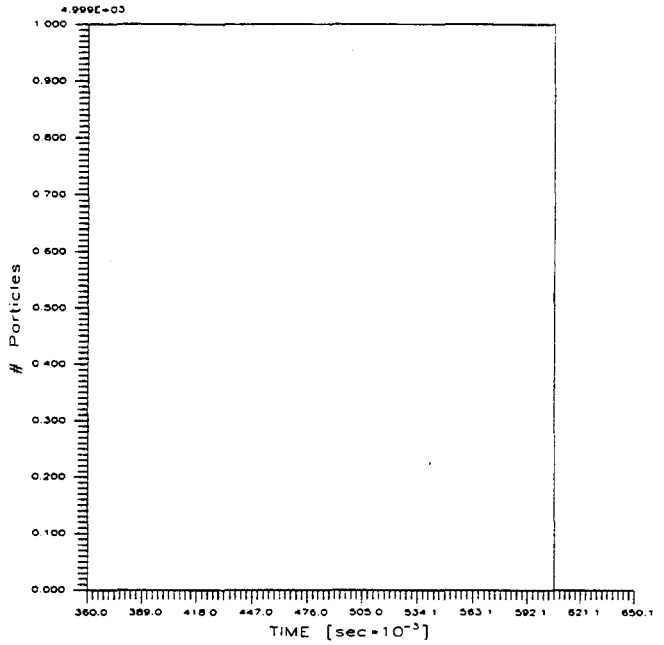

(b)

Fig. 4. Simulation with space charge for 5-booster turns with $N_t = 5000$, $N_b = 128$, MSC = 1, $\alpha_1^E = 3.0 \times 10^{-3}$. (a) Longitudinal emittance versus time. (b) Percentage particle loss versus time.

the case for a larger number of bins. For example, the tracking results with $N_b = 256$ and MSC = 10 are very similar to the results with $N_b = 128$ and MSC = 1. In both cases, $N_t = 5000$. However, changing MSC from 10 to 50 in the $N_b = 256$ case does not improve the result by very much. This is because the redistribution of particles in the bins is not big enough when the application of space-charge is too frequent, and the errors of successive applications are no longer random. This is especially true when the bin number is small. For example, with $N_b = 128$, the fractional growth of bunch emittance before transition is 0.3% when $N_t = 40000$ and MSC = 1. However, we see the a larger growth of 0.83% instead when $N_t = 5000$ and MSC = 10. The results of the latter simulation are shown in Fig. 5(a) and (b). For $N_t = 5000$ and $N_b = 128$, we find from Figs. 4 and 5 that the improvement in growth before transition is minimal when we increase MSC from 1 to 10. An analysis of the randomness of error is presented in Appendix C.

V. RESULTS OF SIMULATIONS WITH SPACE CHARGE

These simulations were all performed with $N_t = 5000$, $N_b = 128$, MSC = 10, and $\alpha_1^E = 3.0 \times 10^{-3}$. We preferred MSC = 10 because this would lead to a smoother application of the space-charge force, although it would not help much in the reduction of statistical errors. The result for the change in bunch emittance through transition as a function of initial bunch emittance is shown in Figs. 6. Note that in the simulations with space charge, a different value of initial bunch emittance corresponds to a different intensity according to Table 1. Comparing Figs. 2(a) and 6, we can see the extra growth of bunch emittance due to space-charge mismatch, although the effect is not big. The data in Fig. 6 tend to have the $\sqrt{\epsilon_L}$ behavior, although different points correspond to different bunch intensities. We do not see any particle loss across transition because the largest initial bunch emittance was only $\epsilon_L = 0.16$ eV-sec corresponding to the 5-turn intensity. When space charge is turned off in Fig. 2(b), we also see no particle loss at and below this initial bunch emittance. We may conclude that microwave growth due to space charge was small in the simulations and the dominating mechanism is nonlinear effect.

A simulation was also performed with $\alpha_1^J = -3/2$ or $\alpha_1^E = -5.6 \times 10^{-3}$ and initial bunch emittance 0.16 eV-sec. This implies that the nonlinear time in Eq. (3.1) vanishes. The only contributions to transition crossing are space charge and higher-

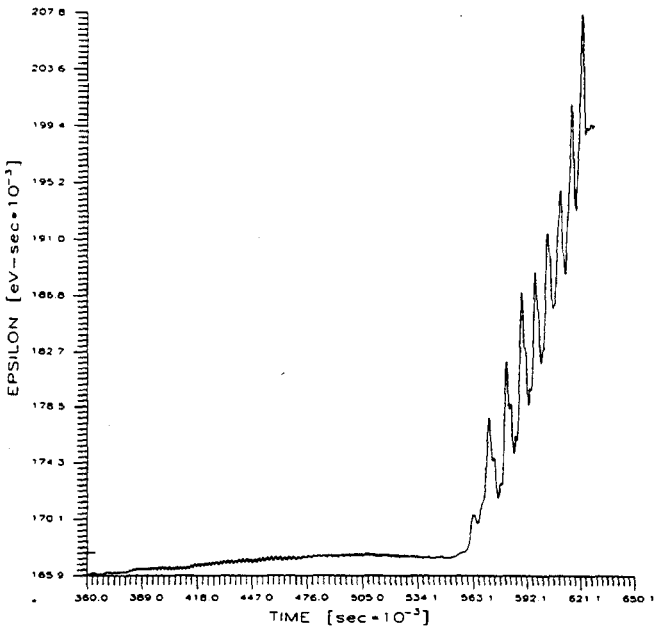

(a)

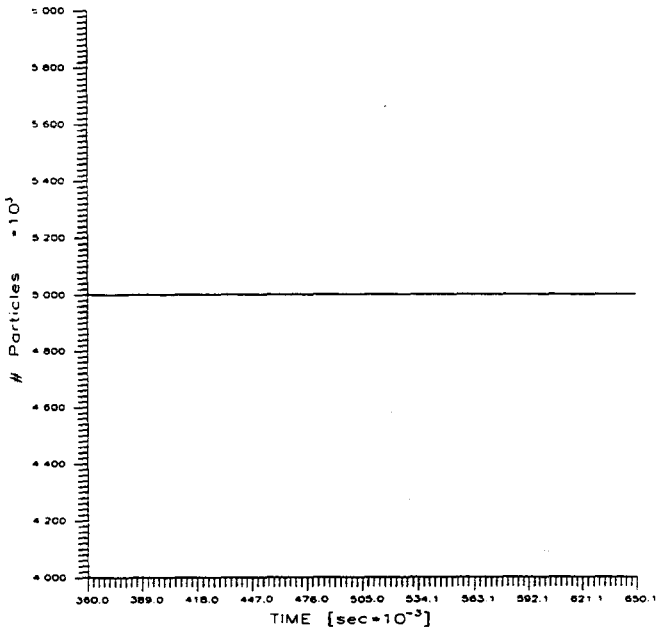

(b)

Fig. 5. Simulation with space charge for 5-booster turns with $N_t = 5000$, $N_b = 128$, MSC = 10, $\alpha_1^E = 3.0 \times 10^{-3}$. (a) Longitudinal emittance versus time. (b) Percentage particle loss versus time.

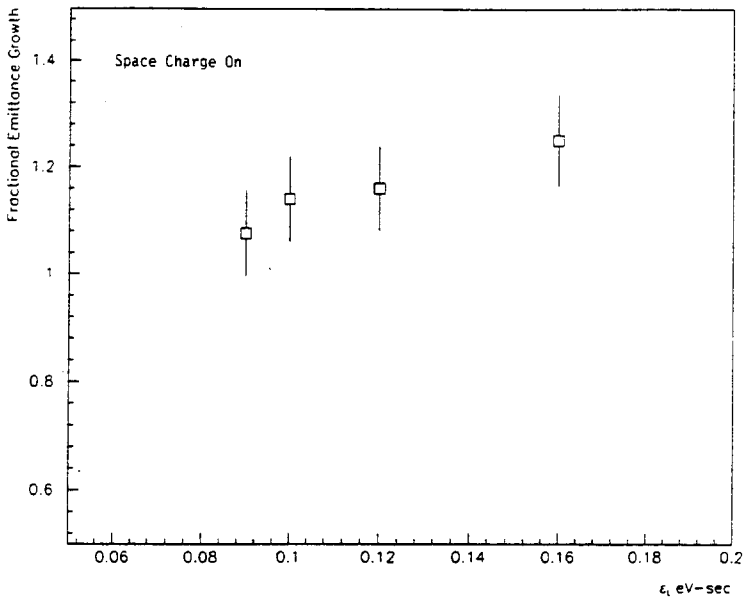

Fig. 6. Change in bunch area as a function of initial bunch emittance with space charge.

order nonlinearity. The fractional growth across transition was found to be 6%. On the other hand, we see from Fig. 2(a) that the growth was 15.5% if space charge was turned off but $\alpha_1^E = 3.0 \times 10^{-3}$ was retained. This gives another indication that nonlinearity dominates over space charge.

VI. COMPARISION WITH EXPERIMENT

The simulation results for emittance growth across transition agree in general with the values observed in reality.[7] However, particle losses were observed at 2 turn when the initial emittance was larger than 0.11 eV-sec. The disagreement may arise from the fact that the effect of the MR impedance other than space charge had not been included in the simulations. The effective impedance per harmonic of the space charge at transition is about 3.5 Ω according to Eq. (2.6). Although we do not know accurately the impedance per harmonic of the MR, we believe that it is at least 10 Ω. Of course, in the actual performance of the MR, there can also be other contributions such as noises, mismatch, etc, which had not been included in the simulations. As a result, we do not consider the above disagreement between simulations and experimental measurements an actual discrepancy.

APPENDIX A. STATISTICAL ERROR DUE TO BINNING

At rf position ϕ, a particle receives an energy gain due to space charge per turn

$$E_{sc} = e^2 h^2 \omega_0 \frac{gZ_0}{2\beta\gamma^2} \left.\frac{\partial\lambda}{\partial\phi}\right|_{\phi} , \tag{A.1}$$

where λ is the linear number density of the bunch per unit rf radian. The rf wavelength is divided equally into N_b bins. Let n_i be the number of macro-particles in the ith bin at some turn. Then the bunch density there is

$$\lambda_i = \frac{n_i}{\Delta\phi} \frac{N_0}{N_t} , \tag{A.2}$$

where

$$\Delta\phi = \frac{2\pi}{N_b} \tag{A.3}$$

is the bin size in rf radian. The last factor in Eq. (A.2) scales N_t, the number of macro-particles tracked, to N_0, the actual number of particles in the bunch.

We first evaluate E_{sc} for particles in the ith bin in the time domain. Following essentially Ref. 5, we obtain

$$\left.\frac{\partial\lambda}{\partial\phi}\right|_i = \frac{n_i - n_{i-1}}{(\Delta\phi)^2} \frac{N_0}{N_t} . \tag{A.4}$$

Since n_i is statistical and is usually much bigger than 1, the rms error (or square root of variance) is

$$\Delta \left.\frac{\partial\lambda}{\partial\phi}\right|_i = \frac{\sqrt{2}N_b^2 N_0}{4\pi^2 N_t} \sqrt{n_i} = \frac{\sqrt{2}N_0}{4\pi} \sqrt{\frac{N_b^3}{N_t}} . \tag{A.5}$$

where Eq. (A.3) and $\langle n_i \rangle = N_t/N_b$ have been used. This error is therefore large at injection when $\gamma = 9.5$ and decreases by almost four times near transition where $\gamma = 18.75$.

For a Gaussian bunch the number density is

$$\lambda(\phi) = \frac{N_0}{\sqrt{2\pi}\sigma_\phi} e^{-\phi^2/2\sigma_\phi^2} , \tag{A.6}$$

where σ_ϕ is the rms bunch length in rf radian. The maximum of the gradient of λ occurs at $\phi = \sigma_\phi$, giving

$$\left.\frac{\partial\lambda}{\partial\phi}\right|_{max} = \frac{N_0 e^{-1/2}}{\sqrt{2\pi}\sigma_\phi^2} . \tag{A.7}$$

Thus, the fractional error per turn is

$$\frac{\frac{\partial\lambda}{\partial\phi}}{\frac{\partial\lambda}{\partial\phi}\Big|_{\max}} = 2\pi^{\frac{1}{2}} e^{\frac{1}{2}} \left(\frac{\sigma_\phi}{2\pi}\right)^2 \sqrt{\frac{N_b^3}{N_t}} \ . \tag{A.8}$$

At injection $\sigma_\phi \approx \pi/7$ rf rad and gradually decreases to 0.082 rf rad at transition. The fractional error at transition therefore decreases to only $\sim 4.5\%$ of its value at injection.

A higher-order differentiation formula can be used instead of Eq. (A.4). For example, if we use

$$\begin{aligned}
\left.\frac{\partial\lambda}{\partial\phi}\right|_i &= \frac{n_{i+1} - n_{i-1}}{2\Delta\phi} \ , \\
\left.\frac{\partial\lambda}{\partial\phi}\right|_i &= \frac{3n_i - 4n_{i-1} + n_{i-2}}{2\Delta\phi} \ , \\
\left.\frac{\partial\lambda}{\partial\phi}\right|_i &= \frac{-n_{i+2} + 4n_{i+1} - 3n_i}{2\Delta\phi} \ ,
\end{aligned} \tag{A.9}$$

respectively, for the center, backward, and forward differences, the error will be reduced by a factor of 2 in Eqs. (A.5) and (A.8).

We next pursue the problem in the frequency domain. This is usually necessary if we want to incorporate impedances other than space charge. A fast Fourier transform leads to a density spectrum of

$$\tilde{\lambda}_m = \frac{1}{2\pi} \sum_{j=1}^{N_b} \left(\frac{n_j}{\Delta\phi}\right) \left(\frac{N_0}{N_t}\right) e^{im\phi_j} \Delta\phi \ . \tag{A.10}$$

The voltage gained per turn by a particle in the ith bin is proportional to

$$\begin{aligned}
v_i &= \frac{N_0}{2\pi N_t} \sum_{m=-N_b}^{N_b} im \sum_{j=1}^{N_b} n_j e^{im(\phi_j - \phi_i)} \\
&= -\frac{N_0}{2\pi N_t} \sum_{m=1}^{N_b} \sum_{j=1}^{N_b} n_j m \sin m(\phi_j - \phi_i) \ ,
\end{aligned} \tag{A.11}$$

which is in fact the same as $-\partial\lambda/\partial\phi$ of Eq. (A.4). The variance of v_i is

$$\mathrm{Var}(v_i) = \frac{N_0^2}{4\pi^2 N_t^2} \sum_{m=1}^{N_b} \sum_{j=1}^{N_b} n_j m^2 \sin^2 m(\phi_j - \phi_i) \ . \tag{A.12}$$

The summation over m can be approximated by an integral to give

$$\sum_{m=1}^{N_b} m^2 \sin^2 m(\phi_j - \phi_i) = \frac{N_b^3}{6}\left[1 - \frac{3}{16\pi^2}\frac{1}{(i-j)^2}\right] . \tag{A.13}$$

Since there is no $i=j$ term, $(i-j)$ varies from 1 to N_b-1. The above sum is therefore $\sim N_b^3/6$, and

$$\mathrm{Var}(v_i) = \frac{N_0^2}{24\pi^2}\frac{N_b^3}{N_t} . \tag{A.14}$$

Finally, the fractional rms error is

$$\frac{\Delta v_i}{v_i} = \frac{\sigma_\phi^2 e^{\frac{1}{2}}}{\sqrt{12\pi}}\sqrt{\frac{N_b^3}{N_t}} , \tag{A.15}$$

to be compared with Eq. (A.8). Note that the error in the frequency-domain computation is larger than the error in the direct time-domain computation, although both of them follow a "cubic rule."

APPENDIX B. PROBLEM OF MSC

If space charge is applied once per turn (MSC = 1), the rms error per turn is ΔE_{sc} given by Eqs. (A.1) and (A.5). If we set MSC = M, space charge is applied M times per turn in the amount of $1/M$ of E_{sc} at each application. The rms error for each application is therefore

$$\Delta E_{\mathrm{sc}}^M = \frac{\Delta E_{\mathrm{sc}}}{M} . \tag{B.1}$$

If successive applications of space charge to particles in a bin were *random*, the total rms error per turn would accumulate to

$$\sqrt{M}\Delta E_{\mathrm{sc}}^M = \frac{\Delta E_{\mathrm{sc}}}{\sqrt{M}} , \tag{B.2}$$

which is $\sqrt{M}$ times smaller than when $M = 1$.

APPENDIX C. PROBLEM OF RANDOMNESS

A particle makes a synchrotron oscillation in $1/\nu_s$ turns. Therefore, between two successive applications of space charge (MSC = M times per turn), the average rf angle through which the particle moves is given by

$$\delta\phi = \frac{2\sqrt{2\pi}\sigma_\phi \nu_s}{M} . \tag{C.1}$$

In the above, we have assumed a bi-Gaussian distribution in the longitudinal phase space and all particles oscillate with the same synchrotron frequency. With N_b bins, number of macro-particles per bin in the *bunch region* is

$$n_b \approx \frac{\pi}{\sigma_\phi} \frac{N_t}{N_b} . \tag{C.2}$$

Outside the bunch region, number per bin is essentially zero. Thus, between two successive space-charge applications, the number of macro-particles moving out of or moving into a certain bin is

$$\delta n_b^{\pm} \approx \frac{n_b \delta\phi}{2\pi/N_b} , \tag{C.3}$$

where $2\pi/N_b$ is the size of a bin in rf radian. Combining Eqs. (C.1) to (C.3), the total change of number of macro-particles in a bin is

$$\delta n_b = \delta n_b^+ + \delta n_b^- \approx \frac{2\sqrt{2\pi} N_t \nu_s}{M} , \tag{C.4}$$

and the fractional change is

$$\frac{\delta n_b}{n_b} \approx \frac{4\sigma_\phi \nu_s N_b}{\sqrt{2\pi} M} . \tag{C.5}$$

At the beginning of the MR cycle, the bunch is rather long, having $\sigma_\phi \sim \pi/7$. The synchrotron tune is also rather large, $\nu_s \sim 0.012$. Therefore, with $N_t = 5000$, the number of macro-particles moving into and out of a bin is

$$\delta n_b \sim \begin{cases} 301 & M = 1 , \\ 30 & M = 10 , \end{cases} \tag{C.6}$$

independent of the number of bins. Of course, some of these particles that move out of the bin may not be inside the bin originally, but are transferred from neighboring bins. The percentage changes in particles per bin for bin number $N_b = 512$, 256, and 128 are given in Table II. We see that for $N_b = 512$, the particles in each bin are changed completely for $M = 1$ and mostly for $M = 10$. Therefore, we expect the space-charge error to reduce by $\sqrt{10}$ when we vary MSC or M from 1 to 10. For $N_b = 256$, the particles are only partially altered with $M = 10$. Therefore, the reduction in error is less than $\sqrt{10}$. For $N_b = 128$, only 11% of the particles move into and out of the bin when $M = 10$. As a result, we see very little reduction in space-charge error in the simulation when M is increased from 1 to 10.

Although the fractional change is proportional to $\sigma_\phi \nu_s$ which decreases to zero at transition, as was pointed out in Appendix A, the fractional space-charge error decreases to only 4.5% of its value at injection. Therefore, it is sufficient to discuss the problem of randomness only near injection.

MSC	$N_b = 512$	$N_b = 256$	$N_b = 128$
1	440%	220%	110%
10	44%	22%	11%

Table II: Percentage particle change in a bin between two successive applications of space charge for different bin number N_b and MSC.

REFERENCES

1. S. Stahl and J. MacLachlan, Fermilab Report TM-1650, 1990.

2. K. Johnsen, *Effects on Nonlinearities on Phase Transition*, CERN, Symposium on High Energy Accelerators, Geneva, 1956, Vol. 1, p.106.

3. See for example, A. Sørenssen, Particle Accelerators **6**, 141 (1975).

4. K.Y. Ng, *Some Estimation Concerning Crossing Transition of the Main Injector*, Fermilab Report TM-1670 (MI-30), 1990; also these proceedings.

5. J. Wei, *Longitudinal Dynamics of the Non-Adiabatic Regime on Alternating-Gradient Synchrotrons*, Ph.D. thesis, State University of New York at Stony Brook, 1990.

6. J. Wei, *Transition Crossing in the Main Injector*, these proceedings.

7. I. Kourbanis, K. Meisner and K.Y. Ng, *Experimental Study of the Main Ring Transition Crossing*, these proceedings.

LONGITUDINAL AND TRANSVERSE INSTABILITIES AROUND A γ_T JUMP

S.Y. Lee*

Brookhaven National Laboratory, Upton, NY 11973

and

K.Y. Ng

Fermi National Accelerator Laboratory,† P.O. Box 500, Batavia, IL 60510

1. Introduction

When a particle beam is in the transition region, the phase-slip parameter

$$\eta = \frac{1}{\gamma_T^2} - \frac{1}{\gamma^2} \tag{1}$$

goes through zero. This reduces the spread in revolution frequency inside the beam by so much that collective instability growths can no longer be Landau damped. With the implementation of a γ_T jump, η dips down to zero only for a very short but finite time interval, typically less than 0.5 ms or 1 ms, which is necessary in order to minimize transverse emittance growth.[1] Besides this, during the jump the phase-slip factor is roughly given by

$$|\eta| \approx \left| \frac{1}{(\gamma_T - \Delta\gamma_T/2)^2} - \frac{1}{\gamma_T^2} \right| \approx \left| \frac{\Delta\gamma_T}{\gamma_T^3} \right| , \tag{2}$$

where $\Delta\gamma_T$ is the amount of jump, which is negative for the Main Injector. The duration of the jump is typically about 10 ms. Thus, the spread in revolution frequency may still be small enough and the time long enough for collective microwave instabilities to develop. The purpose of this paper is to examine the microwave thresholds in both the longitudinal and transverse modes.

*Work performed under the auspices of the U.S. Department of Energy.

†Operated by the Universities Research Association, Inc., under contract with the U.S. Department of Energy.

2. Longitudinal microwave threshold

Let us start with the longitudinal microwave threshold for a Gaussian bunch developed by Krinsky and Wang.[2] The threshold longitudinal impedance per harmonic is given by

$$\frac{Z_{\|}}{n} = \frac{2\pi|\eta|(E/e)}{I_p}\left(\frac{\sigma_E}{E}\right)^2 , \tag{3}$$

where E is the energy of the synchronous particle and σ_E the rms energy spread of the beam. For a Gaussian bunch, the peak current is

$$I_p = \frac{eN}{\sqrt{2\pi}\sigma_\tau} \tag{4}$$

where N is the number of particles per bunch each carrying charge $e = 1.602 \times 10^{-19}$ Coulomb, and σ_τ is the rms bunch length in time. We try to express $Z_{\|}/n$ in terms of quantities which are constants near transition, such as the rf voltage $V_{\rm rf}$, rf phase ϕ_0, and 95% bunch area

$$S = 6\pi\sigma_E\sigma_\tau . \tag{5}$$

Since we are interested in the region around γ_T jump, where η given by Eq. (2) is finite, the rf bucket should be well defined and therefore Eq. (5) holds. One may argue that the bunch area is not a constant of motion because it usually grows during transition. However, the purpose of a γ_T jump is to eliminate the two tails developed in the longitudinal phase space due to nonlinear effects, as well as any collective instabilities if the jump were absent. Therefore, when a γ_T jump is properly implemented, the bunch area should remain the same before, during, and after the jump.

After some algebraic manipulation, we obtain the result

$$\frac{Z_{\|}}{n} = \frac{(2\pi)^{\frac{7}{4}} f_0^{\frac{1}{2}} h^{\frac{1}{4}}}{Ne}\left(\frac{S/e}{6\pi}\right)^{\frac{3}{2}}\left(\frac{|\eta|}{E/e}\right)^{\frac{3}{4}}(V_{\rm rf}\cos\phi_0)^{\frac{1}{4}} , \tag{6}$$

where $h = 588$ is the rf harmonic number of the Main Injector and $f_0 = 90.2$ kHz is the revolution frequency. Substituting Eq. (2) into Eq. (6), we obtain the threshold impedance

$$\frac{Z_{\|}}{n} = 10.0\ [\Omega]\left(\frac{N}{6\times10^{10}}\right)^{-1}\left(\frac{S}{0.4\ [\text{eV-s}]}\right)^{\frac{3}{2}}\left(\frac{V_{\rm rf}\cos\phi_0}{2.78\ [\text{MV}]\cos 37.6^\circ}\right)^{\frac{1}{4}}(|\Delta\gamma_T|)^{\frac{3}{4}} , \tag{7}$$

where $\gamma_T = 20.4$ has been used. The result is plotted in Fig. 1 versus bunch area for different rf voltage $V_{\rm rf}$ with the rate of acceleration $\dot{\gamma}_T = 163\ \text{sec}^{-1}$ kept constant.

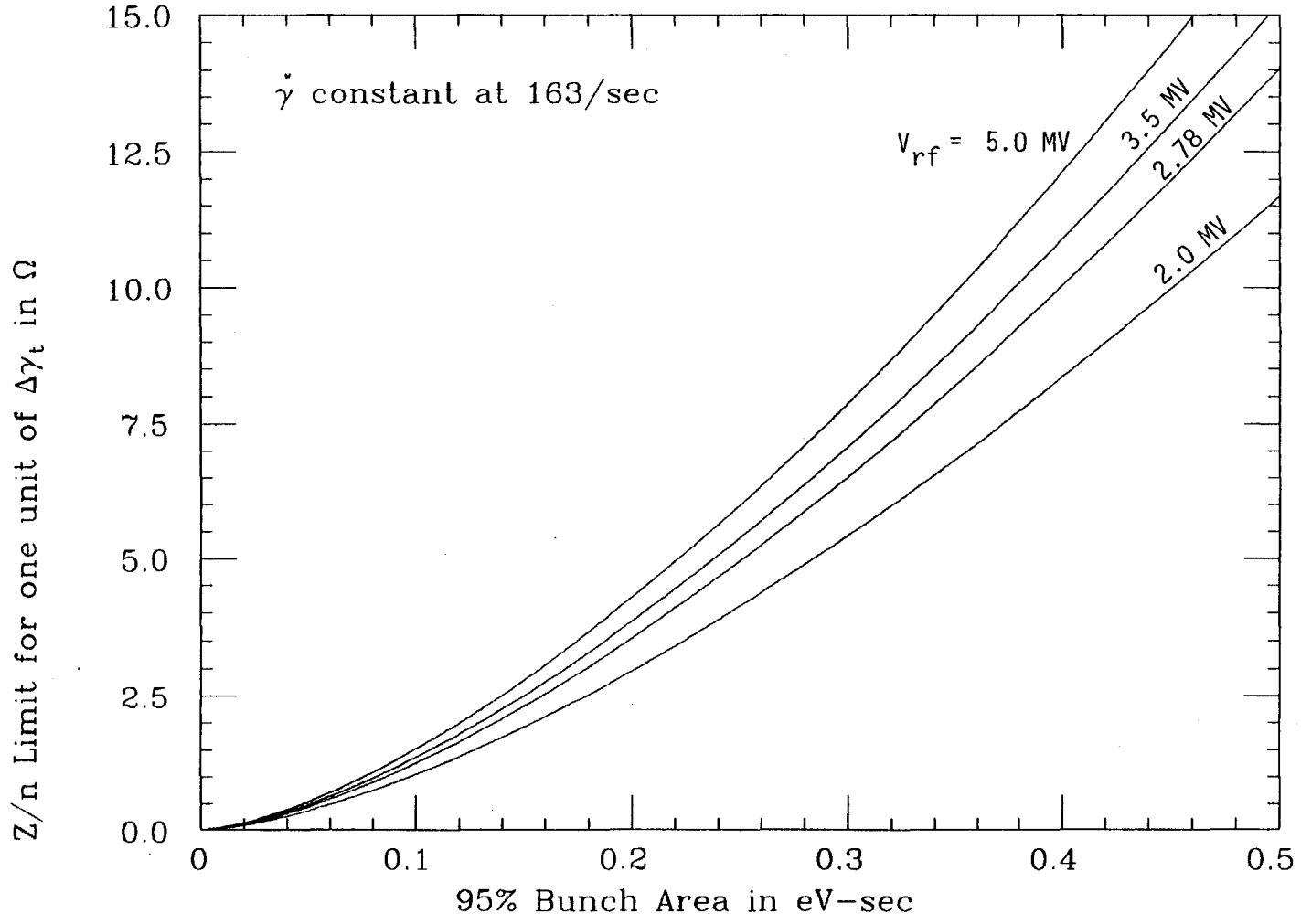
15.0
12.5
10.0
7.5
5.0
2.5
0.0
0
0.1
0.2
0.3
0.4
0.5
$\dot{\gamma}$ constant at 163/sec
V_{rf} = 5.0 MV
3.5 MV
2.78 MV
2.0 MV
Z/n Limit for one unit of $\Delta\gamma_t$ in Ω
95% Bunch Area in eV-sec

Figure 1

3. Transverse microwave threshold

The transverse impedance threshold for transverse microwave instability for a Gaussian bunch developed by Ruth and Wang[3] is given by

$$Z_\perp = \frac{4\sqrt{2}(E/e)}{I_p \bar{\beta}} \left(\frac{\sigma_E}{E}\right) |(n-\nu)\eta - \xi\nu| \ , \tag{8}$$

where $\bar{\beta}$ is the average beta function, ν the betatron tune, and ξ the chromaticity defined as the ratio of the fractional tune spread to fractional momentum spread. The harmonic number n is the position of the broad-band transverse impedance driving the instability. In terms of the 95% bunch area S, we have

$$Z_\perp = \frac{4}{3}\frac{\nu(S/e)}{NeR} |(n-\nu)\eta - \xi\nu| \ , \tag{9}$$

where $R = 528.3$ m is the average radius of the Main Injector. With a tune of $\nu = 22.42$, an evaluation gives

$$Z_\perp = 2.3 \left[\frac{\mathrm{M}\Omega}{\mathrm{m}}\right] \left(\frac{N}{6\times 10^{10}}\right)^{-1} \left(\frac{S}{0.4\ [\mathrm{eV\text{-}s}]}\right)^{\frac{3}{2}} |(n-\nu)\eta - \xi\nu| \ . \tag{10}$$

This result is plotted in Fig. 2 as a function of bunch area.

The harmonic n of the driving broad-band is usually taken as the ratio of R to $b \approx 5$ cm, the half-width of the beam pipe; or $n \approx 10400$. Then, during the γ_T jump,

$$(n-\nu)\eta = \mp 1.23 |\Delta\gamma_T| \ , \tag{11}$$

which can be comparable to $\xi\nu$ depending on the pulsing of the correction sextupoles. In other words, unless special care is taken in the control of the chromaticity, the transverse impedance threshold can dip down to a dangerously tiny value.

4. Conclusion

We see that the longitudinal microwave threshold before and after a γ_T jump of one unit is only $Z_\parallel/n = 10\ \Omega$ in the present proposed operation.[4] It is in fact the lowest in the whole cycle of the Main Injector as is shown in Fig. 3 for a possible cycle (without γ_T jump). Although the total time for the γ_T jump is of the order of

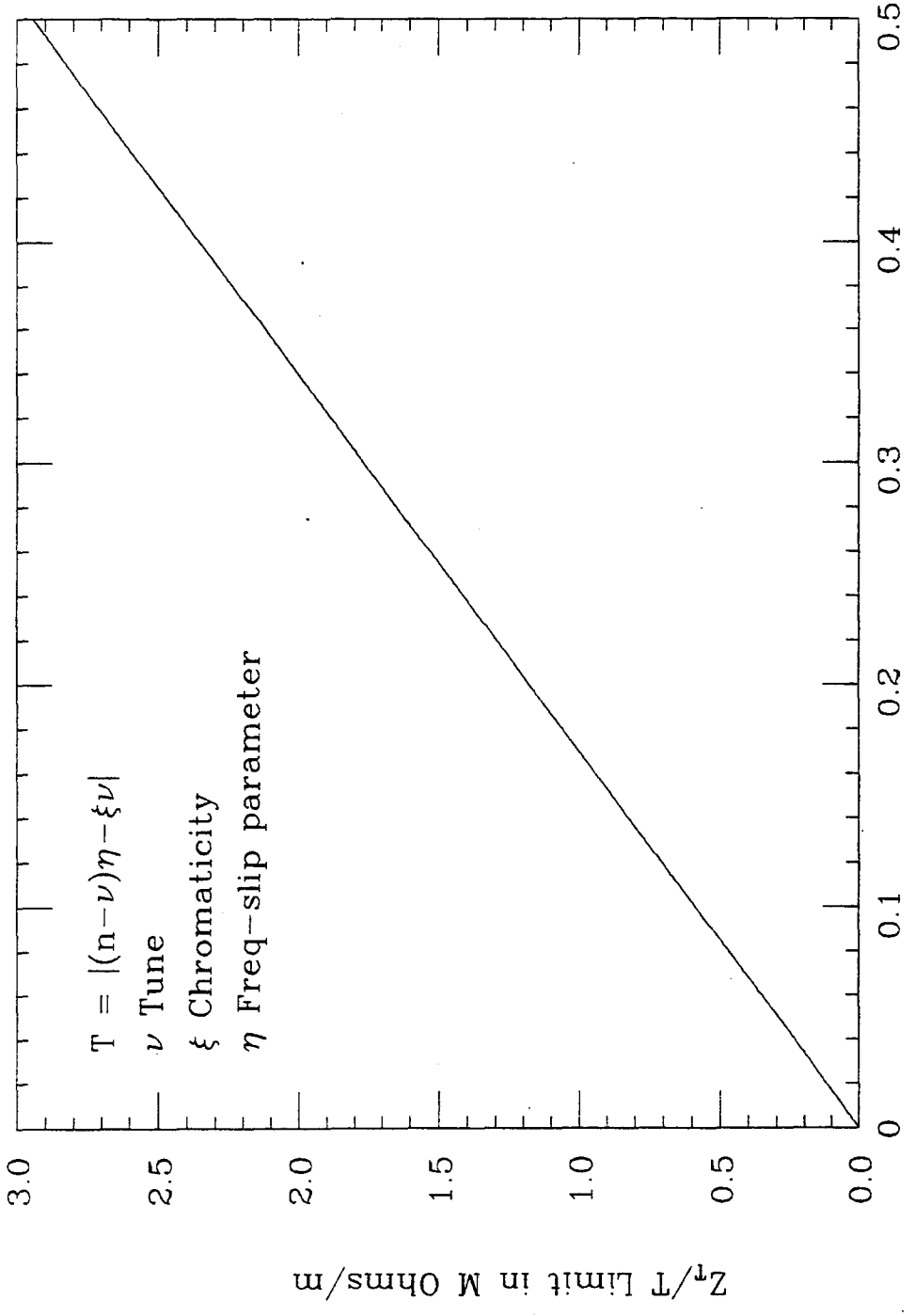
Z_τ/T Limit in M Ohms/m
3.0
2.5
2.0
1.5
1.0
0.5
0.0
0
0.1
0.2
0.3
0.4
0.5
95% Bunch Area in eV−sec
T = $|(n-\nu)\eta-\xi\nu|$
ν Tune
ξ Chromaticity
η Freq−slip parameter

Figure 2

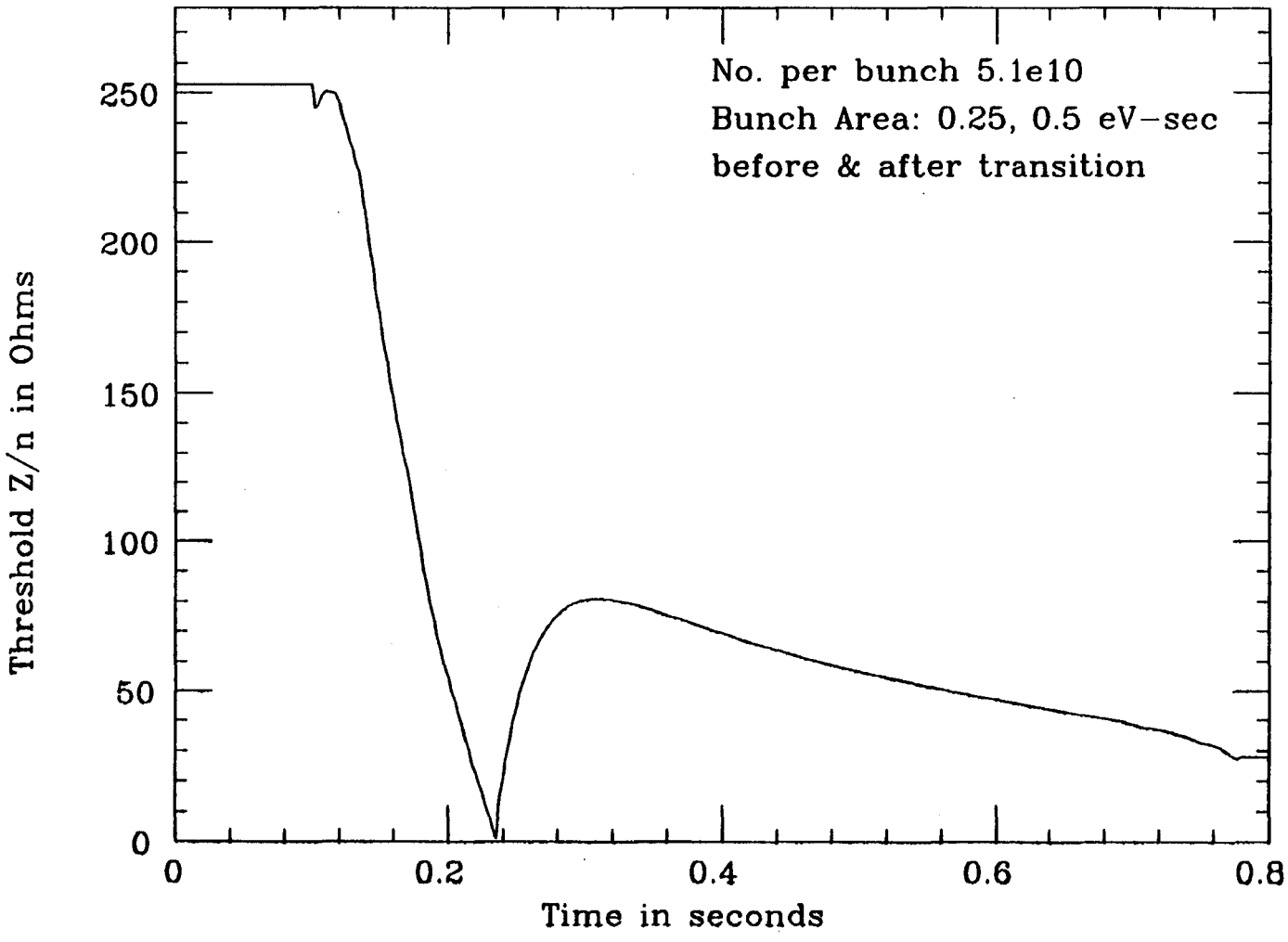
No. per bunch 5.1e10
Bunch Area: 0.25, 0.5 eV-sec
before & after transition
Threshold Z/n in Ohms
250
200
150
100
50
0
0
0.2
0.4
0.6
0.8
Time in seconds

Figure 3

10 ms, away from which η increases rapidly, nevertheless, microwave growth of the bunch area can still be important.

The transverse microwave threshold can become more stringent if the natural chromaticity is mostly corrected. Thus, the impedance budget is still an important issue even when a γ_T jump is implemented.

REFERENCES

1. K.Y. Ng, *Emittance Growth During γ_T Jump*, these proceedings.

2. S. Krinsky and J.M. Wang, Particle Accelerators **17**, 109 (1985).

3. R. Ruth and J.M. Wang, IEEE Trans. Nucl. Sci. **NS-28**, 2405 (1981).

4. K.Y. Ng, *Main Injector rf Cycle and Z/n Limit*, Fermilab MI-0029, 1990.

A COMPARISON OF MATCHED AND UNMATCHED γ_T JUMP SCHEMES IN THE MAIN INJECTOR

A. Bogacz, F. Harfoush, S. Peggs
Fermi National Accelerator Laboratory

INTRODUCTION

The dynamical parameter γ at which a nominal (on-momentum) particle in a synchrotron passes through transition is called γ_T, and has a value which depends purely on geometrical properties of the magnetic lattice. If the Main Injector lattice is left unperturbed during acceleration, then deleterious effects causing beam loss and emittance growth occur when $\gamma \approx \gamma_T$, that is, when the energy of the accelerating particles is in the vicinity of the transition energy. This is illustrated in Figure 1a. These effects, and analyses of their severities, are discussed elsewhere in these proceedings. Here we consider only one subject - ways in which the optics of the Main Injector lattice can be modified so that γ_T is modified significantly for a short period of time, without having too much effect on other single particle properties of the lattice. If the lattice can be changed rapidly from one optic to another, then transition can be "jumped", and the deleterious effects of transition crossing can be minimized.

Figures 1b and 1c illustrate monopolar and bipolar γ_T jump schemes, which differ by a factor of two in the amount of γ_T perturbation required. It is assumed in all the cases discussed here that, for the Main Injector to pass through transition gracefully, it is necessary that

$$| \gamma - \gamma_T | > 0.65 \qquad 1$$

This condition has been derived elsewhere in these proceedings. In a monopolar jump scheme it demands a perturbed lattice with $\Delta\gamma_T = -1.3$, and in a bipolar scheme it demands two lattices, with $\Delta\gamma_T = \pm 0.65$.

Transition comes when phase stability is lost - when the extra time a slightly off-momentum particle takes to circulate the synchrotron is zero, due to cancellation between the increased path length and the increased particle speed. Since the relative rate of change of speed β with respect to the off-momentum parameter $\delta = \frac{\Delta p}{p_0}$ is given by

$$\frac{1}{\beta}\frac{d\beta}{d\delta} = \frac{1}{\gamma^2} \qquad 2$$

then γ_T is given by

$$\frac{1}{\gamma_T^2} \equiv \frac{1}{C_0}\frac{dC}{d\delta} = \frac{1}{C_0}\int_0^{2\pi} \eta \, d\theta = \frac{2\pi}{C_0} \langle\eta\rangle \qquad 3$$

where C is the circumference of the closed orbit, η is the dispersion function, and θ is the accumulated bend angle. The angle brackets $\langle\ \rangle$ represent an average over bending dipoles, all of which have the same bending radius and angle in the Main Injector. So, the goal of a γ_T jump scheme is to change the average dispersion in the dipoles. This is achieved by changing the strength of special perturbation quadrupoles, which in practice must be capable of very fast response.

Ideally, the change in γ_T should not be accompanied by any gross change in horizontal or beta functions, in horizontal or vertical tunes, or even in the dispersion function itself. In practice, one or more of these ideals must be sacrificed to some extent, since the γ_T quadrupoles inevitably modify the beta functions at least locally, and an average change in the dispersion function is the design goal. The issue here is, how "gross" are the changes? Simplicity of design is also an issue - the strengths of the perturbation quadrupoles, their number, and the number of their families, should also be minimized. The tracking performance of a perturbed lattice is also an important concern.

Two prototypical γ_T jump schemes for the Main Injector are compared in these regards below. They are called "matched" and "unmatched" for short, referring to whether or not the dispersion perturbation is matched. A relatively large dispersion wave circulates the Main Injector when the perturbation quadrupoles are turned on in the unmatched scheme. The results presented below are for the application of such schemes to the contemporary MI_15 lattice.

TUNE SHIFTS, BETA FUNCTION WAVES, AND DISPERSION WAVES

When the focussing strength of a quadrupole is perturbed by a small amount q, the horizontal and vertical tunes shift by

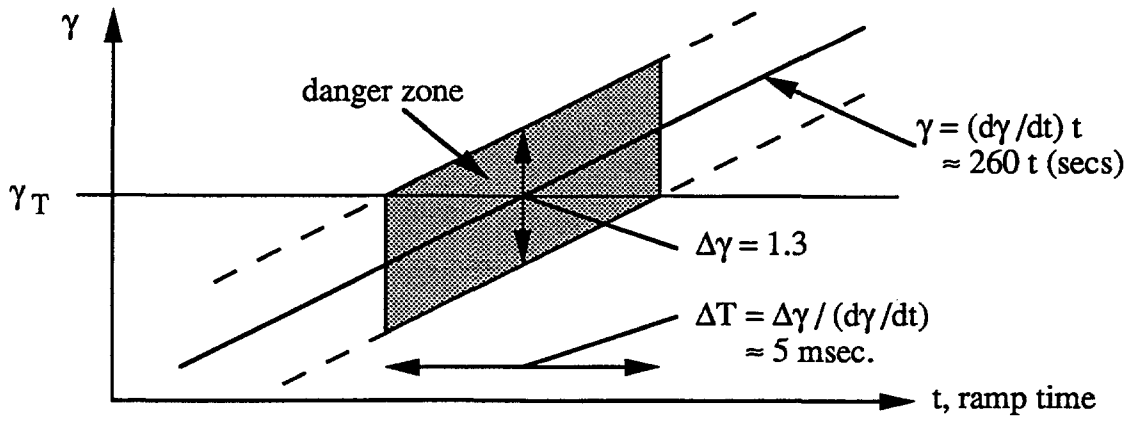

Figure 1a The transition crossing danger zone, in the absence of a γ_T jump

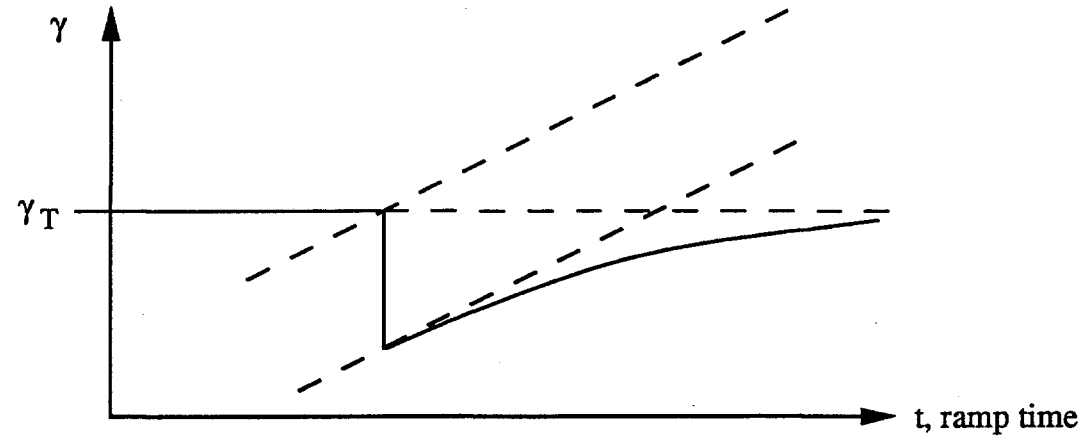

Figure 1b A monopolar γ_T jump, with $\Delta\gamma_T = -1.3$

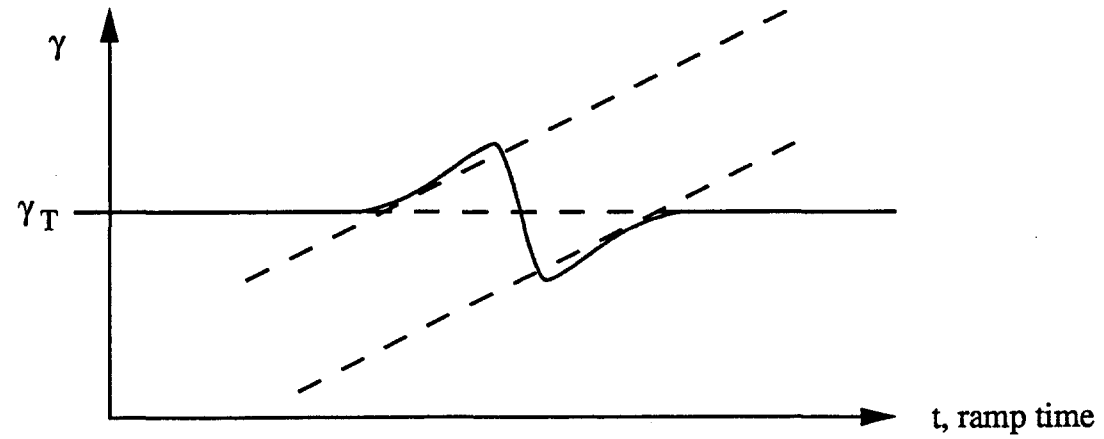

Figure 1c A bipolar γ_T jump, with $\Delta\gamma_T = \pm 0.65$

$$\Delta Q_H = \frac{q\beta_{H\,quad}}{4\pi}, \qquad \Delta Q_V = -\frac{q\beta_{V\,quad}}{4\pi} \tag{4}$$

where β now stands for a beta function, not a speed. Positive q means stronger horizontal focussing.

Downstream from the perturbation there is a free wave perturbation of the horizontal beta function, according to

$$\frac{\Delta\beta}{\beta} = -q\,\beta_{quad}\,\sin[2(\phi-\phi_{quad})] \tag{5}$$

with a phase which advances twice as fast as the betatron phase advances. In the vertical plane the first negative sign on the right hand side is replaced by a positive sign. Of course, if the free wave "escapes" to circulate the ring, equation 5 must be replaced by a solution satisfying periodic boundary conditions. There is also a free horizontal dispersion wave downstream of the perturbation, given by

$$\frac{\Delta\eta}{\sqrt{\beta}} = -q\,\eta_{quad}\sqrt{\beta_{quad}}\,\sin(\phi-\phi_{quad}) \tag{6}$$

which advances at half the speed of the beta function wave, in step with the betatron phase.

Most of the circumference of the Main Injector lattice MI_15 is composed of matched arc FODO cells, with a betatron phase advance of approximately 90 degrees per cell. No free betatron wave will escape these arcs if the perturbing quads are arranged in pairs, either with identical strengths 90 degrees in phase apart, or with equal and opposite strengths 180 degrees apart. Similarly, no free dispersion wave will escape if the pairs are of identical strength 180 degrees apart in phase, or of equal and opposite strength 360 degrees apart.

THE MATCHED CONFIGURATION

Neither kind of free wave escapes if identical strength perturbing quadrupoles are arranged in groups of four, with 90 degrees of betatron phase advance - one FODO cell - between neighbors. This is the basis for the "matched" γ_T jump scheme. In one half of MI_15 there are two arcs, a long one with 20 arc FODO cells and a short one with 6 arc FODO cells. Hence it is possible to

have 24 perturbation quads in each half, for a total of 48 in the complete lattice. They are placed at focussing quadrupoles, where their effect on the horizontal dispersion, and hence on γ_T, is the greatest. Essentially, these quadrupoles merely retune the standard arc FODO cell, decreasing or increasing the matched value of dispersion in a cell. Hence the change in γ_T is first order in the strength of the quadrupoles.

The main drawback to this scheme is that a second family of perturbation quadrupoles is required in a dispersion free region, in order to compensate for the tune shift accumulated through the retuning of the 48 arc FODO cells. Since the second family is in a dispersion free region, there is no need to avoid dispersion waves, so the quadrupoles are arranged in pairs, 90 degrees apart in phase. In the MI_15 lattice there is only one place in each half where 2 straight FODO cells appear - in a region where design dispersions are small, but non-zero. It is possible to have 3 perturbing quads of the second type here, powered with relative strengths 1:2:1, for an effective total of 8 in the whole lattice. This second family is powered with a strength approximately 6 times the strength of the first, and with opposite polarity. Table 1 records various configuration parameters for the matched γ_T jump scheme.

THE UNMATCHED CONFIGURATION

In the unmatched γ_T jump scheme there is only one family of perturbation quadrupoles, with a member at every other horizontally focussing quadrupole in the arc FODO cells, 180 degrees apart in phase. Neighboring quadrupoles have opposite polarities. This is similar to the scheme already in use in the Fermilab Booster [1-3], and as studied here is almost exactly the original scheme proposed for the Main Injector [4]. It is possible to put 10 quadrupoles in each long arc, and 2 in each short arc, for a total of 24 quadrupoles in the complete MI_15 lattice. There is no free beta wave and no net tune shift, to first order in the perturbation strength. Hence there is no need for a second family of tune compensation quadrupoles.

However, the main disadvantage of this scheme is that while a large global dispersion wave is created that is of first order in perturbation strength, the desired effect, an average change of dispersion, is of second order. In a pure FODO cell lattice there is no first order effect at all, since flipping the polarities of all the perturbation quadrupoles would result in exactly the same lattice. The first order term in the variation of $\Delta\gamma_T$ is still negligible in the MI_15 lattice, where the "polarity symmetry" is somewhat broken. Table 1 also records configuration parameters of the unmatched γ_T jump scheme.

SCHEME	$\Delta\gamma_T$	FAMILY NUMBER 1		FAMILY NUMBER 2	
		number	strength $\frac{\Delta(kL)}{(kL)_{ARC}}$	number	strength $\frac{\Delta(kL)}{(kL)_{ARC}}$
Matched	−1.3	48	−.055	6	.334
	−0.65		−.029		.159
	0.65		.031		−.157
Unmatched	−1.3	24	.074	none	

Table 1 Strengths and configurations of perturbation quadrupoles in matched and unmatched γ_T jump schemes.

OPTICAL PERTURBATIONS

The description of lattice perturbations given above, in equations 4, 5 and 6, is based on the assumption that the quadrupole strengths are all small enough that first order perturbation theory is adequate. Unfortunately, this is not completely true for either scheme. Table 1 shows the strength of the quadrupoles, normalized to the strength of the regular arc quadrupoles. Note, for example, that the relative strength of the second family in the matched scheme is not small compared to one, especially when a monopolar jump of $\Delta\gamma_T = -1.3$ is considered. The optical behavior of both schemes is shown in detail in Table 2, in comparison with the nominal case, "OFF".

In all cases, the vertical beta functions are negligibly disturbed. This is not too surprising, since the perturbing quadrupoles are always at horizontally focussing locations. Also, it is implicit in all cases that the net horizontal and vertical tune shifts are negligibly small, of order 10^{-3}, although they are not exactly zero in either scheme.

In the matched scheme, the removal of tune shifts is performed through explicit tuning of the two family strengths, relative to one another. When $\Delta\gamma_T = -1.3$ in a monopolar jump, the optical

solution is not acceptable, because the maximum horizontal beta function rises to 433 meters. In a bipolar scheme with $\Delta\gamma_T = \pm 0.65$, the perturbations are much more modest - although still not negligible - with a maximum horizontal beta of 98 meters. These distortions come because the relative strength of the second family of quadrupoles is large, as big as 0.16 in the bipolar case. Worse, two of these quadrupoles are placed back to back, for an effective strength of 0.32 times a regular arc quadrupole.

Most of the problems with the matched scheme are due to this single quadrupole. If it is possible to modify the Main Injector lattice to include 3 straight FODO cells in a dispersion free straight, instead of 2, then the maximum effective strength will halve, and these problems will be significantly eased. The monopolar ($\Delta\gamma_T = -1.3$) distortions would then be reduced to the current level of the bipolar ($\Delta\gamma_T = \pm 0.65$) distortions, and the bipolar distortions would probably become negligible. Since only the first family of quadrupoles affects the dispersion strongly, none of the matched configurations suffer from excessive variations in the dispersion.

SCHEME	$\Delta\gamma_T$	β_H min (m)	β_H max (m)	β_V min (m)	β_V max (m)	η min (m)	η max (m)
OFF	0.0	10.9	56.7	10.9	78.9	−0.12	2.07
Matched	−1.3	1.3	432.7	10.3	83.5	−1.75	4.61
	−0.65	4.68	81.0	10.9	80.1	−0.47	2.64
	0.65	8.86	97.5	10.9	80.3	−0.31	2.29
Unmatched	−1.3	8.86	65.4	10.7	82.0	−7.71	9.59

Table 2 Optical perturbations in matched and unmatched γ_T jump schemes.

In the unmatched scheme, the minimum and maximum horizontal beta functions are negligibly disturbed, by less than 20% . However, the minimum and maximum dispersions reach extreme values of −7.7 and 9.6 meters, leading to a reduced dynamic aperture for off-momentum

particles. This effect, studied in the section on tracking below, is especially critical at transition time when the momentum width of the beam is at its largest. Another deleterious effect of these large dispersion swings is the significant modification of the strength of the Johnsen effect, due to the variation of γ_T with momentum. This is discussed elsewhere in these proceedings [5].

TRACKING RESULTS

Tracking was performed to find the dynamic aperture relative to a closed orbit which was displaced by a range of constant momentum offsets, $\Delta p/p = 0.0$ through to 0.009, appropriate for transition crossing. The tracking code used, TEAPOT, converts all elements of a design lattice into thin elements. Elements can have multipole field errors and misalignment errors, either systematic or random. In the Main Injector lattices studied there were no misalignment errors. Only the systematic dipole bend magnetic errors listed in Table 3 were included.

Component	N	b_N (r_0 = 1 m)	b_N (r_0 = 1 inch) * 10^{-4}
Eddy current	2	.528	3.405
	4	−20.9	−.087
	6	−10282.	−.028
Saturation	2	.033	.215
	4	44.2	.184
	6	16960.	.046
TOTAL	0	0.0	0.0
	2	.561	3.620
	4	23.24	.097
	6	6677.	.018

Table 3 Systematic multipole errors in the dipole bends used for tracking

The b_N and r_0 values reported there correspond to the coefficients and to the reference radius in a multipole expansion of the vertical magnetic field, given by

$$B_{VERT} = B_0 \left[1 + \sum_{N=0}^{\infty} b_N \left(\frac{x}{r_0} \right)^N \right] \qquad 7$$

The values in the TOTAL rows, from the $r_0 = 1$ meter column, are the actual numerical values that were entered into the TEAPOT input file. These results were obtained by J. F. Ostiguy using the Main Injector dipole magnet design [6,7]. Higher order multipoles due to eddy currents and saturation were found to be negligible and therefore were not included. Saturation multipoles were calculated at an excitation corresponding to a transition momentum of 19.10 Gev/c and a dipole field of $B_0 = 0.23707$ Tesla. This level of excitation was obviously not high enough to drive the magnet into real saturation, hence the small values for saturation multipoles.

The dominant multipole field was the sextupole component b_2, with a strength of $3.620 * 10^{-4}$ ($r_0 = 1$ inch), which was almost completely due to eddy currents. This value was consistent with the tracking studies previously performed by Rod Gerig, in which the amount of systematic sextupole coming from all sources was 4.5 units (10^{-4} at 1 inch) at a transition momentum of 17.8 GeV/c [8,9]. The value did not include any contribution due to remanent fields. The expected remanent sextupole would reduce the value by about one unit, but the estimate of its size was relatively inaccurate, compared to the saturation and eddy current estimates. By not including the remanent field effect in the total values we were being somewhat conservative.

Twenty particles were launched with identical horizontal and vertical amplitudes, at intervals of 0.5 centimeters. This amplitude was scaled to correspond to the actual value when $\beta = \beta_{MAX}$ for the standard FODO cell. A particle was considered lost when its displacement exceeded a radius of 1 meter. The time region around transition over which $\Delta p/p$ gets large is about 10 milliseconds, which corresponds to the 1000 turns which were tracked in the Main Injector. Two configurations were selected for study: the unmatched γ_T jump with $\Delta\gamma_T = -1.3$, and the matched γ_T jump with $\Delta\gamma_T = -0.65$. In each case chromaticity correction sextupoles were adjusted to achieve net horizontal and vertical chromaticities of zero.

Results are shown in Figures 2 and 3. In each figure the vertical axis refers to the maximum particle amplitude in centimeters for which the particle is stable (not lost in 1,000 turns). The

horizontal axis is the particle off-momentum value $\delta = \Delta p/p$. Because of the 0.5 centimeter step between each particle, an error bar of total length 1 centimeter is attached to each point on the graph. Two lines with maximum and minimum slopes are drawn by eye to fit the data in each figure. The absolute value of the slope of such a line, $|dx/d\delta|$, is a dispersion-like quantity. For the unmatched γ_T case the size of the slope is 7.1 ± 0.4 meters, roughly consistent with the maximum dispersion of 9.6 meters reported in Table 2, above. For the matched γ_T case there is a definite improvement in maintaining a more constant dynamic aperture over the range of the off-momentum particles. The size of the slope is now 1.65 ± 0.5 meters, consistent with the maximum dispersion of 2.64 meters recorded in Table 2.

CONCLUSIONS

As they have been presented here, neither γ_T transition jump scheme design, matched or unmatched, is entirely satisfactory. However, with further design and development, it is probable that either scheme could be made to work satisfactorily in the Main Injector.

The unmatched scheme has the virtue of simpler hardware requirements - only one family of perturbation quadrupoles is required. Its disadvantages stem from the large induced dispersion wave (hence the name of the scheme), and from the fact that the change in γ_T is only second order in the perturbation strength. Because of the 9.6 meter maximum dispersion, the dynamic aperture is significantly - although not severely - truncated at large momentum offsets. In its favor, the betatron functions and tunes are negligibly affected, at least in an ideal lattice without errors.

The matched scheme requires two quadrupole families to keep the betatron tunes unchanged. There are only 3 reasonable locations in each half of the MI_15 lattice for quadrupoles of the second family. This leads to an unreasonably large perturbation strength at the central location in a monopolar $\Delta\gamma_T = -1.3$ jump, which distorts the linear lattice almost to the point of instability. However, the behavior of the linear lattice in a bipolar jump of strength $\Delta\gamma_T = \pm 0.65$ is reasonable. The full size monopolar jump would probably achieve this level of distortion if a fourth location (per half Main Injector) could be found for a quadrupole in the second family.

One important characteristic of the jump schemes which has not been addressed here is the variation of the α_1 parameter - which controls the variation of γ_T with δ - during the jump. Since α_1 is a key parameter in determining the strength of the critical Johnsen effect, the very reason for having a γ_T jump could be voided if it varies significantly. This issue is addressed in another paper in these proceedings [5].

REFERENCES

1) P. Lucas and J. Maclachlan, *Simulation of space charge effects and transition crossing in the Fermilab Booster,* p. 1114, IEEE PAC, Washington, 1987.

2) K.Y. Ng, *Space-charge effects of transition crossing in the Fermilab Booster*, p. 1129, IEEE PAC, Washington, 1987.

3) W. Merz, C. Ankenbrandt, and K. Koepke, *Transition jump system for the Fermilab Booster*, p. 1343, IEEE PAC, Washington, 1987.

4) S. Holmes, *Main Injector transition jump*, Collected reports of the accelerator and beam line options working group, Breckenridge workshop, August 1989.

5) A. Bogacz, S. Peggs, *Comments on the behavior of* α_1 *in Main Injector* γ_T *jump schemes*, these proceedings.

6) J-F. Ostiguy, *Main Injector dipole magnet: 2 D field computations*, Fermilab note MI-0036, October 1990.

7) J-F. Ostiguy, *Eddy current induced multipoles in the Main Injector*, Fermilab note MI-0037, October 1990.

8) R. Gerig, *Main Injector sextupole requirements*, Fermilab note MI-0026, July 1990.

9) R. Gerig, *Dynamic aperture with* γ_T *jump*, Fermilab note MI-0032, August 1990.

D. Trbojevic and S.Y. Lee

Examination of the Imaginary γ_t Lattice Stability

The lattice of a 150 GeV ring without transition has already been presented at the Second European Particle Accelerator Conference in Nice, France. A design method was discussed in detail in the article from the conference proceedings(1). The lattice presented can be used for the Main Injector although the circumference of the ring measuring 3071.2234 meters is much smaller than the length of the Main Injector design lattice (3319.4188 meters).

The basic FODO cell has a 55° phase advance. There are three dipoles per half cell. The gradient in the FODO cell quadrupoles is equal to 220 kG/m. The quadrupoles are 0.5 meters long. A low beta cell is used(1) to provide the matching of the dispersion as well as of other betatron functions between two consecutive FODO cells. The normalized dispersion of this cell is presented in figure 1. The third and fourth quadrant in the χ and ξ normalized disperzsion space contain two FODO cells with six dipoles per cell. The low beta cell occupies most of the two upper quadrants. Two dipoles are placed in the middle of the cell. Because the betatron function β_x is very small through the cell, the effect of the two dipoles on the dispersion is very small.

The Straight Sections:

Ideal extraction and injection designs always require a 90° phase advance between the kickers and injection (fast extraction) and the magnetic septum or between the electrostatic septum and the magnetic septum (slow extraction). Transversely the beam should not be limited by the physical aperture of the downstream element. The straight sections are low beta insertions without dipoles. Two dipoles are taken out from the first half cell of the FODO cell to provide room for kickers for extraction or injection. Figure 2 presents the normalized dispersion space of the straight section. Two more dipoles are removed from the end of the last half FODO cell to allow the dispersion match to the rest of the ring. There are six straight sections. The straight sections are:

- proton injection straight section,
- proton extraction and antiproton injection and extraction straight section,
- proton abort,

- RF straight section,

and two more straight sections whose use has not yet been defined.

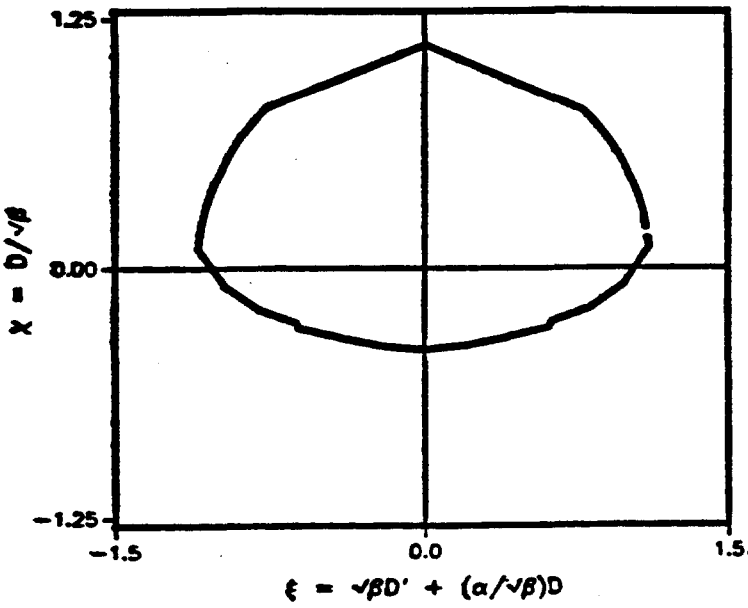

Fig. 1 Normalized dispersion function within repetitive cell.

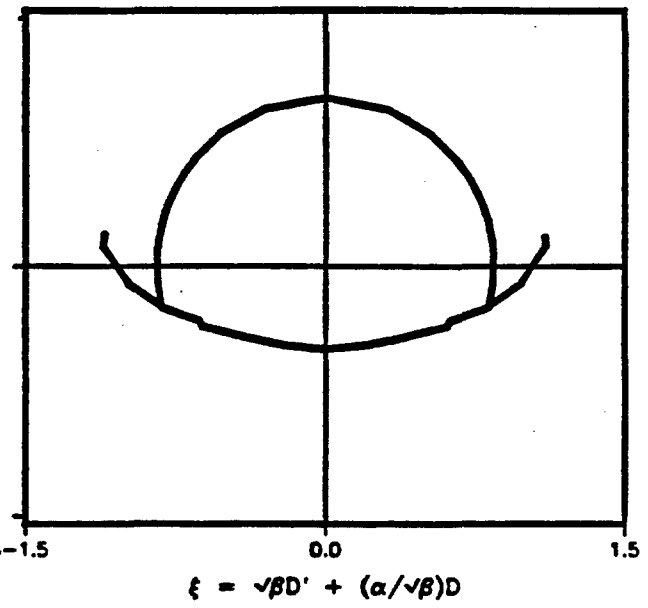

Fig. 2 Normalized dispersion within the straight section together with the two FODO cells.

Figure 3 represents the β_x and β_y betatron functions and dispersion through the repetitive cell with the straight section included. The transition gamma is equal to:

$$\gamma_t = i\ 18.27\ ,$$

and it is an imaginary number. The size of the ring presented in this example is 3071 meters with a radius of 488.8 meters. The horizontal and vertical tunes are slightly higher than 18, and the maxima of the dispersion function are between 2.7 and -2.7 meters, while the natural chromaticities are $Q_x = -35.5$ and $Q_y = -26.8$.

The straight section has a dispersion of less than 2 meters. The maxima of the betatron function are: β_x = 75 meters and β_y = 78 meters. There are 300 dipoles in the ring with a length of 6.0706 meters. The length of the drift in the middle of the straight section is 19 meters, while the length of the two drifts, where the phase difference is 90° degrees away from the extraction devices is 12.9 meters.

There are three kinds of quadrupoles in the low beta cells. Two triplets have on both sides of the straigth section two defocusing quadrupoles with a length of 2.43 and 2.63 meters and one focusing quadrupole with 4.81 meters. There are three quadrupole buses:

- the first one for the focusing quadrupoles producing a gradient of 220 kG/m in the FODO cells,
- the second focusing quadrupole buss producing 250 kG/m gradient through the focussing quad in the low beta cell,
- the third bus, through the defocusing quadrupoles in the FODO cells as well as through the defocusing quadrupoles in the low beta cells, produces a gradient of -220 kG/m.

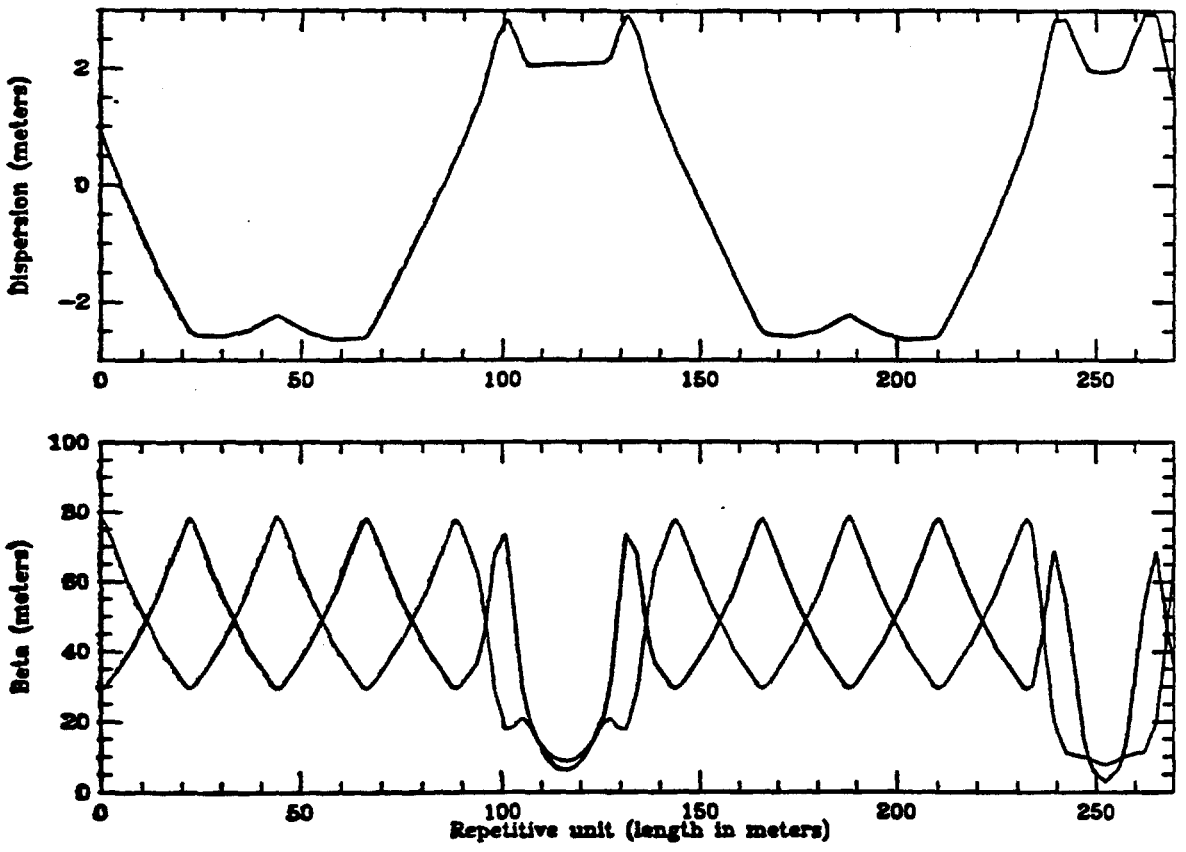

Fig. 3 Betatron functions through the repetitive cell together with the straight section.

S.Y. Lee introduced the chromatic correction scheme where the horizontal focusing sextupoles were placed at the defocusing quads of the FODO cells, while the horizontal focussing sextupoles were placed at the focusing quadrupoles of the FODO cells, due to a negative sign of the dispersion function through these quads. The corresponding betatron functions β_x and β_y in the FODO cells at the horizontally focusing and defocusing quadrupoles, respectively, have maximum values as they would have within an accelerator made exclusively of FODO cells. The sextupoles used in the following calculations are zero length with strengths to compensate the natural chromaticity equal to:

sexth = 0.070614 $1/m^2$ and sextv = 0.19386 $1/m^2$.

1. Off Momentum Behaviour

The stability of the lattice was examined first by introducing the off momentum closed orbit.

TABLE 1.

Momentum Dependence of the Lattice Parameters

$\delta p/p$ (%)	γ_t (GeV)	ξ_x	ξ_y	ν_x	ν_y	β_x (m)	β_y (m)	D_x (m)	x_{co} (mm)
0.00	18.05	0.0	0.0	18.601	17.819	75.34 3.34	78.25 6.26	2.74 -2.72	0.0 0.0
0.00	17.95	0.3	0.6	18.678	17.745	75.14 3.35	76.32 6.45	2.76 -2.76	0.0 0.0
-0.50	17.15	-0.8	-3.3	18.680	17.752	74.73 3.25	87.78 5.56	2.77 -2.91	14.1 -13.7
0.50	18.82	1.0	3.9	18.679	17.756	74.47 3.45	82.65 6.64	2.76 -2.65	13.7 -13.3
-1.00	16.44	-2.2	-8.1	18.688	17.782	74.22 3.15	104.17 4.66	2.77 -3.06	28.9 -27.6
1.00	19.81	1.6	6.9	18.683	17.782	75.75 3.54	89.56 6.82	2.81 -2.55	27.5 -26.1

Parameters of the lattice as:
- γ_t transition gamma,
- ξ_x and ξ_y horizontal and vertical chromaticities,
- ν_x and ν_y horizontal and vertical tunes,

- β_x and β_y a range of the betatron functions,
- D_x a range of the horizontal dispersion function,
- x_{co} maximum horizontal offset of the orbit for an off momentum ray,

where studied by changing each initial momentum $\delta p/p$ with increments of 0.5 % from -1.0 % up to 1.0 %. Each step of this study is presented in table 1.

2. Tunability of the Lattice

The stability of the lattice parameters was examined by introducing an error in the quadrupole gradients of the focusing as well as the defoucusing gradients in the FODO cells. The introduction of an error greater than 1% in $\Delta G/G$ produced very little perturbation with regard to the lattice properties.

A conclusion obtained from these sudies is that the presented lattice without transition is a very stable and well behaved lattice.

(1) D. Trbojevic, D. Finley, R. Gerig, and S. Holmes, "Design Method for High Energy Accelerator Without Transition Energy", Second European Particle Accelerator Conference, Nice, France, June 12-16, 1990, Conference Proceedings.

COMMENTS ON THE BEHAVIOR OF α_1 IN MAIN INJECTOR γ_T JUMP SCHEMES

A. Bogacz, S. Peggs
Fermi National Accelerator Laboratory

INTRODUCTION

Tracking studies of transition crossing in the Main Injector and other Fermilab accelerators, using the code ESME, have shown that the Johnsen effect is the dominant cause of beam loss and emittance blow up [1,2]. This effect is rooted in the variation of γ_T, the transition gamma, with $\delta = \frac{\Delta p}{p_0}$, the off-momentum parameter. Although transition crossing may be well tuned for the nominal particle, perhaps with an 'instantaneous' snap of the radio frequency phase and a γ_T jump scheme, it is not trivial to satisfy the needs of a momentum spectrum of particles. In general, individual off-momentum particles cross transition either too early, or too late. This leads to particle loss and longitudinal emittance growth which is independent of the intensity of the bunch under consideration. A useful parameter characterizing the strength of this effect is the Johnsen time, T_J, which represents the root mean square spread of the transition crossing time [3-6]. This time is proportional to $\frac{\sigma_p}{p}$, the root mean square momentum spread.

The Johnsen time is directly related to the lattice parameter α_1, which is defined by the equation

$$\frac{\Delta C}{C_0} = \alpha_0 \delta + \alpha_1 \delta^2 + ... \qquad 1$$

where C_0 is the nominal closed orbit path length, and ΔC is the increase in path length for an off momentum particle. Unfortunately, more than one definition of α_1 is common in the literature, as discussed in Appendix A. Let the reader beware! As defined here, the coefficients α_0 and α_1 are geometrical properties of the lattice, given by

$$\alpha_0 = \frac{2\pi}{C_0} <\eta_0>, \qquad \alpha_1 = \frac{2\pi}{C_0} <\eta_1> \qquad 2$$

where angle brackets $<>$ denote averaging weighted by bend angle. The quantities being averaged are component dispersions in a momentum expansion of the total dispersion. That is,

$$\eta(s) \quad = \quad \eta_0(s) \quad + \quad \eta_1(s)\,\delta \quad + \quad .... \qquad 3$$

explicitly showing the dependence of the dispersion on s, the accelerator azimuth.

Transition comes for a particle with a macroscopic momentum displacement Δp when a neighboring trajectory, infinitesimally displaced by dp, has the same revolution frequency. If it is assumed that equation 1 is exact (α_2, et cetera, are zero), then it can be shown that the exact condition for transition crossing becomes

$$\frac{1}{\gamma_T^2} \quad = \quad \frac{\alpha_0 + 2\,\alpha_1\,\delta}{1 + \alpha_0\,\delta + \alpha_1\,\delta^2}\;(1+\delta) \qquad 4$$

Keeping only first order terms in δ, this equation can be rearranged to give the γ of the off-momentum particle as it passes through transition,

$$\gamma_T \;=\; \gamma_{T0}\,[\,1 - (\frac{1}{2} + \frac{\alpha_1}{\alpha_0} - \frac{\alpha_0}{2})\,\delta\,] \qquad 5$$

Here γ_{T0} is the γ of the nominal particle as it passes through its transition. However, a more useful quantity is the γ of the nominal particle at the time that the off momentum particle passes through transition. This is given by

$$\gamma_0(\delta) \;=\; \gamma_{T0}\,[\,1 - \delta\,] \qquad 6$$

so that the Johnsen time becomes

$$T_J \quad = \quad \frac{\gamma_0(\frac{\sigma_p}{p})}{\dot{\gamma}} \quad = \quad \frac{\gamma_{T0}}{\dot{\gamma}}\,[\,\frac{3}{2} + \frac{\alpha_1}{\alpha_0} - \frac{\alpha_0}{2}\,]\;\frac{\sigma_p}{p} \qquad 7$$

where $\dot{\gamma}$ is the ramp rate through transition. The Main Injector, for example, has (approximately) $\gamma_{T0} = 20$, $\dot{\gamma} = 240\ \text{sec}^{-1}$, $\alpha_1 = 0$, and $\frac{\sigma_p}{p} = 5.10^{-3}$, so that T_J is about 0.6 milliseconds, or about 60 accelerator turns.

Clearly, if it is not possible to control the Johnsen time, it is futile to arrange for a γ_T jump on a time scale much faster than this. Also, analysis of how α_1 changes should be included as an additional topic in the evaluation of γ_T jump schemes, to ensure that T_J does not rise significantly. On the positive side, if it is possible to measure and control α_1, then it should be possible to make $T_J = 0$, and ameliorate the damage done by the Johnsen effect, by setting

$$\alpha_1 \;=\; -\frac{3}{2}\alpha_0 \;+\; \frac{1}{2}\alpha_0^2 \qquad 8$$

The second term on the right is essentially negligible. The improvement in transition performance might then be dramatic enough that a γ_T jump would no longer be necessary. This may be true especially if α_1 control is combined with RF gymnastic tricks, such as the use of a synchronous phase of 90^0 and a second harmonic cavity, as now being discussed elsewhere [7].

THE DIFFERENTIAL EQUATION FOR THE SUM DISPERSION, η_+

The horizontal closed orbit h(s) is found by solving the differential equation

$$h'' \;+\; \frac{K(s)}{1+\delta}\,h \;+\; \frac{S(s)}{1+\delta}\,h^2 \;=\; G\left(1 - \frac{1}{1+\delta}\right) \qquad 9$$

with periodic boundary conditions. A prime indicates differentiation with respect to s, K is the quadrupole strength, S is the sextupole strength, and G is the dipole bending strength. If h is expanded in a dispersion function series

$$h \;=\; x_{CO} + \eta_0 + \eta_1\,\delta + \ldots \qquad 10$$

which is substituted into 9, three differential equations are obtained by grouping terms according to their order in δ, up to second order. The solution of the lowest order equation is trivial when there are no closed orbit perturbations, $x_{CO} = 0$, so that the remaining two equations become

$$\eta_0'' \;+\; K\eta_0 \;=\; G \qquad 11a$$

$$\eta_1'' \;+\; K\eta_1 \;=\; -G \;+\; K\eta_0 \;-\; S\eta_0^2 \qquad 11b$$

The differential equation for the convenient "sum dispersion", defined by

$$\eta_+ \;=\; \eta_0 + \eta_1 \qquad 12$$

is obtained by adding equations 11a and 11b, to give

$$\eta_+'' \;+\; K\eta_+ \;=\; K\eta_0 \;-\; S\eta_0^2 \qquad 13$$

The source terms on the right hand side of equation 13 depend only on the solution of 11a for the 'normal' dispersion. Solving this differential equation is slightly easier than solving 11b for η_1, and a subsequent calculation of $<\eta_+>$ allows for a direct knowledge of α_1, since

$$\alpha_1 \quad = \quad \alpha_+ - \alpha_0 \quad = \quad \frac{2\pi}{C_0} <\eta_+> - \alpha_0 \qquad 14$$

In order to set the Johnsen time to zero, therefore, it is necessary to set

$$\alpha_+ \quad = \quad -\frac{1}{2}\,\alpha_0 \qquad 15$$

The next section solves equation 13 in a naive FODO representation of the Main Injector, and quantitatively identifies the major factors which affect η_+ and hence α_+ and α_1.

SOLUTION IN A FODO LATTICE WITH EDDY CURRENT SEXTUPOLES

Suppose that an accelerator like the Main Injector is represented as made up purely of FODO cells, as illustrated in Figure 1. The quadrupoles are thin, and there is no drift space. All of the half cell length L is filled with two identical dipoles of bend radius R, which are separated by a thin sextupole representing the field due to vacuum chamber eddy currents, induced during the ramp. There are also two thin chromatic correction sextupoles per half cell, immediately adjacent to the focussing and defocusing quadrupoles. The strength of the (half) quadrupoles is $\pm q$, and of the sextupoles is g_F, g_D, and g_E, where

$$q \quad = \quad \frac{s}{L} \quad = \quad \frac{\sin(\phi_{1/2})}{L} \qquad 16a$$

$$g_F \quad = \quad \frac{(S_F \Delta l)\,\eta_{0F}}{q}, \qquad g_E \quad = \quad \frac{(S_E \Delta l)\,\eta_{0E}}{q}, \qquad g_D \quad = \quad \frac{(S_D \Delta l)\,\eta_{0D}}{q} \qquad 16b$$

In these expressions $\phi_{1/2}$ is the half cell phase advance (about 44 degrees in the Main Injector), while S_F and η_{0F} (for example) are the sextupole gradient and the lowest order dispersion, at the F chromatic sextupole of thin length Δl. From here on s, as defined in equation 16a, is the sine of the half cell phase advance, and not the azimuthal coordinate.

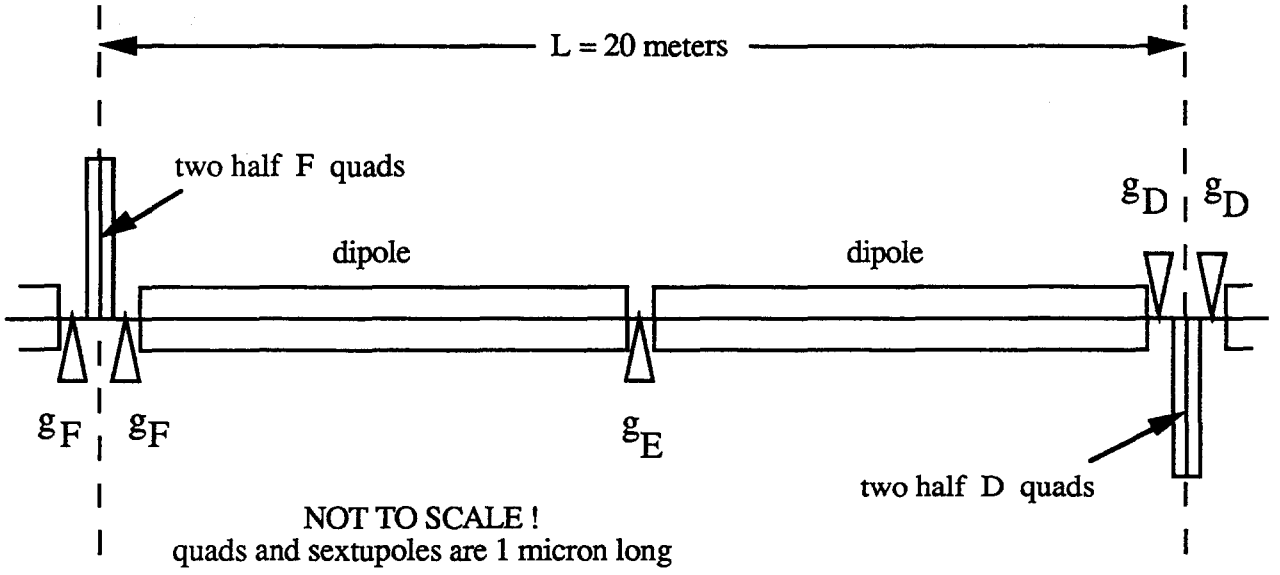

Figure 1 Half of a FODO cell, in a model representing the Main Injector with three sextupole families.

Using these convenient definitions, it can be shown by solving equation 13 that the matched values of the sum dispersion at F, E, and D are

$$\eta_{+F} = \frac{1}{s}\left[\eta_{0F}(1+s)(1-g_F) - \eta_{0D}(1+g_D) - \frac{\eta_{0E}}{2}(2+s)g_E\right] \qquad 17a$$

$$\eta_{+E} = \frac{1}{2s}\left[\eta_{0F}(2+s)(1-g_F) - \eta_{0D}(2-s)(1+g_D) - \frac{\eta_{0E}}{2}(2+s)(2-s)g_E\right] \qquad 17b$$

$$\eta_{+D} = \frac{1}{s}\left[\eta_{0F}(1-g_F) - \eta_{0D}(1-s)(1+g_D) - \frac{\eta_{0E}}{2}(2-s)g_E\right] \qquad 17c$$

Note that $\eta_{+E} = \frac{1}{2}(\eta_{+F} + \eta_{+D})$ when $g_E = 0$, as required by equation 13, which says that the sum dispersion propagates linearly in a quadrupole and sextupole free region. These solutions can be combined to evaluate α_+, since

$$\alpha_+ = \frac{\langle\eta_+\rangle}{R} = \frac{1}{4R}(\eta_{+F} + 2\eta_{+E} + \eta_{+D}) \qquad 18$$

$$= \frac{1}{2sR}\left[\eta_{0F}(2+s)(1-g_F) - \eta_{0D}(2-s)(1+g_D) - \frac{\eta_{0E}}{4}(8-s^2)g_E\right]$$

This expression becomes more direct when the η_0 terms are replaced by their explicit matched solutions

$$\eta_{0F} = \frac{L^2}{R}\frac{2+s}{2\,s^2} \qquad 19a$$

$$\eta_{0E} = \frac{L^2}{R}\frac{8-s^2}{8\,s^2} \qquad 19b$$

$$\eta_{0D} = \frac{L^2}{R}\frac{2-s}{2\,s^2} \qquad 19c$$

Thus, an alternative form for equation 18, parameterized primarily by the sextupoles strengths, is

$$\alpha_+ = \frac{L^2}{R^2}\frac{1}{4s^3}\left[\,8s - (2+s)^2\,g_F - (2-s)^2\,g_D - \frac{(8-s^2)^2}{16}\,g_E\,\right] \qquad 20$$

In order to take stock of the meaning of equation 20, consider the case when only the F and D sextupoles are turned on, at a strength to correct for f times the natural chromaticity.

Independent of the strength of any sextupoles, it can easily be shown that

$$\alpha_0 = \frac{L^2}{R^2}\frac{1}{s^2}\left[\,1 - \frac{s^2}{12}\right] \qquad 21$$

It can also easily be shown that, in order to correct f times the natural FODO chromaticity, $g_F = \frac{f}{2}$ and $g_D = -\frac{f}{2}$, demonstrating the utility of the natural scaling that was introduced, apparently arbitrarily, in equation 16b . Substituting these values (and $g_E = 0$) into equation 20 gives

$$\alpha_+ = \frac{L^2}{R^2}\frac{1}{s^2}\left[\,2 - f\,\right] \qquad 22$$

which immediately leads to

$$\alpha_1 = \frac{L^2}{R^2}\frac{1}{s^2}\left[\,1 - f + \frac{s^2}{12}\right] \qquad 23$$

showing that $\alpha_1 << \alpha_0$ in a simple FODO lattice with the net chromaticity set to zero (f = 1).

CONTROLLING α_1 WITH SEXTUPOLES

The middle sextupole, of strength g_E, can be thought of in (at least) two ways. In the first point of view, it represents the sextupole field caused by eddy currents induced in the vacuum chamber of the dipoles. (Note in passing that this representation is not perfect, since the changes in horizontal and vertical chromaticities are modeled as equal and opposite, whereas in reality they are unequal.) In the second point of view, g_E represents a free knob with which η_+, and hence also α_+ and α_1, can be controlled. The reader may choose either perspective in what follows - or a combination, in which g_E represents the net strength after an independent correction sextupole is powered to over or under compensate the local eddy current sextupole fields. From any perspective, the task of setting the net chromaticities to their desired values is left to the F and D sextupoles. For the sake of a semi-quantitative interpretation, suppose that the F and D sextupoles have their strengths set to compensate for the sum of the chromaticity induced by an eddy current sextupole of strength g_E, plus f times the natural chromaticity.

In this case it is readily shown that the F and D sextupole strengths are given by

$$g_F = \frac{f}{2} - \frac{2 - s^2}{4} g_E \qquad 24a$$

$$g_D = -\frac{f}{2} - \frac{2 - s^2}{4} g_E \qquad 24b$$

Substituting these expressions into equation 20 gives

$$\alpha_+ = \frac{L^2}{R^2} \frac{1}{s^2} \left[(2 - f) - \left(\frac{3}{8}\right)^2 s^3 g_E \right] \qquad 25$$

or, equivalently,

$$\alpha_1 = \frac{L^2}{R^2} \frac{1}{s^2} \left[(1 - f + \frac{s^2}{12}) - \left(\frac{3}{8}\right)^2 s^3 g_E \right] \qquad 26$$

These equations reduce to equations 22 and 23 when $g_E = 0$, as they should. If it is also assumed that the phase advance per cell is (approximately) 90^0, then $s = 1/\sqrt{2}$, and the three compaction factors become simply

$$\alpha_0 = \frac{L^2}{R^2} * 1.917 \qquad 27a$$

$$\alpha_+ = \frac{L^2}{R^2} [\, 4 - 2f - 0.0994 * g_E \,] \qquad 27b$$

$$\alpha_1 = \frac{L^2}{R^2} [\, 2.083 - 2f - 0.0994 * g_E \,] \qquad 27c$$

Typical values for g_E due to eddy current sextupoles in the Main Injector are 2 or 3, showing through equation 24 that they more or less dominate the strength of the F and D families [8].

To test the results of equation 27, and to gain some insight into the prospect of controlling α_1 in the Main Injector, consider a lattice made up of 80 simple FODO cells. In the parameterization introduced above the half cell has a length $L = 20$ meters, and is filled with dipoles of bending radius $R = 3200/2\pi = 509.30$ meters. Figure 2 summarizes results of simulations of such a lattice, using the program MAD (version 8.17)[9] to study the variation in closed orbit path-length as a function of $\Delta p/p$, over a range from -0.003 to $+0.003$. The momentum compaction factor α_P defined by equation A-3 in Appendix A is plotted. Equations A-3 and A-6 are then used to yield values of α_0 and α_1, ready for comparison with the analytic predictions of equations 27a and 27c. Eddy current multipoles higher than sextupole are neglected.

Three cases are considered; no eddy currents with and without complete compensation of the natural chromaticities, $(f,g_E) = (0,0)$ and $(1,0)$, and then complete chromaticity compensation with large but realistic eddy current sextupole strengths, $(f,g_E) = (1,5)$. Each of the plots is linear to a very good approximation, showing that α_0 and α_1 are the dominant coefficients in the α_P expansion. Table 1 shows excellent agreement between the simulated and the predicted values of α_0 and α_1, except for what appears to be a systematic error in α_1 of $0.120 \pm 0.005 \times 10^{-3}$. The source of this small difference is not known, but is not considered to be important. Further comparisons using other design programs are anticipated, to see if the error persists.

If the sextupole family strength parameter g_E is regarded as an external "knob" to control values of α_1, the inevitable conclusion is that the sensitivity to the family is too weak to reduce the Johnsen time to zero, short of using a very large strength or relinquishing control of the net chromaticities. Recall from equation 8 and from Table 1 that the desired value of α_1 is approximately -4.5, but notice that the α_1 sensitivity coefficient in equation 27c is only 0.0994, disappointingly small. This is reflected in the minor changes of α_1 between the second and third rows of Table 1.

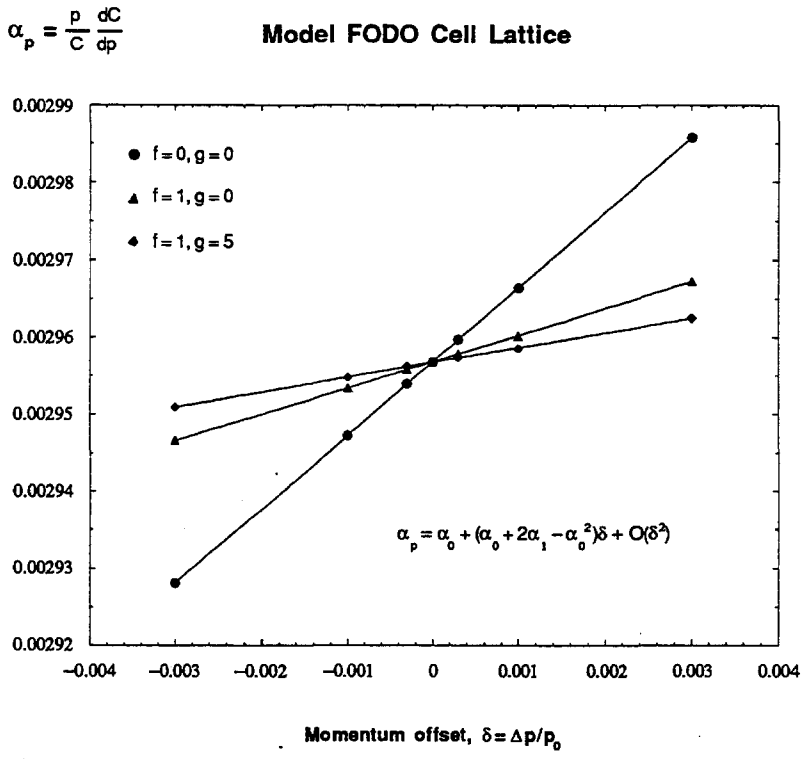

Figure 2 Numerical simulation of momentum compaction factor variation with δ for three configurations of eddy current and chromaticity compensation sextupole strengths.

(f,g_E)	α_0		α_1	
	predicted ($\times 10^{-3}$)	simulated ($\times 10^{-3}$)	predicted ($\times 10^{-3}$)	simulated ($\times 10^{-3}$)
(0,0)	2.956	2.956	3.213	3.332
(1,0)	2.956	2.956	.129	.244
(1,5)	2.956	2.956	−.638	−.512

Table 1 Comparison of predicted and simulated α_0 and α_1 values.

Investigations are currently under way to find an optical configuration that will significantly increase the orthogonality of the three families beyond the unfortunate results of the FODO lattice. An apparently promising candidate involves the introduction of a dispersion wave in the arcs of the Main Injector, around transition time. This begins to resemble an unmatched γ_T jump scheme - except that the lattice perturbation can be introduced slowly, and that the needed size of the dispersion wave is expected to be relatively modest.

BEHAVIOR OF MATCHED AND UNMATCHED γ_T JUMP SCHEMES

The satisfactory agreement between MAD817 simulations and analytic predictions reported in the previous section, for the simple case of a FODO lattice, encourages the use of the program to study the behavior of momentum compaction factors for more realistic Main Injector lattices, where analytic results are no longer tractable. Here we consider two families of Main Injector lattices representing matched and unmatched γ_T jump schemes. These schemes are described in detail elsewhere [10]. It is important to check that the resulting change of α_1 does not greatly affect the Johnsen time T_J, extending the variation of transition crossing time for different parts of a bunch.

The simulation places one thin eddy current sextupoles of strength g_E at the middle of each dipole, with a multipole strength of $b_2 = 0.561\ m^{-2}$. Two families of chromatic sextupoles are used to compensate for both natural and eddy current chromaticities. It is assumed, for the sake of definiteness, that the F and D sextupole strengths are not changed while jumping through transition. Figure 3a summarizes the behavior of the matched scheme with bipolar ($\Delta\gamma_T = \pm 0.65$) and unipolar ($\Delta\gamma_T = -1.3$) excitations. Figure 3b examines an unmatched unipolar excitation - a bipolar jump is not possible in this scheme. The linear character of $\alpha_P(\delta)$ in the realistic range $\delta = -0.01$ to $+0.01$ is apparent in all cases. Note that the vertical scales are significantly different in the two figures - compare the same $\Delta\gamma_T = 0$ case shown in both figures.

Table 2 summarizes the simulation results. Since the arcs in a matched scheme are essentially just a sequence of FODO cells slightly retuned by a quadrupole perturbation, it is expected to produce qualitatively the same results as the FODO lattice in the previous section. Indeed, the values of α_1 recorded in Table 2 are an order of magnitude smaller than α_0, and do not pose any danger to the Johnsen time. By contrast, the unmatched scheme produces large value of $\alpha_1 \approx 1.68\ \alpha_0$, which, according to equation 8, more than doubles the Johnsen time. Also included in Table 2 are the uncorrected chromaticities, ξ_H and ξ_V, with the F and D sextupoles turned off, but with the eddy current sextupoles turned on.

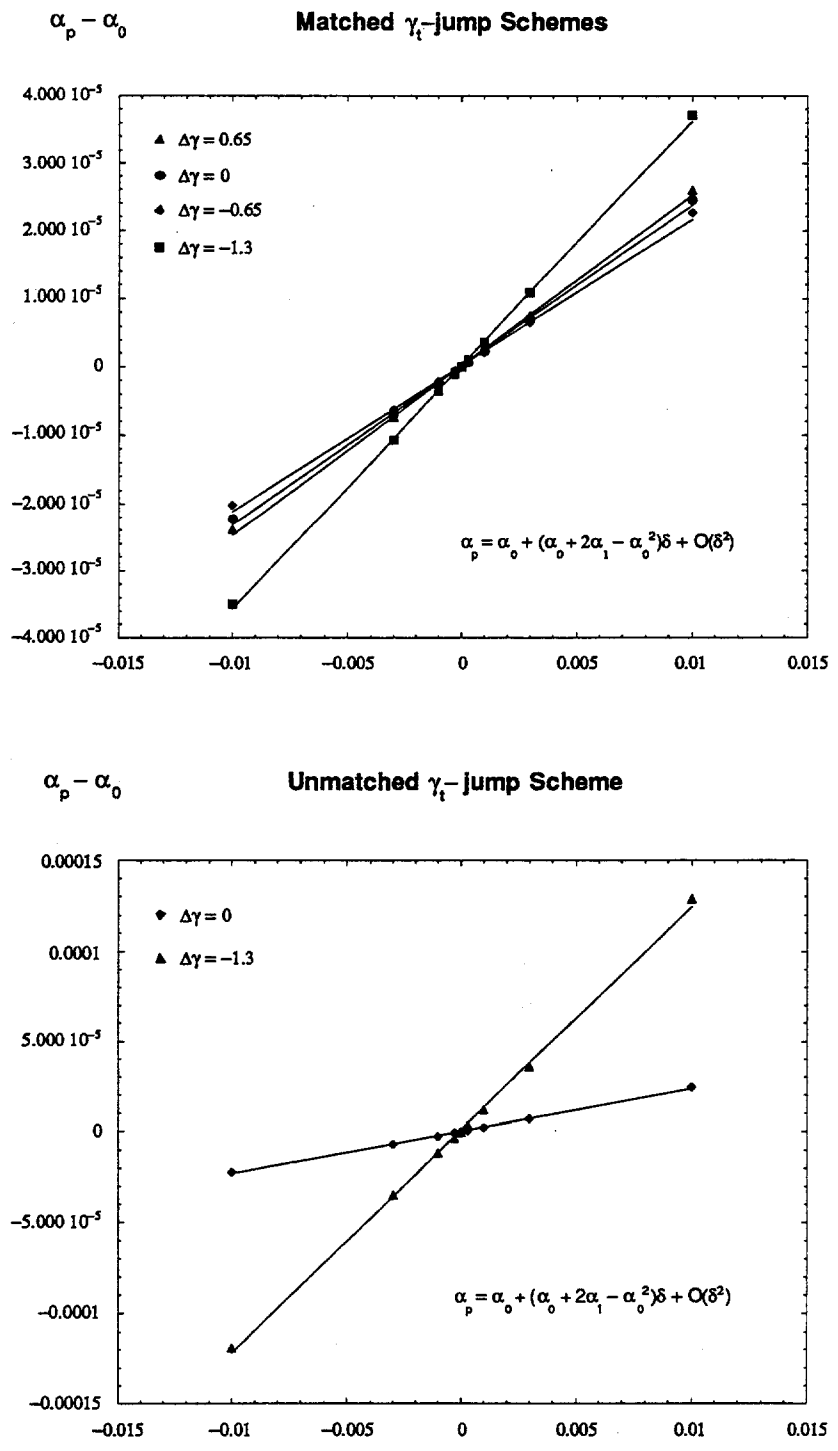

Figure 3 Numerical simulation of momentum compaction factor variation versus δ carried out for various γ_t–jump configurations. The simulation includes eddy current sextupoles and full chromaticity compensation.

Scheme	$\Delta\gamma_T$	α_0 (10^{-3})	α_1 (10^{-3})	ξ_H uncorrected	ξ_V uncorrected
Matched	.65	2.23	.14	−10.6	−46.4
	.0	2.37	−.01	−7.6	−47.3
	−.65	2.53	−.19	−6.4	−48.3
	−1.3	2.70	−.45	−8.5	−49.7
Unmatched	.0	2.37	−.01	−7.6	−47.3
	−1.3	2.70	−4.82	−3.9	−50.1

Table 2 The behavior of momentum compaction coefficients, and of the uncorrected chromaticities, in matched and unmatched Main Injector transition jump schemes.

CONCLUSIONS

General analytical expressions are reported above for the variation of the dispersion function to first order in the off-momentum parameter δ, and for the variation of the closed orbit circumference to second order. This makes it possible to evaluate how the critical Johnsen time (for example) depends on effects like eddy current sextupoles in the Main Injector dipoles, or on transition jump configurations. In the simple but relevant case of a FODO lattice representation of the Main Injector, analytic results are in good quantitative agreement with a lattice design code.

If there is no γ_T jump in the Main Injector, the Johnsen time is typically expected to be about 0.6 milliseconds, or about 60 machine turns. There is no benefit from turning on a γ_T jump much faster than this. Examination of nominal Main Injector transition jump schemes reveals that a matched scheme produces little change in the Johnsen time, but that T_J is more than doubled in the unmatched scheme.

A third family of sextupoles might be used to deliberately and practically control the Johnsen time, without modifying the nominal transition momentum. (Two other sextupole families are used to achieve the desired net chromaticities.) Such control, especially when used in conjunction with RF gymnastics, may make transition crossing so innocuous that it becomes unnecessary to include a transition jump in Main Injector designs.

However, the Johnsen time in a FODO lattice is quite insensitive to a third family of sextupoles located at the middle of the half cells. The good news is, then, that eddy current sextupoles are not expected to significantly affect transition crossing performance. The bad news is that using mid-cell sextupoles to control the Johnsen time is not practical. Continuing investigations suggest that a modest dispersion wave significantly improves the orthogonality of three families of sextupoles.

REFERENCES

1) S.A. Bogacz, *Transition crossing in the Main Injector - ESME simulation*, these proceedings.

2) I. Kourbanis and K.Y. Ng, *Main Ring transition crossing simulations*, these proceedings.

3) K. Johnsen, *Effects of non-linearities on the phase transition*, CERN symposium on high energy accelerators and pion physics, Vol. 1, p. 106, 1956.

4) A. Sorenssen, *Crossing the phase transition in strong focusing proton synchrotrons*, Particle Accelerators Vol. 6, pp. 141-165, 1975. This is an excellent review article.

5) P. Faugeras, A. Faugier, J. Gareyte, *Effets chromatiques et passage de la transition a grand $\Delta p/p$*, CERN SPS Improvement note No. 130, 1978.

6) S. Peggs, *Transition crossing time shifts*, Fermilab note AP 90-004, 1990.

7) J. MacLachlan and J. Griffin, private communication.

8) J-F Ostiguy, *Eddy current induced multipoles in the Main Injector*, Fermilab note MI-0037, October 1990.

9) H. Grote and C. Iselin, *The MAD program users reference guide*, CERN note CERN/SL/90-13 (AP), 1990.

10) A. Bogacz, F. Harfoush, and S. Peggs, *A comparison of matched and unmatched γ_T jump schemes in the Main Injector*, these proceedings.

APPENDIX A. RELATIONS BETWEEN α_1 AND OTHER PARAMETERS

For reference purposes, this appendix describes how the three definitions of α_1 and the one definition of α_P, all of which are common in the literature, are related. It has already been released as Fermilab Main Injector note MI-0038, by MacLachlan, Ng, and Peggs, with only minor differences.

The "circumference" definition of α_1, as defined in equation 1 and used throughout above, comes from expanding the difference in the circumference of the closed orbit, $\Delta C = C - C_0$, as a polynomial in the off momentum parameter, $\delta = (p - p_0) / p_0$,

$$\frac{\Delta C}{C_0} = \alpha_0 \delta + \alpha_{C1} \delta^2 + ... \qquad \text{A-1}$$

The definition introduced by Johnsen is very similar

$$\frac{\Delta C}{C_0} = \alpha_0 \delta + \alpha_0 \alpha_{J1} \delta^2 + ... \qquad \text{A-2}$$

The variation of the transition energy γ_T with δ is directly described by α_P, defined through

$$\alpha_P(\delta) = \frac{1}{\gamma_T^2(\delta)} = \frac{p}{C}\frac{dC}{dp} = \alpha_0 + \alpha_{E1} \delta + ... \qquad \text{A-3}$$

This introduces the ESME definition of α_1 .

Note that equation A-3 represents the <u>local</u> derivative at some momentum p . WARNING - when used with a constant momentum offset, some lattice design codes return $\alpha_P(\delta)$, but some return

$$\frac{p_0}{C_0}\frac{dC}{dp} = \alpha_0 + \alpha_{C1} \delta + ... \qquad \text{A-4}$$

Comparing equations A-1 and A-2 gives

$$\alpha_{J1} = \frac{\alpha_{C1}}{\alpha_0} \qquad \text{A-5}$$

Performing the differentiation in equation A-3 and expanding gives

$$\alpha_{E1} = \alpha_0 + 2\,\alpha_{C1} - \alpha_0^2 \qquad \text{A-6}$$

Although this paper has conveniently taken equation 1 to define $\alpha_1 = \alpha_{C1}$, the selection is (somewhat) arbitrary. The reader is NOT implored to adopt one or another of the definitions introduced here, but rather is asked to be careful to specify which definition he or she is using. He or she IS implored not to invent any more definitions for α_1.

TRANSVERSE EMITTANCE GROWTH DURING γ_T JUMP

King-Yuen Ng

Fermi National Accelerator Laboratory, P.O. Box 500, Batavia, IL 60510*

I. INTRODUCTION

Acceleration of a particle beam across transition will usually lead to an increase in the bunch area and a loss in beam intensity. This is because (1) different particle crosses transition at different time leaving behind two tails in the longitudinal phase space, and (2) the beam becomes microwave unstable when the phase-slip factor $\eta = 1/\gamma_T^2 - 1/\gamma^2$ is negligibly small. Tracking simulation[1] indicates that particle loss will be about 20% and the bunch area growth can be a factor of $2 \sim 3$ for the proposed Fermilab Main Injector. These problems can be avoided by implementing a γ_T jump system, which consists of pulsing quadrupole magnets to change the optics of the accelerator in such a way as to drop γ_T of the machine *instantly* as the beam approaches transition. Under this situation, the particles cross transition so fast that none of the nuisances mentioned above would have time to develop. However, changing the optics of the ring instantly will lead to a sudden growth in the transverse emittance of the beam, which is certainly undesired. To preserve the transverse emittance, the γ_T jump has to be performed adiabatically. It is the purpose of this paper to find out the shortest time of the jump so that the transverse emittance will not be disturbed significantly.

II. THE MODEL

Consider the particle in the bunch which has the largest fractional energy offset δ (corresponding to 95% bunch area). This particle has a maximum transverse offset of $X_p^i\delta$ from the synchronous orbit, where X_p^i is the maximum momentum dispersion of the ring. Now for the performance of γ_T jump, the quadrupoles are pulsed so that the maximum dispersion changes to the final value of X_p^f in n turns. Suppose that the

*Operated by the Universities Research Association, Inc., under contract with the U.S. Department of Energy.

dispersion is changed evenly as $k = (X_p^f - X_p^i)/n$ per turn. Therefore, this particle is performing betatron oscillations about a different closed orbit in a different turn.

The equation of motion of x, the transverse displacement of the particle from the synchronous orbit, is, in our simplified model,

$$x'' + K(s)(x - X_p\delta) = 0 \ , \tag{2.1}$$

where the prime is differentiation with respect to s, the distance measured along the synchronous orbit from some reference point where the dispersion is a maximum and the betatron function β is a local maximum, $K(s)$ is the quadrupole strength, and

$$X_p = X_p^i + mk \ , \tag{2.2}$$

is the our assumed dispersion for the mth turn. This is the model of of an oscillator driven by a force $K(s)X_p\delta$, which changes abruptly whenever the particle passes through the reference point at every turn. The particle position x as well as the angle x' are therefore continuous at the reference point. This model is reasonable because the pulsing of the quadrupoles during the γ_T jump is performed in such a way that the phase advance and tune of the accelerator ring are essentially unchanged.

According to the equation of motion, the transverse position of the particle at the mth turn relative to the synchronous orbit is

$$x_m = (X_p^i + mk)\delta + a_m \cos\psi + b_m \sin\psi \qquad m = 0,\ 1,\ 2,\ \cdots \ , \tag{2.3}$$

where ψ is the Floquet phase advance along the synchronous orbit measured from some reference point. For every revolution around the ring ψ increases by $\mu = 2\pi\nu$, where ν is the betatron tune. For convenience, we set $\psi = 0$ at the beginning of every turn. In general a_n and b_n are proportional to the square root of the betatron function β along the ring. However, since we are interested in only the reference point, we have

$$\begin{aligned} x_m{}^- &= (X_p^i + mk)\delta + a_m && \text{beginning of } m\text{th turn}, \\ x_m{}^+ &= (X_p^i + mk)\delta + a_m\cos\mu + b_m\sin\mu && \text{end of } m\text{th turn}, \end{aligned} \tag{2.4}$$

and

$$\begin{aligned} x_m'{}^- &= \frac{b_m}{\beta} && \text{beginning of } m\text{th turn}, \\ x_m'{}^+ &= -\frac{a_m}{\beta}\sin\mu + \frac{b_m}{\beta}\cos\mu && \text{end of } m\text{th turn}. \end{aligned} \tag{2.5}$$

Here, a_m and b_m/β represent the betatron oscillation amplitude and angular deviation at the reference point. The emittance of this off-energy particle is therefore given by

$$\epsilon = \pi\gamma\frac{r_m^2}{\beta} \qquad \text{with} \qquad r_m = \sqrt{a_m^2 + b_m^2} \ . \tag{2.6}$$

From the continuation of x_m and x'_m across the reference point, we obtain

$$\begin{aligned} a_m &= -k\delta + a_{m-1}\cos\mu + b_{m-1}\sin\mu \ , \\ b_m &= -a_{m-1}\sin\mu + b_{m-1}\cos\mu \ . \end{aligned} \tag{2.7}$$

The eventual maximum transverse displacement of the particle will be given by

$$x_{\max} = X_p^f\delta + r_n \ , \tag{2.8}$$

where r_n is the betatron amplitude at the nth turn.

III. SPECIAL CASES

1. Integer tune

If the tune ν is an integer, the particle returns to its original position after each turn, although the off-energy closed orbit is altered every turn. Thus the betatron amplitude is always equal to $mk\delta$ in the mth turn, if we start with $a_0 = b_0 = 0$. The final transverse displacement is therefore

$$x_{\max} = X_p^f\delta + nk\delta = (2X_p^f + X_p^i)\delta \ , \tag{3.1}$$

which is the same as having the quadrupole pulsed to the final value in only one turn.

2. Half-integer tune

Starting from $a_0 = b_0 = 0$ and a half-integer tune, it is obvious that $b_n = 0$. Since the off-energy closed orbit changes by the same amount every turn, the displacement of the particle can be followed easily. The results for the first 7 turns are listed in Table I. We see that the amplitude of betatron oscillation r_n is either zero or one unit of the shift of the off-energy closed orbit $k\delta$ depending on whether the turn number is even or odd. Therefore, the maximum transverse displacement of the beam is

$$x_n = \left[X_p^f + \frac{1}{n}(X_p^f - X_p^i)\right]\delta \ . \tag{3.2}$$

Turn No.	Dispersion Change in k	a_n in $k\delta$	
		beginning	end
0	0	0	0
1	1	−1	1
2	2	0	0
3	3	−1	1
4	4	0	0
5	5	−1	1
6	6	0	0

Table I: Betatron oscillation amplitude for the first 7 turns at half-integer tune

IV. GENERAL SOLUTION

With any other tunes, the betatron oscillation of the particle is in between the worst scenario of integer tune and the best scenario of half-integer tune. The betatron oscillation amplitude of the off-energy particle can be computed from Eqs. (2.7), which we rewrite as

$$\begin{pmatrix} a_n \\ b_n \end{pmatrix} = O \begin{pmatrix} a_{n-1} \\ b_{n-1} \end{pmatrix} - \begin{pmatrix} 0 \\ k\delta \end{pmatrix} , \tag{4.1}$$

where

$$O = \begin{pmatrix} \cos\mu & \sin\mu \\ -\sin\mu & \cos\mu \end{pmatrix} \tag{4.2}$$

is the transportation matrix of one revolution around the ring from the quadrupole back to the quadrupole or just the rotation matrix of an angle μ. We can easily iterate Eq. (4.1) to give

$$\begin{pmatrix} a_n \\ b_n \end{pmatrix} = O^n \begin{pmatrix} a_0 \\ b_0 \end{pmatrix} - \sum_{m=1}^{n} O^{n-m} \begin{pmatrix} 0 \\ k\delta \end{pmatrix} . \tag{4.3}$$

If the initial betatron oscillation is negligibly small or $a_0 \sim 0$, $b_0 \sim 0$, Eq. (4.3) reduces to

$$\begin{pmatrix} a_n \\ b_n \end{pmatrix} = -k\delta \sum_{m=1}^{n} \begin{pmatrix} \cos(n-m)\mu \\ \sin(n-m)\mu \end{pmatrix} , \tag{4.4}$$

which can be summed easily to give

$$\begin{pmatrix} a_n \\ b_n \end{pmatrix} = -k\delta \begin{pmatrix} \mathcal{R}e \\ \mathcal{I}m \end{pmatrix} e^{-i\frac{n-1}{2}\mu} \frac{\sin\frac{n}{2}\mu}{\sin\frac{1}{2}\mu} , \tag{4.5}$$

or

$$\begin{pmatrix} a_n \\ b_n \end{pmatrix} = -k\delta \begin{pmatrix} \frac{\sin\frac{n}{2}\mu\cos\frac{n-1}{2}\mu}{\sin\frac{1}{2}\mu} \\ \frac{\sin\frac{n}{2}\mu\cos\frac{n-1}{2}\mu}{\sin\frac{1}{2}\mu} \end{pmatrix} . \tag{4.6}$$

The betatron oscillation amplitude is therefore

$$r_n = \frac{\Delta X_p \delta}{n} \left| \frac{\sin\frac{n}{2}\mu}{\sin\frac{1}{2}\mu} \right| , \tag{4.7}$$

where we have made the substitution $k = \Delta X_p/n = (X_p^f - X_p^i)/n$.

It is clear from Eq. (4.7) that when the betatron tune is an integer, nothing can be gained by pulsing the quadrupoles adiabatically, as was pointed out in Section III. When the tune is of half-integer, the result of Section III.2 is reproduced.

As is shown in Eq. (4.7), r_n is very sensitive to the tune. For example, if the residual tune $[\nu] = 0.25$, r_n vanishes exactly whenever n is a multiple of 4. This peculiar result comes about because a_0 and b_0 are not exactly zero to begin with and that our model, Eq. (2.1), has been too simple. In order to obtain a more meaningful result, we replaced $|\sin n\mu/2|$ by its maximum value unity, except when the tune is very near to an integer. Then the betatron amplitude becomes

$$r_n = \frac{\Delta X_p \delta}{n} \left| \frac{1}{\sin\frac{1}{2}\mu} \right| . \tag{4.8}$$

We see that the last factor is roughly less than 2 when the residual tune is between 0.15 and 0.85.

V. ADIABATIC CRITERION

We would like the final betatron oscillation much less than the initial betatron oscillation. Therefore, the adiabatic criterion is

$$\frac{\Delta X_p \delta}{n} \frac{1}{\left|\sin \frac{1}{2}\mu\right|} \ll A_\beta \ , \tag{5.1}$$

where A_β is the amplitude of betatron oscillation at maximum β before transition, which is related to the normalized emittance ϵ by

$$\epsilon = \pi\gamma \frac{A_\beta^2}{\beta} \ . \tag{5.2}$$

For the Main Injector, $\epsilon = 20\pi$ mm-mr (95%), maximum $\beta = 57$ m, and $\gamma_T = 20.4$. Therefore $A_\beta = 0.00748$ m. One proposal[2] of γ_T jump boosts the momentum dispersion according to

$$X_p = 2.2 + 4.8(\Delta\gamma_T)^{\frac{1}{2}} \text{ m}, \tag{5.3}$$

or $\Delta X_p = X_p^f - X_p^i = 4.8$ m for $\Delta\gamma_T = 1$. The fractional momentum spread is

$$\delta = 6.00 \times 10^{-3} \Delta\gamma_T^{-\frac{1}{4}} \left(\frac{S}{0.4 \text{ eV-s}}\right)^{\frac{1}{2}} \left(\frac{V_{\text{rf}} \cos\phi_0}{2.78 \text{ [MV]} \cos 37.6^\circ}\right)^{-\frac{1}{4}} \ . \tag{5.4}$$

The proposed tune is $\nu = 22.42$, giving $1/|\sin\mu/2| = 1.032$. In order that the nonadiabatic increase in transverse phase space is less than 1%, the minimum number of turns for pulsing the quadrupole should be 40 or for a minimum pulsing interval of 0.44 ms. This gives $\dot{\gamma} = 2260$ sec^{-1}. If a jump of $\Delta\gamma_T = 1.5$ is preferred, $X_p^f - X_p^i = 5.88$ m and $\delta = 5.42 \times 10^{-3}$. The minimum number of turns becomes 44 or 0.49 ms, corresponding to $\dot{\gamma} = 2050$ sec^{-1}. Note that if the tune were far away from an half-integer, the minimum number of turns would become much bigger.

REFERENCES

1. J. Wei, *Transition Crossing in the Main Injector*, these proceedings.

2. S.D. Holmes, *Main Injector Transition Jump*, Fermilab Internal Report MI-0008, 1989.

BETATRON ADIABATICITY DURING A γ_T JUMP

S.G. PEGGS
Fermi National Accelerator Laboratory

INTRODUCTION

An off-momentum proton undergoing betatron oscillations around a closed orbit has a total horizontal displacement of

$$x_P = a_P(s)\cos(\phi(s)+\phi_0) + \eta_P(s)\,\delta \qquad 1$$

where $\delta = \frac{\Delta p}{p}$ is the off-momentum displacement, a_P is the betatron amplitude, η_P is the dispersion function, and $\phi(s)$ is the betatron phase at a distance s around the machine azimuth from a $\phi(0)=0$ reference point. The subscript p stands for 'physical' coordinates, as opposed to 'normalized' coordinates (which, below, carry no subscripts). In normalized coordinates, displacements x_P and η_P are divided by $\sqrt{\beta(s)}$, and rotation in phase space is circular, so that

$$\begin{aligned} x &= a\cos(\phi_\beta) + \eta(s)\,\delta \\ x' &= a\sin(\phi_\beta) + \eta'(s)\,\delta \\ \phi_\beta &= \phi(s) + \phi_0 \end{aligned} \qquad 2$$

where x' is the normalized transverse angle. In the linear approximation assumed here the normalized betatron amplitude a is constant. If the unperturbed Main Injector is crudely represented as a pure FODO cell lattice, it is reasonable to approximate the normalized dispersion η as a constant, and its slope η' as zero.

When a pure FODO cell lattice is perturbed in a γ_T jump scheme, the goal is to modify the average value of the dispersion function. In an "unmatched" scheme, a large dispersion wave circulates the lattice. Assuming that the perturbation is turned on linearly in a time of τ accelerator turns, the (normalized) dispersion becomes

$$\begin{aligned} \eta &= \eta_0\left[\,1 + \alpha\frac{t}{\tau}\cos(\phi_\eta)\,\right] \\ \eta' &= \eta_0\,\alpha\frac{t}{\tau}\sin(\phi_\eta) \end{aligned} \qquad 3$$

$$\phi_\eta = \phi(s) + \phi_1$$

Here the dimensionless parameter $\alpha \equiv (\eta_{MAX} / \eta_0) - 1$ measures the strength of the dispersion wave. Its value is $\alpha = (9.59 / 2.07) - 1 = 3.6$ in the case of the unmatched γ_T jump scheme reported elsewhere in these proceedings [1]. By contrast, the dispersion during a "matched" γ_T jump is given by

$$\eta = \eta_0 [\, 1 + \alpha \frac{t}{\tau} \,] \qquad 4$$

$$\eta' = 0$$

where now the parameter α represents the size of a constant dispersion offset, equal to 0.11 in the scheme also reported in these proceedings [1].

Suppose that there is an instantaneous small change in dispersion at a fixed azimuthal location, given in terms of amplitude D and phase θ by

$$\Delta\eta = D \cos(\theta), \qquad \Delta\eta' = D \sin(\theta) \qquad 5$$

It is easily shown that there is a corresponding instantaneous change in betatron amplitude, given by

$$\Delta a = -D \delta \cos(\phi_\beta - \theta) \qquad 6$$

where ϕ_β is the betatron oscillation phase of a particular trajectory at that point. This discrete equation must be transformed into a differential equation, in order to evaluate the total effect that an unmatched or a matched γ_T jump scheme has on the amplitude of a given particle. In the case of an unmatched scheme, the dispersion change in equation 5 is given, for a small time step of Δt, by

$$D = \frac{\alpha \eta_0}{\tau} \Delta t, \qquad \theta = \phi_\eta \qquad 7$$

so that

$$\frac{da}{dt} = - \frac{\alpha \eta_0 \delta}{\tau} \cos(\phi_\beta - \phi_\eta) \qquad 8$$

The differential equation is slightly but significantly different for a matched scheme, since in this case $\theta = 0$, so that

$$\frac{da}{dt} = -\frac{\alpha \eta_0 \delta}{\tau} \cos(\phi_\beta) \qquad 9$$

The consequences of equations 8 and 9 are now evaluated for unmatched and matched γ_T jump schemes.

"UNMATCHED" γ_T JUMP SCHEME

In an unmatched scheme, the two phases in equation 8 are given, on turn number T, by

$$\phi_\beta = 2\pi Q\, T + \phi(s) + \phi_0, \qquad \theta = \phi(s) + \phi_1 \qquad 10$$

where Q is the betatron tune. (It is important to note that T is an integer, advancing discretely at the end of every turn, while t is continuous, advancing smoothly). Substituting 10 into 8 shows that the cosine term is constant during each individual turn, so that the amplitude at the end of turn T is given by

$$a(T) = a(T-1) - \frac{\alpha \eta_0 \delta}{\tau} \cos[\, 2\pi Q\, T + (\phi_0 - \phi_1)\,] \qquad 11$$

Adjusting the constant phase $\phi_0 - \phi_1$ to be π, in a worst case analysis, the amplitude growth after τ turns is given by

$$a(\tau) - a(0) = \frac{\alpha \eta_0 \delta}{\tau} \sum_1^t \cos(2\pi Q t) = \frac{\alpha \eta_0 \delta}{\tau} \left| \frac{\sin(\pi Q \tau)}{\sin(\pi Q)} \right| \qquad 12$$

This demonstrates the possibility of a resonant build up of size $\alpha \eta_0 \delta$, if Q and $Q\tau$ are both close to an integer. In general, however, this will not be the case, and it is reasonable to replace the term inside the absolute modulus brackets by the value 1 .

A practical demand to place on the minimum jump rise time τ is that the typical fractional increase in betatron amplitude should be much less than one. That is,

$$\frac{a(\tau) - a(0)}{\sigma_\beta} = \frac{\alpha}{\tau} \frac{\sigma_p}{\sigma_\beta} \ll 1 \qquad 13$$

Since $\frac{\sigma_p}{\sigma_\beta}$, the ratio of root mean square beam sizes due to momentum offsets and betatron oscillations, is of approximately 10 at transition, and recalling that $\alpha \approx 3.6$ in the unmatched scheme, it is reasonable to demand that

$$\tau \gg 40 \qquad 14$$

That is, the rise time for turning on an unmatched γ_T jump should be at least 40 turns, in order to avoid unreasonable growth in the betatron size of the beam.

"MATCHED" γ_T JUMP SCHEME

The situation is much less severe in the case of a matched scheme, which is almost trivial to describe. In this case there is strong phase averaging during a single turn, since it is reasonable to approximate the betatron phase by

$$\phi_\beta = 2\pi Q t + \phi_0 \qquad 15$$

After substitution into 9 and integration gives

$$a(T) = a(T-1) - \frac{\alpha \eta_0 \delta}{\tau} \frac{\cos(2\pi Q(T+1/2) + \phi_0) \sin(\pi Q)}{\pi Q} \qquad 16$$

The numerator in the final term here is of order one, but the denominator πQ is approximately 60, reducing the amplitude growth considerably. Even in a worst case analysis, there is no need to apply a lower bound on τ in the case of a matched scheme.

CONCLUSIONS

In a matched γ_T jump scheme, there is no need to place a lower limit on the rise time of the perturbation quadrupoles.

In an unmatched γ_T jump scheme, it is necessary that the rise time of the perturbation quadrupoles be at least 40 accelerator turns, about 0.4 milliseconds, in order that there shall not be significant transverse emittance blow up. This estimate is consistent with the one reached

independently by Bill Ng, also reported in these proceedings [2]. It is probably not, in practice, a significant restriction.

REFERENECES

1) A. Bogacz, F. Harfoush, and S. Peggs, *A comparison of matched and unmatched γ_T jump schemes in the Main Injector*, these proceedings.

2) K.Y. Ng, *Betatron adiabaticity during a γ_T jump*, these proceedings.

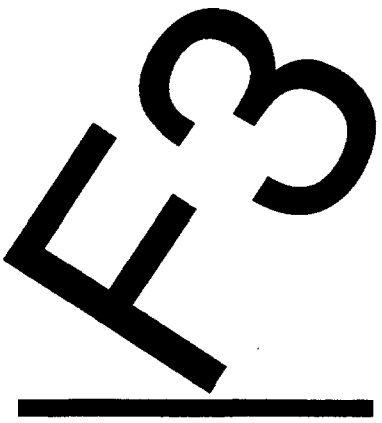

TRANSVERSE INSTABILITIES AND IMPEDANCES

TRANSVERSE INSTABILITY AND IMPEDANCE ISSUES FOR THE FNAL MAIN INJECTOR UPGRADE -- A SUMMARY

S. Chattopadhyay*, R. Cappi**, P. Colestock†, J. Crisp†, W. Gai††,
G. Jackson†, C. Moore†, D. Neuffer†††, S. Saritepe†, P. Zheng†

(Reported by: S. Chattopadhyay)

1. Review of Present Status and Knowledge

None of the existing FNAL accelerators and storage rings are presently known to be limited by transverse instabilities. However, there exists no precise knowledge about "how far from instability" these machines are safely operating in reality. There are reasons to suspect that some of these accelerators may be at the border of, or not too far from instability. Knowledge of transverse phenomena, presently observed or anticipated, for the specific accelerators are summarized below:

LINAC: A new 200 MeV, 850 MHz side-coupled RF structure will be used as linac in the present upgrade project. No calculations exist, but estimation of transverse Beam Break-Up (BBU) effect with the upgrade parameters will be desirable. Presently, there is no knowledge of potential problems.

DEBUNCHER: At present, there is too little intensity in this machine for instabilities to occur operationally. None are expected with the upgrade either.

ACCUMULATOR: Present limitations are due to multiple intrabeam scattering and ion trapping by antiprotons. Suspicious transverse growths have been observed in the past, but no data points to transverse instabilities. The impedance posed to the beam is expected to be dominated by the stochastic cooling hardware, e.g. pick-ups, etc. These have been estimated. Calculations of the instability thresholds for current should be straightforward to perform with the upgrade parameters.

BOOSTER: Though there are no operational transverse instabilities, there is occasional "fast" beam loss around "transition." Since peak current increases roughly by a factor of two at transition and the upgrades call for an increase of current by a factor of three, the booster need to be studied. Transverse problems are expected.

MAIN RING: A lot of calculations have been done on Main Ring instabilities, all using calculated transverse impedances. There is a known vertical instability at injection, and another just as the beam reaches maximum energy. Head-tail instability has been a problem because the Main Ring sextupoles are not currently strong enough to produce large enough positive chromaticities. Higher order RF modes need to be studied, since the RF cavities will be recycled in the main injector ring.

TEVATRON: Suffers from basically the same problem as in the Main Ring, except for different reasons and probably different impedances.

This work was supported by the Director, Office of Energy Research, Office of Basic Energy Sciences, Materials Sciences Division, of the U.S. Department of Energy under Contract No. DE-AC03-76SF00098.

*LBL; **CERN; †FNAL; ††ANL; †††LANL

Estimates of transverse limitations for the FNAL upgrade will require knowledge of the transverse impedances in the accelerators involved. At present, there are no measurements of transverse impedances available for any of the FNAL accelerators. Currently, there are plans to make measurements with the beam, both bunched and unbunched, in the Booster, Accumulator, Main Ring and the Tevatron. In addition, a program of "bench measurement" of impedances on spare beamline structures in electronics laboratory has just been initiated. These are basically wire measurements in which a network analyzer is use to simulate harmonic beam signals, such that impedance vs. frequency data may be obtained.

Transverse dampers have been used occasionally at FANL to stabilize beams. There exist both analog "slow dampers" and digital bunch-by-bunch "superdampers". However, FNAL has had very spotty success with the design and operation of these transverse damping systems. In particular, there is no knowledge of their ultimate capacity and effectiveness. Such knowledge will be important for their applicability to the upgrade. Studies of the limits of the present dampers have just started and exploring new types of dampers for the future is an area of active interest now operationally.

2. Required Present and Future Work

It was the opinion of the working group that the following topics need to be addressed and worked on for all FNAL accelerators involved in the upgrade:

A. Impedance Measurement and Estimate Program

(i) Bench measurement in the laboratory
(ii) Measurement with beam in the rings
(iii) Calculation from realistic models and simple estimation of transverse impedance from existing longitudinal data.

B. Estimates and calculation of Transverse Instabilities (threshold currents, growth rates, etc.)

C. Diagnostics and cures (feedback dampers especially).

D. Measurement of instabilities via controlled experiments on beams.

The topics B and C would have significant implications for Landau Damping and required feedback capacity. All four rings, the Booster, Accumulator, Main Ring/Main Injector and the Tevatron would have to be subjected to the topics A through D above for a full evaluation of the FNAL upgrade.

In the limited effort during the workshop, we had made an attempt to address issues A through D, albeit in a sketchy fashion and to provide recommendation for future work. We report them in the following discussion, in that order.

3. Impedance Measurement and Estimation

(a) Bench measurement

Many devices, such as RF cavities and ferrite kickers, have been measured in the laboratory to ascertain their longitudinal impedance. Based on discussions within the transverse instability group, it is clear that it is imperative to initiate a transverse impedance measurement program.

The longitudinal measurements were done using the now standard synthetic pulse technique. Basically, a current carrying wire strung down the center of the vacuum chamber simulates the beam. By measuring the change of amplitude and phase of a sine-wave signal (reflected *or* transmitted), one can calculate the longitudinal impedance of a structure.

The present plan is to execute the transverse measurements in a similar manner. Transverse measurements are expected to be more subtle and sensitive than the longitudinal ones, but with care can certainly be performed. In order to make a signal which mimics the transverse motion of the beam, and to simultaneously detect the deflecting wakefields generated by the transverse impedance of the device under test, a balanced pair of wires will be used. The characteristic impedance of this transmission line will be 200 Ω for reasons of simplicity of construction, reasonable tolerances and sensitivity. The 50 Ω coax to 200 Ω balanced pair transformer has been designed and construction has begun. It is envisioned that once the experimental hardware has been perfected, a cylindrical pill-box RF cavity will be measured first. Since the deflecting modes can be calculated both analytically and using finite-element codes, a comparison of measurement, simulation, and theory will verify the validity and accuracy of this technique.

The working group recommends that the following devices be tested for their transverse impedance, as listed in TABLE-I below.

TABLE-I

Booster	Accumulator	Main Ring/Main Injector	Tevatron
• RF cavity • Dipole magnets • Kickers	• Cooling PUs and kickers dominate, but their responses are known. No measurements are necessary.	• BPMs • RF cavity • Kickers • Lambertson • Bellow • Shielded bellow	• RF cavity • Separators • Kickers • BPMs • Bellows

In the Booster, the dipole magnets are expected to dominate the transverse impedance. This prejudice stems from the fact that there is no beam pipe inside the dipole magnets, whose laminations are thus exposed to the beam. Image currents are flowing along laminations, which have a very odd cross-section. Moreover, these magnets are of the combined-function type. It is expected that the horizontal impedance will be a function of the vertical position and vice-versa, thus coupling the two degrees of freedom. In addition, the effect of the magnet sagitta on the measurements must be understood.

The Booster RF cavities should be measured to find if there are any high-Q modes which may cause transverse coupled bunch instabilities. Both horizontal and vertical impedance should be measured, since the power feed and bias stems break the cylindrical symmetry of the cavities.

The Booster kicker magnets are of the window-frame variety, and therefore could have extremely high transverse impedances. Since these measurements will also be done on the Main Ring/Main Injector and Tevatron kickers, this should only require a minimal amount of extra work for the sake of completeness.

In the Accumulator, the various stochastic cooling pickups and kickers should dominate the transverse impedance in the region above 1 GHz. Their impedance has been well calculated and measured. Therefore no bench measurements of Accumulator structures are necessary, unless some low frequency structure is expected to be troublesome.

The Tevatron is considered to be the cleanest machine at Fermilab from a transverse impedance point of view. But measurement of the transverse impedance of the Tevatron is important for two reasons: first, since the intensities expected in the machine in the various upgrade stages are rapidly increasing, present instabilities will get worse and new instabilities will begin. Therefore, objects which are suspected of having large transverse impedances (e.g., RF cavities, kickers, BPMs, bellows) should be measured. Second, the helical orbit upgrade for the Tevatron collider requires twenty electrostatic separator tanks, whose primary purpose is to

provide transverse deflections. Estimates of the transverse impedance of a tank suggest that coupled bunch instabilities may become a problem.

Because many components in the Main Ring will be transferred over into the Main Injector, it is important to measure their transverse impedance now while there is time to make corrective modifications. Two cases in point are the RF cavities and the Lambertsons. In addition, it is important to understand how to build low impedance kicker magnets.

The present Main Injector design calls for the construction of Tevatron type stripline beam position monitors to replace the present Main Ring split-box detectors. The basis of this decision was the prejudice that the split-box geometry had a much higher transverse impedance. Certainly, Main Ring and Tevatron monitors should be measured and compared to justify this decision.

The subject of bellows and their shielding has been posed in the past with regards to the Main Ring. During an extended shut-down, "Z/n" parts were added to every major bellow in the Main Ring. In order to understand the effect of bellows and their shields on Main Injector performance, transverse and longitudinal impedance measurements are necessary.

An integral part of the bench measurements is the theoretical understanding and simulation modeling of the results. Both analytical study for simple devices and finite-element computation for complicated devices are necessary, in order to compare with measurements. In addition, understanding the computations by finite-element methods for three-dimensional geometries involving ferrite materials will be desirable.

(b) Beam measurement

In addition to bench measurements of beamline structures, spare or otherwise available, in the laboratory whenever possible, the working group strongly recommends measurement of the total transverse impedance of all the rings via direct excitation of the circulating beam. Such a measurement gives direct information about the total ring impedance seen by the beam in circulating the ring in all its phenomenological aspects. There are various methods of direct beam measurement of the ring impedance. One could measure the coherent transverse tune ($\nu_\perp$) or coherent synchrotron tune (ν_s) as a function of beam current (I), for given bunch lengths (σ_ℓ), for example. Controlled rate of head-tail instability growth (τ_g) as a function of chromaticity (ξ) also yields information on transverse impedance. A transverse beam transfer function (BTF) measurement via a network analyzer is probably the most straightforward. While such a measurement will be relatively easy for the Main Ring and the Tevatron and will probably be unnecessary for the Accumulator (owing to its well estimated impedance), it poses the greatest challenge for the Booster. This is so because of two reasons: it is very important to measure the total Booster transverse impedance and it is probably most difficult to do so because of the ramped nature of the Booster, with ramping times of typically ten milliseconds. Measurements will therefore have to be relatively fast during ramping the beam. We illustrate via an example, for expository purposes, a possible technique for measuring the Booster transverse impedance during ramping in the following. One can measure the imaginary part, $\mathrm{Im}(z_\perp)$, of the transverse impedance from the coherent betatron frequency shift $\mathrm{Re}(\Delta\omega_\beta^m)$ in the m^{th} synchrotron satellite:

$$\mathrm{Re}(\Delta\omega_\beta^m) = -\frac{N_b e c}{4\pi^2 Q\beta(E/e)\sigma_\tau} \cdot \frac{1}{(m+1)}[\mathrm{Im}(z_\perp)]$$

where N_b is the number of particles per bunch, Q the betatron tune, σ_τ the rms bunch length, E the energy and $\omega_{\beta m} = (n+Q)\omega_0 + m\omega_s$ is the frequency in the m^{th} synchrotron band for the betatron line near n^{th} revolution harmonic. For an 8 GeV beam with 3×10^{10} p/bunch, $4\sigma_\tau \approx 10$ns and $Q \approx 6.8$, one obtains,

$$\mathrm{Re}\left(\Delta\omega_\beta\right)_{m=0} \approx 270 \times 10^{-6}\, z_\perp$$

A possible signal analysis scheme is shown in Fig. 1 below.

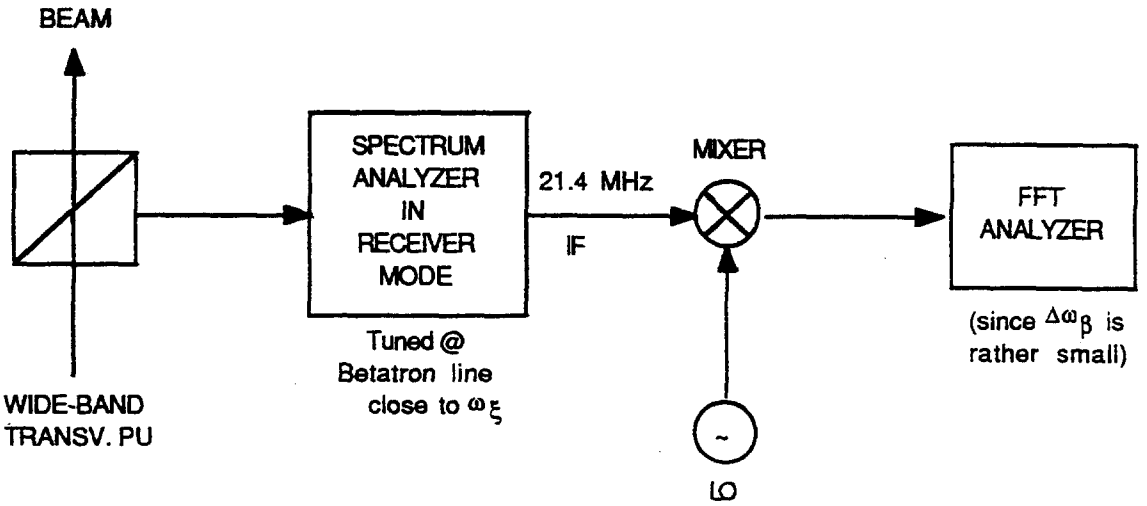

FIGURE 1

Assuming a longitudinal impedance for the Booster of $|z_\parallel/n| \sim 100\ \Omega$ (J. Crisp, private communication), one can speculate a transverse impedance, $z_\perp = \frac{2c}{b^2 w_0}\left|\frac{z_\parallel}{n}\right|$, of 30 $M\Omega/m$ (b = 3cm). Expected observable frequency shift is thus

$$\mathrm{Re}\left(\Delta\omega_\beta\right)_{m=0} \approx 2\pi \times 1.3\ \mathrm{kHz}$$

If we demand a resolution of 20% (260 Hz), one would require a measurement time of about 3.5 ms, just barely doable.

4. Instability Estimates

The working group recommended the following topics and agenda for future work on instability estimates:

(a) In absence of data on transverse impedances, estimate limits *or "upper bounds"* on $z_\perp$, (both resistive and reactive and both resonant and nonresonant), from various instability considerations.

(b) Estimate allowable *"reactive"* components (leading to coherent tune shifts) in relation to *available frequency spreads* in the beam (from space-charge, octupoles, synchrotron tune spreads, etc.). This is the fundamental issue of *Laundau Damping*, e.g., estimated $(z_\perp)_{\mathrm{reactive}}$ for Booster may significantly exceed the allowable value for Landau Damping.

(c) Compute what "octupolar" pattern, strength and arrangement would be desirable for all rings to obtain nonlinear tune-spreads.

(d) Once impedances are known, do a thorough computation of beam instabilities using any of the existing codes such as BBI, ZAP, etc.

All the tools and some expertise already exist at Fermilab. Development of more expertise was deemed desirable.

For the sake of exposition, the group attempted to obtain scaled estimates of instabilities for the Booster. This is given below.

The FNAL upgrade requires the Booster to handle 6×10^{10} protons/bunch, with transverse emittance of $\epsilon_\perp = 20\pi$ mm-mrad and longitudinal emittance of $\epsilon_\parallel = 0.5$ eV-sec. Extrapolated from measured data at 1.0×10^{12} total number of protons in the Booster (IEEE Trans. Nucl. Sci., Vol. NS-22, No. 3, 1975, Gray et al.), one obtains the following Table-II for the coherent Laslett tune-shifts at injection, 8 msec and 18 msec into the Booster ramp cycle:

TABLE - II

	Injection	8msec	18msec
$\Delta\nu^{\text{coherent}}_{\text{vertical}}$	–0.11	–0.05	–0.025

The inductive wall component to this coherent shift is expected to be small, based on the RF mode and magnet data. The transverse impedance of the magnets can be speculated from the measured data for longitudinal impedance $z_\parallel$ as a function of frequency, provided by J. Crisp and reproduced in Fig. 2 below.

Since incoherent tune-spreads are negligibly small, one expects significant growth at "transition" due to lack of Landau Damping. Indeed detailed calculations done previously (Cornacchia) show threshold behavior at transition. One needs a tune spread of .05 – .02, obtained by other means, to counteract this growth. This can be achieved either with octupoles *or* a higher harmonic additional RF cavity giving synchrotron tune spreads.

The measured resonant frequency, shunt impedance and Q of the Booster accelerating cavities are shown in Table-III below (from Cornacchia)[1]. The URMEL-predicted transverse mode structure of the same cavities is shown in Table-IV. (Cornacchia.)[1]

TABLE-III
Measured Longitudinal Modes of Booster RF

f (MHz)	R (Mohm)	Q
52.3	0.43	1300
85.8	1.56	3380
109.7	0.15	2258
167.2	0.07	1960
171.5	0.07	1190
225.4	0.33	2090
318.1	0.09	1570
342.6	0.50	530
391.0	0.11	460
448.8	0.48	3590
559.7	0.07	430
685.9	0.71	2440

Taken together with the magnet data of Fig. 2, the longitudinal broadband impedance of the Booster is estimated to be $|z_\parallel/n| \sim 120\ \Omega$. The corresponding transverse broadband impedance is estimated to be $|z_\perp| \sim 40\ \text{M}\Omega/\text{m}$.

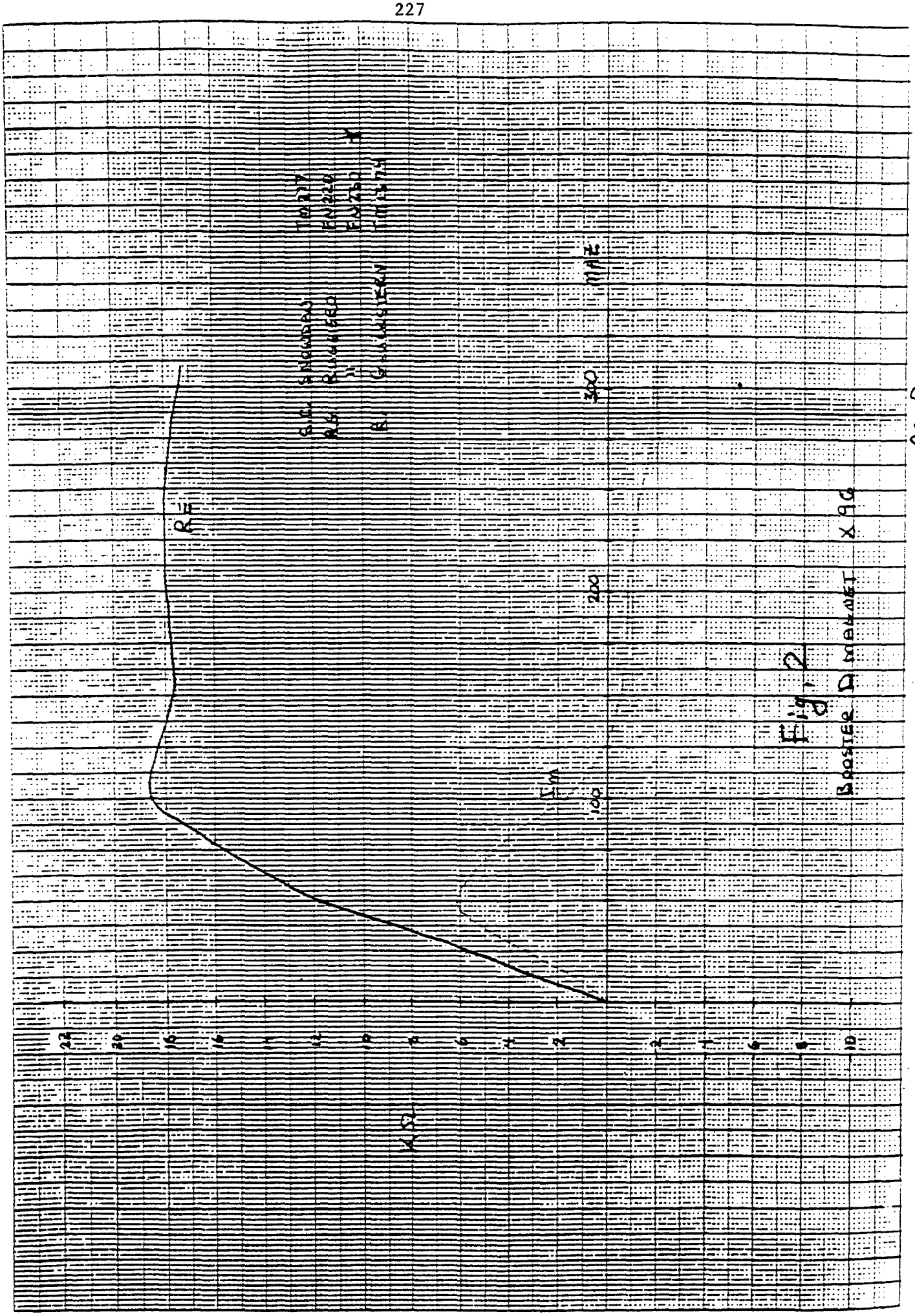
S.M. SNOWDEN
R.G. RAWLINGS
R.J. GALLIGAN
TO 27
EN 220
EN 270
TM 274
REF
MHz
300
200
100
I m A
22
20
18
16
14
12
10
8
6
4
2
2
1
.6
.4
.2
.1
BOOSTER D MAGNET X 96

Fig. 2

461510

TABLE-IV
URMEL-predicted Transverse Modes of Booster RF

f (MHz)	R (Mohm)	Q
69.35	0.38	2620
74.5	0.24	2778
79.78	0.5	2779
108.32	0.387	3255
113.74	0.13	3342
119.95	0.37	3539
123.92	0.17	3682
126.61	0.15	3561
128.6	0.19	3386
143.86	0.41	4461

Based on these data, a preliminary calculation using the computer code ZAP[2] indicates that no transverse coupled bunch instability is expected at any energy in the booster except at injection with a growth time of 40 ms, much longer than the cycle time. Longitudinally, however, one expects severe coupled bunch motion requiring an RF HOM-reduction by a factor of thirty and/or using a higher harmonic Landau cavity together with a longitudinal damper (Cornacchia)[1].

Initial calculations indicate that the Tevatron is expected to be unstable from the transverse coupled bunch instability at full intensity required for the upgrade.

5. Diagnostics and Cures

The Booster, Main Ring and Tevatron all have similar diagnostic detectors available: A resistive wall monitor having an impedance of about 0.25 ohm and bandwidth of several GHz, horizontal and vertical 50 ohm striplines that are one meter long and have a bandwidth of about 1 GHz, and a DC beam current monitor. In addition, there are flying wires for beam profile monitoring.

The Tevatron has tuned detectors also to monitor the horizontal and vertical Schottky signals. These have been used (and can be used for impedance measurement purposes) to measure the beam transfer function by driving a broad bandwidth resistive gap.

The Booster BPMs consist of 6 inch long horizontal and vertical striplines sharing the same enclosure. The Main Ring BPMs are constructed from a split-box type of detector. The Tevatron BPMs are 18 cm. long striplines.

Recommended additions: Currently there are no detectors in the Booster which can monitor the transverse position prior to RF capture. A simple capacitive style detector could be used having a bandwidth of about .1 to 10 MHz.

Regarding transverse dampers, there is only a vertical damper in the Booster. The signal from a stripline detector is sampled and held on a bunch-by-bunch basis and delayed by one turn through a variable length of cable. Normal operation uses up to 100 W of power, leading to 10 keV/c transverse momentum kick. The gain of the loop is such that a displacement of 1 mm vertically is required to generate this transverse momentum kick. Up to 500 Watts are available in the two amplifiers that are used to apply the position error differentially to a stripline detector. The amplifiers have a 0.1 to 200 MHz bandwidth. The adequacy of this damper for "injection damping" with the upgraded Booster beam parameter is yet to be determined.

In the Main Ring, there exist both horizontal and vertical slow dampers. The position signal is obtained from the BPM system which uses a split-box style of pickup. Information is transmitted from the B1 service building through a TV link to the FØ building where it is applied to the beam. The horizontal deflector has a 4 inch gap and the vertical has a 2 inch gap, both are 48 inches in length and have a maximum plate to plate voltage of .2 kV. The amplifier bandwidth is 5 kHz to 4 MHz.

There is also a vertical fast damper in the Main Ring. Each bunch position is digitized using a 6-bit ADC, delayed with a memory buffer by one turn and applied to the original bunch. The deflector consists of a 50 ohm stripline having a 2 inch gap and 55 inch length driven differentially with 2 kW amplifiers. The bandwidth is 4 – 200 MHz.

The horizontal and vertical fast dampers in the Tevatron are modeled after the Main Ring fast damper. Position information from a stripline detector is digitized with an 8 bit ADC and delayed through a memory buffer by one turn. The error signal is applied differentially to a 50 ohm stripline having a plate separation of 2.5 inches and 55 inches in length. The amplifiers can produce 5 kW and have a .01 to 200 MHz bandwidth.

In summary, with the exception of booster beam position monitor at injection before RF capture, there seems to be adequate diagnostics in all FNAL rings to allow beam monitoring. The additional Booster diagnostics recommended here will be crucial for the upgrade. One needs to evaluate the Booster damper capacity and the required upgrade for three times the present intensity, as required by the FNAL upgrade. There are indications of transverse quadrupole modes in the Accumulator driven by trapped ions. One may thus require a transverse quadrupole feedback. Finally reactive feedback in the Tevatron should be investigated in view of possible mode-coupling instabilities.

6. Suggested experiments on beams

The working group recommended the following experiments with beams to be performed in FNAL complex of machines:

(i) Tevatron "mode coupling experiment": Investigate frequency shifts of m = 0 and m = –1 (m = synchrotron mode number) lines as a function of beam current.

(ii) Study transverse damping in the Tevatron with damper on/off.

(iii) Accumulator: Put charge back into the "core" and look for emittance growth.

(iv) Perform experiments to understand "transition" in the Booster from transverse point of view.

(v) Possible measurements on the Dynamic Aperture in the Booster.

7. Summary

Lack of knowledge of various impedances in the FNAL chain of accelerators prevented the group from being able to calculate various instabilities in detail. Simple and crude illustrative estimates are therefore provided only for a few spotty cases. However, potentially dangerous impedances have been identified and their measurement procedure outlined. In addition, possible experiments with beam are suggested. Since the Booster appears in the first stage of the whole chain of accelerators, it is likely to be the limiting machine in the upgrade. Lack of detailed operational knowledge of the Booster makes it an even more important object of study for the future. The Booster has to be "understood" for further progress. Possible future plans of attack for the Booster, the Accumulator, the Main Ring and the Tevatron were discussed in detail during the workshops and these plans are attached for further reference in the Appendix.

References:

1. M. Cornacchia, "Observations and Computations of Higher Energy Collective Effects in the Fermilab Booster," LBL-22978.

2. Calculations done by P. Colestock on a version of ZAP provided by K. Ng during the Workshop.

APPENDIX

Booster: Plan of Attack

Transverse Instabilty Study Group

June 25, 1990

- Given upgrade parameter requirements (N,σ,ε), what are the tranverse impedance requirements
- Experimental techniques for measuring transverse impedance in a a fast ramping accelerator
- Beam detectors required for instability research and feedback
- Transverse feedback requirements for the upgrade
- Transition effects (joint session with transition crossing group)
- Dynamic aperture measurement techniques

Accumulator: Plan of Attack

Transverse Instability Study Group

June 25, 1990

- Bunched beam stability during the extraction process

- Impedance calculations based on known devices

- Compile list of experiments and beam diagnostics useful for diagnosing transverse instability of the extracted beam

- Design a quadrupole feedback system

Main Ring: Plan of Attack

Transverse Instability Study Group

June 26, 1990

- What is the impedance causing the observed 8 GeV vertical coupled bunch instability?
- Given the upgrade parameters (N,s,e) for the upgrade, what Main Ring or Main Injector transverse impedance is required (?)
- Estimate Transverse coupled bunch growth rates based on Main Ring RF cavity modes.

Tevatron: Plan of Attack

Transverse Instability Study Group

June 26, 1990

- Measure transverse impedance of electrostatic separators, RF cavities, and kicker magnets.
- Plan mode-coupling experiment measuring tune of m=0 and m=-1 spectral lines as a function of current
- Look at strpipline signals for Tevatron 150 GeV vertical instability, look for higher head tail modes
- Use BBI-Moses to predict transverse fast blow-up
- Meausre transverse tune vs. beam intensity per bunch during fixed target operations, record bunch lengths
- Measure damping strengths (times) of the superdampers

Transverse Instability Estimates in the Fermilab Booster and Main Ring.

P. Colestock and **S. Saritepe**
Fermi National Accelerator Laboratory*
Batavia, Illinois, USA

October 7, 1990

1 Introduction

The working group on transverse instabilities concluded that it would be beneficial to make estimates of transverse instabilities in the synchrotrons at Fermilab, based on knowledge of transverse impedances in the various components. Much of the necessary information in the form of bench or beam impedance measurements is, unfortunately, not yet available. However, some estimates of instability current thresholds and growth rates can be made based on the scant measured database, as well as on calculated impedances using currently available numerical codes. In this respect, the results presented here can only serve as crude indications of trends and point to areas where more experimental work is needed. Once the experimental impedance database has been improved, a critical assesment of the viability of current theoretical models can be carried out, both regarding the impedance calculational algorithms, and the onset of instabilities in the rings.

The basis of the estimates given here is the computational package, ZAP[1], which provides a comprehensive model of most of the relevant instabilities in synchrotrons. Due to the lack of time and available data, we have restricted our consideration of instabilities to the Booster and Main Ring, though the latter is relevant to the proposed Main Injector, since many of the same cavities and other components will be used. In the following, we present estimates for transverse single bunch and coupled bunch modes in the Booster and the Main Ring. We will also summarize the experimental and theoretical work necessary to improve the credibility of these estimates.

*Operated by Universities Research Association,Inc., under contract with the United States Department of Energy

BOOSTER		
Circumference	474.2	m
Beam Energy (Injection)	400	MeV
Beam Energy (Extraction)	8.9	GeV
Horizontal Tune	6.8	
Vertical Tune	6.8	
Number of bunches	84	
Particles/bunch	$2(6) \times 10^{10}$	
Horizontal Emittance	10	π mm-mr
Vertical Emittance	10	π mm-mr
Equivalent beam pipe radius	5	cm
γ_t	5.44	
rms momentum spread $(\sigma p/p)$	0.006	

Table 1: Booster parameters (performance extrapolated to after the linac upgrade).

2 Booster

The relevant ring parameter values are listed in Table 1. It was assumed that projected intensity levels will cover the range up to three times current levels.

2.1 Single Bunch Modes

In the Booster, the most significant transverse modes were found to be the "transverse fast blowup" or "fast head-tail instabilities [2],[3]. In the first case, the average current threshold for instability is given by

$$I = \frac{4\ (E/e)\ \nu_s}{|Z_\perp|^{WB} < \beta_\perp > R}\ \mathrm{Max}(b, \frac{{\sigma_l}^2}{b}) \tag{1}$$

where E is the particle energy, ν_s is the synchrotron tune, $|Z_\perp|^{WB}$ is the wide band impedance of the ring, $< \beta_\perp >$ is the ring-averaged amplitude fuction, R is the average ring radius, b is the average vacuum pipe radius and σ_l is the rms bunch length. If $\sigma_l > (4\sqrt{\pi}\ \frac{\beta}{3})b$, then the so called "fast head-tail instability" is dominant[3], with threshold current given by

$$I = \frac{4\ (E/e)\ \nu_s}{Im(Z_\perp) < \beta_\perp > R}\ \frac{4\sqrt{\pi}\beta\sigma_l}{3} \tag{2}$$

where β is the relativistic beta factor. In these calculations, since $Z_\perp^{WB}$ is not measured, it is assumed that $Z_\perp^{WB}$ is related to $Z_\parallel^{WB}$ by

$$Z_\perp = \frac{2R}{\beta b^2}\ (Z_\parallel/n)^{WB} \tag{3}$$

Frequency (MHz)	Transverse Impedance (MΩ/m)	Q
694.1	3.8	26200
744.8	2.4	27780
797.8	5.0	27790
1083.2	38.7	32550
1137.4	1.3	33420
1199.5	3.7	35390
1239.2	1.7	36820
1266.1	11.5	35610
1286.0	1.9	33860
1438.6	4.1	44610

Table 2: Harmonics, transverse impedances and Q's as computed by URMEL for the Booster cavities.

In addition, the contribution of each rf cavity is included via

$$|Z_\perp| = \frac{2R}{\beta b^2}(Z_\parallel/n)^{WB} + \frac{2R}{\beta b_{rf}^2}\, N\, (Z_\parallel/n)_{rf}{}^{WB} \tag{4}$$

where N is the number of cells and b_{rf} is the beam pipe radius at the cavity entrance.

With this model, we find that current beam intensities are too low in the Booster to cause this instability within a range of $Z_\parallel/n$ values considered to be consistent with measurements [5]. The upgrade intensities, however, should fall above threshold especially near injection. These results are presented for a range of expected operating conditions and feasible operating conditions in Figures 1,2.

2.2 Coupled Bunch Modes

Previous theoretical work in this area has indicated the potential for coupled bunch oscillations occuring around transition in the Booster[4]. Since transverse impedances have not been measured, these calculations were based on numerical eigenmode solutions with the URMEL code [6]. A list of calculated values is shown in Table 2 for reference.

For this work, the Sacherer-Zotter formulation was used[7], which gives the growth rate for a specific coupled bunch mode in terms of the transverse impedance, the bunch shape, beam current and other parameters. The results of studies using the above mentioned theoretical estimates indicate overall stability against transverse coupled bunch modes except near transition. In this region, growth rates were found to be on the order of the acceleration time in the Booster. It is to be cautioned, however, that little information has been compiled to date to confirm the impedance values used in this work.

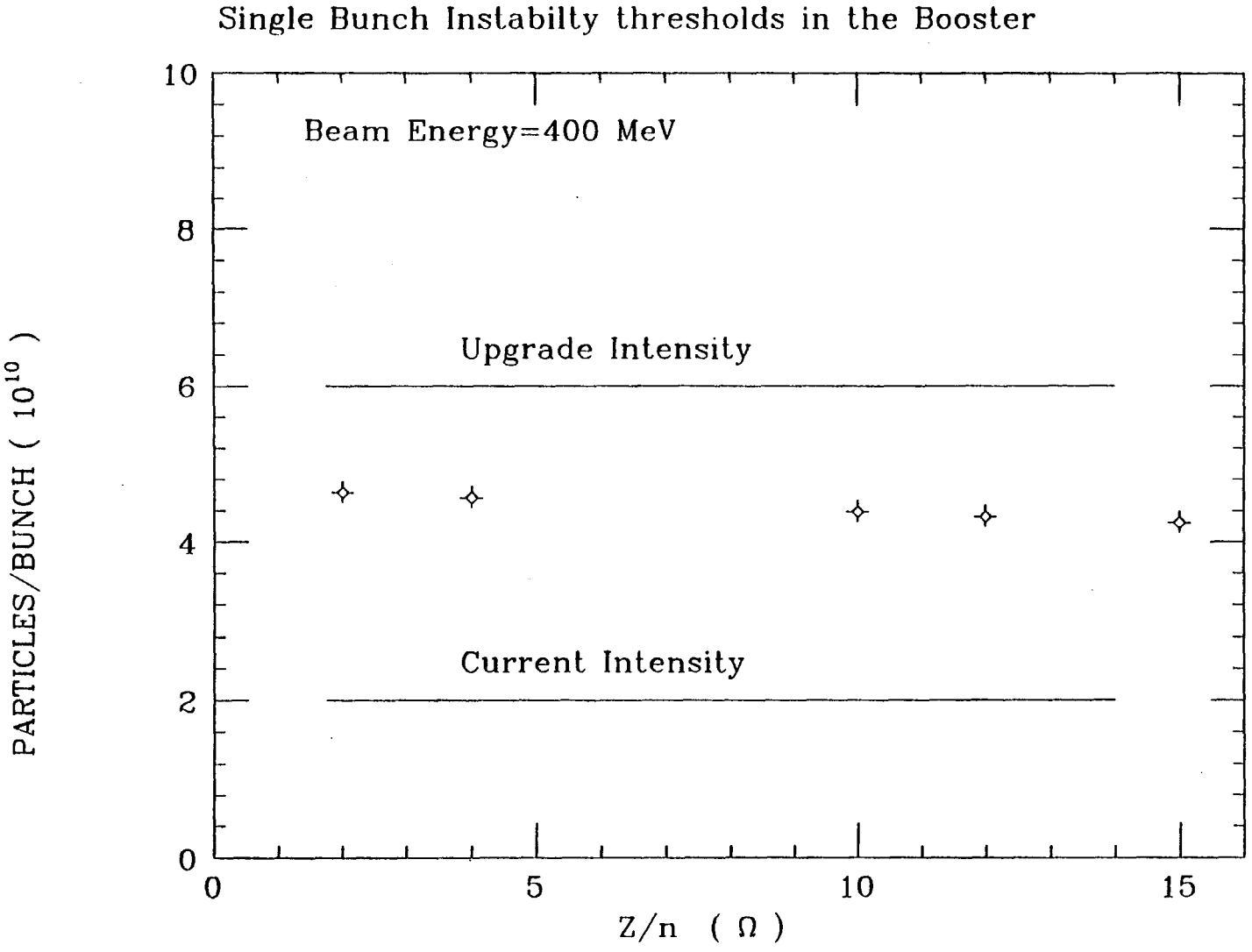

Figure 1. Transverse single bunch instability thresholds in the Booster.

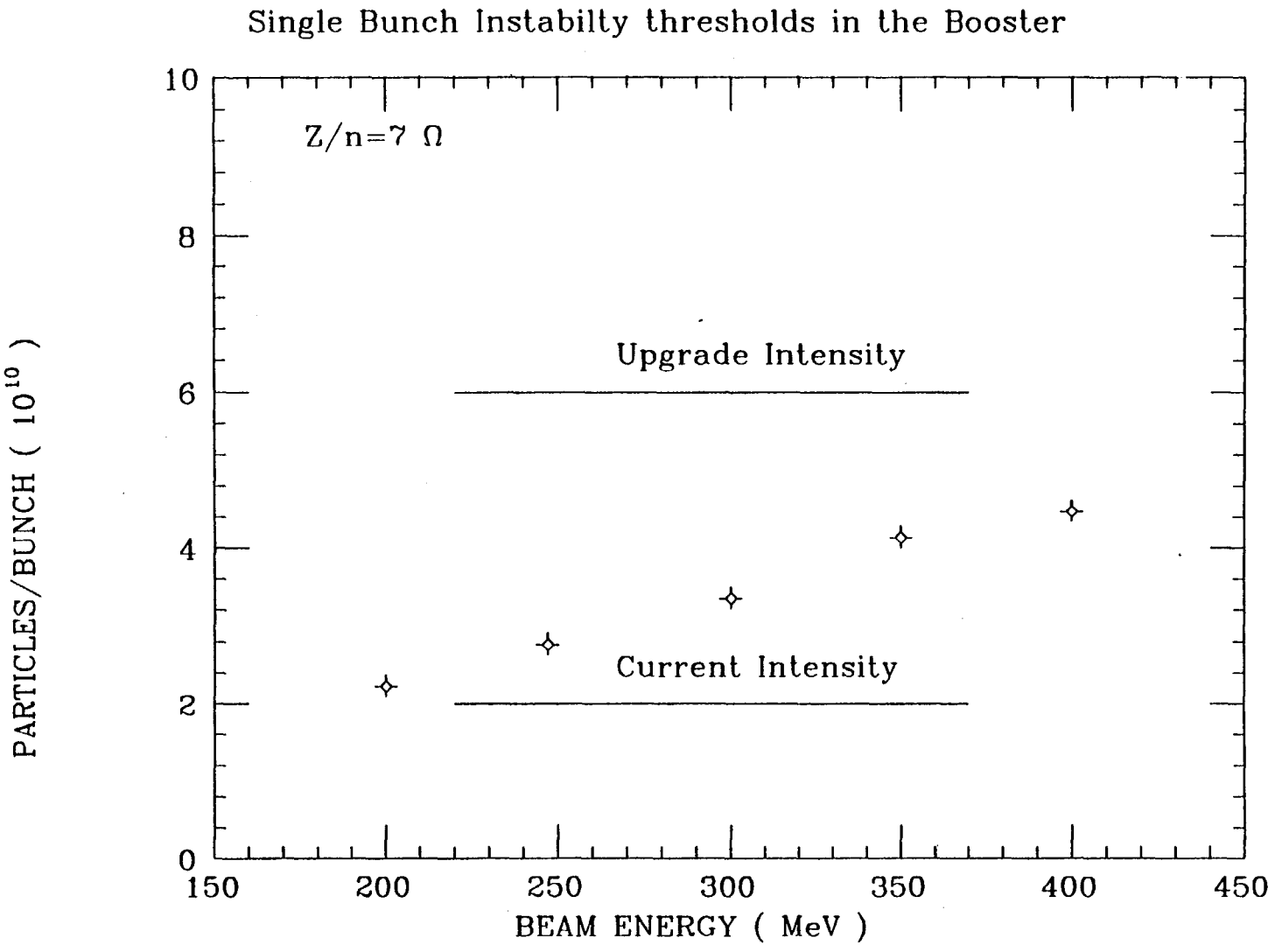

Figure 2. Transverse single bunch instability thresholds in the Booster for a particular value of $Z_{\|}/n$.

MAIN RING	$\bar{p}$ Production	Fixed Target Operation	Collider Operation	
Circumference	6280	6280	6280	m
Beam Energy	120	150	150	GeV
Average β_x	51.60	51.60	51.60	m
Average β_y	51.49	51.49	51.49	m
Horizontal Tune	19.38	19.38	19.38	
Vertical Tune	19.42	19.42	19.42	
Number of bunches	84 (bunch rotated)	1000	1 (Coalesced)	
Particles/bunch	$2(6) \times 10^{10}$	$2(6) \times 10^{10}$	$1(3) \times 10^{11}$	
Horizontal Emittance	15	15	15	π mm-mr
Vertical Emittance	15	15	15	π mm-mr
Equivalent beam pipe radius	3.61	3.61	3.61	cm
γ_t	17.7	17.7	17.7	
chromaticity $\Delta Q/(\sigma p/p)$	-30,+30	-30,+30	-30,+30	
rms momentum spread $(\sigma p/p)$	0.002 (bunch rotated)	0.001	0.0005	
Number of RF cavities	18	18	18	
Max. RF Voltage	4	4	4	MV

Table 3: Main Ring parameters (performance extrapolated to after the linac upgrade).

3 Main Ring

Similar calculations were carried out for the Main Ring with machine parameters given in Table 3. Again, in this case little experimental information was available, so that it was necessary to rely on theoretical estimates of ring impedance. A list of calculated cavity modes used in this study is given in Table 4 for reference.

3.1 Single Bunch Modes

In the Main Ring, the present estimates place the value of $Z_{||}/n$ at 2-4 Ω. For a value of 2 Ω, we find the Main Ring is currently stable to transverse single bunch modes, as shown in Figure 3. However, for expected upgrade intensities, $Z_{||}/n \approx 2\ \Omega$ is marginally stable at injection, and the uncertainty in $Z_{||}/n$ will likely lead to single bunch instabilities under some operating conditions. From Figure 4, it is observed that the most unstable period is at lowest beam energy, or at injection.

Frequency (MHz)	Transverse Impedance (MΩ/m)	Q
230.44	0.0005	27696
361.98	0.0648	32927
397.82	3.2972	32177
453.67	1.9312	36554
551.42	0.0265	40773
566.05	0.7453	40750
700.07	0.1254	45692
739.74	0.0112	47068
856.10	0.0541	47841
881.04	0.0438	49562
932.75	0.0826	37630
1007.80	0.0126	54993
1036.02	0.0031	57635
1063.21	0.0081	47001
1157.52	0.0146	43153
1197.31	0.0001	59018
1227.68	0.0002	33412
1255.23	0.1794	39831
1257.48	0.0001	35305
1269.85	1.7276	33786
1293.01	2.3933	36165

Table 4: Harmonics, transverse impedances and Q's as computed by URMEL for the Main Ring cavities.

3.2 Coupled Bunch Modes

With other parameters being roughly equal, the instability thresholds are expected to increase with energy. Hence, it is easily understood that the Main Ring was found to be stable to transverse coupled bunch modes over the entire range of expected operating conditions. Though, as before, it must be cautioned that little is known experimentally about the actual ring impedances.

4 Needed Work

It should be clear from the previous discussion that a vigorous program is needed to measure the transverse impedance of ring components as well as to measure directly the impedance with the beam. This program should include (1) bench measurements of beam components (2) beam measurements of the full ring and (3) verification of existing impedance codes. This latter task could provide a valuable

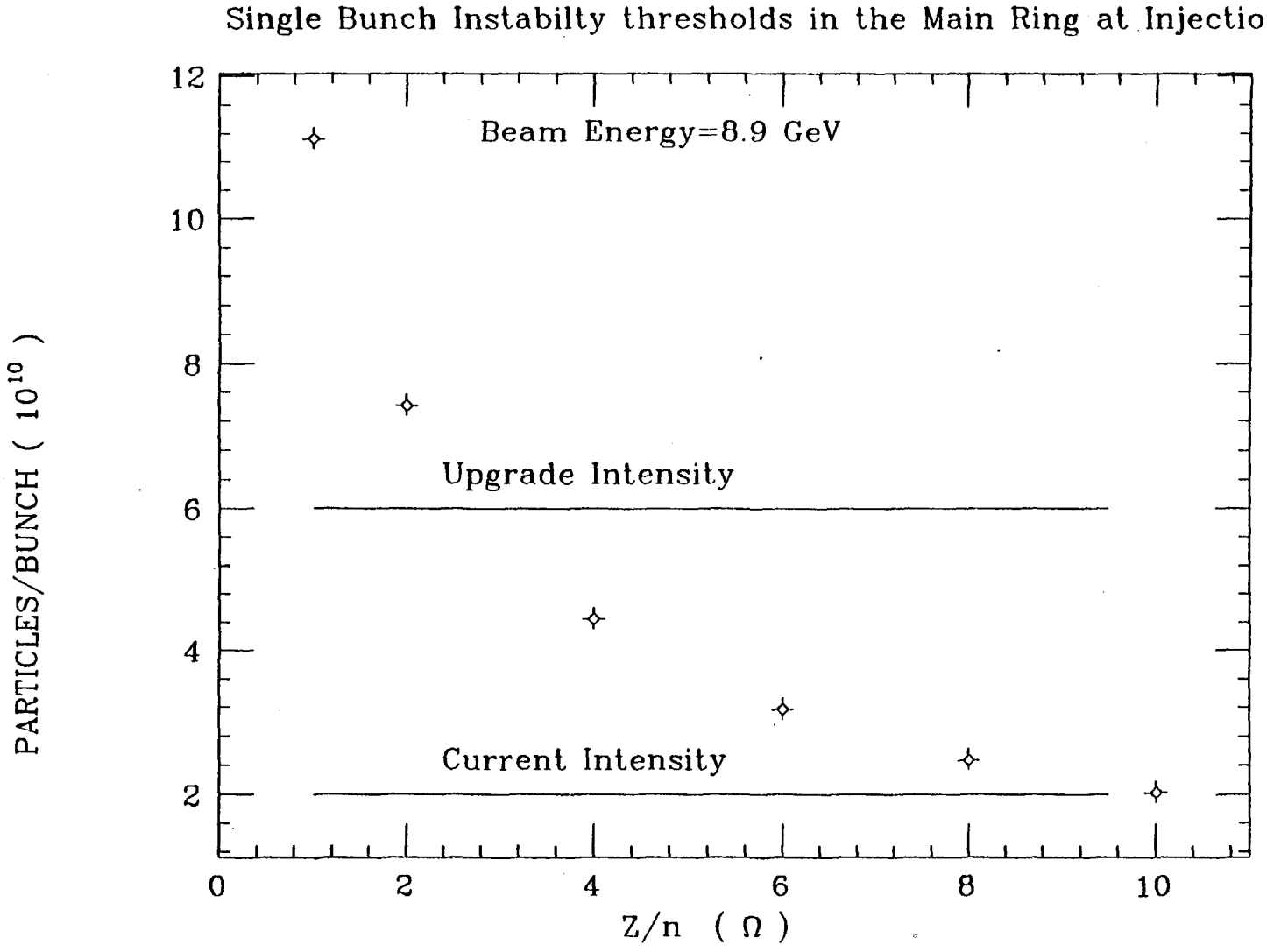

Figure 3. Transverse single bunch instability thresholds in the Main Ring as a function of $Z_{\|}/n$ of the ring. Current estimates put this value at 2-4 Ω.

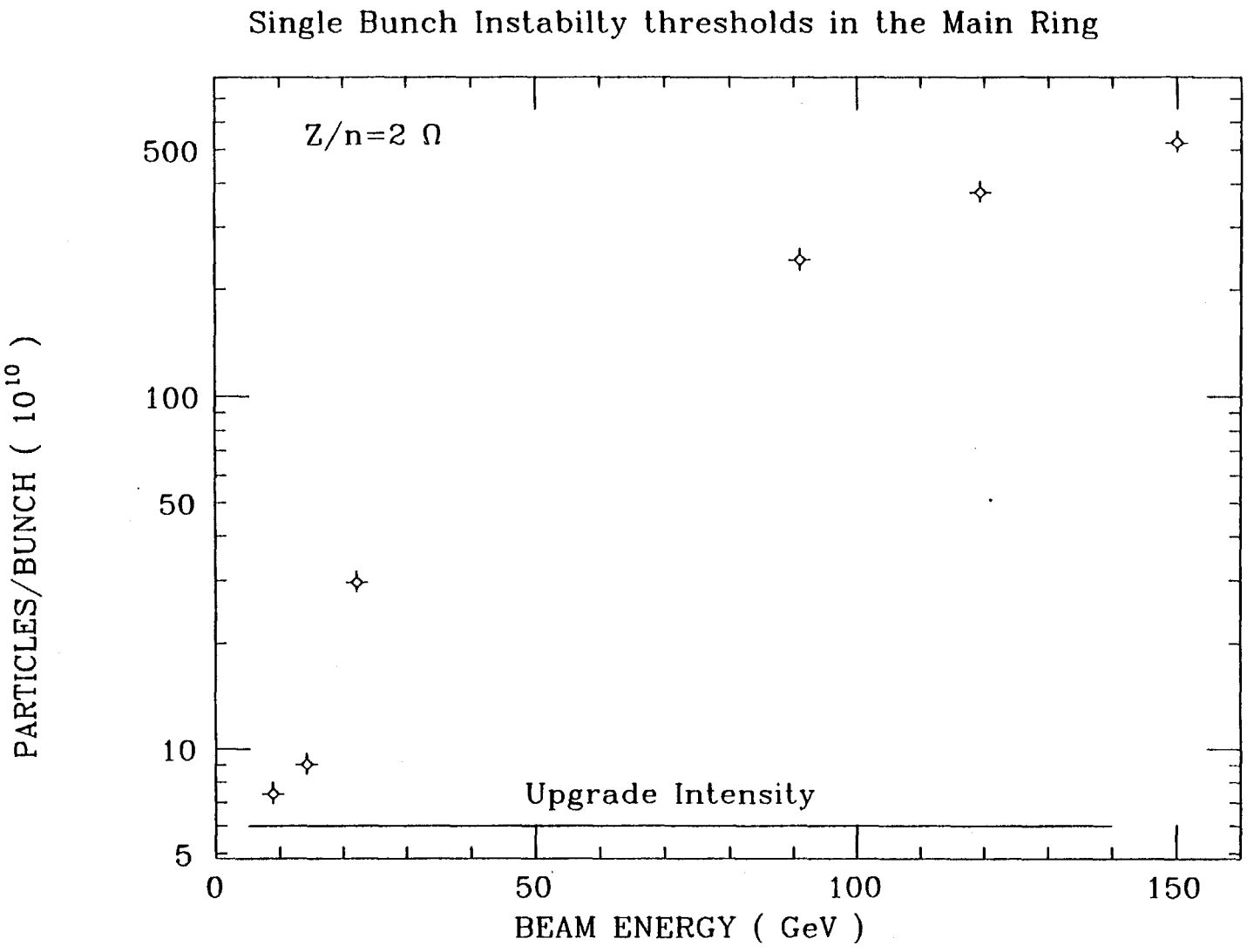

Figure 4. Transverse single bunch instability thresholds in the Main Ring as a function of beam energy. The most unstable conditions occur at lowest beam energies.

extension of measurements, provided a fully credible computational code exists. Further recommendations concerning these measurements and associated techniques are given in Section 3 of the transverse instability group's report.

5 Summary

Using largely calculated impedances of the Booster and Main Ring synchrotrons, estimates were made of the transverse single bunch and coupled bunch modes expected in these devices. The most significant instability growth occured for single bunch modes near injection in the Booster. While current operating conditions were found to be stable, expected upgrade intensities could give rise to the onset of these modes. Other types of transverse instabilities were found to be largely stable over the range of expected operation, but it should be cautioned that the impedances used for these estimates have not been measured experimentally. A comprehensive program to improve the confidence in the impedance values is needed.

References

[1] M.S.Zisman, S. Chattopadhyay and J.J.Bisognano; "ZAP Users Manual"; Lawrance Berkeley Laboratory Report LBL-21270

[2] R.D.Ruth and J.M.Wang; IEEE Trans.Nucl.Sci. NS-28, 2405 (1981)

[3] R. Ruth; in "Accelerator Physics Issues for a Superconducting Super Collider, Ann Arbor, December 1983; ed:M.Tigner, University of Michigan Report No:UMHE 84-1, p:151

[4] J.Crisp, Private Communications, see workshop proceedings.

[5] M. Cornacchia; "Observations and Computations of Higher Energy Collective Effects in the Fermilab Booster"; Lawrance Berkeley Laboratory Report LBL-22978

[6] C.Palm, U.Van Rienen and T.Weiland, DESY M-85-11, 1985.

[7] B.Zotter and F.Sacherer; " Transverse Instabilities of Relativistic Particle Beams in Accelerators and Storage Rings"; Proc.First Course of Int.School of Particle Accelerators, Erice 1976, CERN 77-13, p:175

Review of Impedance Measurements at Fermilab

G. Jackson, Fermi National Accelerator Laboratory, MS 308, P.O. Box 500, Batavia IL, 60510

Abstract

A substantial number of longitudinal impedance measurements have been done at Fermilab in the past and are continuing up to this time. Until the present no systematic transverse impedance measurements have been attempted. The longitudinal impedance measurements consist of both stretched wire measurements of individual vacuum components and accelerator based experiments to measure the total impedance of a number of rings. This paper will review both types of measurements. In addition, ideas and plans for future experiments are discussed.

Longitudinal Impedance

As a charged particle beam travels around an accelerator near the speed of light β, it produces a current I_b. As the charge circulates, an equal and opposite current flows on the inner surface of the beam pipe. In a perfectly conducting beam pipe of uniform cross-section, this image current does not generate longitudinal electric fields which feed back onto the beam. In the case of a beam pipe with changes in cross section or with finite resistance, longitudinal electric fields are generated which cause the beam to suffer an energy change ΔE. Using Ohm's Law, one can define the longitudinal impedance Z_L as the ratio of this feedback voltage V_L and the beam current, or

$$Z_L = \frac{-V_L}{I_b} = \frac{-\Delta E}{e\, I_b} \quad , \qquad (1)$$

where the relationship between the voltage and the longitudinal electric field E_z is

$$V_L(\omega) = \int_z E_z(z)\; e^{j\omega z/\beta c}\; dz \quad . \qquad (2)$$

Basically, the voltage as defined in equation (2) is proportional to the Fourier transform of the longitudinal electric field. Using equations (1) and (2) Ohm's Law has been written in the frequency domain, where by the principle of superposition each frequency can be treated independently. For the remainder of this

paper, the quantities of impedance, voltage, and beam current will always be treated in the frequency domain.

Small Step Change in Radius

As an example of the impedance seen by the beam at a pipe discontinuity, the case of a step change in the radius of a cylindrical beam pipe is quite instructive. Let us assume that the beam travels from a section of beam pipe of radius **b** to one of radius **d** (greater than **b**). A sketch of this geometry is shown in figure 1. In the limit of low frequencies, the impedance of this geometry is [1]

$$Z_L = j\omega L_s \quad , \qquad (3)$$

where the inductance of the radial step is given by

$$L_s = 0.12\,\mu_o \frac{(d-b)^2}{d} \quad . \qquad (4)$$

This linear dependence on frequency is substantially accurate until the cutoff frequency of the beam pipe is approached. It is this behavior that the Q=1 resonator (also called broadband and Z_L/n) model is designed to reproduce.

The name Z_L/n describes the parameterization of this model in such a way as to enable designers to compare the broadband impedance of circular accelerators with dissimilar revolution frequencies. Since values of the impedance at the synchrotron sideband frequencies near the revolution frequency harmonics are used to calculate instability growth times, the frequency ω in equation (3) is replaced by $n\omega_r$, where ω_r is the angular revolution frequency. Dividing both sides of the resultant equation by **n**, the relationship for the broadband impedance Z_L/n is computed.

Resonant Cavities

In the case of a narrow impedance resonance, such as those created by structures like RF cavities, trapped normal modes referred to as TM or TE are excited by the passage of the beam [2]. Only the TM modes have longitudinal electric fields capable of accelerating or decelerating the beam. The frequencies of such modes in a right cylindrical cavity with no openings are given by [3]

$$\omega_{mnp} = c\sqrt{\frac{x_{mn}^2}{R^2} + \frac{p^2\pi^2}{d^2}} \quad , \qquad (5)$$

where R is the radius of the cylinder, d is its length, and x_{mn} is the nth root of the equation $J_m(x)=0$. For instance, in the right cylindrical cavity shown in figure 2, the frequency of the lowest significant TM mode, called TM_{010}, is approximately

$$f_{010}\,[\mathrm{Hz}] = \frac{1.15 \times 10^8}{R\,[\mathrm{m}]} \qquad (6)$$

Deviations from this equation are caused by the fact that the beam pipe attached to such a structure shifts the frequency by a small amount. Note that the frequency of the lowest mode is independent of the length of the cavity.

An electrical circuit model describing the beam/cavity coupling of this mode is shown in figure 3. The beam is treated as a current source which, when applied to an impedance, generates a voltage which acts back on the beam. The impedance of this circuit is given by Ohm's Law $V_L(\omega) = I_b(\omega)\, Z_L(\omega)$, where

$$Z_L(\omega) = \frac{R}{1 + jR\,(\omega C - 1/\omega L)} \qquad (7)$$

If one eliminates the resistance R, it is simple to show from equation (7) that the resonant frequency of the lumped LC circuit is

$$\omega_o = \sqrt{\frac{1}{LC}} \qquad (8)$$

Plugging equation (8) into equation (7) and rearranging factors, the impedance of the cavity may be expressed as

$$Z_L(\omega) = \frac{R}{1 + j\frac{RC}{\omega}(\omega^2 - \omega_o^2)} \qquad (9)$$

Multiplying equation (9) by its complex conjugate, the magnitude squared of the impedance is given by

$$\left|\frac{Z_L(\omega)}{R}\right|^2 = \frac{1}{1 + \frac{R^2C^2}{\omega_o^2}(\omega^2 - \omega_o^2)^2} \qquad (10)$$

The point at which this quantity reaches half of its peak value occurs when the fractional frequency deviation from the resonant frequency

$$\delta = \frac{\omega - \omega_0}{\omega_0} \tag{11}$$

reaches the value

$$\delta_{1/2} = \frac{1}{2 R C \omega_0} \tag{12}$$

The quality factor **Q** for this mode is defined to be the stored power divided by the energy loss per turn, or equivalently the resonant frequency divided by the full frequency difference between the half peak values on either side of the resonant frequency. In terms of the variables in equation (12),

$$Q = \frac{1}{2 \delta_{1/2}} = R C \omega_0 \tag{13}$$

Plugging the definitions of δ and **Q** into equation (9), in the limit where $\delta << 1$, the equation for the impedance of a narrow resonance is written as

$$Z_L(\omega) = \frac{R}{1 + j 2 Q \delta} \tag{14}$$

where the three parameters ω_0, **R**, and **Q** completely describe the properties of the resonance.

In contrast to the small step case, where a single parameter Z_L/n could be used to describe the magnitude and shape of the longitudinal impedance, in the case of narrow resonances no such convenient mechanism to compare dissimilar circular accelerators exist. The contributions of each cavity structure in each accelerator must be independently evaluated and added to the broadband value at the appropriate frequencies.

Beam Position Monitors

Because there can be up to 200 beam position monitors in a number of Fermilab circular accelerators, the contribution of these detectors to the impedance of the accelerator can be quite substantial. A good example is the case of a stripline pickup upon which a fraction α of the beam image charge is carried. If the upstream detector signal cable and the stripline have the same characteristic impedance Z_0 (which is almost always the case), then the longitudinal impedance seen by the beam is [4]

$$Z_L(\omega) = \frac{\alpha}{2} Z_0 \left(1 - e^{-j 2 \omega l / c}\right) \tag{15}$$

where l is the length of the stripline. Figure 4 shows the real and imaginary contributions of this impedance when $Z_0=\alpha=1$. Note that the real and imaginary parts of the impedance are both periodic in frequency (up until the cutoff frequency of the beam pipe or until signal attenuation down the stripline becomes significant). With $Z_0= 50\Omega$ and $\alpha=1/2$ per monitor location (combining all pickup striplines) the total impedance for 200 monitors is $5k\Omega$. This is to be compared to the total longitudinal impedance of the RF cavities, which is approximately $3M\Omega$ on resonance.

Usually, beam position detector striplines are very short, putting the frequency of the first peak in the real part of the impedance up around 1GHz. In addition, often beam position pickups are not striplines at all, but capacitive beam current detectors.

Kicker Magnets

A class of beam line elements containing complex materials also contributes to the longitudinal impedance in a circular accelerator. The dominant members of this group are transverse beam kickers. At Fermilab there are two basic types of kicker magnets, referred to as "C-magnets" (figure 5) and "Window-frame magnets" (figure 6).

From the point of view of kicker magnet design, the Window-frame type of magnet is simply two parallel C-magnets, yielding twice as much kick for the same pulsed current per copper conductor. On the other hand, a Window-frame type kicker, especially one without the copper strips shown in figure 6, presents a much higher impedance to the beam. This is due to the fact that the azimuthal magnetic field generated by the beam prefers to concentrate inside the high-μ environment of the ferrite or iron laminations. Since these fields are doing work in this material, energy must be extracted from the beam, therefore requiring the existence of longitudinal voltages (and impedance).

Another significant component to these magnets are the current carrying conductor bars. They act like striplines, contributing an impedance which depends on the type of impedance matching with exterior cables, power supplies, and terminations.

Beam-Based Measurements

There have been many measurements of the longitudinal impedance of Fermilab rings. Many of the more systematic measurements are actively being pursued at present. They can be divided into two classifications. The first group consists of experiments aimed at measuring longitudinal impedance as a function of frequency, without assuming a model for the frequency dependence of the beam pipe impedance. These measurements are always done by perturbing a coasting, or DC, beam. The second set of experiments, typically done with bunched beams, are designed to determine the quantity Z_L/n.

Assuming a Q=1 resonator model, where the center frequency is the cutoff frequency of the beam pipe, Z_L/n is the magnitude of the impedance of this resonator.

Coasting Beam Measurements - Theory

The basis of this measurement is simply Ohm's Law. In the frequency domain, we know that $V_L(\omega)=I_b(\omega)\, Z_L(\omega)$. Given a DC beam with an rms fractional momentum spread σ_δ, a RF kicker applying a sinusoidal voltage of angular frequency ω to the beam causes a current $I_b(\omega)$. Coupled to the longitudinal impedance, this current produces another voltage at the same frequency . These two voltages add vectorially, changing the amplitude and phase of the beam current $I_b(\omega)$. This scenario is quite familiar to designers of microwave power amplifiers called klystrons. Figure 7 is a sketch of a klystron, showing the input cavity which initially modulates the electron beam current (originally DC), the intermediate cavities used to increase the modulation, and the final output cavity which extracts the power. In the case of klystrons, power is only produced in a narrow frequency range (determined by the Q of the cavities). In the case of the measurements to be described below, a very broad frequency range is required. Therefore, specialized RF kickers and current monitors have been developed and installed in a number of Fermilab accelerators.

Given an input voltage modulating a DC accelerator beam and the measured beam current response, how is the impedance calculated? The standard method is to derive the steady state response of the beam phase space using the Vlasov equation. Let $\Psi(\theta,\varepsilon,t)$ represent the time evolution of the this phase space density distribution, where θ is the azimuthal coordinate around the ring and ε is the energy. The Vlasov equation is then written as

$$\frac{\partial \Psi}{\partial t} + \omega \frac{\partial \Psi}{\partial \theta} + \dot{\varepsilon} \frac{\partial \Psi}{\partial \varepsilon} = 0 \qquad . \qquad (16)$$

The rate of change of energy in the third term, caused by the external voltage V_0 of frequency Ω and beam induced longitudinal voltage U_0, has the form

$$\dot{\varepsilon} = \frac{e\,\omega_0}{2\pi} (V_0 + U_0)\, e^{j\,(m\theta - \Omega t)} \qquad . \qquad (17)$$

Assuming that the perturbation to the phase space distribution is small, one can split it into two terms

$$\Psi(\theta,\varepsilon,t) = \Psi_0(\varepsilon) + \Psi_1(\varepsilon)\, e^{j\,(m\theta - \Omega t)} \qquad . \qquad (18)$$

The first term is simply the original distribution, depending on energy but independent of azimuth. The second term reflects the oscillatory portion of phase space, and is linearized by assuming the energy and azimuthal components of the distribution are separable.

In order to calculate the beam induced longitudinal voltage, the longitudinal impedance $Z_L(\Omega)$ must be multiplied by the beam current modulation $I_b(\Omega)$, which is simply the perturbed portion of the phase space distribution integrated over all energy

$$I_b(\Omega) = e\,\omega_0 \int_{-\infty}^{\infty} \Psi_1(\varepsilon)\, d\varepsilon \qquad (19)$$

Combining the above equations and solving for the inverse response of the beam $R=V_0/I_b$, the final result is derived

$$R(\Omega) = \frac{1}{\dfrac{j\,e\,\omega_0^2\, I_0 |\eta|}{2\pi\, E_0} \displaystyle\int \frac{\dfrac{\partial \Psi_0(\omega)}{\partial \omega}}{\Omega - m\omega}\, d\omega} + Z_L(\Omega) \qquad (20)$$

where η is the momentum compaction, I_0 is the DC beam current, and E_0 is the central beam energy. Besides the longitudinal impedance, all variables in equation (20) are measured, including $\Psi_0(\omega)$. The effect of the impedance is to simply shift the measured inverse response. Note that since the beam frequency distribution Ψ_0 is zero everywhere except near revolution harmonics, a beam response can only be measured when $\Omega = n\omega_0$, n=1,2,3,.... After measuring these quantities and evaluating the complex integral in the denominator, the longitudinal impedance can be derived at each revolution harmonic.

Coasting Beam Measurements - Accumulator

To date, coasting beam impedance measurements, also called longitudinal beam transfer function measurements, have only been performed in the Accumulator [5] and Tevatron. A typical experimental setup used for the Tevatron measurements is shown in figure 8 (the Accumulator apparatus is very similar).

Recent Accumulator measurements were made by kicking the beam with the broadband RF (suppressed bucket) system called ARF2 [6] and measuring the resultant beam current modulation with a resistive wall monitor [7]. A Hewlett-Packard 3577A network analyzer was used to generate the external RF signal applied to the beam, measure the current modulation, and calculate the inverse response. The

frequency distribution of the beam $\Psi_0(\omega)$ was measured using a Hewlett-Packard 8568B spectrum analyzer connected to a resonating quarter-wave longitudinal pickup centered at revolution harmonic 126.

Figure 9 shows the result of a typical beam frequency distribution measurement. This Schottky spectrum [8] is generated by the particle nature of the beam, where the power per frequency interval is proportional to the beam frequency density in that interval. Therefore, above the noise floor the shape of this curve is the shape of the beam frequency distribution. Since the vertical scale is logarithmic, with a factor of 10 of power per division, this distribution is known over 4 order of magnitude in density. Note the full frequency width of the plot is 5kHz, and the revolution frequency of the Accumulator is roughly 630kHz.

The result of a pair of longitudinal transfer function measurements across revolution harmonic 13 is shown in figure 10. The only difference between the two traces is the direction of the network analyzer frequency sweep. The top plot is the amplitude on a logarithmic vertical scale and the bottom plot contains the phase normalized to zero degrees far from resonance. Note that unlike a harmonic oscillator whose phase rolls through a total of 180° as the drive frequency is swept through resonance, the phase rolls through 360°. Since the frequency width of the beam is proportional to harmonic number, and the 95% width of the measured Schottky distribution in figure 9 is approximately 700Hz, one would expect the width of the transfer function phase response at harmonic 13 to be ten times less. Checking with figure 10, this expectation is confirmed.

Transforming the data in figure 10 into real and imaginary parts and taking the inverse of each point, the inverse response of the beam is derived. The units of this curve is proportional to ohms, and is typically plotted on the complex plane. Figure 11 is such a plot calculated from the data in figure 10. Starting a low frequency and working around to high frequency, the data in figure 11 starts in the upper left corner, works its way around the origin, and ends up in quadrant 1 near the imaginary axis. Starting with a symmetric frequency distribution and assuming that the impedance is zero, the inverse response curve would be symmetric about the imaginary axis. The effect of longitudinal impedance is to shift this curve.

Coasting Beam Measurements - Tevatron

As mentioned previously, the Tevatron longitudinal transfer function measurement setup is sketched in figure 8. The expectation was to acquire data which looked very similar to that taken in the Accumulator. Figure 12 is the result of a Tevatron longitudinal transfer function at harmonic 1100. Instead of a smooth curve, a very structured, spiked response was measured. As can be seen in figure 13, where a number of revolution harmonic scans are superimposed, the spikes are not noise or instrument response resonances.

What was the cause of these spikes? A logical hypothesis was that the momentum distribution of the beam had holes in it. Since the Tevatron did not have a dedicated longitudinal Schottky detector, the

non-resonant resistive wall monitor was used. Due to signal-to-noise considerations, low frequency Schottky scans were required. But because the minimum resolution bandwidth of a Hewlett-Packard 8568B spectrum analyzer is 10Hz, revolution harmonics greater than 100 were required. Figure 14 contains such a scan, which showed no signs of holes. Since the resolution bandwidth was 10Hz and the spectrum scale was 50Hz per division, it was conceivable that the holes would not show up. In order to work around this limitation, a Schottky scan at a factor of five higher frequency was taken. At 100Hz per division there still was no sign of such holes (figure 15).

In order to clear up this mystery, two new measurements were added in the next Tevatron study period. The first was to use a new, high frequency dynamic signal analyzer called the Hewlett-Packard 3588A. With a range up to 150MHz and resolution bandwidths less than 0.1Hz, unambiguous frequency distribution measurements were possible. In addition, it was suggested [9] that since signs of self bunching instability were sometimes evident at the main Tevatron RF acceleration cavity resonant frequency of 53MHz, that perhaps some kind of frequency mixing phenomenon was taking place. The measurement aimed at investigating this hypothesis consisted of monitoring the longitudinal transfer function with a parallel spectrum analyzer on a much wider frequency span set up to record the maximum power at all frequencies while the measurement was active (max hold mode).

A longitudinal transfer function at harmonic 1114 was done to verify that the spikes still existed in the data. Figure 16 is the result, showing a different pattern of spikes (no two beam injections ever have the same spike structure). Connecting the new dynamic signal analyzer to the resistive wall monitor and centering on the eleventh revolution harmonic, the longitudinal Schottky scan in figure 17 was taken. With a 9.8Hz full span and a resultant 88mHz resolution bandwidth, spikes in the momentum distribution of the beam are clearly visible. The deepest spike is 1.5Hz from the right edge of the beam density distribution. Multiplying by 100, one would expect to find the deepest spike in the transfer function measurement 150Hz to the left of the edge of the upper frequency phase roll. Checking with figure 16, this is indeed the case. Therefore, the source of the spikes in the transfer function measurements has been found, verifying the original hypothesis.

At 0.98Hz per division, the biggest hole in the momentum distribution in figure 17 seems to have a width of approximately 0.2Hz or smaller (since again the resolution bandwidth is a limitation). Even at this frequency span, the time per spectrum update is 40.96 seconds. Reducing the span, and hence the resolution bandwidth, by a factor of two increases the total scan acquisition time to 20 minutes.

The second experiment discussed above was done in parallel. The Hewlett-Packard 8566B spectrum analyzer was set to a full frequency span of 1MHz, so that roughly two revolution harmonics per division would be visible. The resolution and video bandwidths were kept between 10kHz and 30kHz so that the sweep time remained near 30msec. With the spectrum analyzer in max hold mode, the peak power per bin of all sweeps was constantly displayed. The sweep rate combined with max hold provided a means of recording the excitation of any frequencies besides the one being driven by the network analyzer.

Figure 18 contains the data from one of the first such measurements, where the network analyzer swept through the 1113 revolution harmonic (rightmost peak in the figure). Note that a number of revolution harmonics below the driven harmonic were excited. In addition, a curiosity is the fact that harmonics above the driven frequency were not also excited. Finally, the polarity of this effect did not depend on the direction of the network analyzer frequency sweep.

What is the cause of this phenomenon? In order to answer this question, a considerable amount of Tevatron accelerator study time was dedicated toward uncovering clues to the physics behind this effect. The first experiments recorded the sensitivity of this effect to the drive frequency. Figure 19 contains the results of a repeat of the measurement in figure 18, just to emphasize the fact that this effect was easily reproducible. Since harmonic 1113 is the resonant frequency of the RF cavities, assumed to be the dominant single source of narrow band impedance in the Tevatron, varying harmonic number slowly away from 1113 was thought to be an interesting experiment. Figures 20 and 21 contain examples where harmonics 1114 and 1115 were excited, with no obvious difference from the 1113 data.

The observation which initiated this type of measurement was a self bunching instability at the RF cavity resonant frequency at harmonic 1113. A perfect example of this instability can be seen in figure 22, where the beam was self bunched during a transfer function measurement. Note that the main peak, which contained 2000 times more power than the network analyzer driven harmonic 1120 (rightmost peak), interacted with that drive harmonic to produce an image power enhancement at harmonic 1106. As can be seen in figure 23, in the absence of this instability and without doing a transfer function measurement, the beam spectrum showed increased power in harmonics 1113 and 1107, but at nowhere near the power levels of the previous plot. After waiting 15 minutes for this self bunching instability to spontaneously disappear, the longitudinal beam transfer function measurement at harmonic 1120 was repeated, with the result shown in figure 24.

How about frequencies much farther away from the RF resonance? Figures 25 and 26 contain the data from transfer function measurements performed at harmonics 2000 and 400, respectively. Besides the variation of the response amplitude, the effect is unchanged. Clearly, the RF resonant impedance is not a factor in the beam physics behind this phenomenon.

A second direction in these studies was the beam current and momentum spread dependence of this effect. Not enough time has been devoted yet to come to any quantitative conclusions, but it is clear that there is a beam current threshold which is momentum spread dependent below which this phenomenon does not occur. Whereas the data in figure 19 was taken when the beam intensity was 6.33×10^{12} protons, figure 27 shows the lack of this effect when the beam intensity has dropped to 2.64×10^{12} protons.

Bunched Beam Measurements

During Tevatron collider operations the processes called bunch rotation [10,11] (for antiproton production) and coalescing [12,13] (for Tevatron proton and antiproton injection) require that the longitudinal impedance of the Main Ring be quite small. In order to ascertain Z_L/n, bunched beam was injected into the Main Ring, accelerated to 150 GeV, and then suddenly debunched by shutting of the RF drive power [14]. By observing the difference between the time when the RF is turned off and when microwave instability begins, a number for Z_L/n can be derived [15].

The basis of this calculation is the equation for microwave stability [16]

$$\left|\frac{Z_L}{n}\right| \leq (1.434)\frac{2\pi\,\eta\,(E/e)}{I_p}\left(\frac{\sigma_\varepsilon}{E}\right)^2 \quad , \qquad (21)$$

where I_p is the peak bunch current. Microwave instability is detected as high frequency beam current modulation which leads to momentum width increase (longitudinal phase space emittance growth). If the inequality in equation (21) is satisfied, the beam is microwave stable. If for instance the momentum spread is decreased until the inequality is violated, microwave instability will ensue.

As shown in the sketch in figure 28, when the RF drive power is cut off the longitudinal phase space distribution of the beam shears linearly away from its original shape (left) to the slanted distribution (right). Since the dynamics of proton trajectories is conservative, the phase space area of the beam does not change. Therefore, the instantaneous momentum spread decreases from σ_i to σ_f. At some point σ_f decreases enough to cause the beam to become microwave unstable, a state identified by monitoring a resistive wall monitor for growth in beam power at high (GHz) frequencies. Since the decrease of momentum spread with time is calculable, Z_L/n can be derived.

In principle this method for determining the Z_L/n should be valid. Unfortunately, the broad band contribution to the impedance of the Main Ring is not dominant at all frequencies. In particular, the shunt impedance of the Main Ring RF cavities is 3MΩ at 53MHz. Figure 29 shows the beam current spectrum in the Main Ring at injection. The frequency scale runs from 0Hz to 10 times the RF frequency. Note that besides the dominant 53MHz beam harmonics, that remnant longitudinal coupled bunch oscillations from the Booster are evident (smaller two peaks between 0 and 53MHz). Given short bunches and a typical beam intensity of 2×10^{12} protons in the Main Ring, the beam current component at 53MHz is 30mA. Using Ohm's law, the beam induced voltage in the RF cavities is roughly 100kV, whereas the nominal RF voltage applied to the beam at injection or flattop is approximately 900kV. Therefore, the beam induced RF bucket is only 3 times smaller than the phase space bucket produced by the RF drive amplifiers.

What is the effect of this large beam loading voltage on the debunching method of broadband impedance determination? A program of Main Ring experiments were undertaken to answer this question. When the beam is injected from the Booster into the Main Ring, a detector sensing the 53MHz

component of the beam current will jump from zero to a value approximately equal to twice the DC beam current. If the Booster and Main Ring RF voltages were exactly matched in frequency, phase, and longitudinal phase space bucket area, the detected rms current would remain constant. Any mismatches would tend to cause oscillations in this level with a frequency of twice the synchrotron frequency. Figure 30 is an example of just such a measurement, using a resistive wall monitor as the beam current detector and the Hewlett-Packard 8568B spectrum analyzer in zero span mode (the span is literally set to zero) as the fixed frequency narrow band filter and rms detector. The resolution and video bandwidths were set to 10kHz. Injecting into the Main Ring with the RF cavity drive already off, the beam should debunch in less than a second. As can be seen in figure 31, the beam does not fully debunch.

The Main Ring RF cavities are fitted with shorts which can be used to decrease the shunt impedance at 53MHz. Performing the same experiment reported in figure 31, but shorting 16 of the 18 RF cavities, a very different picture emerges in figure 32. Instead of a persistent 53MHz beam current component, the signal goes to the noise floor and then slowly oscillates. In fact this oscillation, and the faster oscillations after 40ms in figure 31, are caused by the beam undergoing coherent synchrotron quadrupole mode oscillations caused by the factor of 3 change in bucket area when the RF was turned off.

When all 18 RF cavities were shorted, a 53MHz beam current response resembling the one expected in the case of no beam loading was observed. As shown in figure 33, there is still a small amount of beam loading occuring, but the beam current modulation power is 6 orders of magnitude smaller than the initial value.

The effect of beam loading on the shape of the beam longitudinal phase space shape was calculated using a multiparticle computer simulation. Starting with the initial phase space profile and RF beam loaded voltage phase shown in figure 34, the test particles were tracked around the ring for 75ms. At the end of that time, the new phase space profile shown in figure 35 was found. Note that not only was the simple model of linear shearing incorrect, but the beam also decelerated. This deceleration was confirmed in the Main Ring by observing the orbit of the beam move to the inside of the vacuum chamber during the measurements shown in figure 31. Finally, figure 36 contains the 53MHz beam current time dependence calculated from the simulation data. The similarity between this result and the Main Ring measurements confirm the hypothesis that beam loading in the RF cavity invalidates previous Z_L/n experiment results.

Stretched Wire Measurements

In order to check ring impedance calculations and to provide guidance in the interpretation of beam-based impedance measurements, stretched wire measurements of beamline components on the bench are necessary. These measurements can be done in the time domain (pulses simulating the beam) or frequency domain (swept sine wave) [17]. Using the pulse technique one can either study the

attenuation of the signal through the beam pipe section to derive a model dependent number for the impedance, or the output signal can be digitized and Fourier transformed to derive the longitudinal impedance as a function of frequency. Since the frequency resolution and range are determined by the number of points digitized and the digitizing rate respectively, present ADC and memory technology place severe constraints on the utility of this approach. In the measurements done at Fermilab, only the frequency domain measurements have been systematically performed.

Measurement Technique

Figure 37 contains a sketch of the presently favored experimental apparatus used at Fermilab and other facilities [18] to measure longitudinal impedance. A network analyzer generates a swept sine wave which is transmitted from port 1 to a section of beam pipe via 50Ω characteristic impedance cable. Since the characteristic impedance of a coaxial line in air or vacuum of inner diameter **d** and outer diameter **D** is

$$Z_C = 60\,\mathrm{Ln}\left(\frac{D}{d}\right) \quad , \qquad (22)$$

the combination of the 1/128" diameter stretched wire and the beam pipe form a characteristic impedance of hundreds of ohms. The reflections caused by propagating a high frequency TEM transmission line wave across the boundary to this beam pipe impedance from the 50Ω cable are minimized by making the impedance change gradual using the end cones. After passing through the device under test (DUT), the signal goes through another end cone back to the cable connected to the input port (port 2) of the network analyzer. In order to remove residual effects of the cones, the attenuation of the cables, and the phase advance with frequency due to the electrical length of the signal path, a reference pipe is also measured. The transmitted signals in port 2 and the reflected signals in port 1 from both measurements are compared, and the impedance of the DUT is calculated.

In principle, an inner wire can be chosen large enough to maintain a constant 50Ω impedance inside the beam pipe. For reasons to be reviewed later, the stretched wire should be as thin as possible to avoid distorting the impedance measurement. An alternative method, sketched in figure 38, of matching impedances using resistive networks is also used [19,20] by other researchers.

The network analyzer internally compares the transmitted (port 2) and reflected (port 1) sine waves to the output signal, calculating the amplitude change and phase shift for each frequency point in its frequency sweep. Because most of these measurements are made in the microwave regime, the standard parameterization of this information is in the form of a "scattering" matrix, a 2x2 matrix composed of complex numbers called S-parameters. The reflected voltage phasor divided by the output voltage phasor is called S_{11}, and the similarly normalized transmitted power (voltage into 50Ω) is called S_{21}. Both network analyzer ports have a 50Ω characteristic impedance. If a lossless 50Ω cable connected the two

ports, the amplitudes of S_{11} and S_{21} would be 0 and 1 respectively. The phase of S_{21} at a given frequency would be the electrical length of the cable times 2π times the frequency.

Calculating Impedance from Scattering Parameters

The hardest part of these measurements is the extraction of the longitudinal impedance of the DUT from the S-parameter data. The first problem is extraction of sometimes very large (or small) impedance values given finite network analyzer accuracy. The second problem involves the calculation of longitudinal impedance for an extended device whose length is comparable to the wavelengths being transmitted through the structure.

Study of the first problem is useful for two reasons. Primarily, it leads to the derivation of longitudinal impedance vs S_{21} or S_{11}. Second, the discussion of which parameter to use given a certain DUT involves path length and measurement accuracy criterion which should be reviewed.

Figure 39 is a sketch of a circuit diagram in which a voltage source V_0 coupled to a series resistance R_0 (model of port 1 of the network analyzer) is connected to a variable termination resistance **R**. The current flowing though the resistors is

$$I = \frac{V_0}{(R_0 + R)} \qquad (23)$$

The power dissipated in the termination resistor is

$$P_R = I^2 R = \frac{V_0^2 R}{(R_0 + R)^2} \qquad (24)$$

This power is maximized when $R=R_0$, the condition which also guarantees that the reflection parameter S_{11} is zero. Therefore, the definition of S_{11} can be written as the fractional power mismatch with respect to optimum, such that

$$S_{11}^2 \equiv \frac{P_{R_0} - P_R}{P_{R_0}} = 1 - \frac{4 R_0 R}{(R_0 + R)^2} \qquad (25)$$

Describing S_{11} in terms of decibels (0db defined as full reflection), figures 40 and 41 are plots of this equation. In the case of figure 40 the range of **R** (labelled series resistance) is from 1Ω to 1MΩ, showing the expected dip to -∞db at R_0=50Ω. As the series resistance rises, the reflection coefficient approaches unity (0db). Figure 41 is a close-up of this region, showing that if the accuracy of the network analyzer

were 0.01db, that the maximum resistance which could be distinguished from an open termination ($\infty\Omega$) is approximately 100kΩ.

The next step in this discussion is to examine the circuit diagram relevant to the stretched wire longitudinal impedance measurements. This diagram is sketched in figure 42. The voltage source V_0 and initial resistor R_0 describes port 1, and the final termination resistor R_0 simulates port 2. The DUT is described as a series resistance **R**. The current flowing through the resistors is

$$I = \frac{V_0}{(2R_0 + R)} \quad . \qquad (26)$$

The ratio of the voltage at port 2 **V** and the voltage source V_0 is calculated by multiplying both sides of equation (26) by R_0, with the result

$$\frac{V}{V_0} = \frac{R_0}{(2R_0 + R)} \quad . \qquad (27)$$

The transmission scattering parameter S_{21} is defined to be the ratio of the voltage phasor measured at port 2 and the output voltage phasor. It is normalized such that maximum transmission is parameterized as unity (0db). This will occur when the series resistance **R** is zero. Therefore, multiplying the right hand side of equation (27) by 2 for this normalization, the definition of the transmission scattering parameter is

$$S_{21} = \frac{1}{\left(1 + \frac{R}{2R_0}\right)} \quad . \qquad (28)$$

A plot of equation (28), with S_{21} described in decibels ($20\text{Log}_{10}[S_{21}]$), can be found in figure 43. Given that most modern network analyzers can achieve 80db of dynamic range, resistances up to 1MΩ can be measured. On the other hand, low series impedances are again limited by the accuracy of the analyzer. In figure 44 a close-up of the series resistance range of 1Ω to 100Ω is plotted. In order to measure a 1Ω series resistance, an accuracy of 0.1db is required.

The second issue which must be addressed is the length of the DUT, and the errors which will occur if the inverse of equation (28) is applied

$$R = 2R_0 \frac{1 - S_{21}}{S_{21}} \quad , \qquad (30)$$

or with the subtraction of the reference

$$R = 2R_o\left(\frac{1}{S_{21_{DUT}}} - \frac{1}{S_{21_{REF}}}\right) \quad . \qquad (31)$$

Perhaps the clearest example of the errors possible when measuring an extended device comes from splitting the DUT into two thin impedances of value R/2 each separated by an electrical length **L**. If the parameter **k** is defined by

$$k = \frac{2\pi f}{c} \quad , \qquad (32)$$

where **c** is the speed of light and **f** is the frequency generated by the network analyzer, then the apparent impedance **Z** is [21]

$$Z = \frac{R}{S_{21}}\sqrt{S_{21}^2\cos^2 kL + \sin^2 kL} \quad . \qquad (33)$$

The plot of this equation, which relates the measured total apparent impedance to the actual total longitudinal impedance, is shown in figure 45 for R=1. Note that the uncertainty in the measurement is at most a factor of $1/S_{21}$, always more than the actual value. In addition, the phase of the signal at port 2 is distorted. Clearly, frequencies whose wavelengths are much longer than the DUT are necessary for accurate measurements.

In the case of the impedance contribution of the cones at the end of the beam pipe sections, the gentler the slope, the lower the inductance (and hence impedance) contributions. According to the above discussion, the difference between the apparent and real longitudinal impedance is thus minimized. Therefore, even though the cones are separated by a distance large compared to the wavelength of the signal, the contribution of the cones with respect to the impedance of the DUT is negligible.

Finally, in the spirit of equation (28), the inverse of equation (25) for the case of the impedance measurement apparatus is

$$R = 2R_o\frac{1 - S_{11}}{S_{11}} \quad . \qquad (34)$$

Note that equation (34) has the same form as equation (30) in the transmission measurement of longitudinal series impedance. The main difference between the two methods, besides the range of impedances for which the network analyzer has sufficient accuracy, is that in the case of the reflection measurement the phase information is much more difficult to handle. A reference plane must be defined

at the center of the DUT in order for the real and imaginary parts of the longitudinal impedance to be properly separated.

Initial Small Cavity Measurement

To start off systematic stretched wire longitudinal impedance measurements the small right cylindrical cavity drawn in figure 46 was studied. The characteristic impedance of the "beam pipe" and the wire was 125Ω. Since no impedance matching was done between this pipe and the 50Ω cables to and from the network analyzer, a reference pipe (also drawn) was needed to subtract the measured impedance contribution of the reflections.

According to equation (5), in the range of frequencies below 6GHz (range of the network analyzer) two TM modes were expected to be observable.

Mode	Calculated Frequency (Ghz)	Measured Frequency (GHz)	Frequency Difference (GHz)
TM_{010}	3.076	3.577	0.501
TM_{011}	4.521	4.524	0.003

The above table contains the mode designations, the calculated mode center frequencies, and the measured frequencies. Note that the frequency shift (measured minus calculated) of the TM_{010} mode is quite substantial. In the absence of a stretched wire, when the cavity was excited by a small probe, no such frequency shift was observed. Therefore, the existence of the stretched wire itself is distorting the measurement.

In order to understand the severity of this effect, the existence of the wire must be incorporated into the calculations that led to equation (5). In the absence of the wire the solution for the longitudinal electric field in a right cylindrical cavity is

$$E_z = J_0\left(\frac{x_{on}\, r}{R}\right)\cos\left(\frac{\pi\, z\, p}{d}\right)\exp(-j\,\omega_{onp}\, t) \qquad (35)$$

The boundary condition at the radius of the cavity wall is that the longitudinal electric field is zero, a condition enforced in the equation by the Bessel function. At the center of the cavity the electric field is largest. When a wire of radius a is stretched down the center of the cavity the longitudinal electric field at the surface of the wire must also be zero. Simply stating the solution to this new boundary value problem, the Bessel function in equation (35) is replaced by the factor

$$J_0\left(\frac{x_{on}\, r}{R}\right) \Rightarrow J_0\left(\frac{\bar{x}_{on}\, r}{R}\right) Y_0\left(\frac{\bar{x}_{on}\, a}{R}\right) - J_0\left(\frac{\bar{x}_{on}\, a}{R}\right) Y_0\left(\frac{\bar{x}_{on}\, r}{R}\right) \quad , \tag{36}$$

where in the case of the TM_{01P} modes, to first order,

$$\bar{x}_{01} = x_{01} - \frac{Y_0(x_{01})}{J_1(x_{01})} \frac{J_0\left(\frac{x_{01}\, a}{R}\right)}{Y_0\left(\frac{x_{01}\, a}{R}\right)} \quad . \tag{37}$$

Applying these new boundary conditions and solving for the wire radius dependent mode frequencies, the expected frequency shift due to the wire can be calculated. Applying this calculation to the TM010 mode, a frequency of 3.583GHz is expected, a value very close to the measurement.

In order to minimize the effect of the wire, its radius should be kept as small as possible. The frequency shift depends logarithmically on the ratio of the wire and cavity radii. Therefore, factors of ten in this ratio only make factors of two or three differences in the magnitude of the frequency shift. In addition, the wire causes a decrease in the Q of these modes, further changing the results of the measurement.

These limitations are quite severe when RF cavities or other high-Q devices are being tuned to precise frequencies. For this reason stretched wire measurements are not utilized in these applications. On the other hand, for the types of information which is needed for instability research, small frequency shifts are not often important. Second, even though the Q of the mode is diminished by the existence of the wire, calculations [22] have shown that the shunt impedance is also diminished by almost the same amount, such that the value of the ratio R/Q is preserved. Finally, often the beam pipe elements under measurement are not high-Q at all, so the effect of the wire becomes truly negligible.

Tevatron RF Cavity Measurement

A Tevatron RF cavity under repair for a small vacuum leak was connected to the longitudinal impedance measurement apparatus. The cavity was cold, and therefore detuned away from its nominal resonant frequency of 53.1MHz. In addition, the coaxial power coupler to the cavity was disconnected, changing the loaded-Q of the system. There were two reasons for measuring the longitudinal impedance of this cavity. First, no records existed of previous impedance measurements of these cavities, and there was some question as to the density and placement of higher order resonance modes. Second, questions were raised concerning the estimation of Z_L/n in the Tevatron and the appropriateness of including contribution of the cavities, which was assumed to be approximately 1Ω.

Figure 47 contains plots of S_{21} and S_{11} stretched wire measurements of this Tevatron RF cavity, which had one foot sections of beam pipe and impedance matching cones on both sides. First, note the periodic effect of the cones on the transmitted and reflected amplitudes. Second, as frequency is

increased the amplitude of these signals monotonically decreases due to the skin depth induced increase in coaxial transmission line conductor resistance. Using equation (30) on the S_{21} data in the figure, the magnitude of the impedance spectrum is calculated and plotted in figure 48. The longitudinal impedance was sampled every 47.72kHz, which happens to be the revolution frequency of the Tevatron. The lowest line is the fundamental 53.1MHz acceleration mode of the RF cavities. Its peak amplitude should have been roughly 350kΩ, but because the cavity was cold the resonant frequency actually occurred between the nearby sampled points. Two other high impedance modes can be seen near 150MHz and 1.85GHz. On this scale and up to 3GHz, there is no evidence of a broadband longitudinal impedance contribution from RF cavities. The vertical scale is expanded by 100x in figure 49, and a linear growth in impedance with frequency becomes evident.

The contribution of the impedance matching cones on the measured R/Q of the high impedance modes should be negligible, but needs to be subtracted if a sensitive measurement of Z_L/n from the RF cavities is required. Figure 50 shows the measured S-parameter characteristics of the reference system. In most respects the S_{11} data is quite similar to that shown in figure 47. On the other hand, the transmission data contains none of the deep null spikes seen in figure 47. Applying equation (30) to the transmission data, the impedance of the reference pipe is plotted in figure 51. The average magnitude of the impedance rises linearly with frequency at exactly the same rate as the baseline impedances in figure 49, both slopes consistent with a Z_L/n of 0.008Ω (500x47.72kHz/3GHz).

Applying equation (31) to the S_{21} data of the RF cavity (DUT) and the reference pipe (REF), the corrected impedance spectrum of a Tevatron RF cavity is calculated and plotted in figure 52. As expected, the peaks of the higher impedance modes are the same height. In figure 53 the same data is plotted on a 100x more sensitive vertical scale. There is no sign of a broadband impedance contribution from the RF cavities. In an attempt to smear out the high-Q modes so as to produce an effective broadband impedance, the data in figure 52 was smoothed by a 5MHz and 50MHz video bandwidth to produce the spectra in figures 54 and 55 respectively. With a maximum of 3GHz, there is no clear linear trend of impedance magnitude with frequency in the background.

Finally, Tevatron RF cavity measurements up to a frequency of 6GHz were made. Unfortunately, similar measurements were not taken with the reference pipe. Therefore, the resultant impedance data in figures 56 and 57 contain no reference data subtractions. Even on the course scale in figure 56, around 5GHz it is possible to see the effects of the impedance matching cones and the attenuation in the coaxial transmission lines. If one subtracts a background with the same slope as that measured in figure 51, the data in figure 57 would again show no sign of a broadband impedance.

Main Ring Kicker Magnets

After the realization that one of the kicker magnets in the Main Ring (at location C48) was of the Window-frame type, systematic measurements of the longitudinal impedance of a spare pair of sections

was carried out. The C48 kicker in the tunnel is made up of three such pairs of sections. The cross section of the kicker magnets is very similar to that shown in figure 6, except that no copper strips exist to short the beam flux around the ferrite core. It is noted that the beam pipe connects to open ceramic on each side of the kicker sections, so that there is no low inductance path for the beam image current to follow the beam. In addition, the copper conductors which carry the kicker current are not impedance matched to their feed cables or the power supplies.

Figure 58 shows the transmission and reflection coefficients acquired from a stretched wire longitudinal impedance measurement on a pair of C48 kicker sections. No reference pipe data was taken. First, note the vertical scale of the transmission coefficient plot. By a frequency of 500MHz the transmitted signal was already attenuated by 60db. Using a repeated measurement of S_{21} which reached up in frequency close to 3GHz, the impedance of the kicker was calculated and plotted in figure 59. Note the broad vertical scale, and the fact that many of the resonance peaks still exceed this values on this scale.

Since no reference pipe data has been taken to date, it is impossible to tell how much of the rise in the impedance with frequency is of a broadband nature. One hint may be found in the data in figure 60, where the measurement in figure 59 was repeated for the case where the copper flux shorting strips have been inserted into the magnet ferrite core. On the same horizontal and vertical scale, note that the impedance of the structure has been significantly reduced. Therefore, assuming an approximate value of 1MΩ of impedance at 3GHz, a value for Z_L/n of 20Ω is calculated. Multiplying by a factor of three to account for the entire C48 magnet structure, this predicts a present Main Ring broadband longitudinal impedance contribution of 60Ω from the kicker! The other lesson to be learned from figure 60 is the value of the shorting strips. Clearly, there was a big reduction in the general measured longitudinal impedance when those strips, as shown in figure 5, were added.

Finally, for the sake of comparison a section of C-frame kicker (similar in cross section to the sketch in figure 5) was measured. It was a spare for a kicker magnet found in the Main Ring (at location A0) called MK90. The result is in figure 61. Compared to the impedances shown in figure 59 and 60 for the Window-frame type of kicker, the C-frame type seems to have almost negligible longitudinal impedance. In fact, the rise in the magnitude of the measured impedance with frequency is consistent with the contributions from the impedance matching cones and attenuation of signal due to conductor resistance in the coaxial transmission lines.

Future Work

This paper has reviewed a number of longitudinal impedance measurements made in a systematic fashion over the past few years. As expected, a large (maybe even larger) number of questions still need to be answered. Therefore, a considerable amount and diversity of work is still needed before practical applications aimed at improving the performance of Fermilab accelerators can be reliably executed.

In the longitudinal regime, the spectrum of the beam-based accelerator impedance must be systematical measured from 47kHz to at least 3GHz. This data must be compared to the results of stretched wire measurements in order to identify and correct the leading contributors of impedance seen by the beam.

In the case of transverse impedance, any type of measurement of either the wire or beam persuasion should be initiated in the near future. All of the instabilities, except a longitudinal coupled bunch instability in the Booster, in Fermilab accelerators are in the transverse plane. Therefore, it is essential that transverse studies begin.

Finally, the measurement and analysis techniques used in both the wire and beam measurements must be better understood and refined. In the case of longitudinal beam based measurements, bunched beam data for the model dependent broadband impedance would provide complementary information. In the transverse case both bunched and unbunched beam measurements must be implemented. More calculations are needed in order to understand stretched wire longitudinal impedance measurements when extended objects at high frequencies are under test. Transverse balanced pair transmission line measurements should start quite soon.

Conclusions

In this paper a broad range of systematic longitudinal impedance measurements at Fermilab have been reviewed. Both beam based and stretched wire based measurements were discussed.

The beam based measurements are not nearly systematic enough yet to either test their validity in the frequency region of known, dominant impedances. In addition, no systematic measurements have yet been attempted over a broad range of revolution harmonics under well understood beam conditions. The occurrences of self-bunching instabilities and the excitation of revolution harmonics below the one under measurement must still be understood and either eliminated or incorporated into the impedance analysis.

The stretched wire measurements are probably only reliable on a qualitative level at this time. Many more calculations are required to understand the effects of distributed impedances and the subtraction of reference data.

Acknowledgements

The data and analysis presented in this paper were a product of the efforts of a large and ever growing number of individuals. The beam based measurements would not have occurred without the calculations and persistence of Xiao-qing Wang, who developed the techniques and numerical analysis for the Accumulator measurements. The bandwidth and precision of the stretched wire measurements were made possible by the professionalism of Dennis McConnell and Brian Fellenz. Theoretical calculations which tested the validity of preliminary stretched wire measurement results were performed by K.Y. Ng, Alex Bogacz, Fady Harfoush, Mike Foley, and Ping-Jung Chou. Multiparticle computer simulations performed by Xianping Lu helped confirm the hypothesis that RF cavity beam loading invalidated earlier longitudinal impedance measurements in the Main Ring. In addition to the people mentioned above, accelerator shifts were manned by the capable and enthusiastic operators Bill Pellico and Todd Sullivan. Helpful advice and support was given by Curtis Crawford, Jim Griffin, Kathy Harkay, Chris Jensen, Quentin Kerns, Jim MacLaughlan, John Marriner, and Dave McGinnis. The recent help of Pat Colestock with calculations, stretched wire measurements, accelerator shifts, and organization is greatly appreciated.

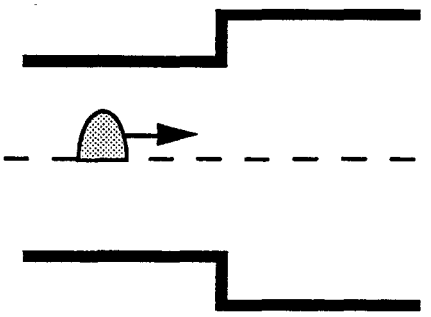

Figure 1: Beam travelling down a circularly symmetric beam pipe in which there is a step change in pipe radius.

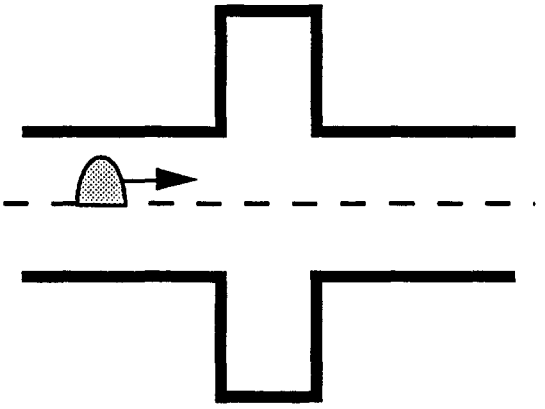

Figure 2: Beam travelling down a circularly symmetric beam pipe attached to a cavity structure.

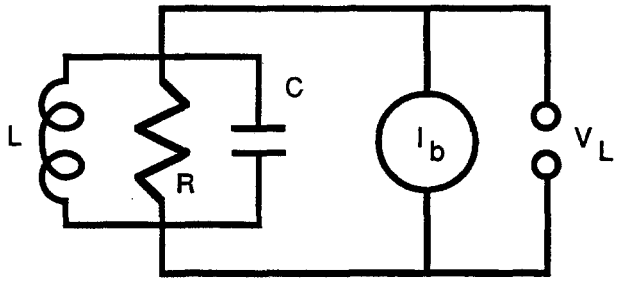

Figure 3: Electrical circuit model of the beam current I_b coupling energy into a specific cavity mode (damped, lumped LC circuit), producing a cavity voltage V_L.

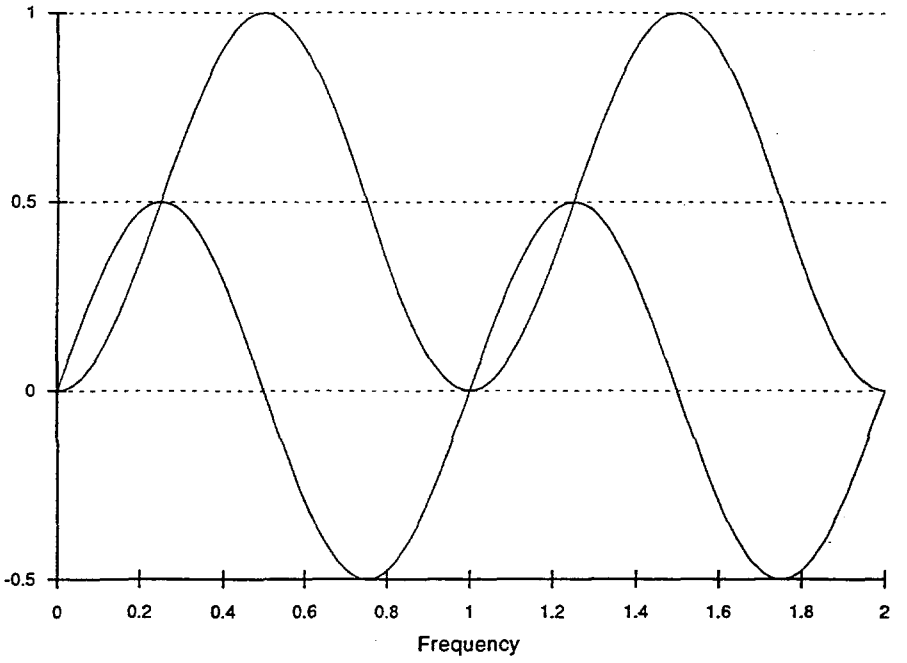

Figure 4: Real and imaginary parts of the longitudinal impedance associated with a stripline beam pickup. As expected, the real part is positive definite.

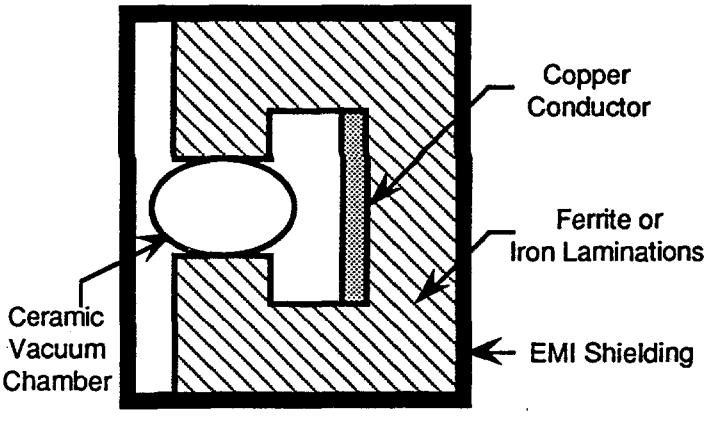

Figure 5: Cross section of the construction of a typical C-magnet type kicker.

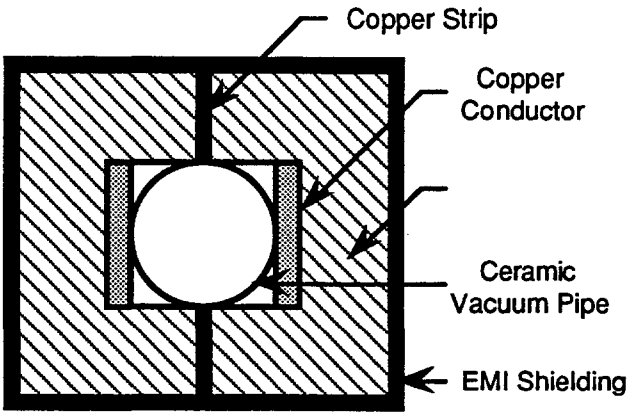

Figure 6: Cross section of the construction of a typical Window-frame kicker magnet.

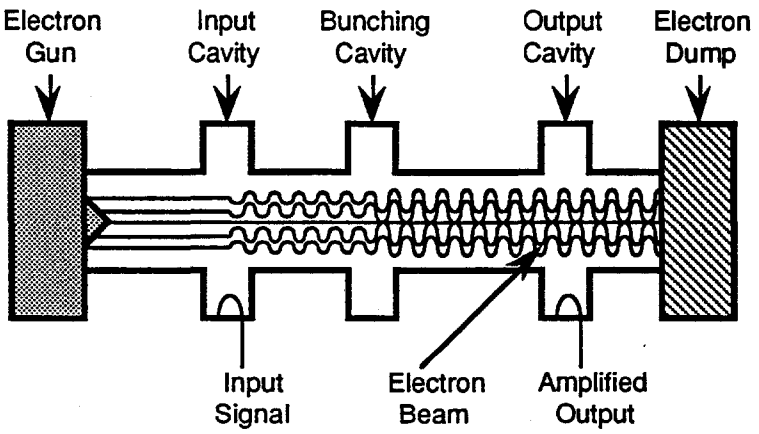

Figure 7: Schematic drawing of a microwave amplifier called a klystron. The electron beam, which is modulated by the first cavity, is further modulated by the intermediate cavity. The output power is coupled out using the last cavity.

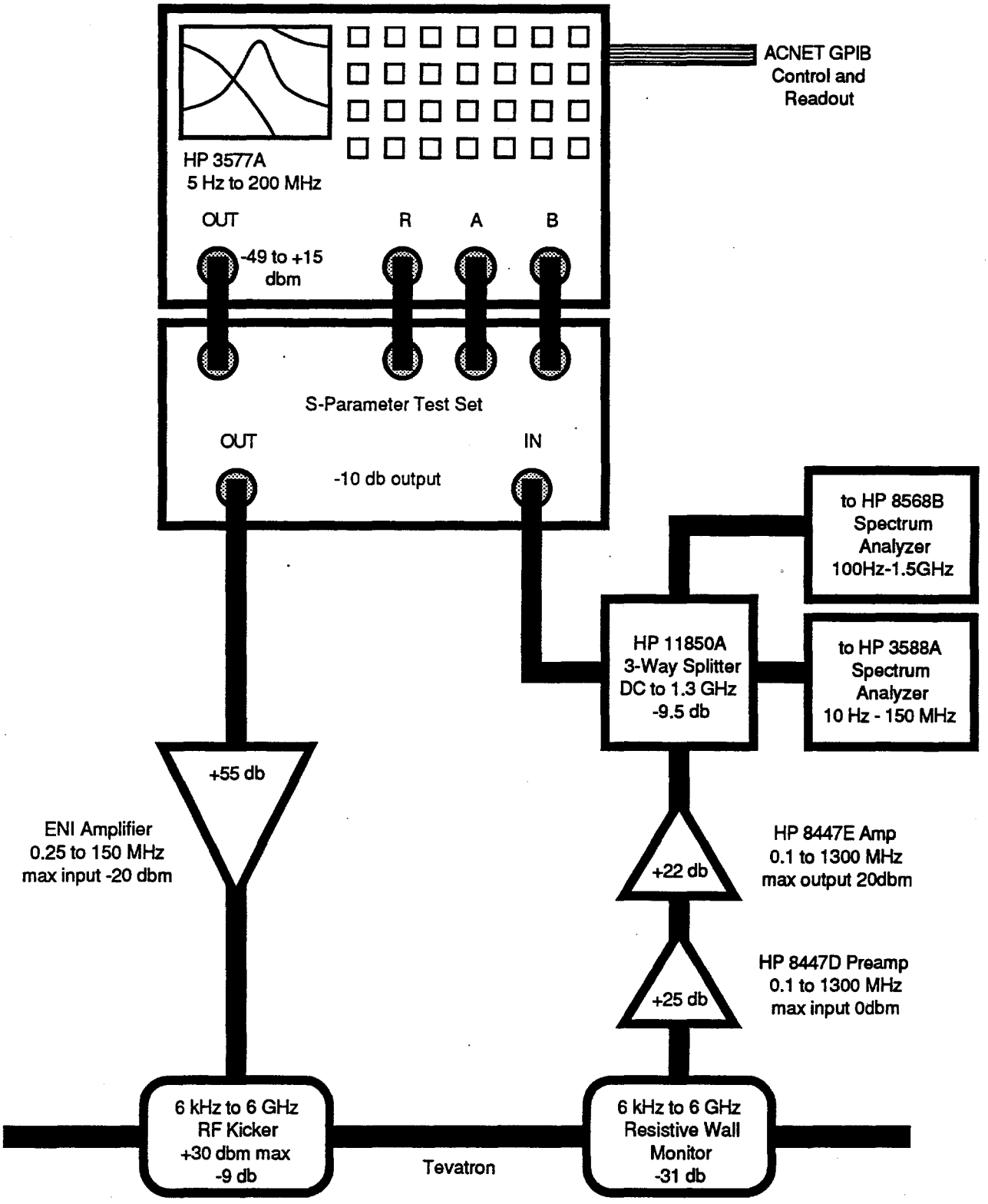

Figure 8: Typical experimental apparatus for beam-based Tevatron measurements of longitudinal impedance as a function of frequency.

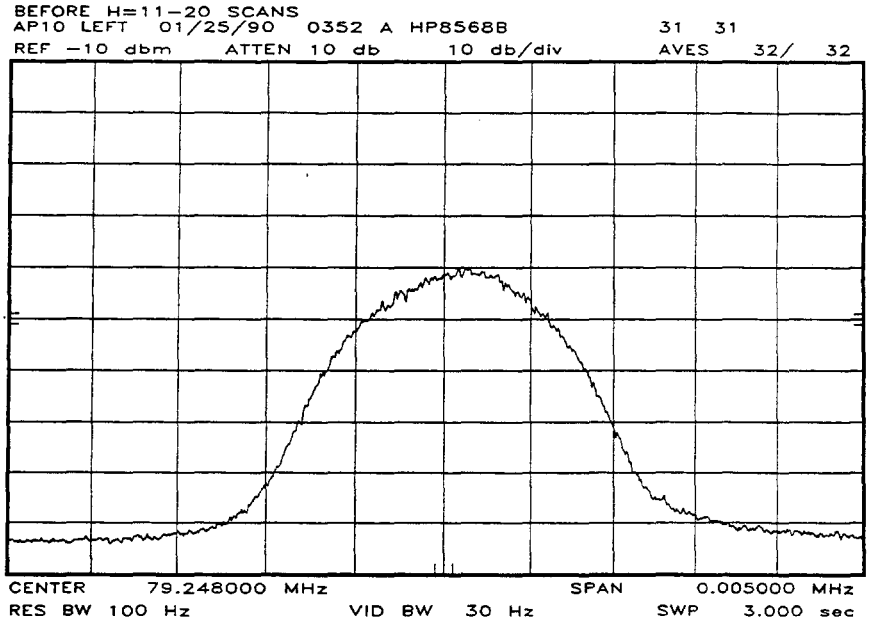

Figure 9: Longitudinal Schottky distribution measurement in the Accumulator at harmonic 126. Above the noise floor, the curve is proportional to the beam frequency distribution $\Psi_0(\omega)$.

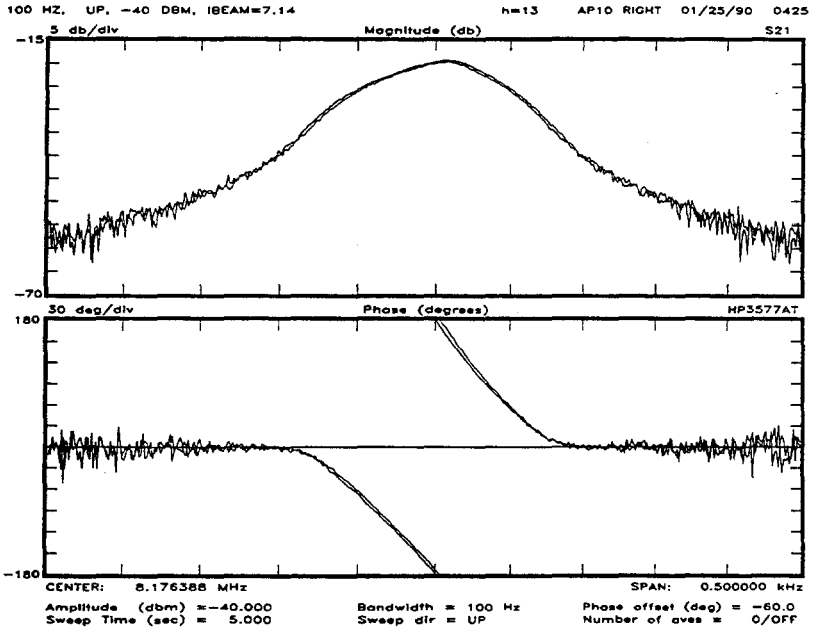

Figure 10: Result of a unbunched beam longitudinal beam transfer function measurement in the Accumulator at harmonic 13. The two traces represent data taken under identical conditions except for the direction of the network analyzer frequency sweep.

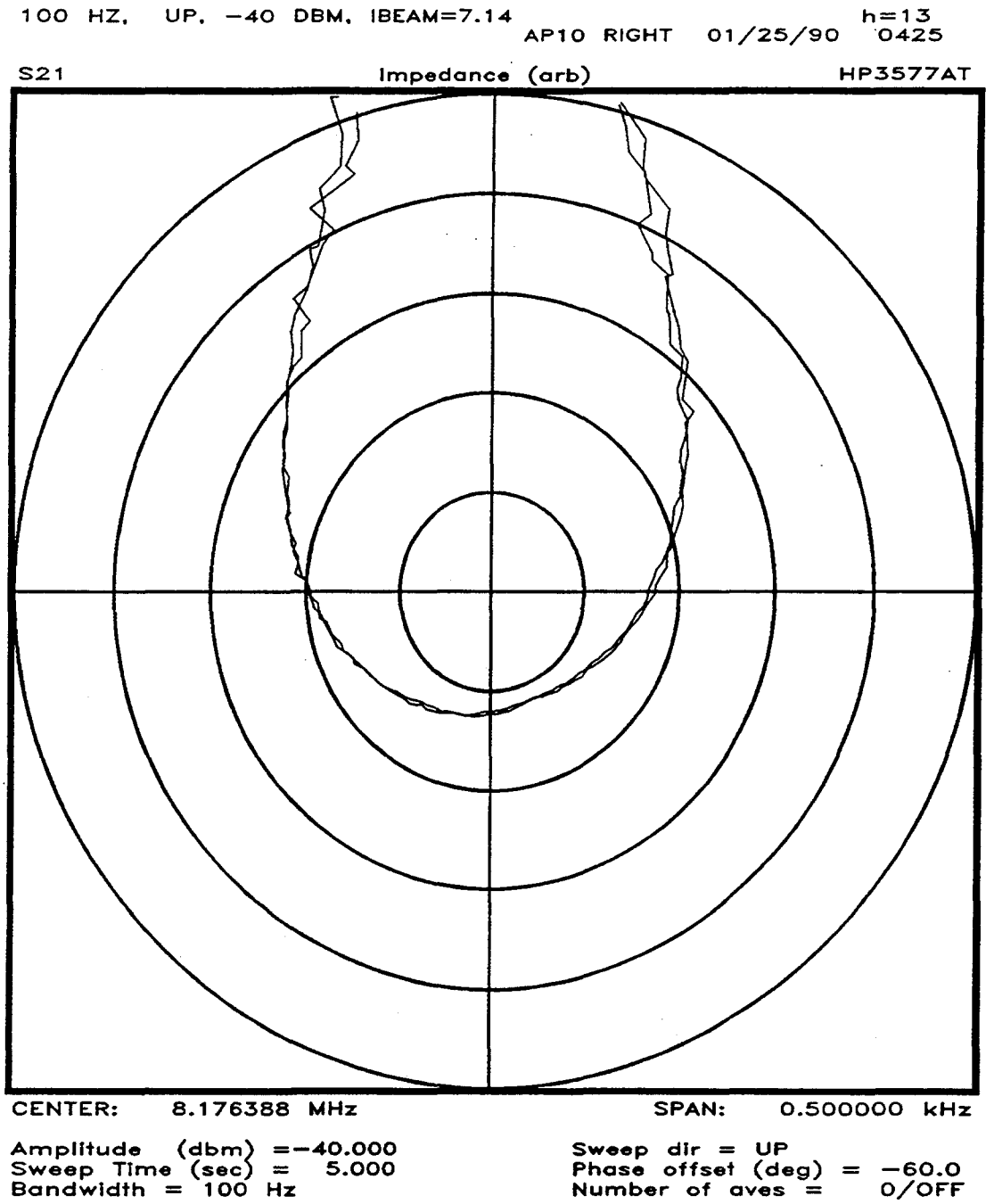

Figure 11: Inverse beam response calculated from the data in figure 10. The shape distortion is caused by the non-symmetric shape of the beam frequency distribution. No noticeable response shift due to longitudinal impedance is evident.

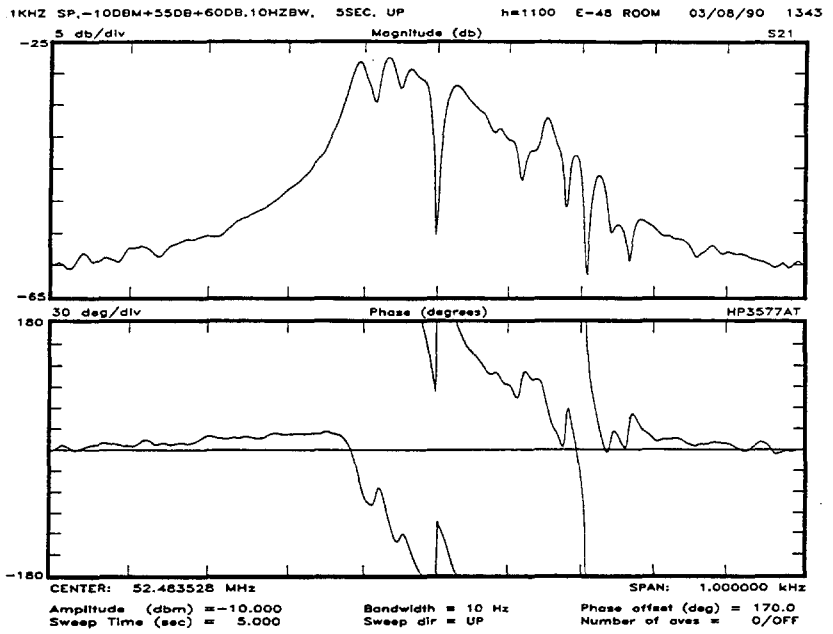

Figure 12: Longitudinal beam transfer function at revolution harmonic 1100 in the Tevatron. In contrast to the Accumulator data in figure 10, note the spikes in the beam response.

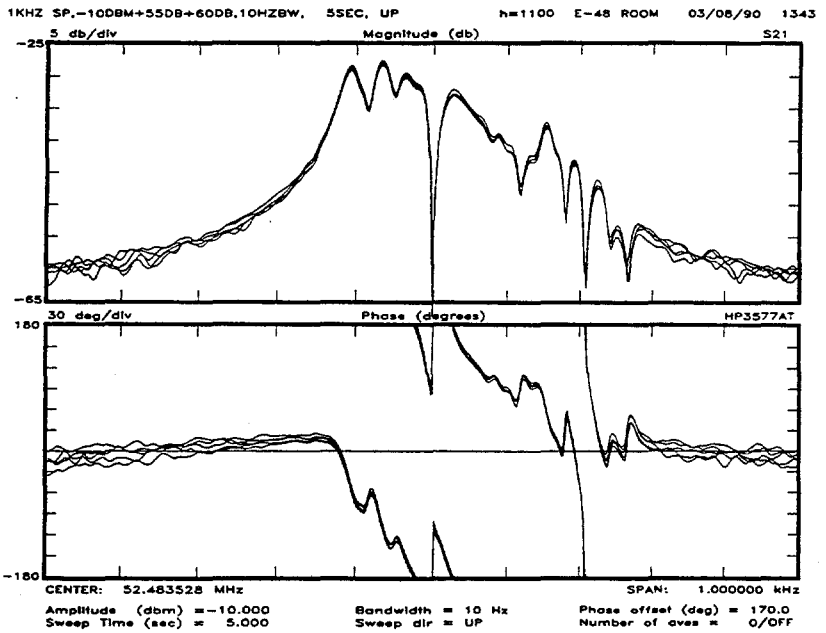

Figure 13: Same as figure 12, except that the longitudinal transfer functions from harmonics 1100 to 1105 are superimposed. Note that the structure in the distribution is not due to noise or resonances in the frequency response of the experimental apparatus.

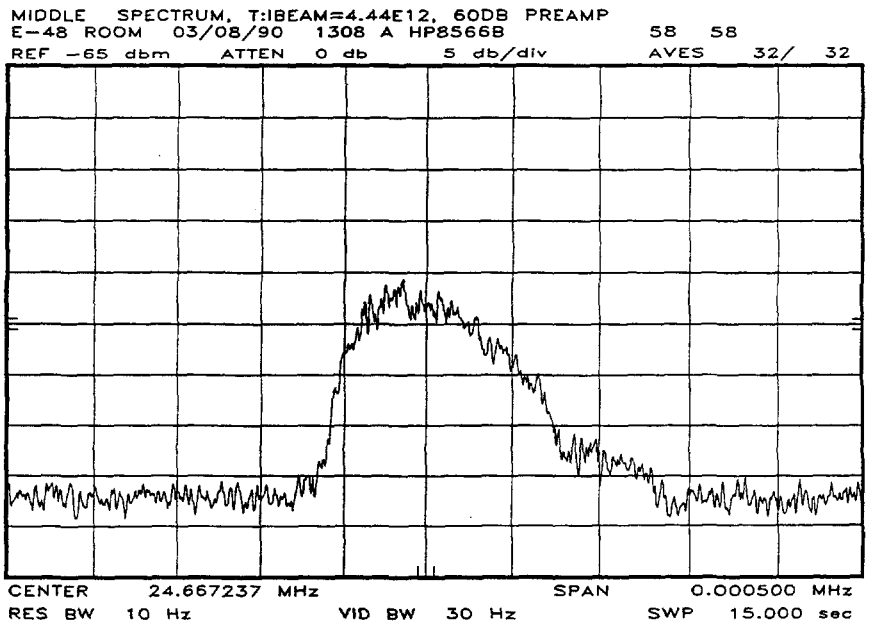

Figure 14: Longitudinal Schottky scan in the Tevatron at revolution harmonic 517. Though reflecting the momentum distribution of the beam when the data in figures 12 and 13 were taken, no sign of holes in the distribution are evident.

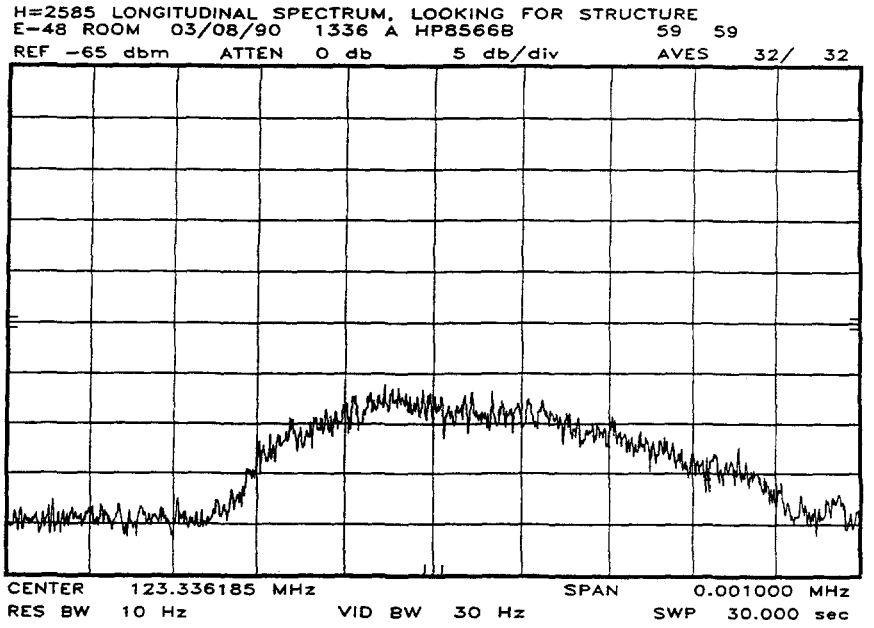

Figure 15: Longitudinal Schottky scan in the Tevatron at revolution harmonic 2585. By going to 5 times the frequency of the scan in figure 14, and therefore not being limited by the minimum frequency resolution of the spectrum analyzer, it was hoped that holes in the beam momentum distribution would become evident.

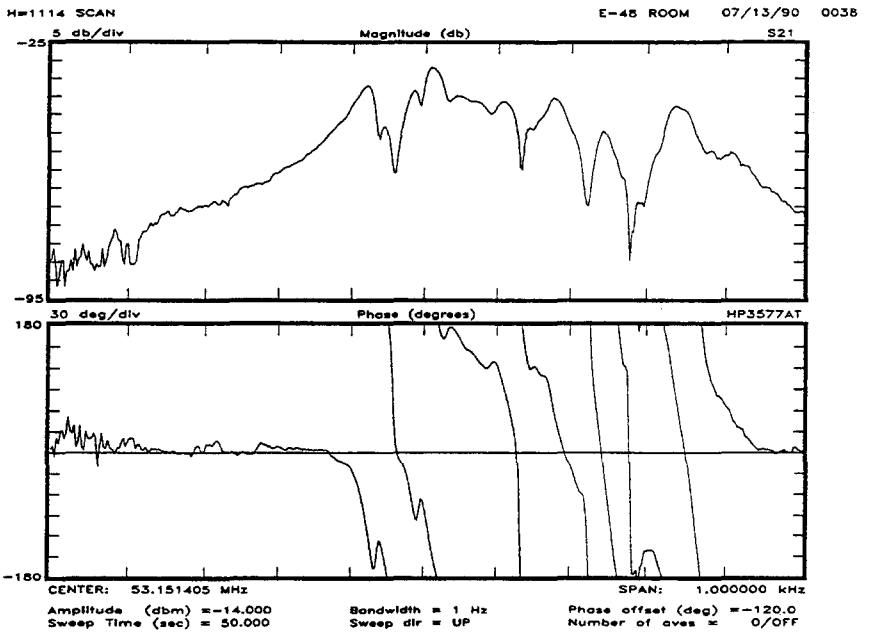

Figure 16: Repeated longitudinal transfer function measurement in a later accelerator study period. The spikes in the response still exist.

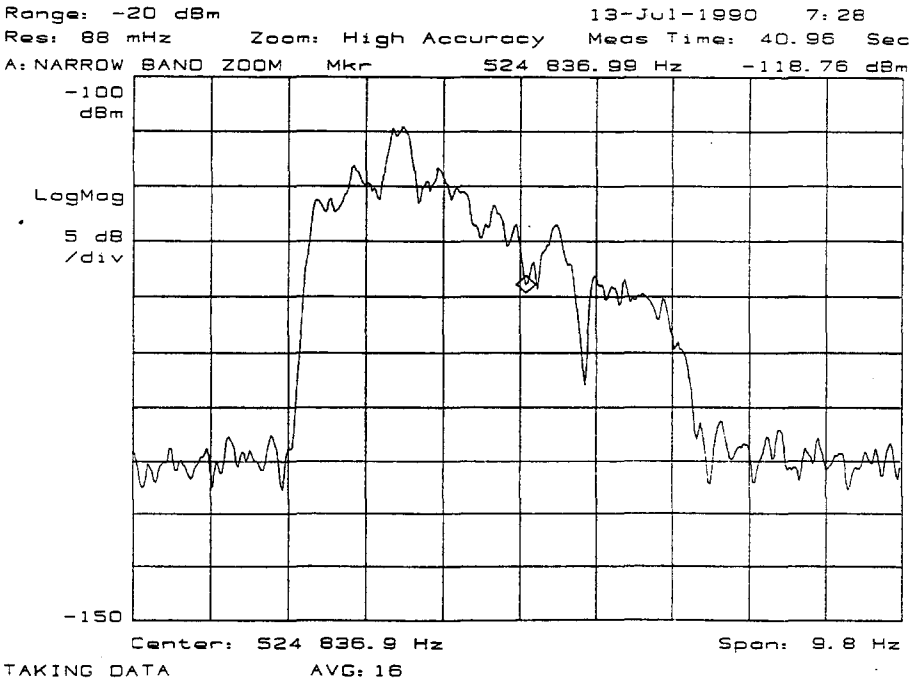

Figure 17: Longitudinal Schottky scan in the Tevatron at revolution harmonic 11. With a resolution bandwidth of 88mHz, holes in the momentum distribution corresponding to the spikes in the data in figure 16 now appear.

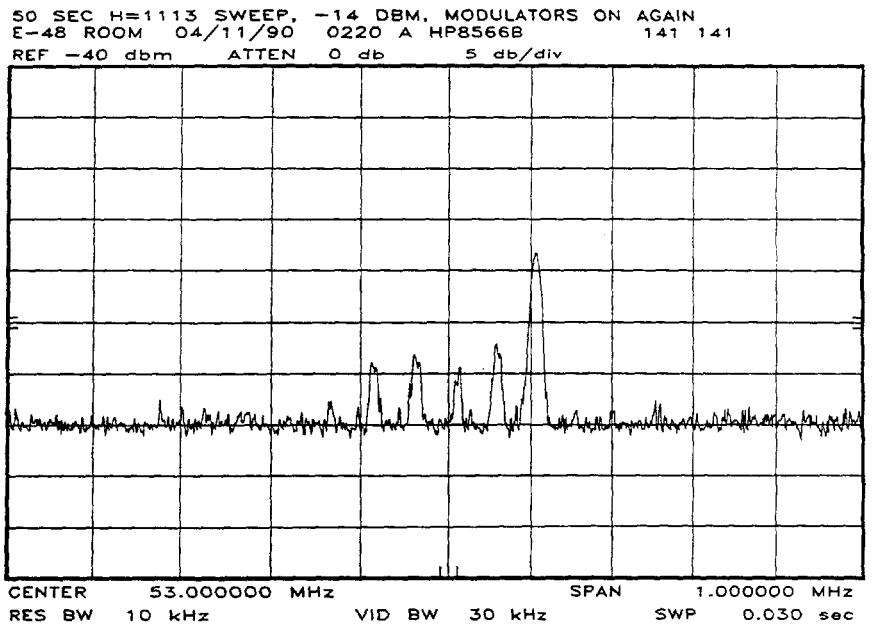

Figure 18: Broad band frequency domain picture of the beam current modulation caused by a longitudinal beam transfer function measurement at revolution harmonic 1113 (rightmost peak). Note that a number of revolution harmonics below the driven frequency are excited.

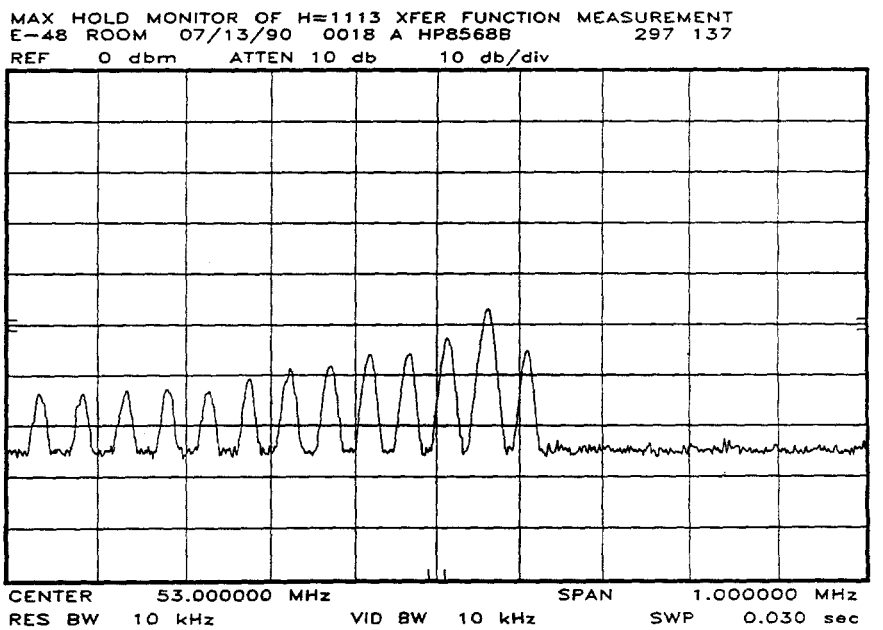

Figure 19: Broadband beam response to a longitudinal transfer function measurement at harmonic 1113 similar to figure 18, except with higher beam intensity (6.33×10^{12} protons).

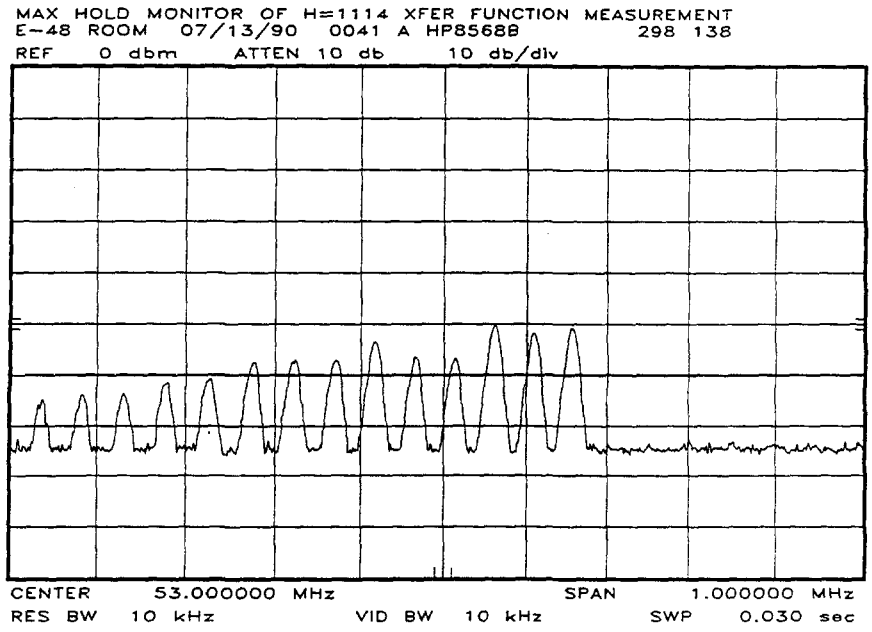

Figure 20: Same as figure 19, except harmonic 1114 is driven by the network analyzer.

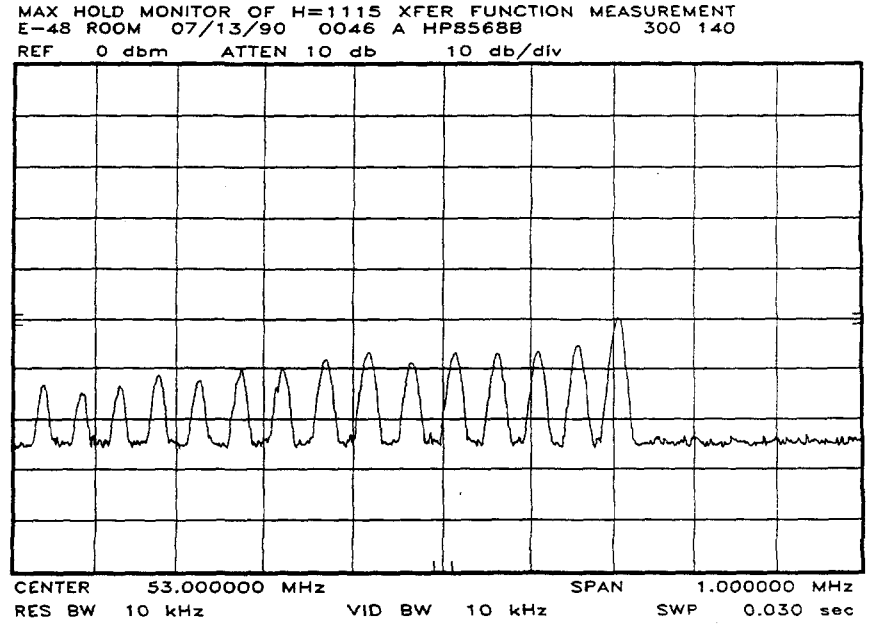

Figure 21: Same as figure 19, except harmonic 1115 is driven by the network analyzer.

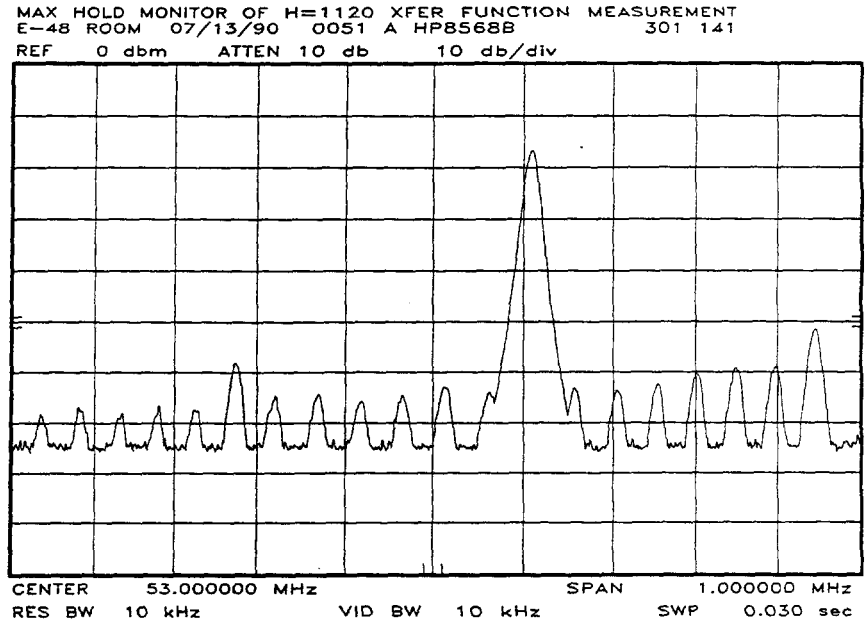

Figure 22: Broadband beam response to a longitudinal transfer function measurement at harmonic 1120 while a self-bunching instability was taking place at harmonic 1113 (RF cavity resonant frequency).

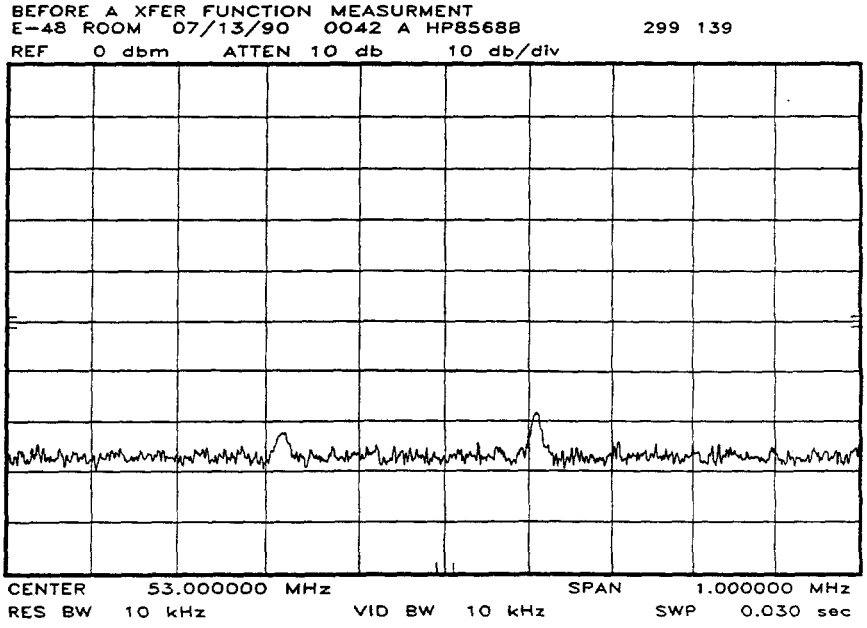

Figure 23: Beam current spectrum without external excitation. Note that harmonics 1113 and 1107 seem to be slightly self excited.

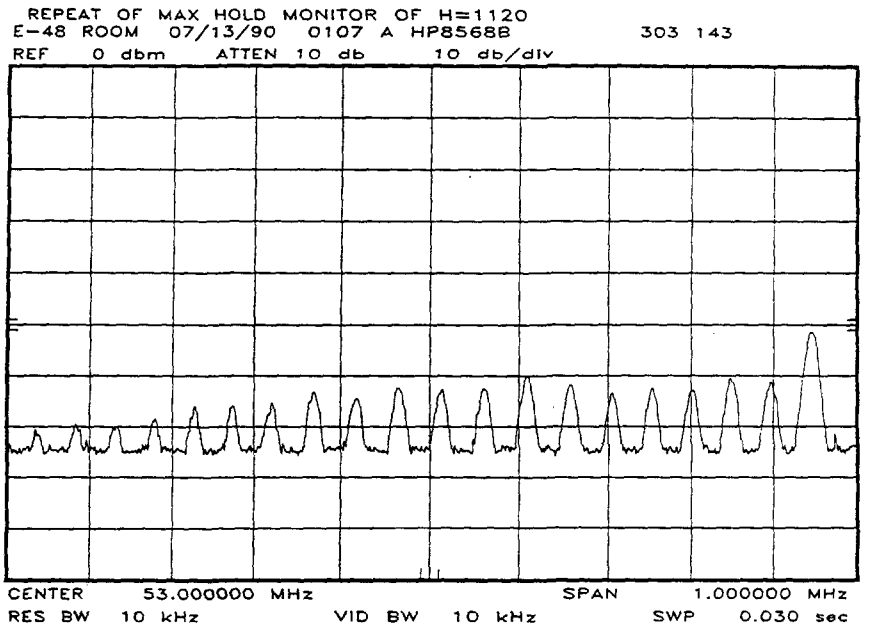

Figure 24: Repeat of measurement in figure 22 after waiting 15 minutes for the self-bunching instability to spontaneously disappear. The distance of the drive frequency from the RF cavity resonant frequency does not seem to affect this phenomenon.

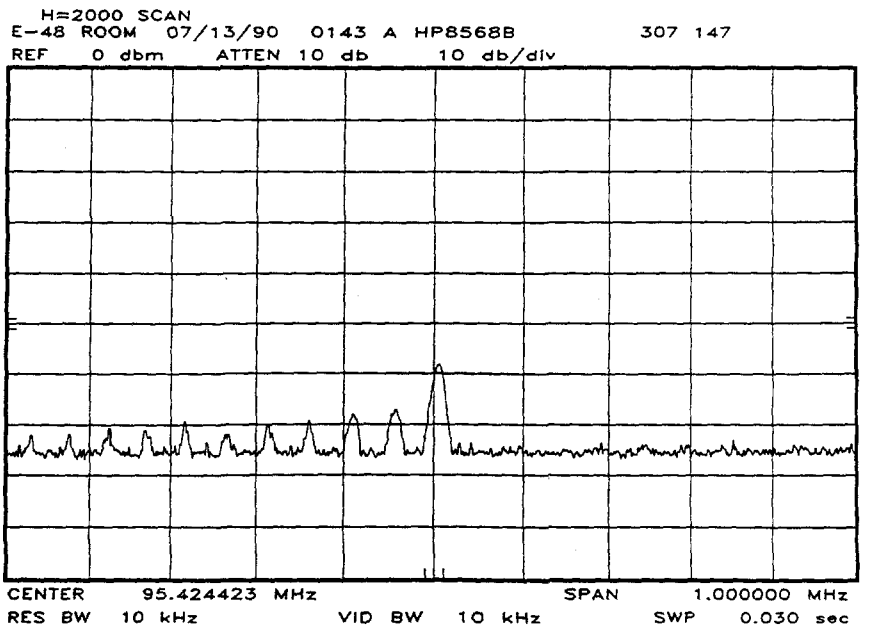

Figure 25: Broadband beam response to a longitudinal transfer function measurement at harmonic 2000. Though the amplitude of the response is smaller than the previous measurements, the nature of this effect is still unchanged far above the RF cavity resonant frequency.

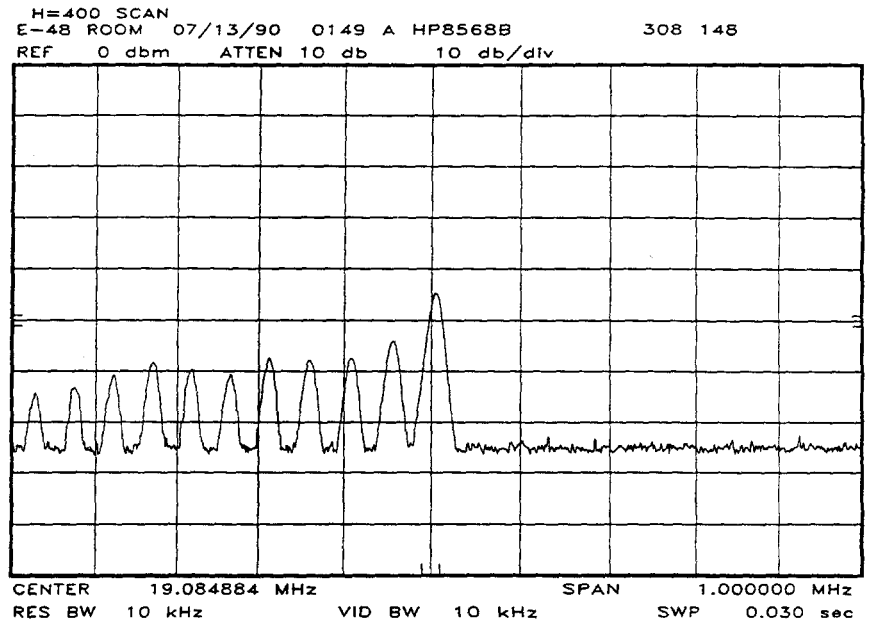

Figure 26: Broadband beam response to a longitudinal transfer function measurement at harmonic 400. Though the amplitude of the response is greater than the measurements near revolution harmonic 1113, the nature of this effect is still unchanged far below the RF cavity resonant frequency.

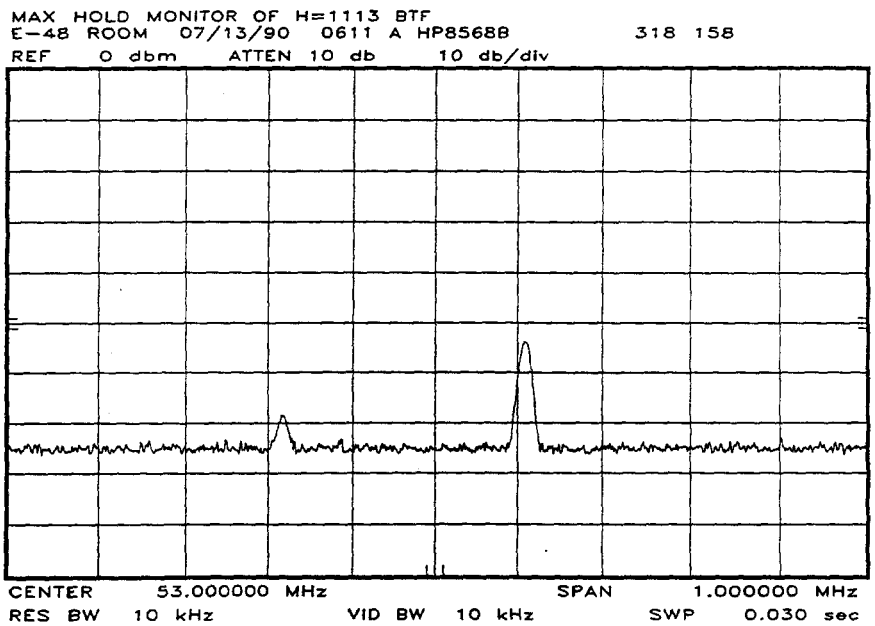

Figure 27: Broadband beam response to a longitudinal transfer function measurement at harmonic 1113. This measurement is identical to the one in figure 19, except that the beam intensity is much smaller (2.64×10^{12} protons). This data clearly shows that this phenomenon does not take place below some beam current threshold.

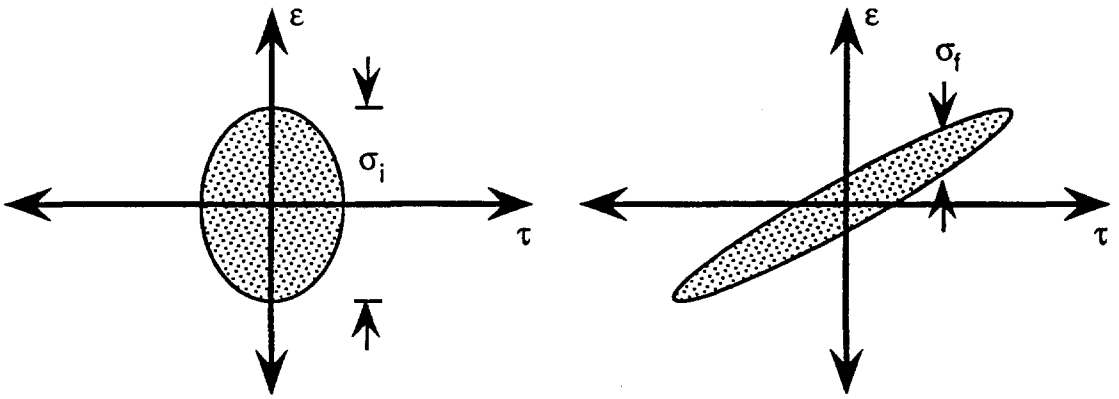

Figure 28: Change in the longitudinal phase space shape of a bunch matched to an RF bucket (left) and some time after the RF drive has been turned off. Note that the instantaneous momentum spread of the beam shrinks as the phase space shape shears linearly.

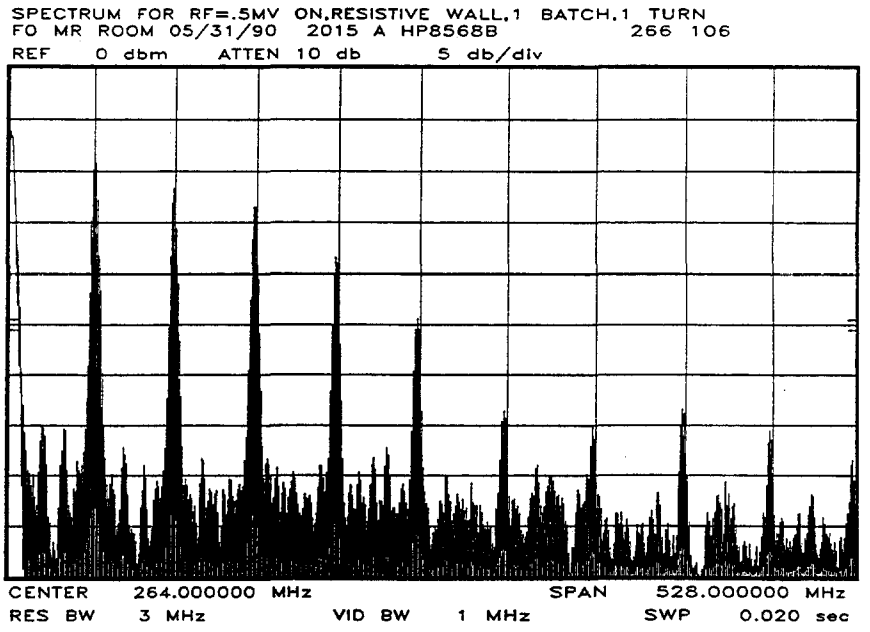

Figure 29: Beam current spectrum in the Main Ring at injection. The frequency scale is from 0 to 528MHz. Harmonics of the 53MHz bunch frequency contain the dominant portion of the beam spectral power.

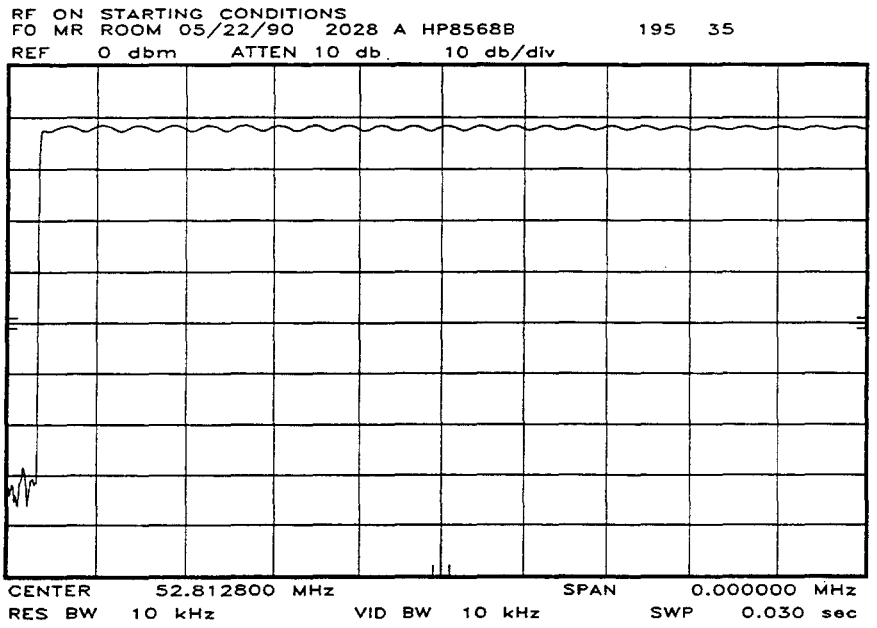

Figure 30: 53MHz component of the Main Ring beam power at injection as a function of time with the RF drive turned on. Due to a small mismatch with the Booster RF system, note that small quadrupole oscillations were initiated.

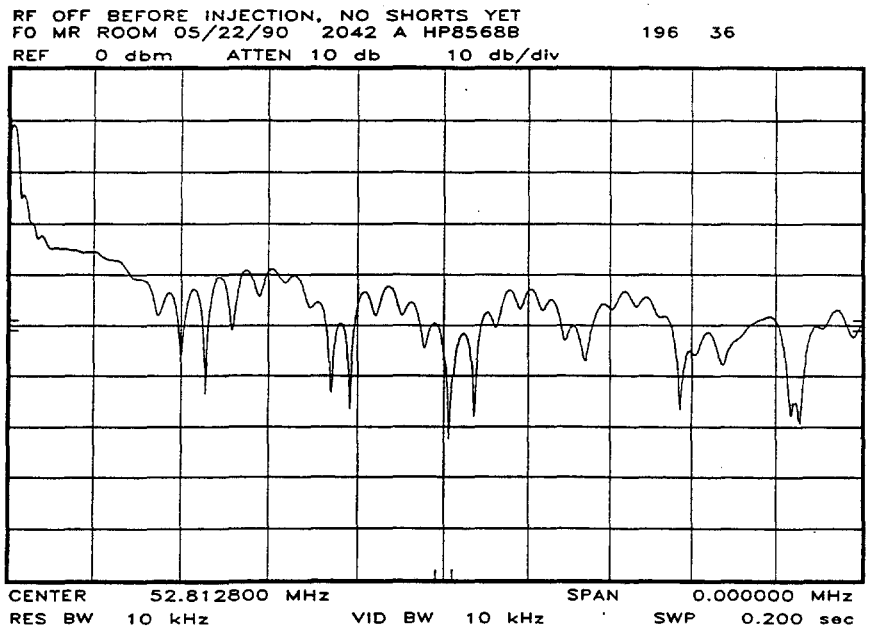

Figure 31: Same as figure 30, except the RF drive was turned off before beam injection. The 53MHz component of the beam current drops by approximately 30db and then starts to oscillate.

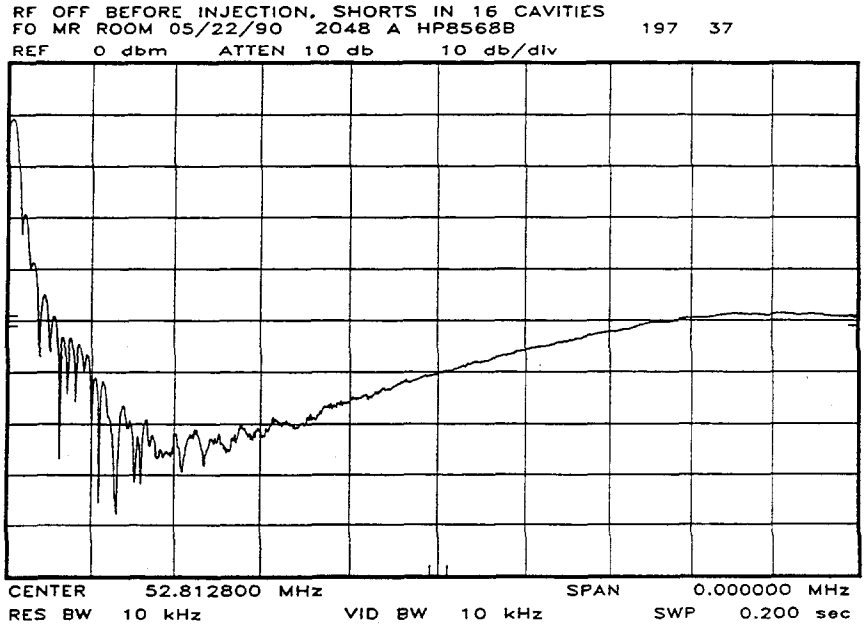

Figure 32: Same as figure 31, but 16 of the 18 RF cavities are shorted. Note that the beam current at 53MHz components drops much further, but then goes into a long wavelength oscillation. The oscillation is a quadrupole oscillation caused by the sudden change from the RF drive phase space bucket to that generated by the beam itself.

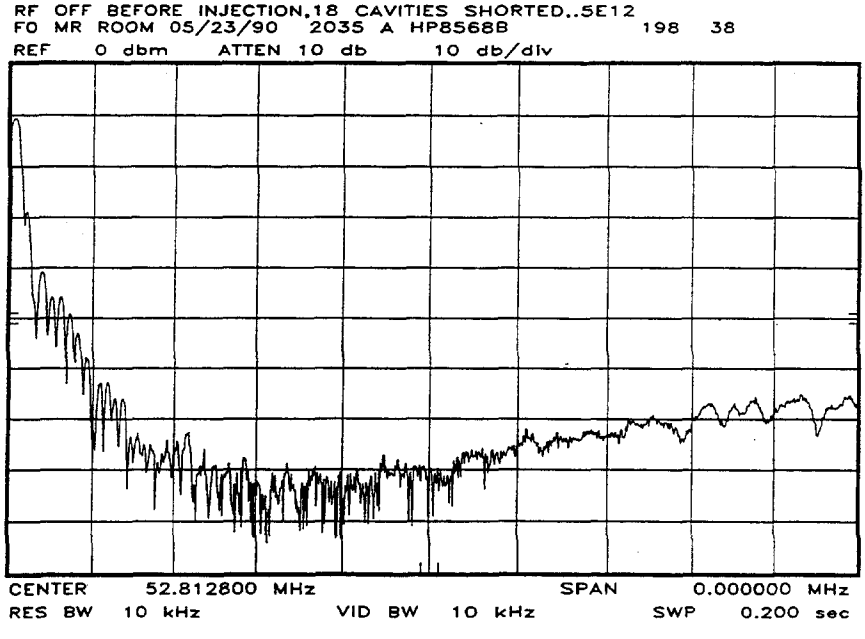

Figure 33: Same as figure 31, but now all 18 RF cavities are shorted. The effect of the beam loading voltage is minimized with only a small residual quadrupole oscillation apparent.

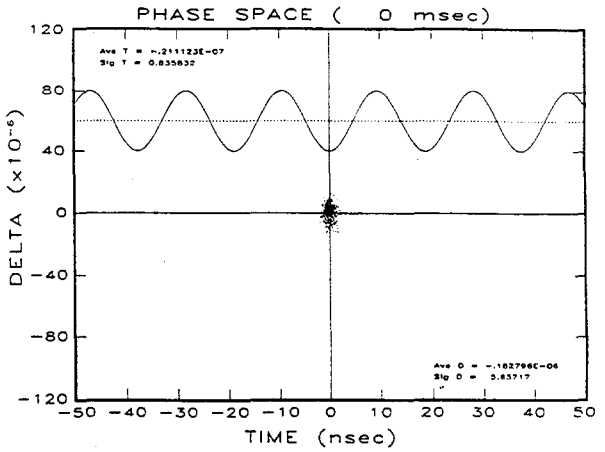

Figure 34: Initial longitudinal phase space distribution used by a multiparticle computer simulation to calculate the phase space evolution of the beam during the debunching process in the presence of beam loading in the RF cavities.

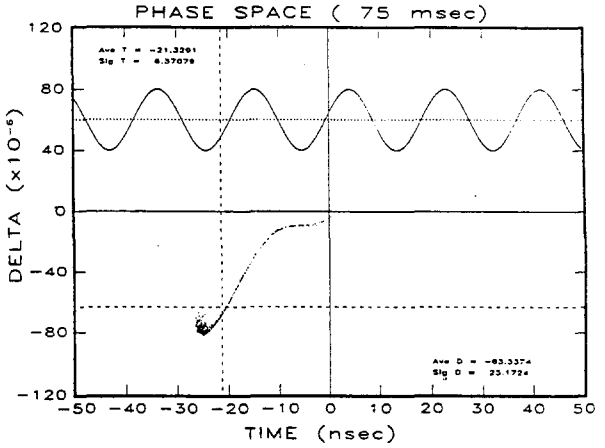

Figure 35: Result of computer simulation after simulating 75ms in the Main Ring. Note that the beam centroid decelerates. In addition, the model of linear phase space shearing is clearly invalid.

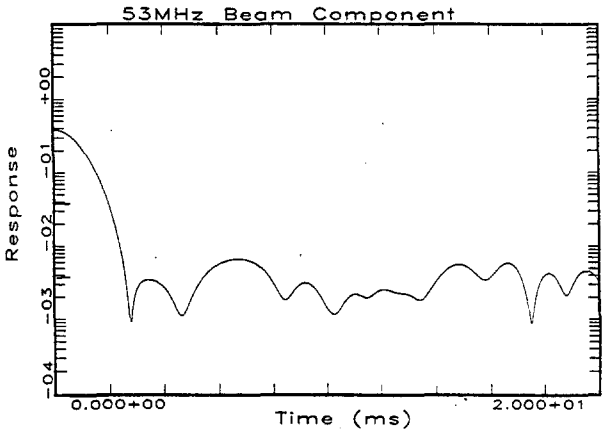

Figure 36: Computer simulation prediction of the 53MHz component of the beam power during the debunching process. The similarity between this result and figure 31 clearly shows that beam loading is the dominant mechanism affecting the beam, and not the Main Ring broadband impedance.

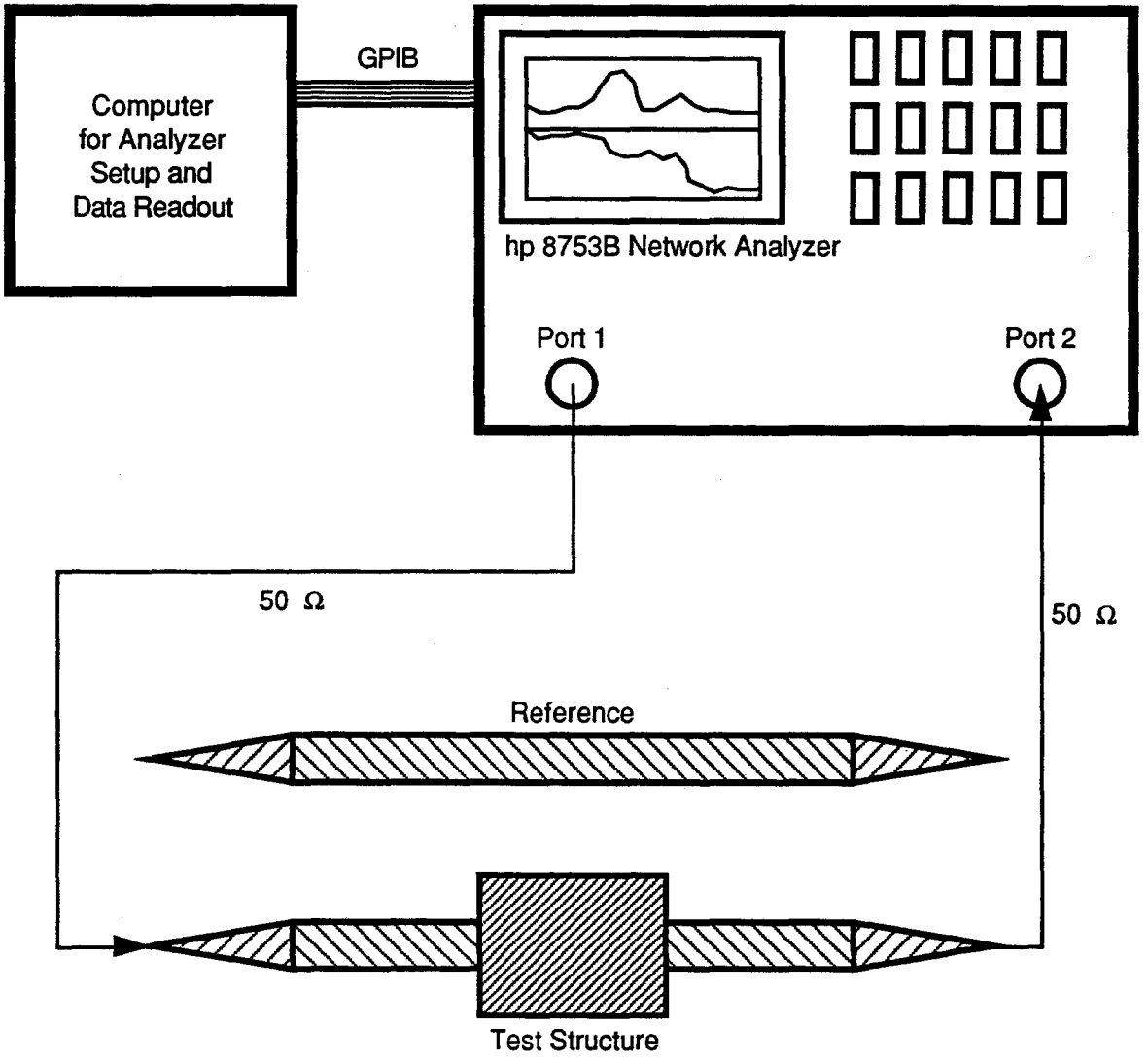

Figure 37: Typical apparatus for measuring longitudinal impedance. The reference pipe is used to subtract the impedance contribution of the impedance matching cones and the signal attenuation in the cables.

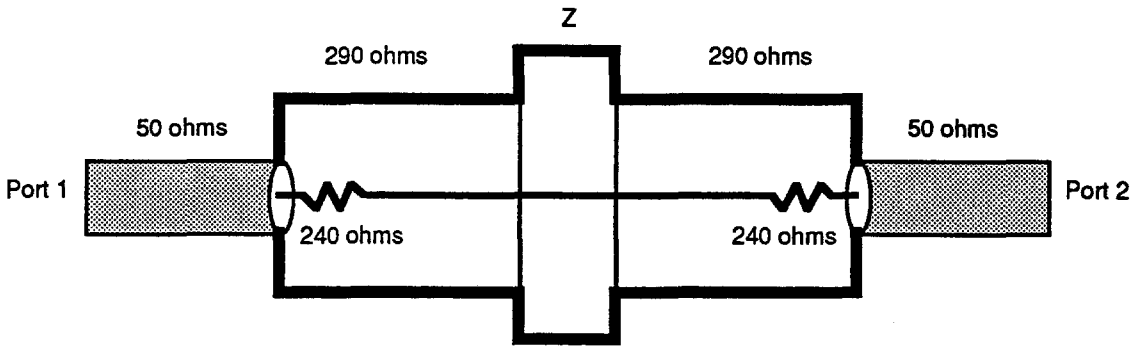

Figure 38: Resistive matching of incommensurate transmission lines used in the past as an alternative to the matching cones used in the apparatus in figure 37.

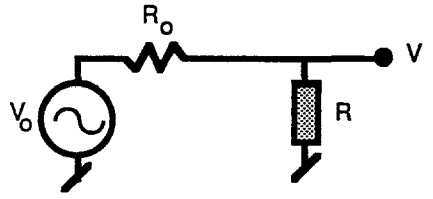

Figure 39: Circuit analog of port 1 of a network analyzer connected to a resistor **R** to ground. It is used to calculate the reflection scattering matrix element S_{11} as a function of the value of **R**.

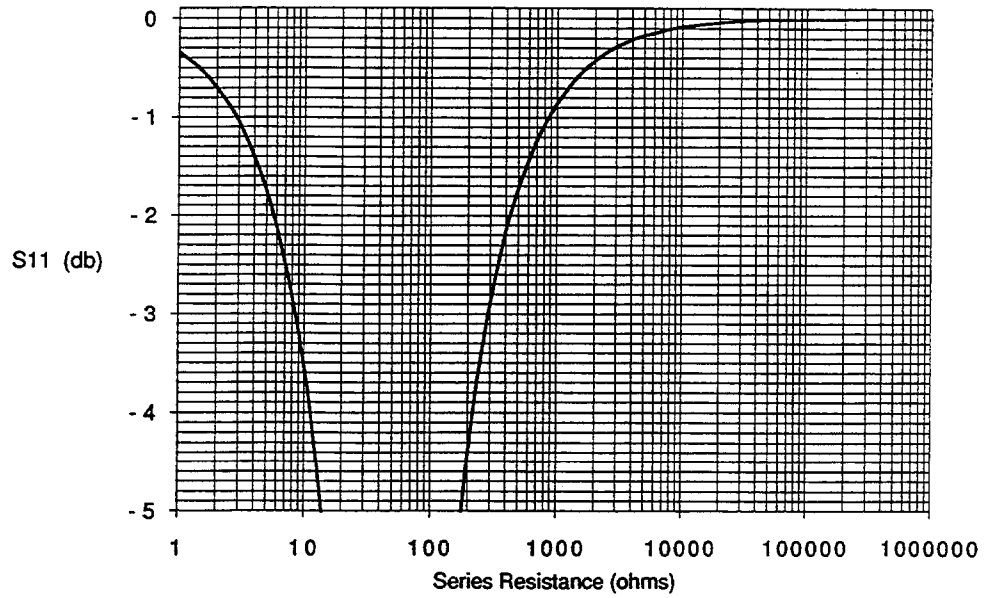

Figure 40: Calculated dependence of S_{11} on series resistance **R** in figure 39 where R_0=50Ω. As expected, reflection is minimized when the series resistance is matched to the source resistance.

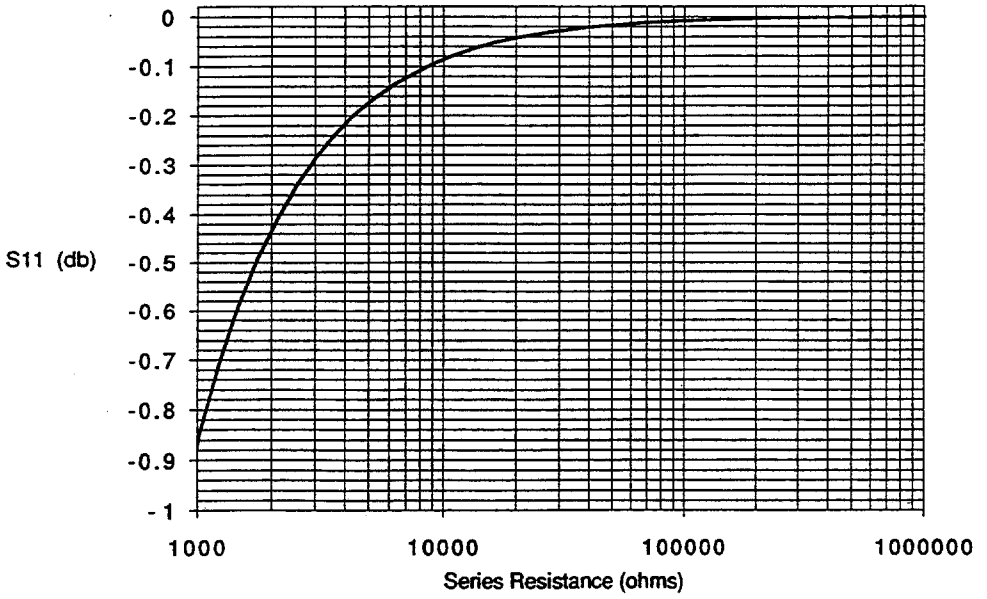

Figure 41: Same as figure 40, but with emphasis on the sensitivity of S_{11} to large series impedance. Note that increased accuracy on the part of the network analyzer is required to distinguish between a completely open circuit and a large series resistance.

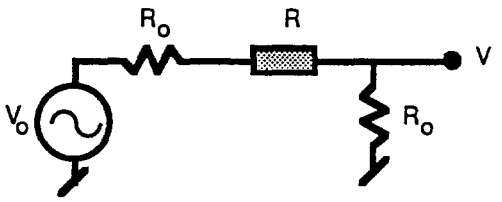

Figure 42: Circuit analog of the longitudinal impedance measurement apparatus sketched in figure 37. Port 1 is the same as in figure 39, port 2 is described by the termination resistor R_0. The DUT has a resistance **R**.

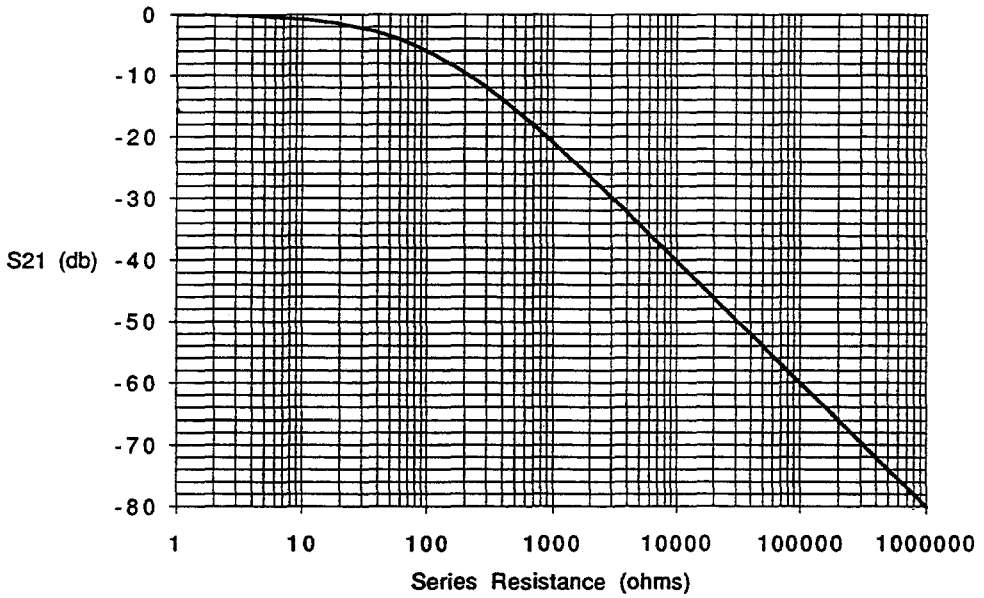

Figure 43: Calculated dependence of S_{21} on series resistance **R** in figure 42 where R_0=50Ω. As the impedance of the DUT increases, the transmission coefficient decreases.

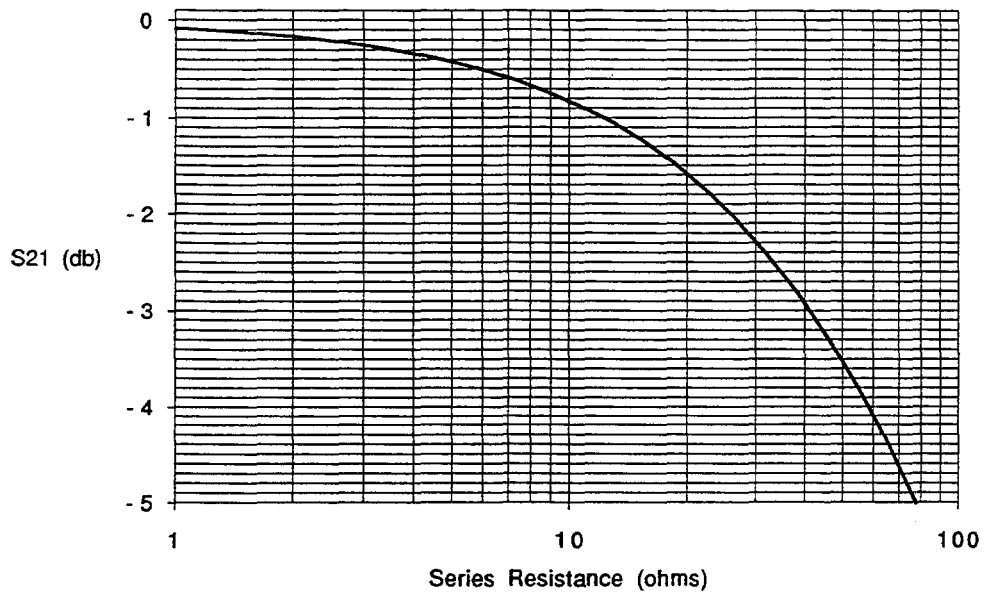

Figure 44: Same as figure 43, but with emphasis on the sensitivity of S21 to small series impedance. An increasing accuracy is required to detect the series resistance as its value decreases.

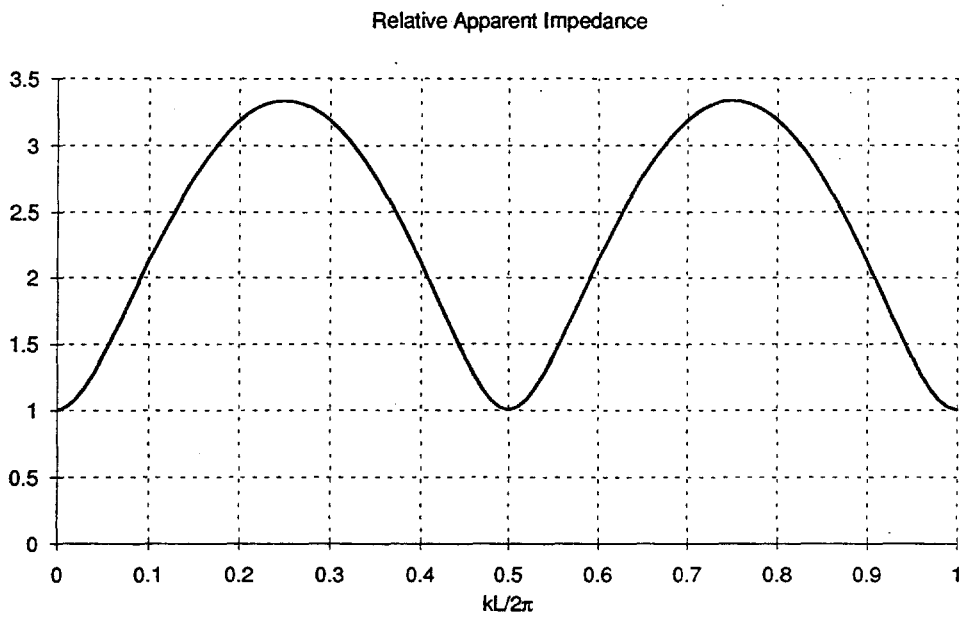

Figure 45: Apparent measured longitudinal impedance for two separated series impedances of value Z/2 relative to the measured value for one lumped series impedance of value Z. This ratio is plotted vs the distance between the two impedances in units of signal wavelength.

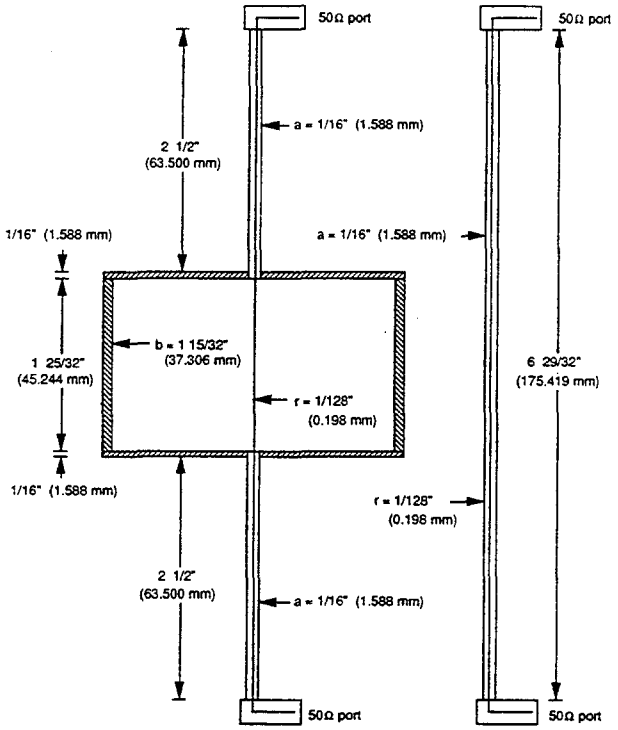

Figure 46: Cross-sectional drawing of the first cavity, and its reference pipe, to be studied in a set of systematic stretched wire longitudinal impedance measurements at Fermilab.

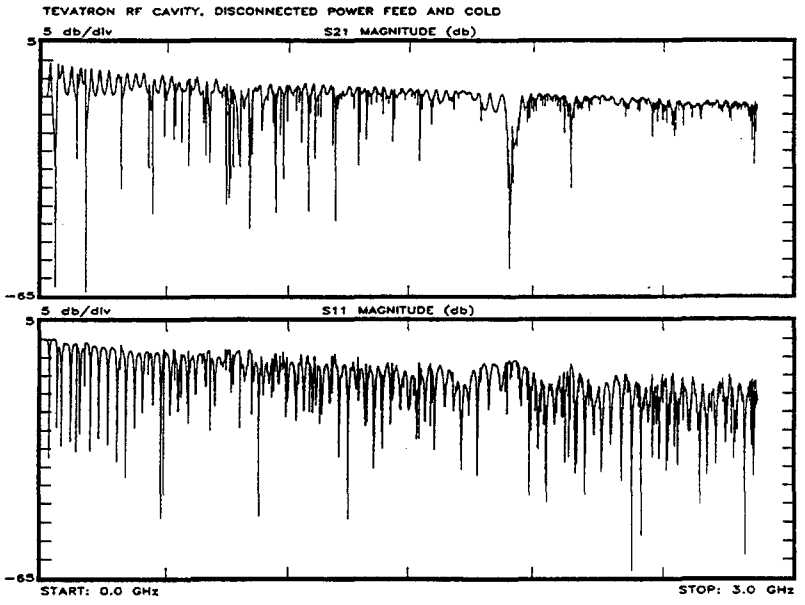

Figure 47: Top frame contains the relative magnitude of the transmitted power through a cold and disconnected Tevatron RF cavity during a stretched wire measurement. Bottom frame contains the reflected power as a function of frequency.

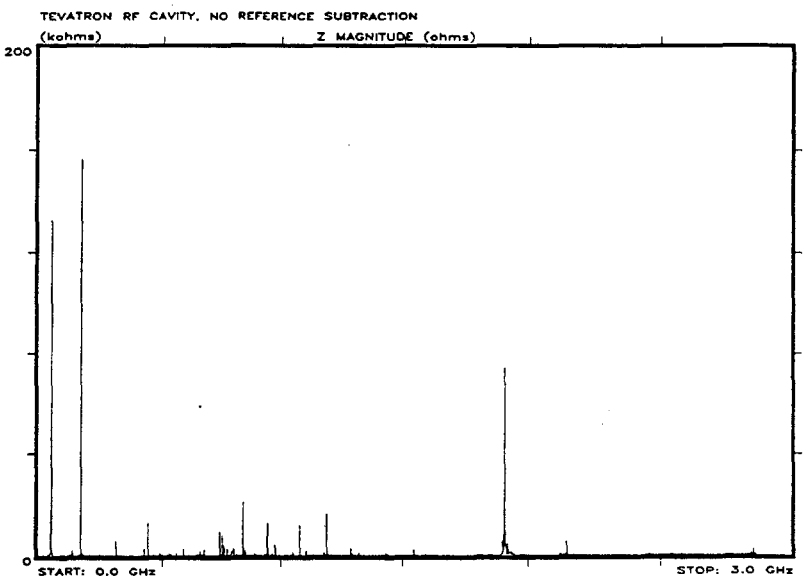

Figure 48: Calculation of the longitudinal impedance of a Tevatron RF cavity using the $S_{2,1}$ data from figure 47. The data is sampled at harmonics of 47.72kHz, and the 53MHz mode fell between the nearest two points. The impedance of this fundamental mode should be 350kΩ.

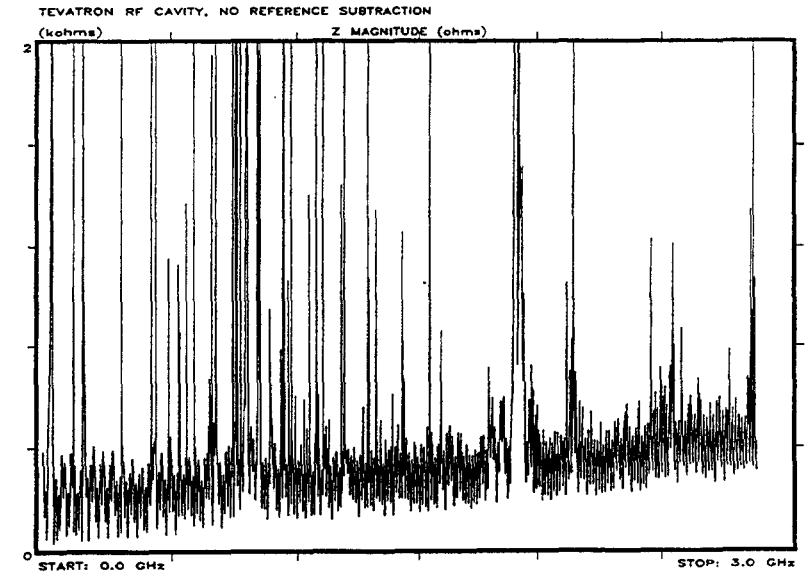

Figure 49: Vertical scale reduced by a factor of 100 to look at the low impedance background of the RF cavity longitudinal impedance spectrum.

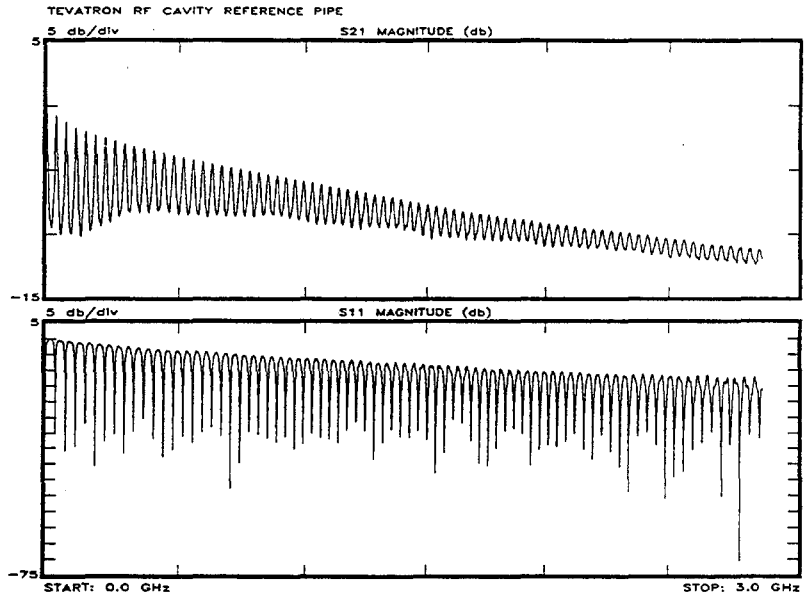

Figure 50: Measurement of the transmission and reflection coefficients of the reference pipe for the Tevatron RF cavity impedance measurements.

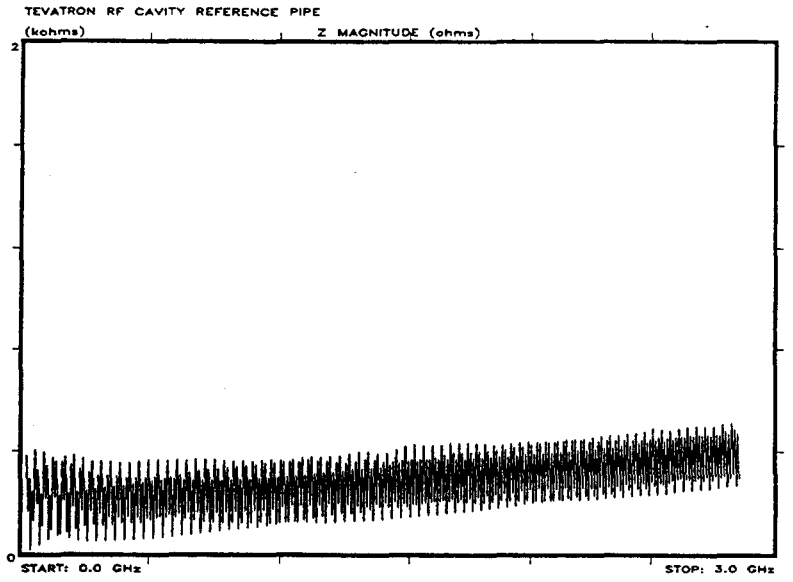

Figure 51: Calculation of the longitudinal impedance of the Tevatron RF cavity reference pipe using the S_{21} data from figure 50.

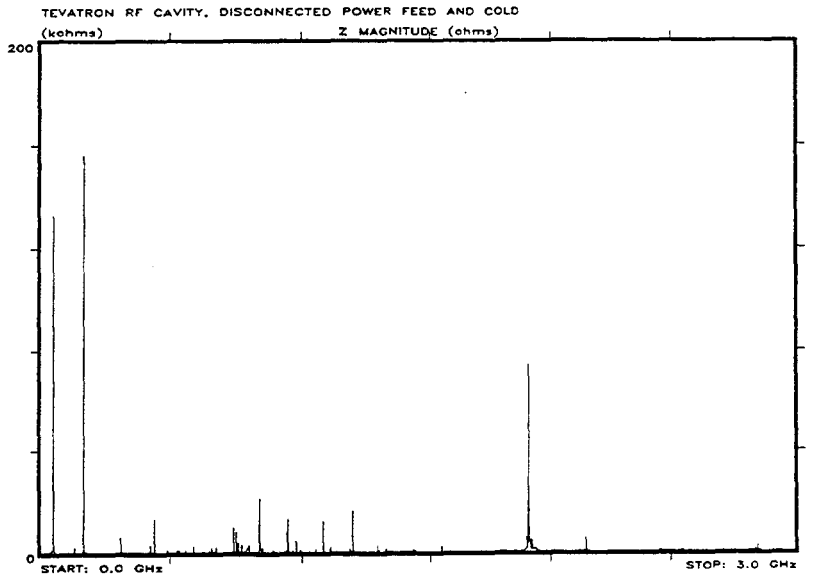

Figure 52: Improved calculation of the longitudinal impedance spectrum of a cold and disconnected Tevatron RF cavity. The data in figure 51 was subtracted from the data in figure 48 appropriately.

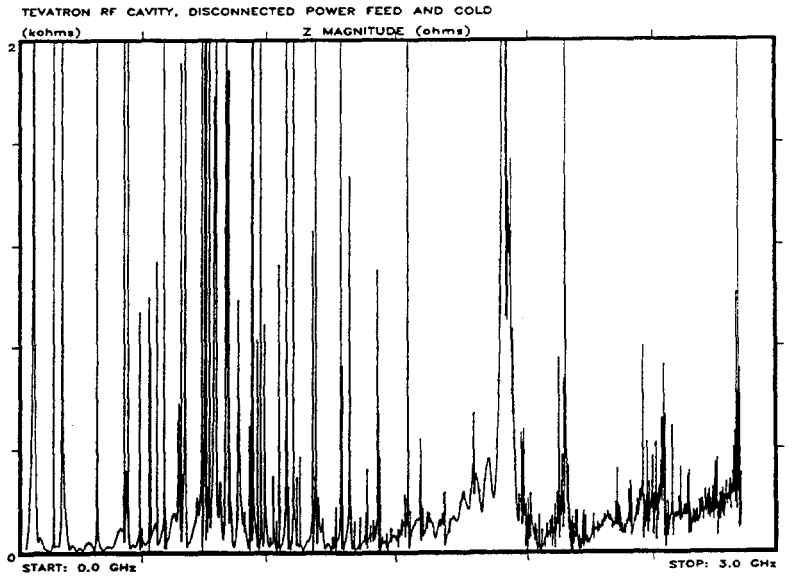

Figure 53: Vertical scale reduced by a factor of 100 to look at the low impedance background of the RF cavity longitudinal impedance spectrum. There is no evidence of a broadband impedance contribution from the cavity.

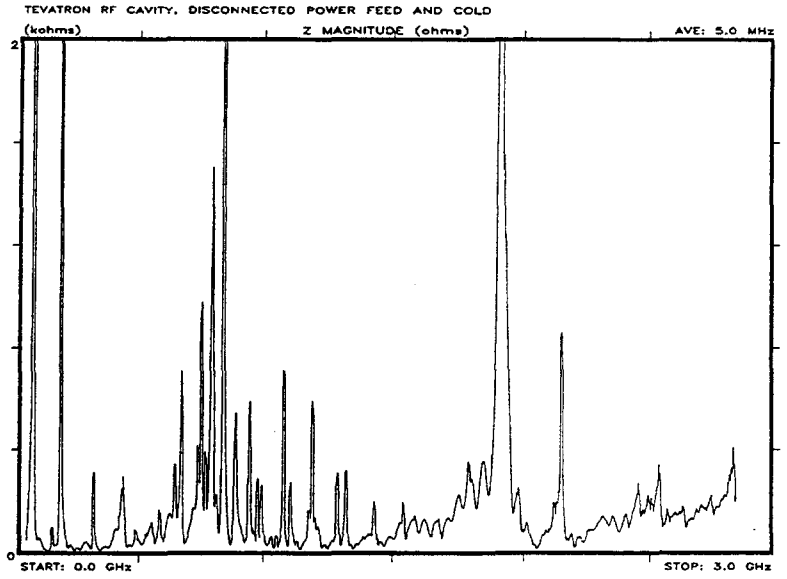

Figure 54: Data in figure 53 smeared using a 5MHz half width square averaging window sweeping across the data in order to simulate a video bandwidth filter. The purpose of this smearing is to try and include dense mode line distributions into a broadband impedance estimate.

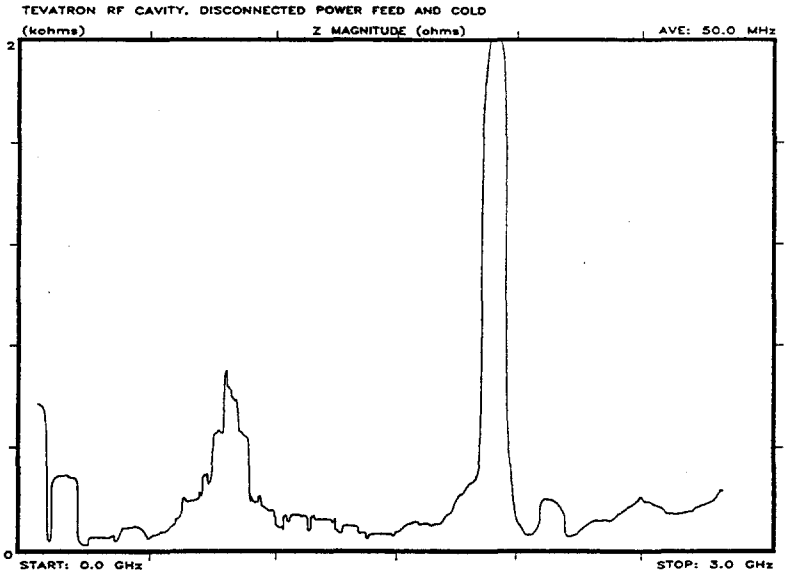

Figure 55: Same as figure 54, except using a wider 50MHz smearing window. Still no sign of a significant broadband impedance contribution to the Tevatron longitudinal impedance from the RF cavities.

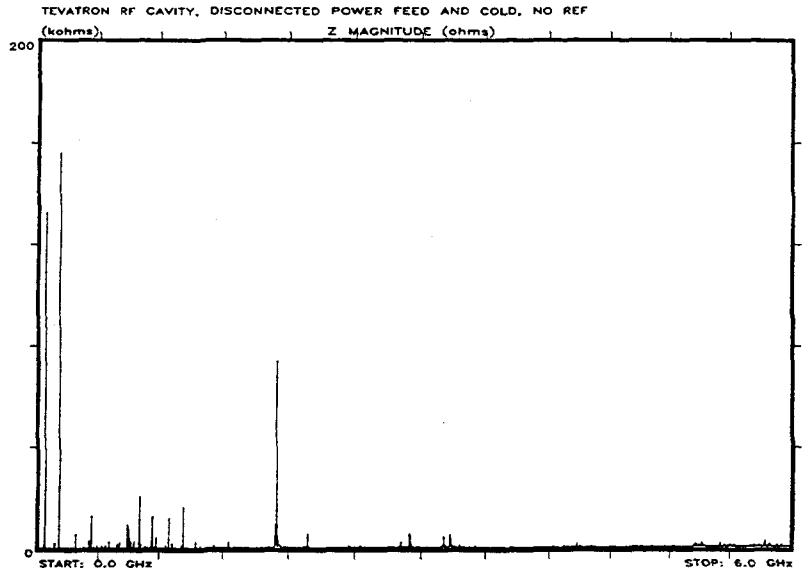

Figure 56: Tevatron RF cavity longitudinal impedance measurement using transmission coefficient data up to 6GHz. No reference pipe subtraction was done. There are no significant modes above 1.8GHz.

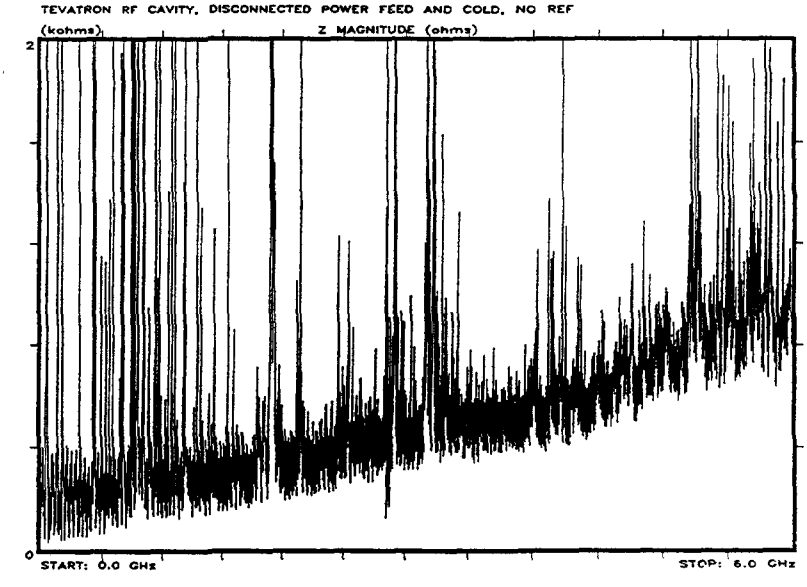

Figure 57: Vertical scale reduced by a factor of 100 over data in figure 56. If the slope in the reference pipe data in figure 51 is extrapolated to 6GHz and subtracted from this data, there is still no evidence of a broadband impedance contribution from the cavity.

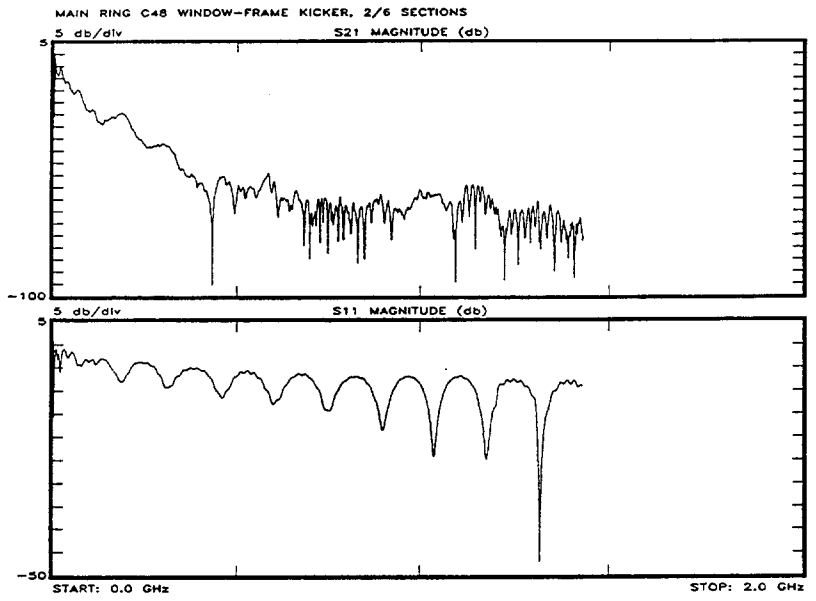

Figure 58: Top frame contains the relative magnitude of the transmitted power through two out of six sections of a Window-frame kicker magnet during a stretched wire measurement. Bottom frame contains the reflected power as a function of frequency. The magnet was similar in cross section to the sketch in figure 6, except to copper strips were inserted into the ferrite core.

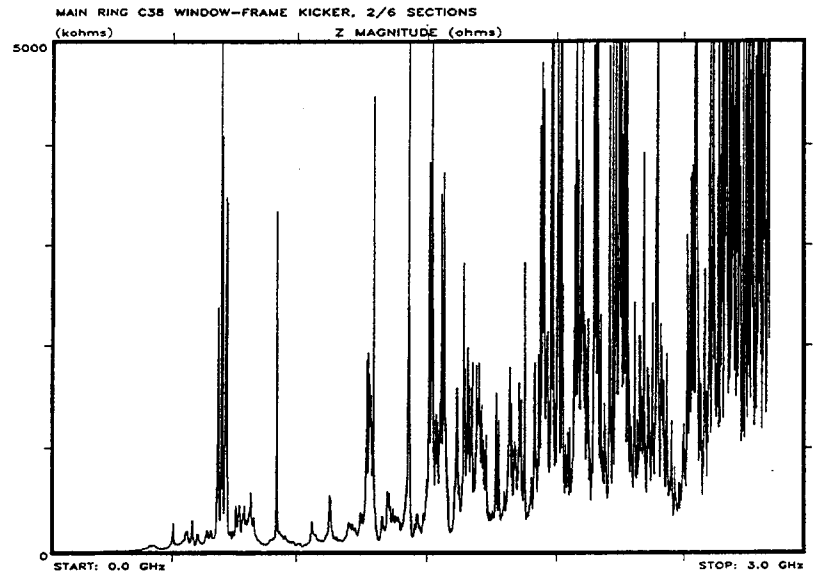

Figure 59: Using S_{21} measurements similar to the ones in figure 58 but extending up to 3GHz, the longitudinal impedance of the pair of Window-frame kicker magnets were calculated. The above plot is on an unusually large vertical scale.

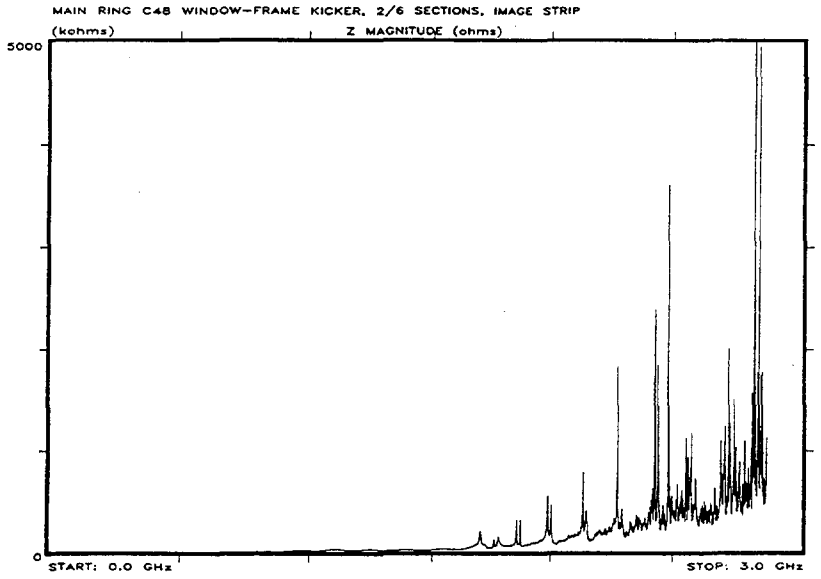

Figure 60: Same as figure 59, except that copper image strips as seen in figure 6 were added. Note the drastic reduction in longitudinal impedance, especially at frequencies above 1GHz.

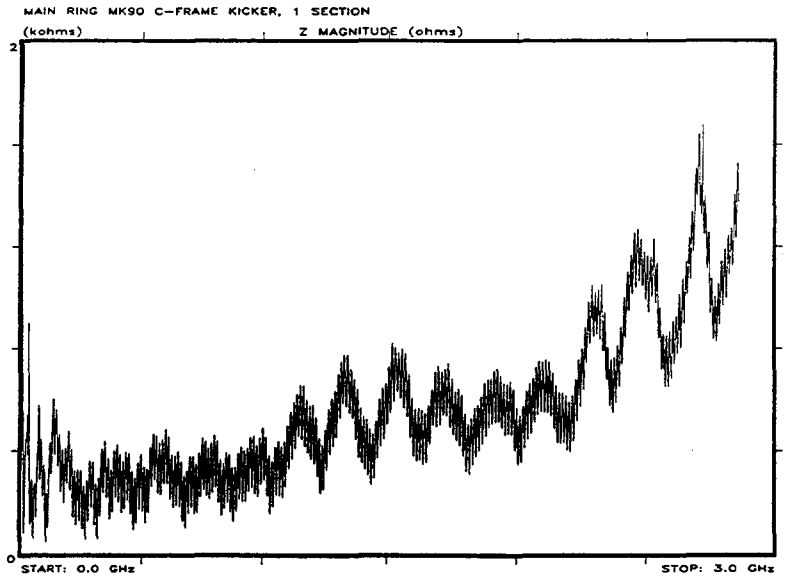

Figure 61: Result of a stretched wire longitudinal impedance measurement of a C-magnet type kicker magnet section with a cross section similar to the sketch in figure 5. No reference pipe measurements were made. Even so, note that the maximum impedance is much smaller than that in the Window-frame type kicker case.

References

[1] H. Hahn and F. Pedersen, "On Coaxial Wire Measurements of the Longitudinal Coupling Impedance", BNL 50870 (1978).

[2] P. Wilson, "High Energy Electron Linacs: Application to Storage Ring RF Systems and Linear Colliders", Physics of High Energy Particle Accelerators, ed. R.A. Carrigan, F.R. Huson, and M. Month, AIP (1982), p.450.

[3] J.D. Jackson, Classical Electrodynamics, John Wiley & Sons (1975), p.355.

[4] K.Y. Ng, Part. Acc. 23 (1988), p.93.

[5] J. Marriner, "Measuring the Wall Impedance with the Network Analyzer", internal Fermilab memo PBAR- 4053 (1985).

[6] Design Report Tevatron I Project, Fermi National Accelerator Laboratory (1983).

[7] C.D. Moore, et. al., "Single Bunch Intensity Monitoring System Using an Improved Wall Current Monitor", Proc. IEEE Part. Acc. Conf., Chicago (1989), p.1513.

[8] J. Borer, et. al., "Non-destructive Diagnostics of Coasting Beams with Schottky Noise", IXth Int. Conf. on High Energy Acc., SLAC (1974), p.53.

[9] J.E. Griffin, private communication.

[10] J.E. Griffin, et. al., "Time and Momentum Exchange for Production and Collection of Intense Antiproton Bunches at Fermilab", IEEE Trans. Nucl. Sci., Vol. NS-30 (1983), p.2630.

[11] V. Bharadwaj, et. al., "Operational Experience with Bunch Rotation Momentum Reduction in the Fermilab Antiproton Source", Proc. IEEE Part. Acc. Conf., Washington D.C. (1987), p.1084.

[12] J.E. Griffin, J.A. MacLachlan, and J.F. Bridges, "Preparation and Study of Bunches Containing 1011 protons in the Fermilab Main Ring", IEEE Trans. Nucl. Sci., Vol. NS-28, No. 3 (1981), p.2037.

[13] P. Martin, K. Meisner, and D. Wildman, "Improvements in Bunch Coalescing in the Fermilab Main Ring", Proc. IEEE Part. Acc. Conf., Chicago (1989), p.1827.

[14] J. Crisp and L. Evans, "Measurement of the Main Ring Longitudinal Impedance", Internal Fermilab memo EXP-139 (1987).

[15] D. Boussard, CERN/LABII/RF/Int./75-2 (1975).

[16] K.Y. Ng, "Measurement of the Main Ring Longitudinal Impedance by Debunching", Internal Fermilab memo TM-1389 (1986).

[17] F. Caspers, "Beam Impedance Measurements Using the Coaxial Wire Method", CERN PS/88-59 (AR/OP), (1988).

[18] H. Hahn and F. Pederson, "On Coaxial Wire Measurements of the Longitudinal Coupling Impedance", Internal Brookhaven National Laboratory memo BNL-50870 (1978).

[19] R.A. Dehn, Q.A. Kerns, and J.E. Griffin, "Mode Damping in NAL Main Ring Accelerating Cavities", IEEE Trans. Nucl. Sci., Vol. NS-18, No. 3 (1971), p.260.

[20] F. Voelker and G. Lambertson, "Beam Impedance of Ferrite Kicker Magnets", Proc. IEEE Part. Acc. Conf., Chicago (1989), p.851.

[21] M. Foley, private communication (1990).

[22] K.Y. Ng, private communication (1989).

CERN EUROPEAN ORGANISATION FOR NUCLEAR RESEARCH

CERN PS/90-71 (PA)
November 1990

TRANSVERSE IMPEDANCE MEASUREMENTS

R. Cappi (CERN-PS)
G. Jackson (FERMILAB, Chicago)

Contribution to the Proceedings of the FERMILAB III Instabilities Workshop
Fermilab (June 1990)

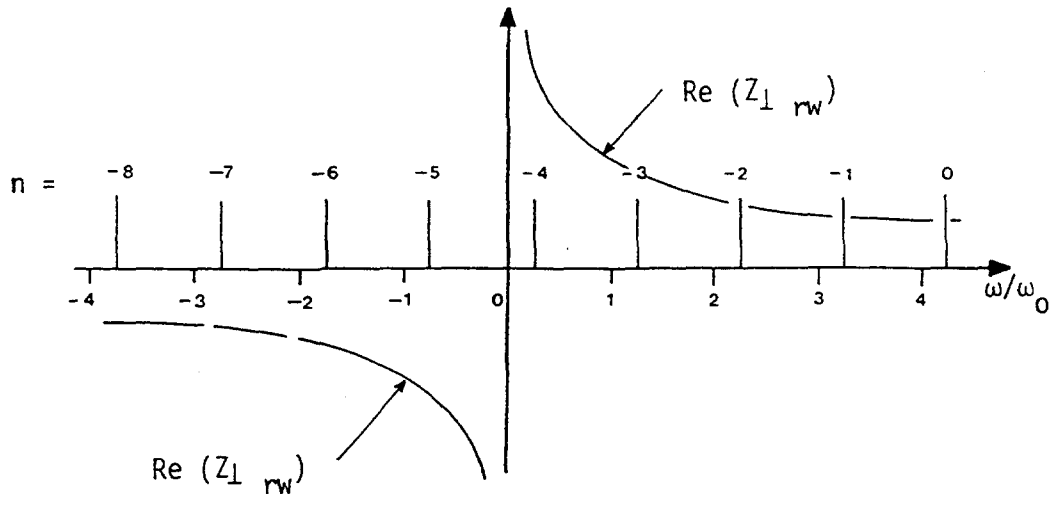

Fig. 1: Transverse mode spectrum and real part of resistive wall impedance

As already mentioned, only the lines "sampling" regions where $(\mathrm{Re}\, Z_\perp) < 0$ are potentially unstable. In our example, only the modes n=-5, -6, -7,..., i.e., the modes corresponding to

$$|\, n \,| > Q \quad \text{and} \quad n < 0$$

also named "slow-waves" [4] are unstable.

Remarks:

a) In reality the spectrum of Fig. 1, when measured with a spectrum analyser shows up as shown on Fig. 2 (power spectrum)

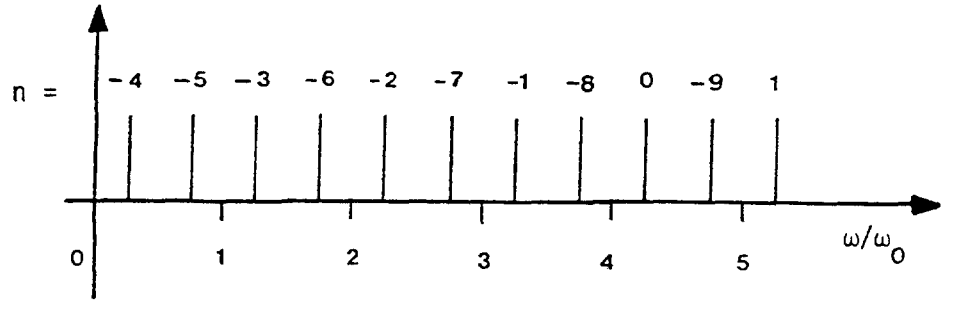

Fig. 2: Mode power spectrum as measured with a spectrum analyser (with frequency spread the lines are widened)

b) The n=-5 mode is the most dangerous as it samples the largest value of $(\mathrm{Re}\, Z_\perp)$.

c) For a narrow band resonator at ω_r, only the modes where $(n+Q)\,\omega_o \cong \omega_r$ will be excited.

2. Landau Damping

The spectral lines (betatron sidebands) at ω_β have a width given by

$$\delta\omega_\beta = \delta\,[(n+Q)\,\omega_o\,] = (\,Q\,\xi - n\,\eta\,)\,\frac{dp}{p}\,\omega_o$$

where: ξ = chromaticity $= \dfrac{dQ/Q}{dp/p}$

η = frequency slip factor $= -\dfrac{d\omega/\omega}{dp/p} = \gamma_t^2 - \gamma^2$

γ_t = γ at transition

dp/p = relative momentum spread (FWHM)

If the rise time τ_r [where $1/\tau_r = -\,\mathrm{Im}\,(d\omega_\beta)$] of the instability is

$$\tau_r > \frac{1}{\Delta\omega_\beta}$$

or in other words if the coherent frequency shift $\mathrm{Im}\,(d\omega_\beta)$ is smaller than the incoherent frequency spread $\Delta[(n+Q)\omega_o]$ then the instability is Landau damped.

In the approximation where no octupoles effects are present, the incoherent frequency spread is equal to zero (or very small) for

$$n = \frac{Q\xi}{\eta}$$

that is for $$\omega_\beta = Q\omega_o\,(\frac{\xi}{\eta} + 1) \equiv \frac{Q\omega_o\xi}{\eta} = \omega_\xi$$

there will be no Landau damping and the mode closest to ω_ξ will be easily unstable. This effect can be useful to probe the transverse impedance over a large range of frequencies. The advantages of using a debunched beam is that the unstable modes emerge only at frequencies where $\mathrm{Re}\,(Z_\perp) < 0$. Using bunched beams, aliasing effects can produce ambiguities in the frequency location of the impedance.

The frequency ω_ξ can be varied by changing the chromaticity value. This allows to probe regions of frequencies where $\mathrm{Re}\,(Z_\perp) < 0$.

By measuring the instability rise time τ_r the value of $\mathrm{Re}\,(Z_\perp)$ can be evaluated as

$$\mathrm{Re}\,(Z_\perp(\omega_\beta)) = \frac{4\pi\,Q\,\gamma\,E_o/e}{c\,I\,\tau_r}$$

3. Experimental Procedure

3.1. Set the beam intensity to an average value.

3.2. Debunch the beam by reducing the RF voltage to 0 and if possible successively on each cavity to minimise beam loading effects.

3.3. Switch off octupoles, if any.

3.4. Set the chromaticity to a given value.

3.5. Check on the spectrum analyzer (connected to a wide band transverse pick-up) if any instability appears at $\omega = \omega_\xi$.... or elsewhere.

If instabilities appear elsewhere reduce the beam intensity.

3.6. If an instability appears close to ω_ξ, measure the rise time by tuning the spectrum-analyser, in receiver mode, to the unstable mode. (N.B. : the rise time can easily be measured as the time interval between two points separated by 20 log e ≡ 9 db in amplitude).

3.7. Repeat from 3.4. with another value of chromaticity.

Remarks : In practice, one can expect to probe three main frequency domains, respectively :

I) $0 \div 5$ MHz II) $5 \div 100$ MHz III) $100 \div 500$ Mhz approx.

In the first, low frequency domain, the resistive wall impedance should dominate. In the second, some transverse higher modes in RF cavities (or other resonators) can eventually be discovered. While in the third interval the vacuum chamber broad band impedance can be measured as

$$\mathrm{Re}\,(Z_\perp(\omega)) = \frac{2c}{b^2\omega_o}\,\mathrm{Re}\,(\frac{Z_{//}}{n})$$

when $Z_{//}/n$ is the broadband longitudinal impedance of the vacuum chamber divided by

$$n = \omega/\omega_o.$$

II) $Z_\perp$ MEASUREMENTS WITH BUNCHED BEAMS

1. A Reminder of the Basic Theory

As in the previous chapter the real frequency shift $\mathrm{Re}\,(\Delta\omega_{\beta m})$ of the betatron frequency $\omega_{\beta m} = (n+Q)\omega_o + m\omega_s$ for a bunched beam is given by [3]

$$\mathrm{Re}\,(\Delta\omega_{\beta m}) = -\frac{N_b\, e\, c}{4\pi\, Q\, E/e\, 4\,\sigma_\tau} \cdot \frac{1}{(m+1)} \cdot \mathrm{Im}\,(Z_\perp)$$

where: N_b is the number of particles in the bunch,

σ_τ is the r.m.s. bunch length in s;

m is the mode of oscillation = 0, 1, 2,...

ω_s is the synchrotron angular frequency and

$Z_\perp$ is the transverse wideband impedance given, for simple round structures, by $Z_\perp = \dfrac{2c}{b^2\omega_o}\dfrac{Z_{//}}{n}$

and $\mathrm{Im}\,(Z_\perp)$ is assumed constant all over the spectrum of the oscillation mode at least for the lowest mode considered herein (m = 0). Such a simplification is generally valid for long (proton) bunches.

Remark: An estimate of the Transverse Mode Coupling instability threshold is given by: $\mathrm{Re}\,(\Delta\omega_{\beta o}) \equiv \omega_s / 2$

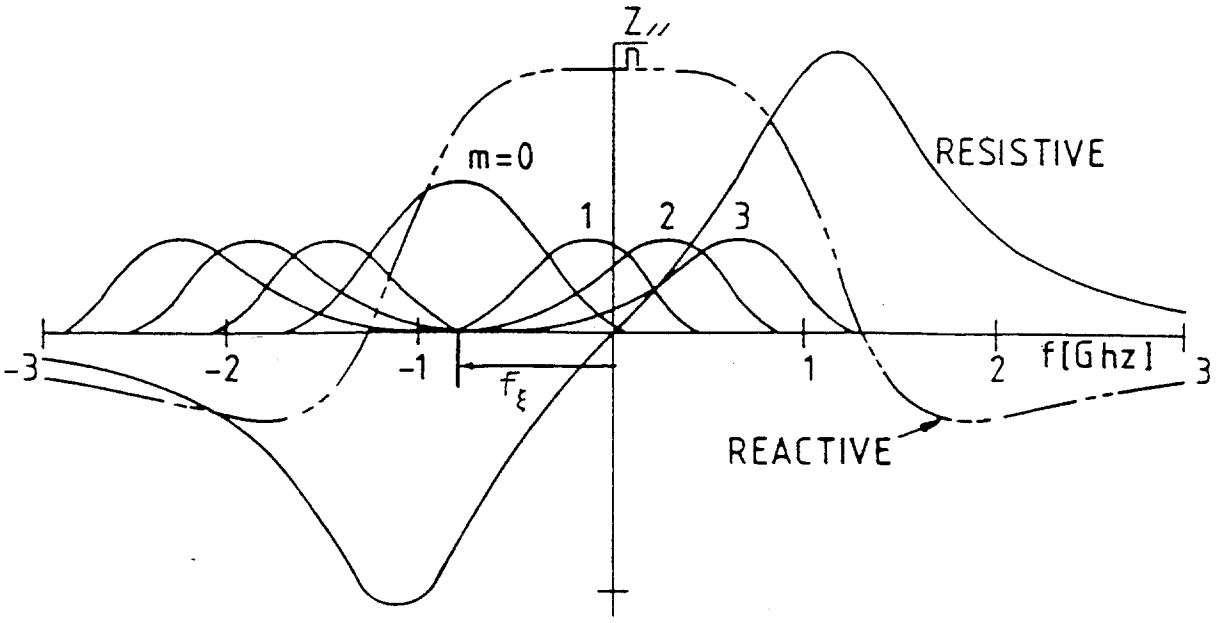

Fig. 3: Shape of the reactive and resistive part of $Z_{//}$ / n (or equiv. $Z_\perp$) versus frequency as well as the shape of the relative amplitude of varius transv. modes for a bunch above transition in a machine with $\xi < 0$.

Measuring the frequency shift of the m = 0 mode as function of N_b/σ_τ one can estimate the value of Im ($Z_\perp$).

2. Experimental Set-Up

As the expected frequency shifts are rather small (some hundred Hz or less, see for example the numerical example below) one has to adopt FFT techniques to improve the frequency resolution as well as shortening the measurement time. As the m = 0 mode is maximum at $\omega = \omega_\xi$, if $\xi \neq 0$ the signal has to be down converted in order to be FFT analysed at low frequency. See Fig. 4.

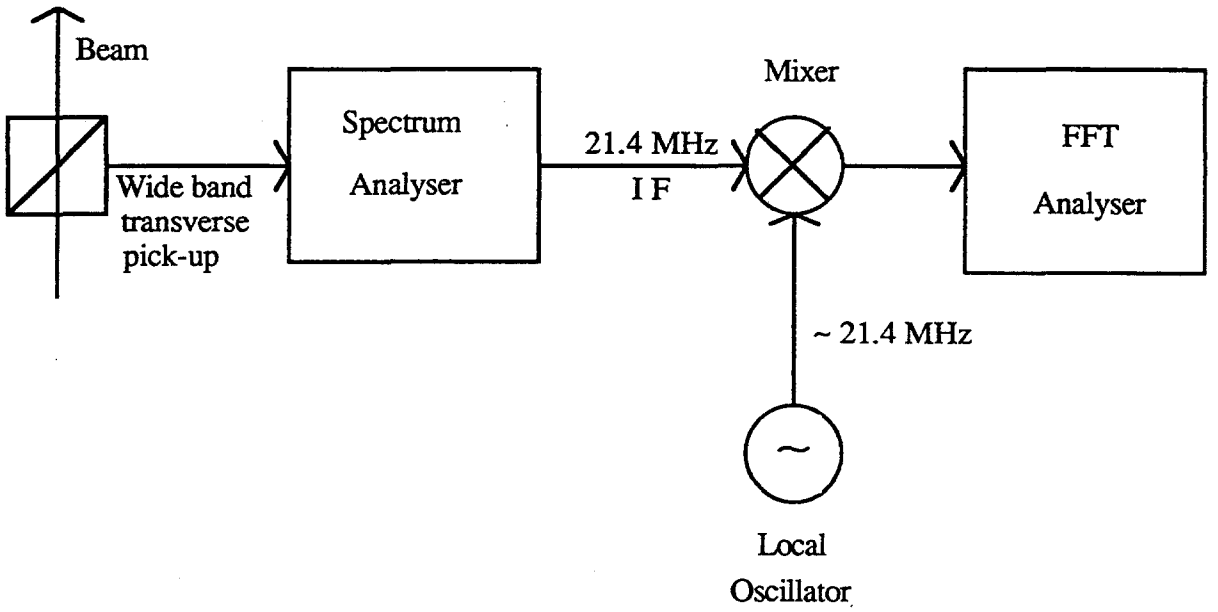

Fig. 4: The signal from a wide band transverse pick-up is first down converted at 21.4 MHz by using a swept-filter spectrum analyser tuned in receiver mode (zero span) to a $\omega_{\beta o} \cong \omega_\xi$. A second local oscillator set at $f \cong 21.4$ MHz mixes the 21.4 1F output of the spectrum analyser down to low-frequency (some KHz) at the input of a FFT analyser (locking the local oscillator to the RF frequency can avoid the frequency shift due to the β variations, if any).

Beam excitation at $\omega_{\beta o}$ as to be provided by powering, for example, a high frequency kicker with a sweeping sinewave synchronised to the measurement.

Numerical example (Machine : Fermilab Booster):

$E = 8$ GeV $\quad R = 75$m $\quad Q = 6.8$ $\quad \beta \cong 1$

$N_b = 3.10^{10}$ p/b $\quad 4\sigma_\tau = 10$ ns $\quad b = 3$ cm

this gives: $\quad \mathrm{Re}(\Delta\omega_{\beta o}) \cong 270.10^{-6}\, Z_\perp$

guessing a $\quad \frac{Z_{//}}{n} \cong 200\ \Omega$ then $Z_\perp = \frac{2c}{b^2\omega_o}\frac{Z_{//}}{n} \cong 30\ \mathrm{M\Omega/m}$

so $\quad \mathrm{Re}\ (\Delta\omega_{\beta o}) / 2\pi \cong 1$ KHz

In order to measure such a frequency shift with a resolution of ~ 10% (100 Hz) one needs a measurement time of ~ 10 ms.

Numerical example No 2 (Machine : Fermilab MR):

$R = 1000$m $\quad Q = 20$ $\quad n = 10^{-2}$ $\quad b = 3$ cm

$E = 8$ GeV $\quad Nb = 10^{10}$ ppb $\quad 4\,\sigma_t = 10$ ns $\quad Zn/n = 10\ \Omega$

this gives: $\quad \mathrm{Re}\ (\Delta\omega_{\beta o}) = 30.10^{-6}\ \mathrm{Im}\ (Z_\perp)$

if: $\quad Z_\perp = \frac{2c}{b^2\omega_o}\frac{Z_{//}}{n} = 22\ \mathrm{M\Omega/m}$

so: $\quad \mathrm{Re}\ (\Delta\omega_{\beta o}) / 2\pi \cong 83$ Hz

REFERENCES

1. See for example: J. Gareyte, F. Sacherer, "Head-Tail Type Instabilities in the CERN-PS and Booster", Proc. 9th International Conference High Energy Accelerators, Stanford 1974, p. 341.

2. F. Sacherer, "Transverse Beam Instabilities-Theory, Proc. 9th International Conference High Energy Accelerators, Stanford 1974, p. 347.

3. B. Zotter and F. Sacherer, "Transverse Instabilities of Relativistic Particle Beams in Accelerators and Storage Rings", Proc. 1st Course of International School of Particle Accelerators Erice 1976, CERN 77-13, p. 175-218;

   N.B. : In contrast to the solution $e^{-i\omega t}$ used in these references, we use $e^{j\omega t}$ in the present note.

4. J. Gareyte, "Beam Observation and the Nature of Instabilities", CERN-SPS / 87-18 (AMS).

☆ U.S. GOVERNMENT PRINTING OFFICE: 1990—543-569